

# Toward Pixel-wise Vision in Epiretinal Visual Prosthesis

Vom Promotionsausschuss der  
Technische Universität Hamburg-Harburg  
zur Erlangung des akademischen Grades  
Doktor-Ingenieur (Dr.-Ing.)

genehmigte Dissertation

von  
Diego Luján Villarreal

aus  
Monterrey, Nuevo León, México.

2017

1. Gutachter: Prof. Dr.-Ing. Wolfgang H. Krautschneider
2. Gutachter: Prof. Dr.-Ing. Hoc Khiem Trieu

Tag der mündlichen Prüfung: Montag, 13. November 2017

# TABLE OF CONTENTS

Abstract .....	8
Preface .....	10
Definition of Dissertation .....	10
Proposal for Pixel-wise Vision .....	12
Challenges Addressed .....	14
Tasks Related to a System Block Diagram .....	15
Structure of Dissertation .....	16
Nomenclature .....	17
 Chapter 1 Introduction to Visual Prosthesis	
1.1 Visual Prosthetic Considerations .....	18
1.1.1 Visual Prosthetics – Definition and Aims .....	18
1.1.2 Retinitis Pigmentosa .....	19
1.1.3 Age-Related Macular Degeneration .....	19
1.2 Minimum Requirements in Artificial Vision .....	20
1.3 Morphological Bases of Visual Prosthesis .....	21
1.4 Visual Prosthesis Design Principle .....	21
1.4.1 Epiretinal Visual Prosthesis .....	21
1.4.2 Subretinal Visual Prosthesis .....	22
1.5 An Overview of Clinical Trials of Current Visual Prosthesis .....	23
1.5.1 Argus I Epiretinal Prosthesis .....	24
1.5.2 Argus II Epiretinal Prosthesis .....	24
1.5.3 Intelligent Medical Applications .....	25
1.5.4 Epi-Ret3 .....	26
1.5.5 Clinical Trials Comparison .....	26
1.6 Limitations of Visual Prosthesis .....	26
1.6.1 Packaging .....	26
1.6.2 Visual Resolution .....	27
1.6.3 Pixel-wise Vision .....	28
1.6.4 Electrodes .....	29
1.6.5 Electrode Array Detachment .....	34
1.6.6 Perceptual thresholds .....	34
1.6.7 Heat Dissipation .....	35
1.6.8 Summary .....	36
1.7 Visual Anatomy, Physiology and Signal Processing .....	36
1.7.1 Visual Anatomy .....	36
1.7.2 Physiology of Retinal Neurons .....	37
1.7.3 Visual Phototransduction and Neurotransmitters .....	38
1.7.4 Synaptic Pathways .....	39
1.7.5 Light and Dark Adaptation .....	40
1.7.6 Receptive Fields .....	41

1.8	Functional Electrical Stimulation.....	41
1.8.1	Basics of Electrical Stimulation .....	41
1.8.2	Pulse Shapes and Timing.....	42
1.8.3	Tissue Damage.....	43
Chapter 2	Biophysically-based Circuit Models	
2.1	Introduction .....	46
2.2	Developed Circuit Models .....	47
2.2.1	Hodgkin and Huxley Modelling of Giant Axon.....	47
2.2.2	Repetitive Firing of Action Potential in Ganglion Cells.....	49
2.2.3	Summary .....	50
Chapter 3	Feasibility of a 32 x 32 Electrode Array	
3.1	Lessons learnt: Basis for this Chapter .....	51
3.2	Selection Of A Suitable Visual Prosthetic Design for Simulation.....	52
3.2.1	Circuit Modelling Design .....	52
3.2.2	Is Circuit Modelling Suitable for Retinal Prosthetic Simulation? .....	54
3.2.3	Finite Element Method (FEM) Modelling Design.....	55
3.3	FEM-based Modelling for Visual Prosthesis.....	56
3.3.1	Introduction.....	56
3.3.2	FEM-based Modelling for Retinal Considerations .....	57
3.4	Feasibility of a 32 x 32 Electrode Array in Epiretinal Implants.....	65
3.4.1	Motivations.....	65
3.4.2	Electrode Amount per Single Array .....	66
3.4.3	Neurostimulator Scheme.....	66
3.4.4	Small Electrode Size .....	66
3.4.5	Short-Current Pulse Duration .....	67
3.4.6	PEDOT_NaPSS Electrode Array .....	68
3.4.7	Methods.....	68
3.4.8	Results.....	69
3.4.9	Discussion.....	70
3.4.10	Electrode Voltage Comparison .....	74
3.4.11	Voltage Limitations .....	75
3.4.12	Trade-off in Visual Prosthesis .....	76
3.5	Outline for the High-level Theoretical Scheme.....	77
3.5.1	Domain Dimensions and Definitions.....	77
3.5.2	Electrode Data.....	77
3.5.3	Proximity of the Cell to Electrodes .....	78
3.5.4	General Outline.....	78
Chapter 4	Parameter Minimization	
4.1	Introduction .....	79
4.1.1	Lessons learnt: Basis for this Chapter.....	79
4.1.2	Aims .....	80
4.2	Pulse Shape Selection for Simulation.....	80
4.3	Summary .....	82

4.4	Methods.....	84
4.4.1	Ganglion Cell Simulation .....	84
4.4.2	FEM-based Model Simulation.....	84
4.5	Results.....	84
4.6	Discussion .....	85
4.6.1	Electrochemical Safety .....	85
4.7	Outline for the High-level Theoretical Scheme.....	88
4.7.1	Pulse Shape and Duration .....	88
4.7.2	General Outline.....	89
Chapter 5	High-level Theoretical Scheme	
5.1	Introduction .....	90
5.1.1	Lessons learnt: Basis for this Chapter.....	90
5.1.2	Motivation .....	92
5.2	High-level Theoretical Scheme .....	93
5.3	Phosphene Shape Description – Understanding the Physical Aspects of Phosphenes .....	94
5.3.1	Introduction and Aims.....	94
5.3.2	Proof of Concept .....	95
5.3.3	Phosphene Shape Description Method.....	98
5.3.4	Principle-based Experimental Observations .....	102
5.3.5	Verification of FEM-based Modelling of Retina .....	103
5.3.6	Proof of the Activation Area .....	103
5.3.7	Results.....	104
5.3.8	Ganglion Cell Activation.....	105
5.3.9	Perceptual Thresholds.....	107
5.3.10	Shape of Visual Perception.....	107
5.3.11	Summary .....	109
5.4	Controlled-shape Phosphenes .....	110
5.4.1	Lessons learnt: Basis for this Chapter.....	110
5.4.2	Aims .....	111
5.4.3	Controlled-shape Phosphene Method.....	111
5.4.4	Electrode Arrangement.....	111
5.4.5	Input Data of the Controlled-shape Phosphene Method.....	112
5.4.6	Activation area generation .....	113
5.4.7	Results.....	114
5.4.8	Discussion.....	114
5.4.9	Axonal Response .....	115
5.4.10	Benefits of the Proposed Electrode Arrangement.....	116
5.4.11	Summary .....	117
5.5	Spatially-based Visual Technique - Boosting Electrode Control over Single Cells .....	117
5.5.1	Lessons learnt: Basis for this Chapter.....	117
5.5.2	Aims .....	117
5.5.3	Introduction.....	118
5.5.4	Literature Review .....	118
5.5.5	Challenges at Hand - Cell and Electrode Density.....	119

5.5.6	Spatially-based Visual Technique Method .....	120
5.5.7	Visual Field of View Relationship .....	121
5.5.8	Input Data of the Visual Technique.....	123
5.5.9	Results and Discussion .....	123
5.5.10	Analysis of Electrode Density and Cells Activated .....	123
5.5.11	Is Cell Density Data a Requirement?.....	125
5.5.12	Electrode Size .....	125
5.5.13	Activation Size: Benefits and Shortcomings.....	126
5.5.14	Visual Acuity.....	127
5.5.15	Dark Gap Response .....	128
5.5.16	Probability Derivation of Cells inside an Arbitrary-Sized Activation Area .....	128
5.5.17	Feasibility of 32 x 32 Array with High Electrode Densities and High Proximities.....	129
5.5.18	Safe Electrode Carrier Size .....	131
5.5.19	Summary .....	131
5.6	Searching Algorithm.....	132
5.6.1	Lessons learnt: Basis for this Chapter.....	132
5.6.2	Aims .....	133
5.6.3	System Realization .....	133
5.6.4	Multi-site electrode Array .....	135
5.6.5	Searching Algorithm .....	136
5.6.6	Input Data of the Searching Algorithm.....	139
5.6.7	Results.....	139
5.6.8	Discussion and Summary .....	140
5.6.9	Challenges of the Multi electrode Array .....	141
Chapter 6	Summary and Outlook .....	
6.1	Main Findings and Discussion .....	144
6.2	Future Work.....	147
References	.....	149
Lebenslauf	.....	155



## ABSTRACT OF DISSERTATION

# Toward Pixel-wise Vision in Epiretinal Visual Prosthesis

Dem Promotionsausschuss der  
Technische Universität Hamburg-Harburg  
zur Erlangung des akademischen Grades  
Doktor-Ingenieur (Dr.-Ing.)

von

Diego Luján Villarreal

Visual prosthetic devices aim to replace dead neurons in the retina and to produce a sense of vision by stimulating electrically neural cells in the visual system. Since decades, artificial vision devices have been struggled to partially restore vision to those suffering retinal degenerative diseases such as age-related macular degeneration and retinitis pigmentosa.

Fundamental research stipulated that 1000+ electrodes per single array is the requirement to upgrade basic issues such as mobility, navigating on interior and exterior environments, reading large-sized letters and independent living. Clinical trials involving visual prosthetic devices implanted in humans have been taking place around the globe. Currently, an artificial vision device that exceeds 100 electrodes per single array has not been implanted.

Retinal implant devices would ideally reproduce accurately natural spatial patterns of activity in ganglion cells. This involves the capacity of each electrode to activate a single cell. Despite notable progress have been recently achieved, current visual prostheses fall short to reproduce a pixelated field of view generated by retinal stimulation. This can be understood as a challenge to such devices to generate a complete visual scene with detail perception.



One of the leading concerns in advanced visual prosthesis and current status in clinical trials is that atypical patterns of retinal activity are induced by stimulation. Forasmuch as phosphenes or spots of light are the single elementary building block in visual prosthesis, the physical basis of visual perception while the retina is electrically stimulated demands a better understanding.

That being said, artificial vision is currently in an early-stage of maturity. In this report, a high-level theoretical study of realistic neural responses in the retina is modeled to address the formerly stated challenges. Computational efficiency in neural modeling, safe stimulus delivery and a deep theoretical thinking for a possible physical realization of electronics are considered. Neural modeling is verified by means of experimental studies from literature.

This dissertation is engaged to design means for improving visual prosthetics by channeling its scope in four avenues: 1) an array of  $32 \times 32$  electrodes per single carrier; 2) parameter minimization as ganglion cells are electrically stimulated; 3) enhancing visual and detail perception towards pixel-wise stimulation and 4) adaptability of visual devices to integrate arrangements of stimulating electrodes in their system.

# Preface

## i. Definition of Dissertation

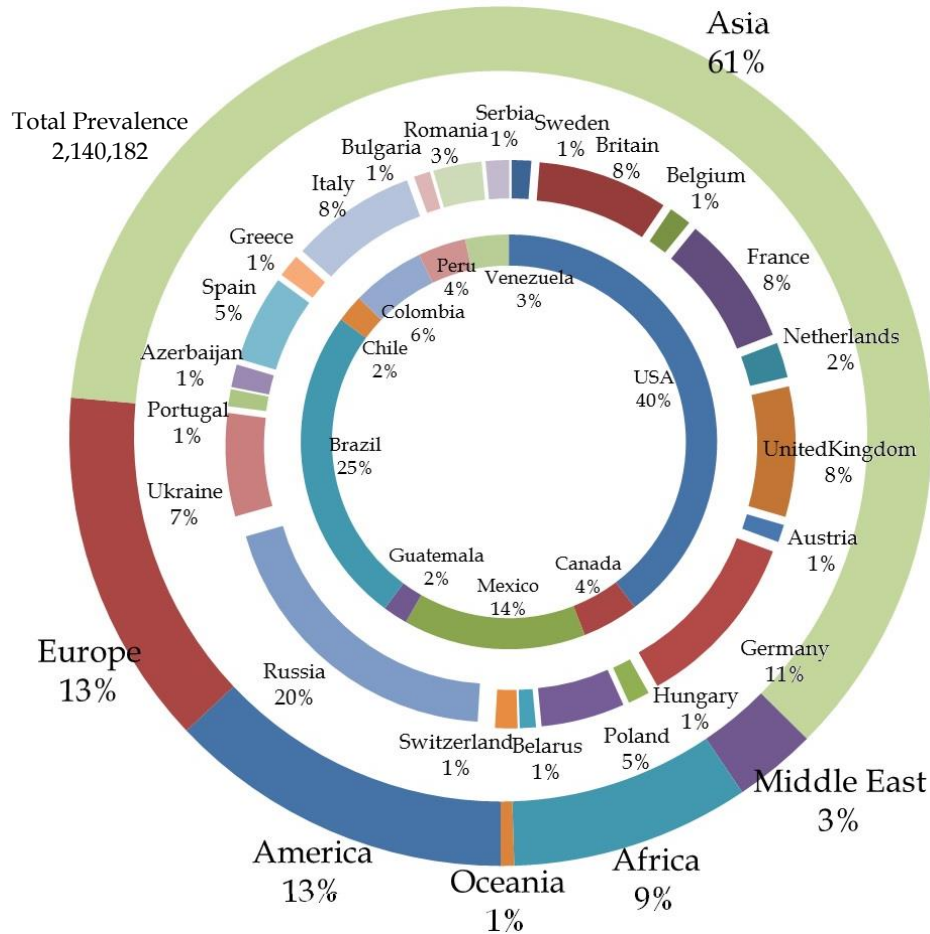
Sight-robbing illnesses such as retinitis pigmentosa and retinal degenerations are the main cause of blindness that affects hundreds of thousand around the globe. Likewise, age-related macular degeneration deprives vision of millions nowadays. The following figure describes the prevalence of retinitis pigmentosa around the world.

One of the leading targets for engineers is to generate a fruitful contribution in cutting-edge fields such as biomedical engineering. High-level theoretical models and computational studies are the cornerstone for realistic applications. Since decades, deep theoretical thinking became the foundation for generating biophysically-based realistic simulations of neurons and theoretical studies of the nervous system. As such, the most important target by far is narrowing the gap between engineering and medicine. As for this report, however, its scope is directed to design means for visual prosthesis to improve electrode amount per single array, investigate parameter minimization and enhance visual perception towards pixel-wise stimulation.

It's not a secret that, despite the challenges so as to overcome functional vision, fundamental research stipulated around 1000+ electrodes per single array are needed to upgrade basic issues such as mobility, independent living and navigating on interior and exterior environments. Currently, a small number of companies such as Second Sight Medical Products (SS), Retina Implant GmbH (RI) and Intelligent Medical Implants GmbH (IMI) have developed a complete visual prosthesis device. Clinical trials *in-vivo* state that patients have perceived light, object localization, distinguish objects, motion and differentiate simple patterns of lines and letters.

Those sight improvements, despite being advantageous for a sight deteriorated patient, need a significant enhancement to be aligned with the success of today's cochlear implant technology. As for its technology, cochlear implant requires among others a minimum of 25 electrode sites for restoring functional hearing, bipolar electrode configuration, pulsatile-fashion and transcutaneous transmission link.

IMI, RI and SS have implanted their corresponding devices in patients with an array of 16, 49 and 60 electrodes. Although offering some vision, the major requirement lies in activating at least 1000 or more pixels for attaining functional vision with small electrodes. Electrode diameters of IMI, RI and SS are 100 and 360, 70 and 200  $\mu\text{m}$ , respectively. Retinal implant devices previously stated likely activate hundreds of ganglion cells simultaneously over a particular region due to the size of the electrode used. Beyond just this coarse stimulation of cells restricts spatial resolution, the activity generated by stimulation remains dissimilar from a healthy retina too. Thus, those vision progresses need a significant enhancement to restore functional vision. Reducing electrode sizes may provide activation of small groups of cells that lead to high resolution patterns. This challenge, though, requires high charge density that can cause irreversible faradaic reactions at the electrode-electrolyte interface. Thus, a neural



Prevalence of retinitis pigmentosa worldwide. Data of prevalence in Europe and America were statistical values calculated with extrapolations of various prevalence or incidence rates against the populations of a particular country or region. The statistics used for prevalence/incidence of Retinitis Pigmentosa are typically based on US, UK, Canadian or Australian prevalence or incidence statistics. Extrapolation calculation is automated and does not take into account any genetic, cultural, environmental, social, racial or other differences across the various countries and regions. Sources: US Census Bureau, Population Estimates, 2004 and US Census Bureau, International Data Base, 2004 and [rightdiagnosis.com](http://www.cureresearch.com/). Data points from <http://www.cureresearch.com/>.

modelling that addresses electrochemical safety is a necessity for generating safe avenues to ensure long-term stable performance of visual prosthesis.

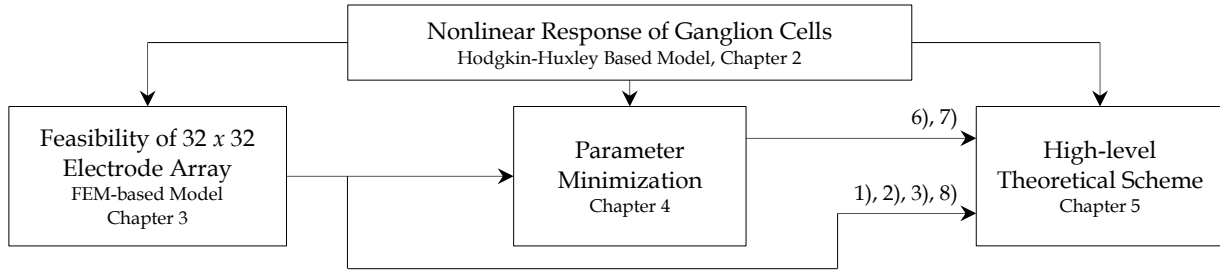
Retinal implant devices would ideally reproduce accurately natural spatial patterns of activity in ganglion cells which involves the capacity of each electrode to reach nearby cells. Although being beneficial for a poorly-eyesight individual, current visual prostheses fall short to reproduce a pixelated field of view generated by retinal stimulation. This can be understood as a challenge to such devices to generate a complete visual scene with detail perception. Recent clinical trials related to Argus II developed by SS did not exhibit an outdoor image perception of an array of narrow spots of light that can be precisely controlled by the system. Argus II developed by SS and Alpha IMS developed by RI reported a best measured visual acuity of 20/1260 and 20/546, respectively.

Nowadays, artificial vision is currently in an early-stage of maturity. Groups of researchers have sought to create richer and more complex patterns to represent visual scenes while the retina is electrically stimulated. As such, the foremost concern on advanced visual prosthesis and current status on clinical trials lies on that atypical patterns of retinal activity are induced by

stimulation. This can be understood as a falling short of current theory of retinal implants to understand the relationships between precept shapes and electrode characteristics, electrode configuration i.e. single- or multi-site, distance of cells to the electrodes and topology of electrode arrangement. Together with a grasp of attaining single-cell selectivity would be then a requirement to align retinal prosthesis with a high-stage of maturity.

## ii. Proposal for Pixel-wise Vision

Pixel-wise visual perception is defined as the generation of very small and independent spots of light by electrode stimulation. These single small spots of light can be thought as one-to-one, electrode-to-pixel, scoreboard-like experience with punctate individual phosphenes. That is, the response per electrode must consist of a small visual perception that carries different information of the external image to the brain. By this means, as incorporating the entire response of the array of electrodes, the cluster of these useful dots of light will generate the target image. In this regard, it is assumed that a full image can be realized by single cell activation per stimulating electrode generating a visual sensation that the brain may interpret as a small spot of light.



Proposal towards pixel-wise vision. Our scheme begins with an understanding of the Hodgkin-Huxley-like mathematical framework of ganglion cells developed by [Fohlmeister, 1989]. This biophysical model is the basic criterion of stimulation of ganglion cells. An array of  $32 \times 32$  electrodes is a requirement of advance visual prosthetics. The feasibility of applying that amount is firstly addressed. Parameter minimization is considered as a core step of a 1000+ electrode array to ensure electrochemical safety during stimulus delivery. Last, the high-level theoretical scheme consists of different but related algorithms that represent a stepwise refinement of electrode stimulation to reach pixel-wise stimulation. This thoughtful method uses as input the geometric and stimulating parameters defined in earlier chapters to ensure accurate threshold currents, high resolution patterns and safety of a 1000+ electrode array while pixel-wise vision is reached. Overall, the inputs of the high-level scheme are geometric parameters, i.e. 1) domain dimensions, 2) proximity of cell to electrode, 3) electrode data ( $32 \times 32$ , size, distribution) and 4) cell location, and stimulating parameters, i.e. 5) injected current, 6) pulse duration, 7) pulse shape, and 8) domain electrical properties.

The proposal to attain pixel-wise vision is shown in next flowchart as a graphical overview of this thesis work. The high-level theoretical scheme is located in the last step which represents a fine-tuning of electrode stimulus towards pixel-wise stimulation. Geometric and stimulating parameters serve as inputs which correspondingly are the outputs of previous top-level steps that have key roles in the overall goal of this thesis work. All inputs are captioned in the flowchart. The contribution of each is explained in sequential order based on its appearance. Note that each provides different inputs to the last step.

The modern biophysically-based neural modelling is frequently based on the mathematical framework developed by [Hodgkin and Huxley, 1952]. They thoroughly validated how ionic currents could be understood as regards of changes in  $\text{Na}^+$  and  $\text{K}^+$  conductances in the axon membrane. Thus, a detailed mathematical model of voltage-dependence and time-dependence

was developed. The existent analytical power of the model became evident when numerical integration accurately reproduced all the key biophysical properties of the action potential. Thus, a neural-based model similar to ours that involves the activation of axons or body cells in the form of extracellular stimulation must include this mathematical framework. The nonlinear model of ganglion cell response was based on Hodgkin and Huxley-like modelling and was developed by [Fohlmeister, 1989]. Throughout this thesis work, it supports all top-level steps as a condition of stimulation by observing the response of membrane potential at various levels of extracellular stimulation.

Realizing functional vision is a major challenge. To achieve detail recognition, the resolution of implants must be increased by increasing both the number and density of electrodes [Weiland et al., 2014]. There is plenty of evidence that a high number of electrodes ranging from 625 [Cha et al., 1992] to 1000+ [Chader et al., 2009] can enhance visual resolution originated by electrical stimulation. This insight is well-correlated to upgrade mobility, independent living and walking in crowded environments [Cha et al., 1992], face recognition [Thompson et al., 2003], reading large-sized letters [Bagnoud et al., 2001; Dagnelie et al., 2006; Chai et al., 2007]. Nowadays, an artificial vision device that exceeds 100 electrodes per single array has not been implanted. Thus, the main inquiry in advanced visual devices remains: Is it feasible to drive 1000+ electrodes inside the retina? Beforehand pixel-wise vision is addressed, the *first aim* of this thesis work is to investigate an array of  $32 \times 32$  electrodes in a single carrier in terms of electrochemical safety, threshold currents and image frequency of 20 fps. Hence, a simplified FEM 3D retinal-based model that addresses this amount of electrodes is developed. In this arrangement, the activation of a cell with the minimum threshold current as seen in earlier experimental works is followed [Keserü et al., 2012; Jepson et al., 2012]. Basic relationships of threshold injected current and distance of the cells to electrodes are analyzed. Experimental results of current thresholds by [Jensen, 2005] and voltage across the electrodes by [Meza et al., 2014] will be compared with our simulation-based findings. Electrochemical safety is examined in terms of charge density, electrode voltage, heat dissipation and current injection. As a result, this model can define input stimulating and geometric parameters such as domain definitions, electrode data ( $32 \times 32$ , size, distribution), domain dimensions and give guidelines for the proximity of the cell to electrodes. Likewise, it can deliver to the next top-level step parameters that must be minimized for safe delivery of stimulus.

The use of small-sized electrodes has become a cornerstone for artificial vision devices to activate small areas of the retina and achieve pixel-wise vision [Weiland et al., 2008]. Ganglion cells of around 1.5 million in healthy human eye extracts different information only from a narrow fragment of the visual space. As an array of electrodes is implanted in the eye with small diameter and some distance, the stimulus of each can elicit activity of nearby cells and send a physiological signal to the brain via the optic nerve [Weiland et al., 2014]. However, high charge density is required by small electrode usage which can cause breakdown of the electrode and adverse tissue reactions [Brummer, 1977]. Thus, the *second aim* in this thesis work is to consider parameter minimization as an essential step to ensure electrochemical safety during stimulus delivery. The minimization of stimulating parameters has been a subject for decades in electrical stimulation, to mention a few [Meza, 2012; Jezernik, 2005]. In general, charge density and electrode voltage have been emphasized regarding visual devices because small-sized electrode is preferably used for high resolution [Lujan (a), 2016]. The minimization of such parameters has been previously investigated while the pulse shape and its duration are varied [Lujan (b), 2016; Meza, 2012]. This technique has generated interesting outcomes as regards prolonging battery lifetime and increasing patient safety. Thus, charge density and electrode voltage will be

examined in terms of pulse shape and pulse duration. Accordingly, parameter minimization can define several input stimulating parameters, such as the duration and shape of the pulse that can ensure safety of an array of 1000+ electrodes while pixel-wise vision is reached.

Clinical trials of both subretinal and epiretinal implants do demonstrate that patients do not experience idealized pixel-wise vision [Weiland et al., 2014]. Thus, visual perception coming from electrically activated cells requires significant improvement for delivering functional vision. As a result, the high-level theoretical scheme is created. It is based on a complex FEM 3D retinal-model and on different but related algorithms that represent a stepwise refinement of electrode stimulation over single cells. As a whole, it can generate a well-defined localization of electrode stimulus and reinforce single-cell selectivity, as it is required for an array of individual responses of cells under accurate control of the electrodes. This scheme can treat randomly distributed cells inside the complex 3D model built to a greater degree of anatomical likeness. The flexibility to indicate different arrangements of stimulating electrodes is contemplated, i.e. single and parallel stimulation. This is required because the unpredictability of the location and lifetime of ganglion cells might require some flexibility for the need of specific patients. Input geometric and stimulating parameters earlier defined in previous chapters are the foundation of the high-level scheme. The inputs of cell location, injected current and electrode density are variables through the implementation of the high-level scheme. As a result of what was learnt in earlier chapters, this will ensure accurate results of threshold currents, high resolution patterns and safe stimulus delivery in an array of  $32 \times 32$  electrodes for pixel-wise stimulation.

The simplified and complex retinal-models were based on an existing electronic scheme that consists of a 64 scalable channel stimulator with low power consumption and small chip area [Meza, 2014]. Neural modelling proof by experimental studies and deep theoretical thinking for a possible physical realization of electronics are considered.

### iii. Challenges Addressed

A significant requirement for visual prosthesis lies on the activation of 1000+ electrodes per single array to upgrade basic issues such as mobility, independent living, navigating on interior and exterior environments and reading large-sized text. Once a device is implanted inside the body, issues associated with stimulus delivery are a common consequence. Safeguarding the operation of stimulators is by far most a crucial issue in neural activation. Safety, in terms of electrical performances, is mainly related to four factors i) charge density injection level; ii) heat generated at tissue due to power dissipation; iii) DC current flow into tissue; and iv) water-voltage window.

Despite that transmitting stimulus from an electrical conductor that makes contact with a nonmetallic part is extremely advantageous for restoring injured senses, electrochemical reactions at the electrode-tissue interface carry out charge injection into the neural tissue. As such, electrolysis of water can be produced in the electrode-tissue interface that can lead to localized pH changes and chemical species formation that damage the tissue or the electrode. Violating charge injection boundary leads to gas bubbling evolution that damage the soft retinal tissue layers. The voltage across the electrodes can cause electrolysis of water once it exceeds the potential range in the positive direction, oxidizing the water and forming oxygen.

Since electronics of any kind dissipates a certain amount of power, heat as a consequence affects the surrounding tissues. For minimizing the voltage from the electrodes which in turn

lowers the power consumption and thus heat dissipation, advanced polymer materials are currently used in practice. PEDOT has been generated considerable attention as a supercapacitor material, large electroactive voltage window, lower impedance and high charge injection limits.

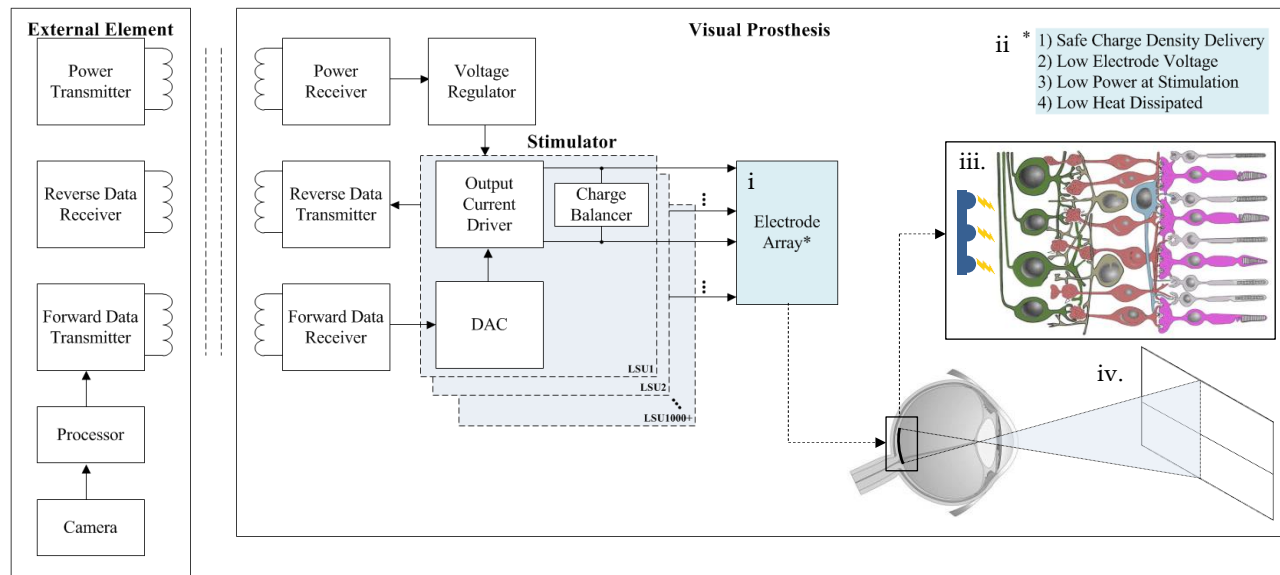
The upgrade of visual prosthetics has been a followed subject since current status on clinical trials has not exhibited an array of independent phosphenes. Visual prosthesis would ideally generate an array of circular-shaped percepts with narrow dimensions that would represent a building block for the pattern of visual perception. However, current retinal implants have attained poor visual acuity during experimental testing [Humayun et al, 2012; Stingl et al., 2013]. This mainly occurs because of the use of electrode size [Jepson et al., 2014] and that current strategies for reaching single-cell selectivity are proven inadequate. Large-sized electrodes in up-to-date implanted devices likely activate hundreds or thousands of cells over their area of stimulation. Thus, visual perception of retinal prosthesis demands small electrode usage to independently activate ganglion cells and replicate natural patterns of activity in the retina. Small electrode size can allow excitation of small groups of cells. Despite that visual reception is improved; however, the exposure of sensitive retinal tissue must be safeguarded because of the charge density required by small electrode dimensions.

Highly interesting, however, the issues not addressed here are the charge balance during electrical stimulation that is crucial for tissue protection. Any mismatch in biphasic pulses contributes to build up residual charge on electrodes, inducing *DC* current flow into tissue. *DC* current flow causes electrode corrosion and the generation of toxic material that damage the tissue. For long term period of implantation, safely injecting pulses is one of the major concerns. Because of the high density of electrodes are required for cell activation, area and power consumption at each electrode becomes a major critical concern. Simultaneously, a growth of electrode impedance and thus the voltage at the stimulator output driver takes place by using large number of small electrodes. As such, low impedance biocompatible materials are a necessity to ensure harmless stimulation. Although high density and long-lasting implant devices may be developed, however, clinical trials are required to overcome major challenges for bioelectronics implants including long-term steady performance of implanted electronics and safe surgical implantation procedure.

## iv. Tasks Related to a System Block Diagram

A simplified system for visual prosthesis consists of a camera, power transmitter and receivers, data transmitter and receiver, some image processor, voltage regulator, output current driver, DAC, charge balancer and an electrode carrier, see next figure. The primary step of a visual prosthesis consists of the external camera to capture some image. After that image is pixelized by the image processor, the signal is translated into activating parameters by an external processor. The activating parameters and power are transferred wirelessly to the visual prosthesis through an RF connection. A voltage regulator receives the corresponding power sent by the external element and converts it into a stable supply voltage for the implant. The forward data receiver decodes the activating parameters such as pulse duration, pulse amplitude, pulse shape, pulse interval, etc. The reverse data transmitter sends out information such as electrode impedance and power indicator of the implant to the external world.

The digital-to-analog converter (DAC) generates an agreeing analog stimulating pulse shape, either current or voltage stimulus, depending on the stimulation topology. This stimulating pulse shape is then amplified by an output driver to generate the output signal to the electrode



Simplified system block diagram for epiretinal visual prosthesis. Step i) deals with the distribution of  $32 \times 32$  electrodes inside the carrier. Single- and multi-site arrangements of stimulating electrodes are addressed, ii) addresses electrochemical safety during cell activation, iii) deals with the current delivery for achieving visual percepts and step iv) addresses the pixel-wise vision. Source, Chen 2013 IEEE International Symposium on Circuits and Systems.

array and retina. The implant produces a pattern of small electrical currents that approximate the initial visual image. The retinal neurons are activated, resulting in a dot pattern at each point of stimulation. A charge balancer cancels the residual charge on the electrode and retinal interface at the end of every stimulation cycle for long-term human safety. The next figure shows the steps to convert the captured image from the camera to an electrical signal sent to the retinal neurons. The steps that are addressed in this report are, i)  $32 \times 32$  distribution of electrodes inside the carrier; ii) electrochemical safety during cell activation; iii) current delivery for achieving visual percepts; iv) percept shape analysis and pixel-wise vision.

## v. Structure of Dissertation

*Chapter 1* explains key theory ingredients associated with visual prosthesis, visual nervous system, signal processing at the retina, an overview of existing artificial vision devices and functional electrical stimulation. *Chapter 2* describes the theory related to circuit models developed by Hodgkin and Huxley and Fohlmeister. *Chapter 3* addresses the feasibility study of a  $32 \times 32$  electrode array including electrochemical safety. It also details feasible solutions that guarantee safe corridors during stimulus delivery. In this specific case, a simplified 3D neural-model of the retina is presented. *Chapter 4* details methods to minimize main parameters while cells are electrically activated. *Chapter 5* introduces the high-level theoretical scheme. Section 5.3 details the phosphene shape description method. Section 5.4 explains the controlled-shape phosphene technique. Section 5.5 describes the spatially-based visual technique. Last, section 5.6 details the searching algorithm. In chapter five, a more complex 3D neural-model of the retina is presented. *Chapter 6* details the summary of this dissertation and future work.



$A$	Electrode carrier area [mm <sup>2</sup> ]
$A_A$	Area of activation area [mm <sup>2</sup> ]
$A_D$	Total chip surface area [cm <sup>2</sup> ]
$A_E$	Electrode cross section area [cm <sup>2</sup> ]
$a'', b'', c'', d'', e'', f'', g''$	Sizes of activation area [μm]
$C_{dl}$	Double layer capacitance [F]
$C_M$	Membrane capacitance [μF/cm <sup>2</sup> ]
$D$	Visual field of view distance [m]
$D_A$	Detail area [mm <sup>2</sup> ]
$d$	Electrode pitch [μm]
$d_s$	dot size [°]
$d', D'$	Distances of Snellen acuity test [m]
$E_D$	Electrode diameter [μm]
$E_{NA}, E_K, E_L, E_{Ca}, E_{AK}, E_{CaK}$	Equilibrium potentials [mV]
$e_T$	Total number of electrodes inside a single array [-]
$F$	Faraday constant [96485 C · mol <sup>-1</sup> ]
$f$	Frequency [Hz]
$G$	Cells activated [-]
$G_{NA}, G_K, G_L, G_{Ca}, G_{AK}, G_{CaK}$	Conductances [mS/cm <sup>2</sup> ]
$g_{NA}, g_K, g_L, g_{Ca}, g_{AK}, g_{CaK}$	Maximum conductances [mS/cm <sup>2</sup> ]
$g_M$	Membrane conductance [mS/cm <sup>2</sup> ]
$I_{CED}$	Cell-electrode distance [μm]
$I_{ED}$	Electrode distance [μm]
$I_{EXT}$	Extracellular current [μA/cm <sup>2</sup> ]
$I_{ION}$	Ionic current [μA/cm <sup>2</sup> ]
$I_{TH}$	Threshold current [μA]
$J_B$	Peak boundary current density in the membrane [A/m <sup>2</sup> ]
$J_E$	Extracellular peak-threshold current density [A/m <sup>2</sup> ]
$J_{ext}$	Extracellular current density injected [A/m <sup>2</sup> ]
$L$	Length of the visual field of view [m]
$l$	Length of electrode carrier [μm]
$l_T, w_T, h_T$	Length, width and gap of total chip attachment [m]
$l_S, w_S$	Total length and width of a single ASIC [m]
$n$	Distance from nodal point to the retina [mm]
$O$	Nodal point
$P_{DEVAVE}$	Average power consumption at device [mW/cm <sup>2</sup> ]
$P_{LSU}$	Power consumed by local stimulator unit [mW]
$P_T$	Power consumption at driver transistor [mW]
$Q_D$	Charge density [mC/cm <sup>2</sup> ]
$Q_{INJ}$	Charge density limit for injection [mC/cm <sup>2</sup> ]
$R$	Universal gas constant [8.31 J · mol <sup>-1</sup> · K <sup>-1</sup> ]
$R_a$	Axoplasm resistance [Ω]
$R_C$	Contact resistance [Ω]
$R_{CT}$	Charge-transfer resistance [Ω]
$R_S$	Solution resistance [Ω]
$T$	Stimulation time [s]
$T_A$	Absolute temperature [°C]
$T_D$	Heat generated by device [°C]
$V$	Visual angle [°]
$VA$	Visual acuity [-]
$V_{DD}$	Supply voltage [V]
$V_{ELE}$	Electrode voltage [V]
$V_M$	Membrane voltage [mV]
$V_{th}$	Threshold voltage [mV]
$W$	Width of the visual field of view [m]
$w$	Width of electrode carrier [μm]
$\Delta t$	Pulse duration [ms]
$\alpha, \beta$	Rate constants
$\epsilon$	Permittivity [-]
$\epsilon_0$	Permittivity of free space [F/m]
$\rho_C$	Cell density [mm <sup>-2</sup> ]
$\rho_E$	Electrode density [mm <sup>-2</sup> ]
$\rho_i$	Axoplasm resistivity [Ω · m]
$\rho_M$	Membrane resistivity [MΩ · m]
$\sigma$	Conductivity [S/m]
$\sigma_q$	Charge density applied [mC/cm <sup>2</sup> ]

# Chapter 1

## Introduction to Visual Prosthesis

### 1.1. Visual Prosthetic Considerations

#### 1.1.1. Visual Prosthetics – Definition and Aims

Visual prosthetic devices aim to replace dead neurons at the retina and to produce a sense of vision by stimulating electrically neural cells in the visual system. Put differently, retinal prosthetic devices substitute nonfunctional photoreceptors and translate outside photic images into electrical signals in the retina such that the information sent to the brain can be perceived as visual images.

Depending on the anatomic position of the electrode array, visual prostheses are categorized in three different approaches: epiretinal (on top of the surface of the retina), subretinal (under the retina), and suprachoroidal (between the sclera and choroid). Current clinical trials include the use of epiretinal implants [Mahadevappa, 2005; Yanai, 2007], a passive subretinal device [Chow, 2004] and an active subretinal device [Zrenner, 2007].

Passive devices depend on incoming light for power, while active devices have an external power source. All of the devices that have been currently tested are manufactured by companies which have the required quality systems and manufacturing skills to produce robust, medical-grade implants.

Despite some efforts, epi- and sub retinal prosthetic devices have strived for decades to partially restore vision to those suffering retinal degenerative diseases such as age-related

macular degeneration and retinitis pigmentosa. Though there have been notable progresses in this field, new devices may face further challenges for safely electrode implantation.

Among eye disease circumstances, some analogous to cataract can be effectively addressed through surgery. Conversely, most of the troublesome blinding conditions are of retinal-based origin with the despair of being the most common by inherited retinal degeneration. These sight-depriving conditions form a broad family of diseases that predominantly affects the light-sensitive photoreceptor cells. Such conditions fall into two categories: 1) degenerations like retinitis pigmentosa that principally affect rod light-sensitive cells and 2) deteriorations such as age-related macular degeneration that primary affect cone cells.

### 1.1.2. Retinitis Pigmentosa

The initial retinal degenerative symptoms of retinitis pigmentosa (RP) are categorized by decreased night vision and the loss of the mid-peripheral visual field [Shintani, 2009]. Light-sensitive rod photoreceptor cells, which are responsible for low-light vision, are the retinal processes affected first during non-syndromic forms of this disease [Soucy, 1998]. Nowadays, there is no cure for retinitis pigmentosa.

RP-like degenerations is estimated to have a prevalence of about 1:3500 around the world. In Europe and the United States, about 350,000 to 400,000 patients suffer from RP and every year between 15,000 and 20,000 patients with RP suffer vision loss.

RP can be related to the phase of dark adaptation that is usually achieved by increasing of sensitivity of rods such that light-sensitive pigments increase their concentration and the threshold for detecting light is reduced, allowing the eye to build a representation of its surroundings. As RP affects mostly rods, the phase of dark adaptation suffers until is lost completely. In RP allied diseases, despite that the number of affected individuals around the globe is relatively small, the disease usually is apparent at birth, in early childhood, or at least in the second or third decade of life.

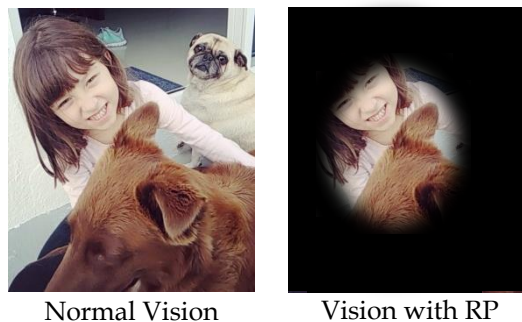


Fig. 1.1 Retinitis pigmentosa degeneration.

### 1.1.3. Age-Related Macular Degeneration

This sight-robbing disease is a second cause of visual impairment. It predominantly affects those over 55 years of age and involves issues such as mobility and independent living. Injuries such as falls related to deprived eyesight produce a costly disease in terms of loss quality of life. Age-Related Macular Degeneration (AMD) causes damage to the macula, a small spot near the center of the retina and the part of the eye needed for sharp central vision.

As AMD progresses, a blurred area near the center of vision is a common symptom. Over time, the blurred area may grow larger and blank spots are developed in the central vision.

The relative rate of rod and cone degeneration is a fundamental characteristic of any disorder affecting photoreceptors, including AMD. During the course of suffering such sight-robbing illness, the retina pigment epithelium cells stop performing their support functions and the rods and cones die, resulting in a loss of central vision [Curcio, 2001]. Chen suggest that rod function may be a more sensitive indicator of early AMD once it was investigated with 16 human volunteers suffering AMD, with age ranged between 50 to 73 (mean 63) [Chen, 2004].

Those who suffer also experience poor night vision symptoms [Kathryn, 2015]. Gui-shuang et al. [Gui-shuang, 1992] suggested that assessing night vision symptoms may be useful to identify patients with early or intermediate AMD who are at relatively high risk of progression.

In the United States of America (USA), it was estimated that about 2 million of people above the age of 55 have AMD, with other 7 million being in the pre-symptomatic phase.



Fig. 1.2 Age-related macular degeneration

## 1.2. Minimum Requirements in Artificial Vision

Spatial resolution has a major impact in visual perception because object and face recognition relies on it. Clinical vision testing begins at a spatial resolution roughly of  $0.5^\circ$  of visual angle which relates to a visual acuity of  $1/35$ . Thus, the main objective of visual prosthetic development is reaching a visual angle of  $0.5^\circ$ . A visual angle of  $2^\circ$  of resolution leads to an enhancement in daily life performance such as object recognition. A visual angle of  $10^\circ$  might be sufficient for mobility and orientation, allowing patients to distinguish large objects and movement with directions. Situations such as safe navigation in active outdoor would be a requisite; stimulation should include eccentricities of  $10\text{--}15^\circ$  [Cha, 1992].

A total of about 1000 electrodes would be necessary for useful artificial vision so as to recuperate functional vision, orientation, face recognition and reading ability [Chader, 2009].

Visual field of view is highly correlated to the visual angle. Assuming some object 6 meters away from the eye, basic trigonometry functions can be used to determine the size of the field of view. For  $10^\circ$  of visual angle, the field of view would be a square of approximately  $1\text{ m}^2$  of size. Table 1.1 lists the requirements of visual prosthesis, starting with the standard visual acuity of healthy retina.

The ultimately aim is to provide the individual a visual acuity of  $6/6$  so as to resolve differences of  $1/60$  of one degree of visual angle. Using basic trigonometry functions, such visual acuity translates to  $5\mu\text{m}$  on the retina. High resolution can be attained by activation small

TABLE 1.1

Visual Acuity	Performance	Pixel Size (Length) [cm]	Pixel per cm [ppcm]	Resolution [arc minute]
6/6	Healthy Retina	0.174	5.7	1
6/12	Driving (mostly in the United States)	0.349	2.86	2
6/15	Normal Reading	0.436	2.3	2.5
6/60	Self-sustained orientation, navigation	1.74	0.57	10
6/180	Aim of visual prosthesis	5.2	0.2	30
6/720	Large object detection <sup>1</sup>	20	0.05	120

<sup>1</sup> This visual resolution can be regarded as an enhancement to distinguish objects larger than 20 cm at 6 meters away from the human eye. Pixel size is regarded as the length of a pixel seen in the visual field of view 6 meters away from the nodal point.

areas of the retina. Such demand requires state-of-the-art development of small electrodes with low-impedance during stimulation.

Advanced electronic packaging is a requirement to protect active components from the corrosive saline environment in the eye. The conditions to assure a safety implantation of electronics are using a virtually hermetic package which protects the electronics against water and ion ingress. An advanced technology should not add substantial size to the electronics since the total implant dimensions requires a small-sized device to safely fit in the eye and ideally fit inside the orbit. Highly interesting, however, advanced packaging techniques are not a part of this report.

### 1.3. Morphological Bases of Visual Prosthesis

As the morphological basis of retina deals with its form and structure once RP or AMD are present, its main objective is to determine whether suitable amount of inner retinal neurons remain in RP and AMD patients so as to act as a platform for the prosthetic device.

[Santos et al., 1997] demonstrated the feasibility to implant a retinal device by indicating that 25% to 30% of ganglion cell are preserved in the inner retinal region in patients suffering either RP or AMD.

Thus, this experimental-based finding demonstrates that blind patients suffering with RP or AMD can restore their sight using visual prosthesis. Although courageously, though, a suitable visual prosthesis should be developed such that visual and detail perception yield natural spatiotemporal activity of cells.

### 1.4. Visual Prosthesis Design Principle

#### 1.4.1. Epiretinal Visual Prosthesis

Such prosthesis locates the microelectrode array in the inner surface of the retina. It directly activates ganglion cells by bypassing all other retinal neurons because of severe rod and cone

photoreceptor impairment that cannot drive synaptic connection started with a photocurrent input, see fig. 1.3.

The microelectrode array is steadied using micro tacks, along with the slight mechanical pressure of the vitreous humor.

If it is required, an external video camera acquires the external images of the surrounding environment. Then, an image processing chip pixel the image and send the information to the implanted electrode array wirelessly via telemetry. The image processing chip drives the information to the implant by converting the image into a spatial and temporal pattern of each point of stimulation. Namely, appropriate underlying neurons are activated for the period between 20 [Lujan (a), 2016] to 60 Hz [Sivaprakasam, 2005] with an ideal resolution of nearby cell stimulation to reach pixelized vision perception [Weiland et al., 2014].

The external camera and image processing chip are generally mounted onto eyeglasses for the patient [Weiland, 2014]. An external transmitter is also required to provide continuous power to the implant.

Apart of reaching the previously challenges, the epiretinal implant system must be able to process images in real time and to prevent any noticeable delays between the camera input and retinal activation, which could confound visual perception. The processing chip requires additional features, such as motion and edge detection [Weiland, 2014].

Epiretinal implants are advantageous due to 1) low surgery risk by placing the microelectrode array within the vitreous humor; 2) mechanical constrain of microelectrode array inside the vitreous humor is minor and could expand its size; 3) retinal neurons from the photoreceptors to bipolar cells are bypassed and stimulation relies only on the function of ganglion cells; 4) external electronics allow to have full control over the image processing and adapt it for each patient; 5) location of epiretinal implants allows the vitreous humor to serve as a heat sink for the implant.

The main disadvantage of epiretinal implants are 1) external camera needs to address motion and edge detection to have a successful performance; 2) visual implants can activate not only cell bodies but also the nearby axons. To be precise, single electrodes may activate additional cell bodies due to excitatory input of synaptic connection [Weiland, 2014]. As a result, a distorted stimulation pattern could occur; 3) while an epiretinal implant can be stabilized by the pressure of the vitreous humor, mechanical fixation using advanced micro tacks may be required to further stabilize the implant onto the inner retinal layer [Majji, 1999]

#### 1.4.2. Subretinal Visual Prosthesis

Such prosthesis locates the microelectrode array between the photoreceptor layer and the retinal pigment epithelium. It directly activates retinal cells by relying on the normal processing of the inner and middle retinal layers [Weiland, 2014], see fig. 1.3. Theoretically, the subretinal space is perhaps the most logical place for implanting some array because the implant replaces the dying or dead photoreceptors by light sensitive microphotodiodes. Further the array is mechanically constrained by the minimal distance between the outer retina and the retinal pigment epithelium [Chader, 2009].

A subretinal implant covers a silicon wafer which contains light sensitive microphotodiodes that generate current signals directly from the incoming light. Then, the resultant current is injected into the underlying retinal cells via arrays of microelectrodes.

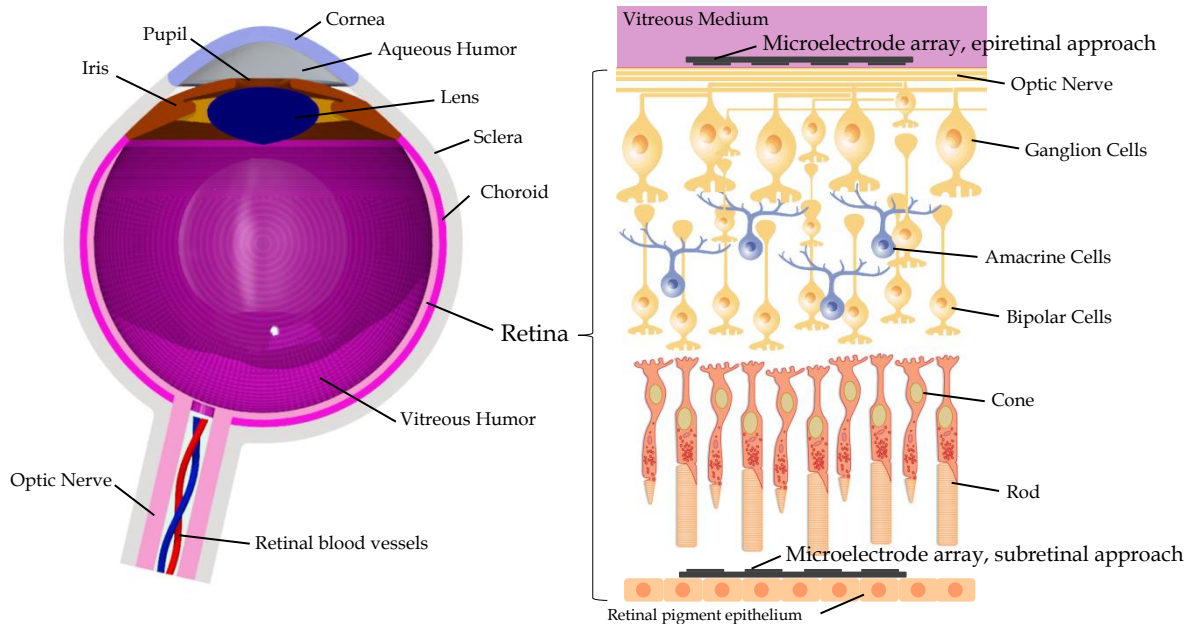


Fig. 1.3 Epi- and subretinal locations inside the human eye. AutoCAD software used for the creation of this figure.

The pattern of microphotodiodes activated by incident light therefore stimulates fractions of bipolar, horizontal, amacrine, and ganglion cells, leading to a visual perception of the original incident image. Some subretinal implants require power from external circuitry to enhance the image signal.

A subretinal implant is advantageous due to 1) the implant principle covers a simple design: light acquisition, processing, and stimulation are all carried out by microphotodiodes mounted onto a single chip; 2) the implant does not require any external hardware beyond the implanted microphotodiodes array; 3) subretinal placement is also more straightforward, as it places the stimulating array directly adjacent to the damaged photoreceptors [Chader, 2009; Weiland, 2014]; 4) the implant allows for ordinary inner retinal processing, thus resulting in a complete known threshold for a visual response; 5) subretinal implants require minimal fixation, as the subretinal space is mechanically constrained and the retinal pigment epithelium [Zrenner, 2002].

The disadvantages of subretinal implants are 1) compact nature of the subretinal space imposes significant size constraints on the implant; 2) close proximity between the implant and the retina also increases the possibility of thermal damage to the retina from heat generated by the implant [Zrenner, 2002]; 3) requirement of functional inner and middle retinal layers. Thus, implants are not advantageous for retinal diseases extending beyond the outer photoreceptor layer [Weiland, 2014]; 4) lack of sufficient incident light to enable microphotodiodes to generate adequate current. This often requires external power source to amplify the effect of the incident image [Weiland, 2014]; 5) surgically more challenge route compared to epiretinal, leading to severe surgical complications [Chader, 2009].

## 1.5. An Overview of Clinical Trials of Current Visual Prosthesis

Current clinical trials include the use of epiretinal implants [Mahadevappa, 2005; Yanai, 2007], a passive subretinal device [Chow, 2004] and an active subretinal device [Zrenner, 2007].

Amongst the retinal prosthesis, each possesses several components which are directed to a specific function. These include an imager to convert light to electrical signal, electronics that



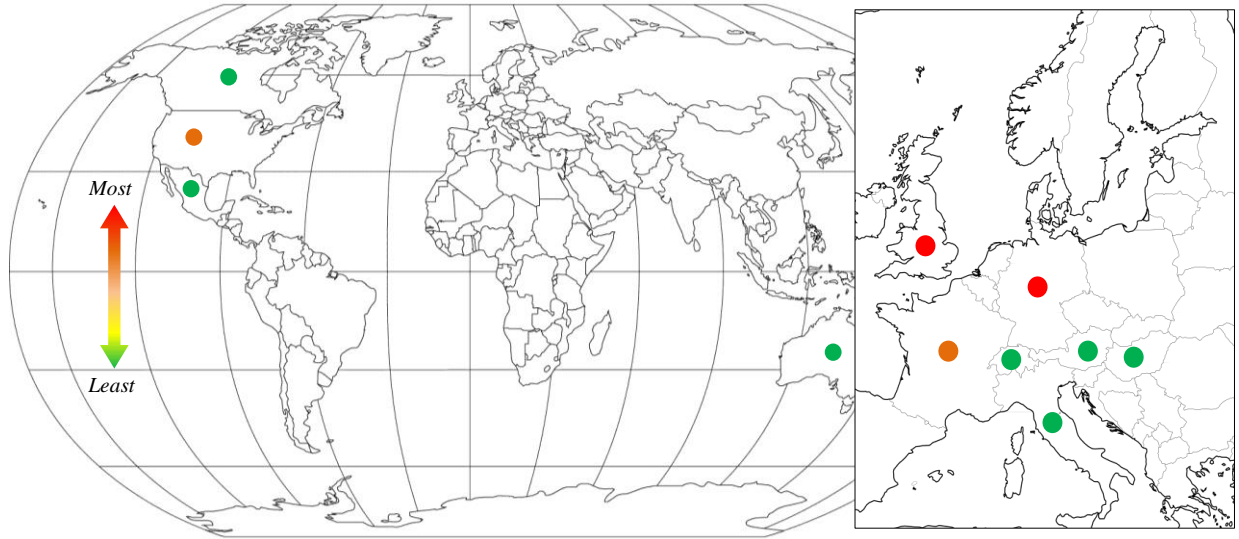


Fig. 1.4 Clinical trials of retina implant throughout the world.

pixel the image and generate enough electrical stimulus pulses and an electrode array that transmit the electric current to activate nearby cells. There are many challenges in realizing high density retinal prosthesis such as patient protection, charge balance mismatch, high degree of flexibility of electrode selection, low power consumption and small chip size [Ortmanns, 2007; Shire, 2012]. Currently 16 studies around the world are being tested, see fig. 1.4. Europe leads with 9 clinical trials. Inside that region, Great Britain leads with 5 clinical trials.

#### 1.5.1. Argus I Epiretinal Prosthesis

The implant was developed at Second Sight Medical Products, Inc. This is first generation design of implanted retinal device [Humayun, 2001]. Such device was implanted behind the ear of the patient and a cable proceeds into the eye, terminating in a  $4 \times 4$  grid of platinum electrodes. Electrode diameter are either  $260$  or  $520\mu\text{m}$ . The components of the retinal implant are essentially a miniature camera mounted behind some eyeglasses that capture external images. A simplified explanation of how retinal prosthetic devices work is as follows: 1) such external images are primary pixelized and sent wireless to a microprocessor that converts the information into an electrical signal; 2) the implant then produces a pattern of small electrical currents that approximate the external visual image; 3) underlying retinal cells are then activated, resulting in a dot-pattern at each point of stimulation; 4) this biological signal is sent via optic nerve to the brain, where the representation of the external visual image is created. As such, the electronic device was implanted in six subjects. With training, all volunteers were capable to distinguish objects from a small set [Yanai, 2007] and detect motion of a moving bar.

#### 1.5.2. Argus II Epiretinal Prosthesis

Developed at the same company of Argus I, the implant received approval in both United States and Europe to treat retinitis pigmentosa [Humayun, 2012]. As such, is an improvement of Argus I and consists of an active implantable device surgically implanted on and in the eye



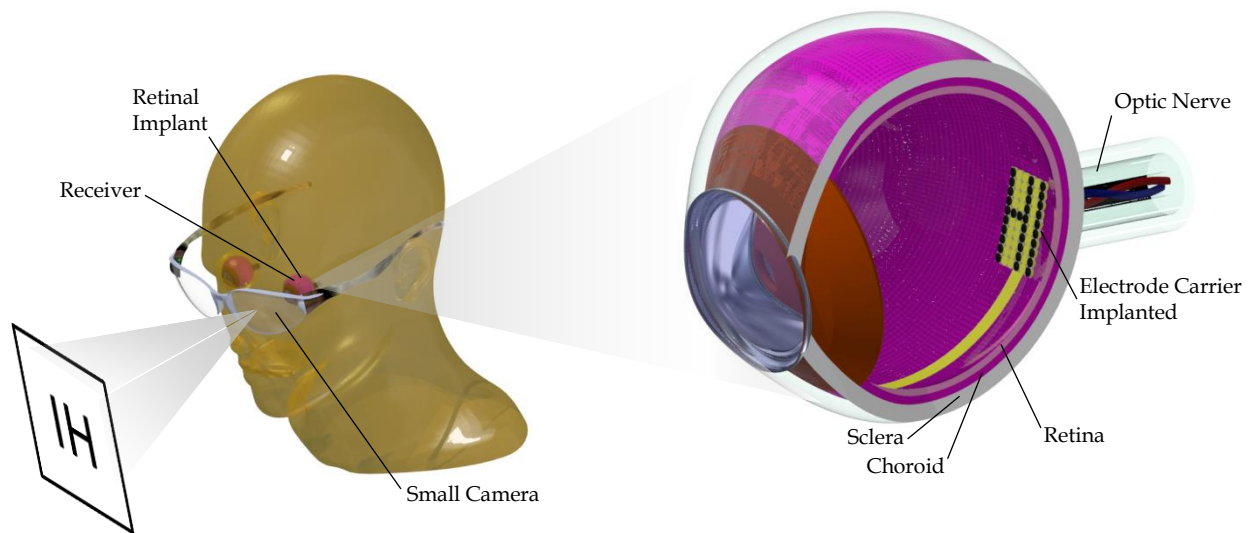


Fig. 1.5 Components of the retinal electronic prosthesis. Images such as from an ad are captured by a miniature camera mounted behind the eyeglasses. These signals are sent to a microprocessor that converts the data into an electronic signal, then to a receiver inside the eye, and finally to a microelectrode implant that stimulates electrically underlying ganglion cells. AutoCAD software was used for the creation of this figure.

(electrode array) and an external unit worn by the user, see fig. 1.5. The external unit consists of a small camera and transmitter mounted on glasses, video processor and battery worn on the belt or a shoulder strap. The electronics were outside the eye connected by cables across the eyewall to the array. Sixty electrodes arranged in a  $6 \times 10$  format were placed on the surface of the retina. The electronics were encapsulated with a hermetic packaging and the lifetime testing estimated to be longer than ten years.

Thirty subjects were enrolled in the United States and Europe between 6 June 2007 and 11 August 2009. All subjects were followed for a minimum of six months and up to 2.7 years. All thirty volunteers were capable to perceive light during electrical activation. Subjects stated to be better with the system “on” at tasks such as in object localization. Letter reading was tested in 22/30 participants. Six of these subjects were capable to identify any letter of the alphabet [Da Cruz, 2013].

Reliability of the prosthesis was also high. Over the follow up time period of this study, all but one device remain implanted and the vast majority of electrodes (94.4%) remain functional. All subjects who received an implant use their systems outside of outpatient clinical setting. In addition, 96% of subjects can localize high-contrast objects on a computer screen significantly better with the system “on” than “off”; 57% can detect the direction of motion of a high-contrast bar significantly better with the system “on” than “off” [Da Cruz, 2013].

In conclusion, the prosthesis system is reliable over the long-term and provided benefit to implanted subjects over this period. The data in this report suggest that on average, prosthesis subjects have improved visual acuity from light perception to at least hand motion, with some improving to at least counting fingers [Lange, 2009].

### 1.5.3. Intelligent Medical Applications

Intelligent Medical Applications developed a device that uses 49 electrodes microfabricated. The electronics module was placed outside the eye. The implant, however, was placed entirely located in the orbit. As it lacks of a camera, this scheme could only be activated in the clinic.

Seven subjects participated and the IMI device was implanted. All subjects could see spots of light and some simple patterns. The electronics were encapsulated with a polymer, thus the implant was removed after several months [Hornig, 2007].

#### 1.5.4. Epi-Ret3

Developed at Epi-Ret Consortium, the device consisted on 25 electrodes. Once miniaturized, the device could be implanted inside the eye. Epi-Ret scheme was designed for semichronic implantation and it lacked on a camera. A feature of such device was an improved contact with the retina. As a result, low perceptual thresholds were found [Roessler, 2009].

#### 1.5.5. Clinical Trials Comparison

Table 1.2 lists all the visual prosthesis currently tested with human volunteers. Table 1.3 lists the current developed devices with their quantity information of electrode number, diameter, and spacing.

TABLE 1.2

Implant	Approach	Subjects	Sight Improvements
Argus I [Humayun, 2001]	Epi	6	Distinguish objects, motion
Argus II [Humayun, 2012]	Epi	30	Perceive Light, object localization
IMI [Hornig, 2007]	Epi	7	Spots of light, simple patterns
Epi-Ret [Roessler, 2009]	Epi	6	Low perceptual threshold
Alpha IMS [Dagnelie, 2011]	Sub	9	Perceive Light, objects, read letters form reduce set.
Bionic Vision [Honert, 2007]	Sup	3	Phosphene perception and localization.

Epi = epiretinal prosthesis. Sub = subretinal prosthesis. Sup = suprachoroidal prosthesis.

### 1.6.Limitations of Visual Prosthesis

#### 1.6.1. Packaging

The devices previously explained are designed or otherwise stated as permanent implants. Therefore protective barrier that encapsulate the electronics is crucial to ensure neither humidity not ions reach them.

[Donaldson et al., 2013] described two methods to attain this barrier: hermetic enclosure and encapsulation. Hermetic enclosure is usually used for current neurostimulation implants. Typical methods for creating such enclosure consist of titanium or ceramic cases joined to a feedthrough that form a hermetic package. A feedthrough is a substrate with multiple isolated conductors [Jiang, 2010]. Here, the size of the package leads an implant with much larger dimensions than those of the enclosed electronics. Argus II used a similar package and due to the boundaries in conductor spacing it was limited to 60 independent channels.

Currently in bioelectronics implants, common spacing of feedthrough conductor is around 1 mm. In contrast, nowadays integrated circuit can achieve a spacing pad of 150  $\mu\text{m}$ , electrode size of less than 25  $\mu\text{m}$  and transistor dimensions of less than 1  $\mu\text{m}$ . This is rather a dimensional

TABLE 1.3

Visual Prosthesis	Number of Electrodes	Elect. diameter [ $\mu\text{m}$ ]	Electrode spacing <sup>2</sup> [ $\mu\text{m}$ ]
[Mahadevappa, 2005]	16	500	800
Argus I [Humayun, 2001]	16	520, 260	800
Argus II [Humayun, 2012]	60	200	575
IMI [Hornig, 2007]	49	100, 360	75, 80 <sup>3</sup>
EPI-Ret3 <sup>1</sup> [Roessler, 2009]	25	100	500
[Reinhard, 2006]	24	100	750
[Rizzo III, 2003]	20	100	620
[Rizzo III, 2003]	100	50	220
[Dagnelie, 2011]	16	50	280
Bionic Vision [Honert, 2007]	33	600	900

<sup>1</sup>Clinical trials stopped, the company is presently closed. <sup>2</sup>Spacing is center-to-center. <sup>3</sup>See figure 8.2.

problem and becomes clear that packaging is a major driver of implant dimension. Encapsulation barrier uses a conformal coating that forms a layer around the electronics. Using such packaging, the conformality of the coating avoids the condensation of incoming water on the surface of the electronics. However, this is very difficult to attain in practice. Once polymers are used to create such protective layer, water vapor can penetrate through the polymer. Retina implants with polymer encapsulation of 1 or 2 year lifetime suggest that more process is required for long-term encapsulation. The IMI device used a conformal protective polymer coating (Parylene) and did not function longer than 2 years [Weiland, 2014].

Alpha IMS has a high density of electrodes, but such density is merely conceivable due to the system has less robust encapsulation technique. Alpha IMS reported the longest device lifetime to be less than 1 year [Stingl, 2013]. Thus there is a tradeoff between securing the electronics for long-term encapsulation and visual perception. Polymers are generally considered not adequate for securing active circuitry for ten years. Water vapor penetration is too hasty [Weiland, 2014]. Ceramics and glass have better water block properties. These materials include films such as silicon nitride, silicon carbide, polycrystalline diamond, and metal thin films. Semiconductor materials like silicon, silicon dioxide, or silicon nitride are very popular because they are resistant to many corrosive environments [Weiland, 2014].

Xiao and colleagues developed an encouraging coating based on ultra-nano crystalline diamond, showing evidence of stability and biocompatibility [Xiao, 2006].

### 1.6.2. Visual Resolution

[Dagnelie et al., 2006], [Cha et al., 2003] and [Thompson et al., 2003] simulated phosphene images using a pixelized vision simulator. These experimental observations used a video headset, computer screen display, or masks [Cha et al., 1992] that convert images into a square pixelated grid similar to what it is expected by an array of artificial vision implant. [Chai et al., 2007] converted images of printed text into various pixelized patterns made up of discrete dots and present them orderly on a computer screen.

In essence, the simulator determines the effects of dot number and spacing on reading speed and face recognition. The results of such trials can suggest minimum specifications of visual devices that may enable blind individuals with visual percepts to achieve the formerly stated challenges [Thompson et al., 2003]. Moreover, it can be beneficial to understand what might be obtained from a visual prosthesis over the foveal projection.

The results from each previously stated works are as follows. [Thompson et al., 2003] found that a  $32 \times 32$  dot resolution and dot size of around 31,5arcmin would allow 83% accuracy in face recognition at high-contrast conditions (darkest gray level 0%). [Bagnoud et al., 2001] simulated an artificial vision device by dividing a  $10^\circ \times 10^\circ$  field into an area of square dots and presented single letters and common four-letter words. They found that 400 and 1200 dot resolution at dot size of <30arcmin and <18arcmin would allow at least 80% correct word recognition at  $0^\circ$  and  $10^\circ$  eccentricity, all respectively. [Dagnelie et al., 2006] learnt that a visual implant with  $16 \times 16$  electrodes and 22.5arcmin may allow reading success. [Chai et al., 2007] found that a  $12 \times 12$  dot resolution and dot size of around  $0.33^\circ$  would permit the subjects to identify every Chinese character without error.

In table 1.4 lists the results formerly explained. The detail area corresponds to the space covered by each dot at the retina and calculated as

$$D_A = (n \cdot \tan[d_s])^2, \quad (1.1)$$

$D_A$  is the detail area,  $n$  is the distance from the nodal points to the retina and  $d_s$  is the dot size given in degrees. Here we assuming that a square punctuate spot of light is produced in the retina.

TABLE 1.4

Reference	Dot Size [ $^\circ$ ]	Dot Grid (No. of dots)	Detail area [mm $^2$ ]
[Chen et al., 2008]	0.1	-	0.00088
[Bagnoud et al., 2001]	0.3	1200	0.0079
[Chai et al., 2007]	0.33	$12 \times 12$	0.0095
[Dagnelie et al., 2006]	0.375	$16 \times 16$	0.012
[Bagnoud et al., 2001]	0.5	400	0.022
[Thompson et al., 2003]	0.525	$32 \times 32$	0.024

### 1.6.3. Pixel-wise Vision

Pixel-wise visual perception is defined as the generation of very small and independent spots of light by electrode stimulation. These single small spots of light can be thought as one-to-one, electrode-to-pixel, scoreboard-like experience with punctate individual phosphenes. As a result, a better perception is created that ultimately will bestow a high-resolution response. As a requirement 1000+ electrodes are needed to upgrade basic issues such as mobility, independent living, navigating on interior and exterior environments and reading large-sized text, see fig. 1.6.

For flicker-free vision, a high density epiretinal implant needs to be stimulated at a frame rate between 20 [Lujan (a), 2016] to 60 Hz [Sivaprakasam, 2005]. A stimulation strategy using parallel to serial electrode activation is usually engaged as fractions of the electrodes are activated in parallel so as to avoid unsafe charge transfer to the tissue [Ortmanns, 2007].

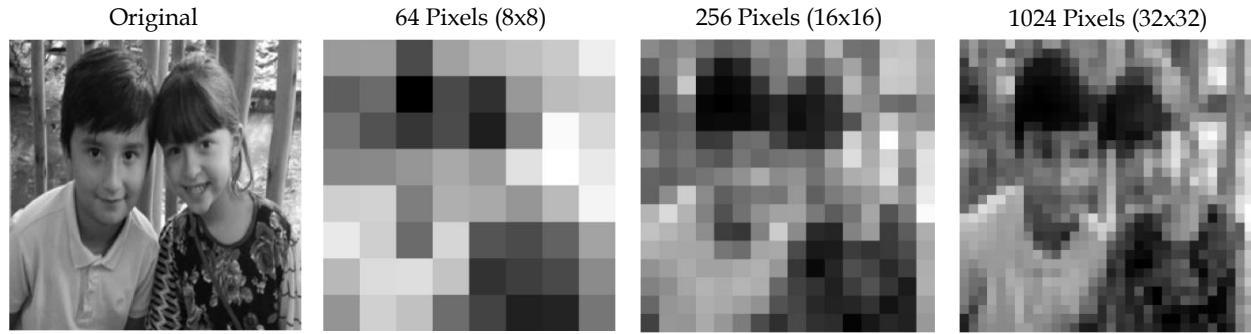


Fig. 1.6 Comparison of pixel resolution. Figure also displays how visual perception becomes clearer once the electrode amount inside some array is increased. Matlab image processing was used for the creation of this figure.

Amongst all state-of-the-art retinal devices, at date none of the implants tested in human patients have produced perceptions of “pixelized vision” [Weiland, 2014]. In spite of Argus II used an external camera and an image processing chip that pixel the image and sent the information to a microprocessor, the best measured visual acuity was 20/1260 [Da Cruz, 2013].

The projected vision that an array of  $6 \times 10$  electrodes could provide was not the case. The spots of light generated by cell activation cannot be precisely controlled by the external camera. Alpha IMS study reported visual acuity in 2 of 9 volunteers, with a best measurement of 20/546 [Weiland, 2014].

As for the experimental testimonies, both Argus II and Alpha IMS, common patients cannot perceive uncomplicated forms and letters instantly; rather they scan their head over objects so as to judge what they are seeing [Weiland, 2014]. In previous clinical trials of both sub- and epiretinal approaches demonstrate that patients do not experience such flawless pixelized sight as shown in many publications. An idea that each electrode produces a similar spot of light as compared with its neighbor is not completely the case.

Argus II clinical trial demonstrated that 55% of single electrodes were capable to produce a spot of light within the safe boundaries. It is clear, however, patients have at least some spatial information of the surrounding. RI and Alpha IMS patients could detect simple patterns of letters and read letters form a reduce set, respectively. Subjects who could read letters clearly acquire data from multiple pixels to reach their own task and have reported form vision in some cases. Nevertheless, the control of the implant upon spots of light is not precisely consistent. Argus II and Alpha IMS grouped together parallel electrodes so as to simultaneously elicit a response [Weiland, 2014].

Nanduri and colleagues investigated the relationship between perception size, stimulus magnitude and frequency [Nanduri, 2012]. What they found is objects increase their brightness as the frequency increases without increasing the size of such object. Thus, pulse rate modulation should be considered as a means of intensity coding for future retinal prosthesis

#### 1.6.4. Electrodes

##### 1.6.4.1. Introduction

A biomedical electrode is a conductor through electricity enters or leaves a non-metallic tissue. Such kinds of electrodes are used in a wide range of applications:

- a. Electrocardiogram bioelectric event detection.
- b. Cardiac pacing and FES therapeutic impulse application.
- c. AC impedance characterization of body tissues.

Biological tissues are rich in electrolytes. As stimulation requires the use of the electrodes, however, metallic electrode comes in contact with an electrolyte and an ion-electron exchange occurs as a result of an electrochemical reaction. Therefore, an electrode-electrolyte interface is created.

#### 1.6.4.2. Electrode-Electrolyte Interface [Pandey, 1996; Fay, 1983]

Once the electrode makes contact with an electrolyte, an interface is thus formed between each phase. The electrode is metallic and has one type of charge carrier called electrons (negatively charged). Electrolyte, however, has two types of carriers, i.e. positively charged cation and negatively charged anion. Deep in the bulk of the two phases, charge carriers are electrically neutral because the net force on the carrier is zero when averaged over a large volume.

At the electrode-electrolyte interface, however, carriers in the two phases start to accumulate at each phase boundary and the interface acts as a barrier in either direction. As the buildup grows at each side, the electric forces (attractive or repulsive interaction between any two charged objects) overwhelm the barrier, resulting in the flow of charges. The charge flow ceases once the electrochemical potentials on each side become equal and reach equilibrium.

#### 1.6.4.3. Parallel-Plate Condenser Helmholtz Model [Xiao-Zi, 2009; Ratner, 2012]

Once a metal is incorporated in an aqueous solvent by release of cations (positive charged ions), it becomes negatively charged. This process continues until equilibrium is attained such that for any cation formed there is ultimately a metal atom formed by reverse process.

Two layers of opposite charges exist and thus a separation is formed resembling a capacitor. By that means, the two oppositely charged sheets constitute absolutely analogous to an electrical capacitor which has two plates of charge separated by some distance. Thus a potential difference is created between the metal and solution, see fig. 1.7a.

Due to the separation of opposite charges, a strong electric field in the space between two charged layers is set up. Under the absence of external current condition, the electrode has a charged double layer and the capacitance is charged. The total impressed current is divided into one crossing the double layer through Faradic resistance and a second charging the capacitance. The drawback on this theory is Helmholtz neglected the relationship between capacitance and potential.

Known simply as the double layer, Helmholtz model consists of a dense layer of ions stuck to the electrode surface boundary. This dense layer can be further divided into inner and outer Helmholtz planes. 1) Inner Helmholtz plane (IHP) is adjacent to the electrode surface and is completely oriented towards water dipoles and absorbed ions. The orientation of water dipoles depends on the specific interaction with the electrode surface. Here, the potential changes linearly with the distance. 2) Outer Helmholtz plane (OHP) represents the locus of the electrical center of positive and negative charge ions. This plane resides at a fixed distance from the metal

due to the water molecules that are between the surface of the metal and ions. Here, the degree of orientation decreases with distance and the potential changes linearly with the distance.

The capacitance can be calculated as follows and determined by the permittivity of electrolyte, the area of the interface and the distance between the two oppositely charged layers

$$C_H = \epsilon_0 \epsilon_r A d^{-1} \quad (1.2)$$

#### 1.6.4.4. Diffuse Layer Gouy-Chapman Model [Karlheinz, 2006]

Known simply as diffusion layer, Gouy-Chapman model consists of ions diffused due to the effect of thermal fluctuations that tend to drive the counterion away from the surface. Gouy and Chapman proposed another layer that extends up to 1  $\mu\text{m}$  from the outer Helmholtz plane towards the bulk solution. Here, the net charge is opposite to that of the Helmholtz inner plane. Deep in the bulk, the ions are held in increasing disorder. This less orderly arrangement constitutes the diffuse layer. As the concentration of charged ions at Gouy-Chapman layer increases, the thickness of such sheet decreases. The ions are thus pushed down into the outer Helmholtz plane. With this modification, it bestowed the freedom to use Maxwell-Boltzmann statistics which can be applied to the charge distribution of ions as a function of distance away from the metal surface. Here, the potential varies exponentially with the distance, see fig. 1.7b.

The differential capacitance normalized by the area is calculated as follows [Srinivasan, 2006]

$$C'_{GC} = \left( \frac{n_0 \epsilon_0^2}{2\pi kT} \right)^{1/2} \cosh \frac{e_0 V}{2kT}, \quad (1.3)$$

$n_0$  is the number of ions positive and negative sign per unit volume in the bulk of the electrolyte and  $V$  is the potential drop from the metal to the bulk of the electrolyte.

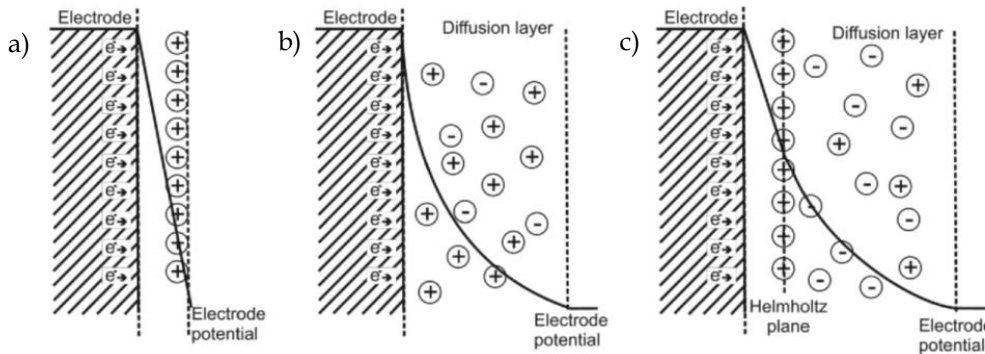


Fig. 1.7, a) Helmholtz model, b) Gouy-Chapman model, c) Stern model.

#### 1.6.4.5. Stern Model [Ahmad, 2006]

Stern combined the ideas of Helmholtz and of that of a diffuse layer and proposed to divide the double layer into two parts: an inner part, named the Stern layer, and an outer part, named the Gouy or diffuse layer, see fig. 1.7c.

Essentially, the Stern layer constitutes of immobile ions which is directly absorbed to the surface boundary of the metal. Due to its size a counterion cannot get infinitely close to the surface but always remain at a certain distance between the surface boundary of metal and the center of the counterion.

Conversely, Gouy-Chapman layer consist of mobile ions. The differential capacitance of the total electric double layer constitutes an important quantity with respect to experimental verification. As regard to Stern modeling, total double layer capacitance,  $C_T$ , is composed of two capacitances in series, the capacitance of Stern layer,  $C_{ST}$ , and the capacitance of diffuse Gouy-Chapman layer,  $C_C$ .

#### 1.6.4.6. Electrodes in Visual Prosthesis

Power consumption and its efficient use is a noteworthy issue for a 1000-or-more electrode implanted device. Amongst of all critical factors, four of them predominate:

- Small electrodes for creating focused areas of excitation.
- Output requirements for neural stimulation.
- Biocompatible materials with low impedance.
- Small area of packaging.

High-resolution visual perception is attained by activating small areas of the retina. Thus, small electrodes are a topmost requirement. Biocompatible materials with low impedance are essential because power consumption from an implanted retinal stimulator contributes to thermal rise at stimulating tissue.

One approach to determining the best electrode size is to draw an analogy to natural vision. An individual with 20/20 vision can resolve differences of 1/60 of one degree of visual angle, which translates to 5  $\mu\text{m}$  on the retina. Thus, it has been argued that to restore vision to this level, one would need electrode diameter of 5  $\mu\text{m}$  [Weiland, 2014].

A second way to determine the best electrode size depends on the high amount of electrodes needed to perform desired visual tasks. Therefore an optimization of electrode size, total area covered by the electrodes (based on the visual angle covered), number of electrodes [Weiland, 2014] and distance between them is a requirement [Lujan (c), 2016].

To date, electrode array require major improvement for safe stimuli and visual acuity. Safe activation of cells require high charge density threshold coming from small electrodes. Thus, electrode materials must support scenarios of any kind. Further, electrode substrate must adjust to the curvature of the human eye without damage the retina. Retinal implant electrodes use photolithography and micromachining to fabricate arrays. Such electrode technology was used by Argus II and Alpha IMS. Using those methods, a higher electrode density can be attained [Weiland, 2014].

Argus II and Alpha IMS used platinum gray and titanium nitride respectively. Typical electrode material in neurostimulation is bulk platinum. The charge injection capacity for such material is 0.1-0.35  $\text{mC}/\text{cm}^2$ . Platinum gray can inject up to 1  $\text{mC}/\text{cm}^2$ , and titanium nitride until 0.9  $\text{mC}/\text{cm}^2$ , which represents an important step for implantable bioelectronics. Invasive electrodes coated with PEDOT have been coined as a supercapacitor material due to its large electroactive voltage window, high chemical stability among conductive polymers, lower impedance and higher charge density injection [Starbird, 2012]. Along with its own properties,



PEDOT has a high capacitance current due to a specific charge injection mechanism, in combination of Faraday (charge transfer) and non-Faraday (double layer capacitance) processes. The larger porous area reported for PEDOT also improves the interaction with biological environments by increasing biocompatibility.

Advanced electrode materials, e.g. conductive polymer like PEDOT-NaPSS [Starbird, 2012] has the property to lower considerably the electrode impedance. While injecting similar amount of charge with low peak voltage, they reduce the power consumption required to activate neurons.

#### 1.6.4.7. Faradaic and Non-Faradaic (Capacitive) Process

Biomedical electrodes interact with the body fluids (electrolyte) in two primary fashions: faradaic and non-Faradaic. Faradaic and non-Faradaic processes occur simultaneously during electrode reactions. In non-Faradaic process, the charge flowing towards in an electrochemical environment gets accumulated at the two sides of each boundary. In such process, there are no charge transfer across the interface and reactions such as adsorption and desorption can take place and modify the structure of the electrode/electrolyte interface [Madou, 2011].

If only non-Faradaic redistribution of charge occurs, the electrode/electrolyte interface may be modeled as a simple electrical capacitor called the double layer capacitor.

Electrodes in which no charge transfer can occur are called polarizable electrodes. In this case, half-cell potential of the electrode results in the formation of a double layer capacitance. Charging or discharging such capacitor influences the bioelectric behavior [Ratner, 2012].

As regards to faradaic process, the electrode may establish ohmic contact with the surrounding electrolyte environment, thereby transferring electrons across the electrode-electrolyte interface via oxidation and/or reduction. All such charge-transfer processes are governed by Faraday's law and hence are called faradaic processes. Electrodes at which faradaic processes occur are known as charge-transfer electrodes [Ratner, 2012]. Further, such electrodes experience a charge-transfer resistance,  $R_{CT}$ , which can be thought of as shunting the non-Faradaic double layer capacitance and whose expression can be derived from the Butler-Volmer equation for small applied signal amplitudes [McAdams, 2010]:

$$R_{CT} = \frac{RT_A}{nF} \frac{1}{i_0}, \quad (1.4)$$

$i_0$  is the exchange current flowing across the interface under equilibrium conditions,  $R$  is the universal gas constant,  $T_A$  is the absolute temperature,  $n$  is the valence of the ions and  $F$  is the Faraday constant. Electrodes in which charge transfer can occur in an unrestricted manner and represent truly a faradaic behavior are called non-polarizable electrodes. Essentially real electrodes are neither perfectly polarizable nor perfectly non-polarizable. Any net current flow across an electrode-electrolyte interface will experience finite faradaic impedance across which some potential will result because of the double layer capacitance.

An electrode system which has low quantity of charge transfer resistance allows electric current pass through the interface almost unrestricted. As a result, low energy is wasted at the interface and the potential formed by the double layer capacitance is relatively small, allowing the system to be non-polarizable.

### 1.6.5. Electrode Array Detachment

Threshold current to activate ganglion cells were found to increase with time of surgery [Mahadevappa, 2005]. The main reason is most likely the lifting off of the array from the underlying tissue, see fig. 1.8. Simulation-based studies have been underscored the importance of controlling the distance between the array and the retina surface [Lujan (a), 2016; (b); (c)].

Therewith the problem lays the charge density to activate cells. The charge density becomes proportional to the square of cell-electrode distance [Lujan (b), 2006]. Once the charge density surpasses its own safe limit, gas bubbling formation may occur, which damages the underlying tissue of the retina.

If subretinal array increases greatly its size, the risk of detaching the entire retina may be possible. The surgery for the Alpha IMS suggests silicone oil injection placed in the eye, which reduces the probability of retinal detachment. Epiretinal implant size is limited because of the small incisions that can be safely made in the eyewall (less than 5 mm) [Weiland, 2014].

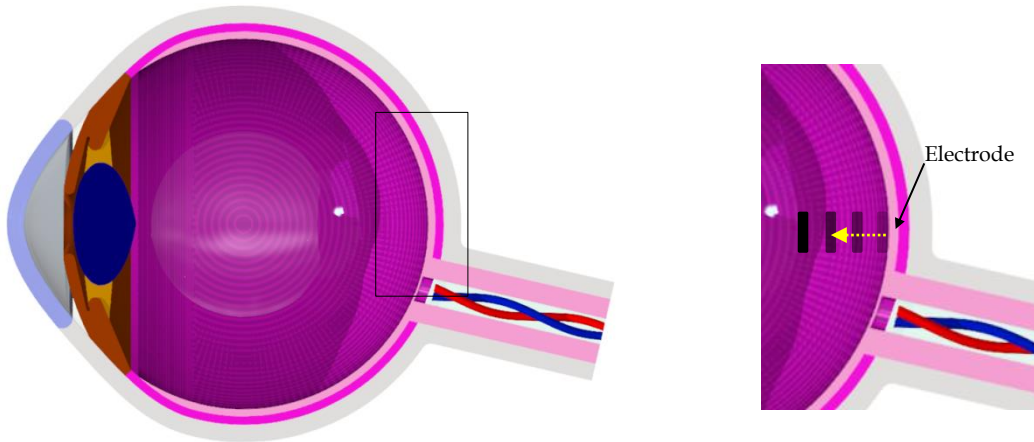


Fig. 1.8 Electrode detachment from retina surface. AutoCAD software was used for the creation of this figure.

### 1.6.6. Perceptual thresholds

Indeed, there exists a threshold current for eliciting light perception. In recent human clinical trials [Mahadevappa, 2005], many subjects were able to perceive light with stimulus current of around 50  $\mu\text{A}$  and electrode-tissue impedance of less than 30  $\text{k}\Omega$ . Although the perceptual threshold is highly dependent on the electrode size and materials as well as the separation between the electrodes and the retina cells, these results make it possible to use such retinal prosthesis device.

For electrode size of 500  $\mu\text{m}$  of diameter, the human trials demonstrated a range for perceptual thresholds between 139 to 702  $\mu\text{A}$  for one volunteer; 130 to 575  $\mu\text{A}$  for a second one. A third volunteer reached 24 to 143  $\mu\text{A}$  for an electrode diameter of 250  $\mu\text{m}$  [Mahadevappa, 2005].

Amongst other clinical trials, electrical stimulation of the retina was performed on awaken volunteers by placing a single 250  $\mu\text{m}$  diameter handheld needle electrode or a 10  $\mu\text{m}$  thick microfabricated array of iridium oxide electrodes of either 400 or 100  $\mu\text{m}$  of diameter on the retina.

Normal-sighted volunteers had thresholds at charge densities below 0.25 and 1.0 mC/cm<sup>2</sup> for 400  $\mu$ m and 100  $\mu$ m diameter electrodes, respectively. The ratio of average charge density thresholds in blind patients to normal-sighted is 22, meaning that a blind patient requires high charge density to activate nearby cells. Strength– duration curves maintained its original shape and were obtained in two blind patients revealing their threshold [Rizzo III, 2003]. Strength–duration curve states the interrelation between stimulus strength and pulse duration.

To elicit light perception of various brightness levels, the stimulators for epiretinal prostheses require an output compliance voltage of  $\pm 10$ V, thus requiring area-consuming high-voltage (HV) transistors [Sooksood, 2011]. The compliance voltage is the maximum voltage that the current source can supply to a load. Recently, simulation-based findings suggest using small electrodes below 10  $\mu$ m coated with biocompatible materials that reduce the compliance voltage below 3.3V [Lujan (a), 2016; (c)].

### 1.6.7. Heat Dissipation

An essential requirement of visual prosthesis device is the integration of electronic circuitry with the microelectrode array. Since electronics of any kind dissipates a certain amount of power, an increasing temperature will affect the surrounding tissues. Thus, power dissipation from an implanted stimulator at electrode-tissue interface contributes to the thermal rise at stimulating tissue. As an exemplary clinical case, significant brain damage was reported with a human patient after diathermy treatment using an implanted deep brain stimulator. In postmortem examinations, acute deterioration in the tissue was shown nearby the lead electrodes due to excessive tissue heating [Nutt, 2001]. Even more moderate temperature increases in tissue can cause significant damage to various cellular functions [Sohee, 2007]. Next, a graphical representation of how heat increase damages the tissue is displayed, see fig. 1.9.

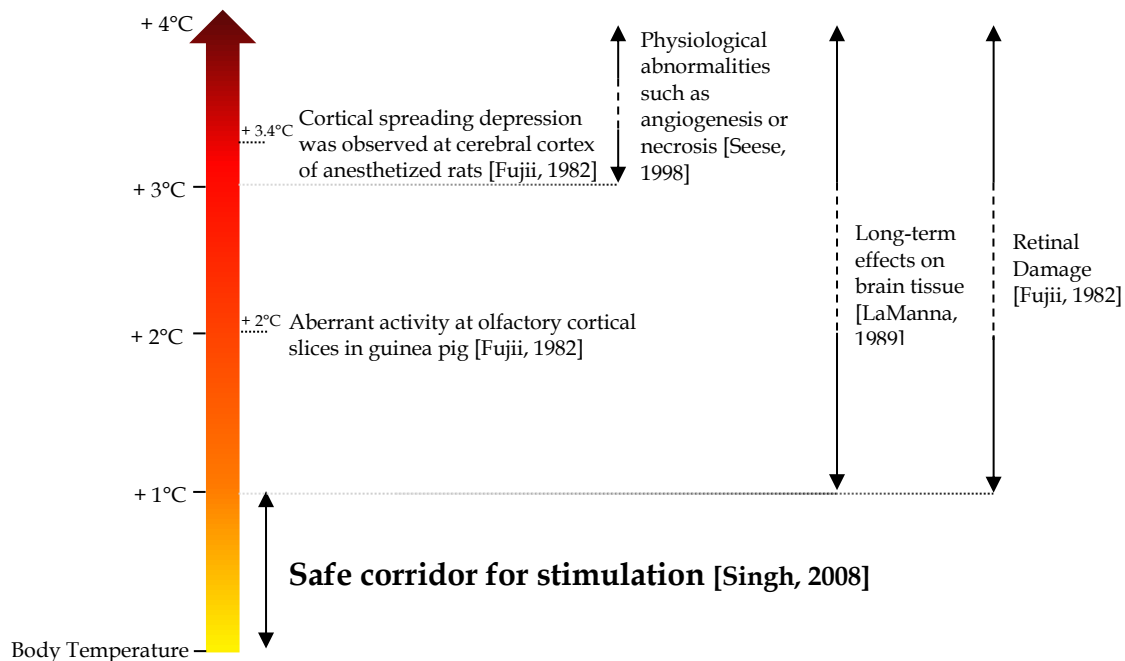


Fig. 1.9 Temperature effect on tissue from several published works.

It is reported that maximum permissible temperature increase in the cortex is about 1°C or maximum power density is 80 mW/cm<sup>2</sup> of exposed tissue area [Seese, 1998]. The neural tissue heating from the retina implant can be calculated using the average power density at the device in the linear approach of  $\Delta T = 1^\circ\text{C}$  per 12.2 mW/cm<sup>2</sup> assuming only heat conduction [Sohee, 2006].

Thus, an essential rule-of-thumb is to prevent any of these thermal consequences. The neural interface devices must be shown not to cause significant temperature increases in the implanted tissue. As regards to visual prosthesis, the liquid environment of the vitreous humor acts as a heat sink that is capable of dissipating a significant amount of power. An electronic chip positioned away from the retina can run at considerably higher powers than a chip positioned on the retinal surface [Piyathaisere, 2003].

#### 1.6.8. Summary

Recent visual prosthesis devices have crossed the gap to develop a 1000+ electrode array [Chen, 2013]. Despite that these devices classify themselves as medical-grade implant, clinical trials are required in order to surpass major challenges for bioelectronics implants including long-term stable performance of the implanted electronics and safe surgical implantation procedure. Previous studies have shown that electrical stimulation of the retinal ganglion cell side (epiretinal stimulation) can produce discrete spots of light and that spatial resolution and partial restoration of vision is possible.

Nevertheless, there is much to learn about nearby cell activation, pixel-wise visual perception, safe implantation, harmless stimulation avenues and technological advances in packaging to be aligned with the success of today's cochlear implant technology.

### 1.7. Visual Anatomy, Physiology and Signal Processing

#### 1.7.1. Visual Anatomy

The human eye reacts to light, provides vision and can distinguish about 10<sup>6</sup> colors. Knowing that perhaps the eye consists of the most complex organ in the human body, however, it's most important parts will be discussed.

The cornea is a transparent and curved frontal unit known as the window of the eye. Its typical segment is about 8 mm in radius. Its main functions are to shield the rest of the eye from germs, dust and other harmful matter. Other functions are to control and focus the entry of light into the eye. As the light strikes the cornea, it bends-or refracts-the incoming light onto the lens. The lens, then, refocuses that light onto the retina so as to begin the visual phototransduction. [Judd, 1975].

The sclera is a tough, white, outer layer of the eyeball. It begins at the edge of the cornea and surrounds the eyeball until it reaches the optic nerve in the back of the eye. Eye movement is controlled by six muscles (not shown in fig. 1.3) that attach at various locations on the sclera [Fekrat, 2006].

The lens has the purpose of refract or bend the light so that an image can be formed on the retina so the brain can distinguish. Although the cornea performs 70% of all necessary bending

of light rays, the lens carries out the other 30% [Fekrat, 2006]. It also comprises a complex task of changing its shape to maintain a clear image or focus on an object as its distance varies. This adjustment of the lens is known as accommodation.

The retina is a photosensitive layer of tissue that enables the sense of sight. The thickness of the retina shows variations inside the human eye, being the thinnest at the foveal floor, 0.1 mm, up to 0.3 mm at the foveal rim. Along this layer, a layered structure with various types of neurons is placed all interconnected by synapses. As the light strikes the retina, a cascade of chemical and electrical events begins and ultimately triggers action potentials to the brain.

The fovea is a small, central pit composed of closely packed cones in the eye. It is located in the center of the macula lutea of the retina. The fovea is responsible for sharp central vision (also called foveal vision), which is necessary in humans for activities where visual detail is of primary importance, such as reading and driving. In the primate fovea (including humans) the ratios of ganglion cells to photoreceptors is about 2.5; almost every ganglion cell receives data from a single cone, and each cone feeds onto between 1 and 3 ganglion cells. Since the fovea does not have rods, it is not sensitive to dim lights. Vitreous Humor is the clear gel that fills the space between the lens and the retina of the eyeball of humans and other vertebrates. The vitreous humor is in contact with the retina and helps to keep it in place by pressing it against the choroid. It does not adhere to the retina, except at the optic nerve disc.

### 1.7.2. Physiology of Retinal Neurons

The retina is a neural portion of the eye and part of the central nervous system. It comprises complex neural circuitry that converts light received at the photoreceptors into action potentials. There are mainly five types of neurons in the retina, see fig. 1.3.

Generally, two types of photoreceptors dominate: rods and cones. Such neurons are the only that are directly sensitive to light. In total, there are about 4.6 million cone cells and 92 million rod cells [Purves, 1997]. Their exact location is the outer nuclear layer, known as the light-detecting portion of the human eye. As a part of their structure, both have an outer segment made up of membranous disks that contain photopigment responsible for beginning phototransduction. After the absorption of light by the photopigment, a cascade of events initiates which in turn changes the membrane potential of the receptor. Absorption of a photon will hyperpolarize the photoreceptor and as a result glutamate released from the presynaptic terminal is decreased [Berson, 2007]. This process is related to the release of the neurotransmitter onto the cells they contact. Next, table 1.5 lists the differences between rods and cones: [Lea, 2001].

As a part of the inner nuclear layer, bipolar cells exist between photoreceptors and ganglion cells. Such cells transfer the information from the outer plexiform cells to the inner retina. Typical bipolar cell shape is cylindrical with a length of 20-30  $\mu\text{m}$  and diameter of 12-15  $\mu\text{m}$  [Publio, 2009]. When activated, bipolar cells display changes in membrane potential or graded potentials. Based on their response, they are distinguished by ON- or OFF-cells [Siegel, 2006].

As a part of the outer plexiform layer, horizontal cells are mainly inhibitory neurons that make synaptic connection with photoreceptors. Once the photoreceptors drive horizontal cells and bipolar cells, the former neuron regulate the photoreceptors via feedback signaling. This feedback loop provides a mechanism for the inhibition of signals from adjacent photoreceptors. Receptive fields of horizontal cells are characteristically large, often several millimeters in diameter [Dowling, 2002].

TABLE 1.5

Rods	Cones
Are unable to detect color	Are able to detect color
Provide low visual acuity <sup>1</sup>	Provide high visual acuity <sup>1</sup>
Are sensitive to dim light intensities	Are sensitive to high light intensities
Are spread approximately even across the retina	Are more numerous in the fovea than elsewhere
Cylindrical shape, 40-60 $\mu\text{m}$ length, 2 $\mu\text{m}$ diameter	Cylindrical shape, 6-30 $\mu\text{m}$ length, 5 $\mu\text{m}$ diameter
Are more numerous than cones (about 20 times higher)	Are less numerous than rods

<sup>1</sup> The main difference is several rods share a connection to the optic nerve whereas each cone has its own connection.

As a part of the inner plexiform layer inside the retina, amacrine cells inhibit neurons and interact with ganglion cells and bipolar cells. Amacrine cells are divided in narrow-field (30-150  $\mu\text{m}$ ), small-field (150-300  $\mu\text{m}$ ), medium-field (300-500  $\mu\text{m}$ ) and wide field (>500  $\mu\text{m}$ ) all based on their dendritic field diameter [Balasubramanian, 2014]. Its functionality is wide because at least 33 different subtypes of amacrine cells exist based just on their dendrite morphology and stratification [Kolb, 2005]. When activated, amacrine cells show graded potentials than action potentials.

Located in the inner surface at the ganglionic layer, ganglion cells are the output neuron of the vertebrate retina. The cells orderly collect the electrical information of the visual signal from bipolar and amacrine cells. Ganglion cells are sizable on average than most preceding retinal interneurons and have large diameter axons capable of passing the electrical signal in the form of transient spike trains [Kolb, 2011]. Ganglion cell diameter is usually ranged between 6 to 30  $\mu\text{m}$ . Unlike the previous cells, retinal ganglion cells do fire action potentials to the brain.

There are about up to 1.5 million ganglion cells in the human eye. On average, each retinal ganglion cell receives inputs from about 100 photoreceptors [Curcio, 1990]. Based on their functionality, at least four kinds of ganglion cells can be identified [Purves, 1997]

1. Midget cells are so called because of their small diameter. Midget cells receive input from relatively few rods and cones. They have slow conduction velocity and respond well to changes in color but weak in contrast.
2. Parasol cells are so called because of their large diameter. Parasol cells receive input from relatively many photoreceptors. They have fast conduction velocity and can respond well to low-contrast stimuli, but weak to changes in color.
3. Bistratified cells receive inputs from intermediary numbers of photoreceptors. Bistratified cells have moderate spatial resolution and conduction velocity.
4. Photosensitive cells contain their own photopigment which makes them respond directly to light even in the absence of photoreceptors.

### 1.7.3. Visual Phototransduction and Neurotransmitters

Visual phototransduction is a sensory transduction process that occurs in the retina through photoreceptors or cells that are sensitive to light. Once the photoreceptors absorb light and phototransduction process is complete, a cascade of events initiates and change the membrane potential of the receptor. As for the retina, this is the primary step that ultimately ends at the ganglion cells sending transient spike trains in form of action potentials to the brain.

The membrane potential of a photoreceptor hyperpolarizes in response to light, causing a reduction in the amount of neurotransmitter released by the photoreceptor onto downstream neurons. An opposite response happens once the photoreceptor depolarizes to dark, causing an increase of glutamate release. Phototransduction thus enables the photoreceptor to encode a light stimulus as a chemical output. As light is converted into electrical signals, it travels to the brain via axons of the retinal ganglion cells.

In the retina, neurons communicate with each other through synapses. Mainly, retinal cells use chemical synapses known as the predominant means for communication between neurons. Chemical synapses involve the release of neurotransmitter substance from presynaptic cells to specialized receptors on postsynaptic cells. As the presynaptic cell is depolarized, the neurotransmitter increases. Therefore, such signal is proportional to the membrane potential of the presynaptic cell.

There are two types of neurotransmitters, excitatory and inhibitory. Excitatory transmitters cause a depolarization in the postsynaptic cell. The inhibitory, though, does the opposite. The predominant excitatory neurotransmitters at the retina are glutamate and acetylcholine. The main inhibitory are GABA and glycine. Both photoreceptor and bipolar cells appear to use glutamate as their own neurotransmitter. Amacrine cells use GABA and glycine as its own neurotransmitter

#### 1.7.4. Synaptic Pathways

A highly simplified network topology of the retina, fig 1.3, starts with the photoreceptors, rods and cones that provide an input to the outer plexiform layer and make synaptic connection with horizontal cells and bipolar cells.

Horizontal cells, as formerly conversed, regulate the photoreceptors via feedback signaling that provides a mechanism for the inhibition of signals from adjacent photoreceptors. Bipolar cells are mainly excitatory neurons and make synaptic connection with amacrine cell and the ganglion cell.

Ganglion cells receive excitatory and inhibitory input from bipolar and amacrine cells, respectively, and transmit the electrical signal in the form of transient spike trains, or action potential, to the brain.

The retina is thus organized into two parallel pathways: the ON pathway which is activated to a local increase of brightness and the OFF pathway which is activated to an increase of darkness [Heckenlively, 2010]. As previously discussed, the response of bipolar and ganglion cells to a light stimulus upon the receptive field center and surround are opposite. The mechanisms of membrane potential changes in bipolar cells in response to light can be summarized as follows.

There are two populations of “on-center” and “off-center” bipolar cells. Each photoreceptor cell synapses on an “on-center” and an “off-center”, fig. 1.10a and b). Each “on-center” bipolar cell, in turn, synapses with an “on-center” ganglion cell. A similar network topology is performed in “off-center” cells.

When the receptive field center receives a light stimulus (on-center process, see fig. 1.10b), the photoreceptors are hyperpolarized [Siegel, 2006]. As a reminder, absorption of a photon hyperpolarizes the photoreceptor and as a result glutamate released from the presynaptic terminal is decreased.

The reduction of excitatory glutamate from the photoreceptor presynaptic terminal causes depolarization of “on-center” bipolar cells. This happens mainly because “on-center” bipolar cells have sign-inverting synapses, i.e. “on center”-cells respond to the hyperpolarization of photoreceptors in light with depolarization (activation) [Reynolds, 2010]. When activated, bipolar cells display changes in membrane potential or graded potentials. Depolarization of bipolar cells results in a rise in the release of glutamate transmitter, which, in turn, results in an increase in the firing of the corresponding “on-center” ganglion cell.

As regards to “off-center” network activation, see fig. 1.10a), such process formerly explained have a similar approach, but “off-center” ganglion cells are activated when darkness is directed towards the receptive field center. In this situation, no such photon is absorbed and photoreceptors are depolarized. Glutamate released by the presynaptic terminals is decreased and “off center” bipolar cells are activated mainly because “off-center” cells have sign-conserving synapses, i.e. are depolarized by the depolarization of the photoreceptor. As formerly argued, the changes of membrane potential of bipolar cells have a direct consequence to the response of ganglion cells. Moreover, such changes are interconnected to the direction of light on the receptive field.

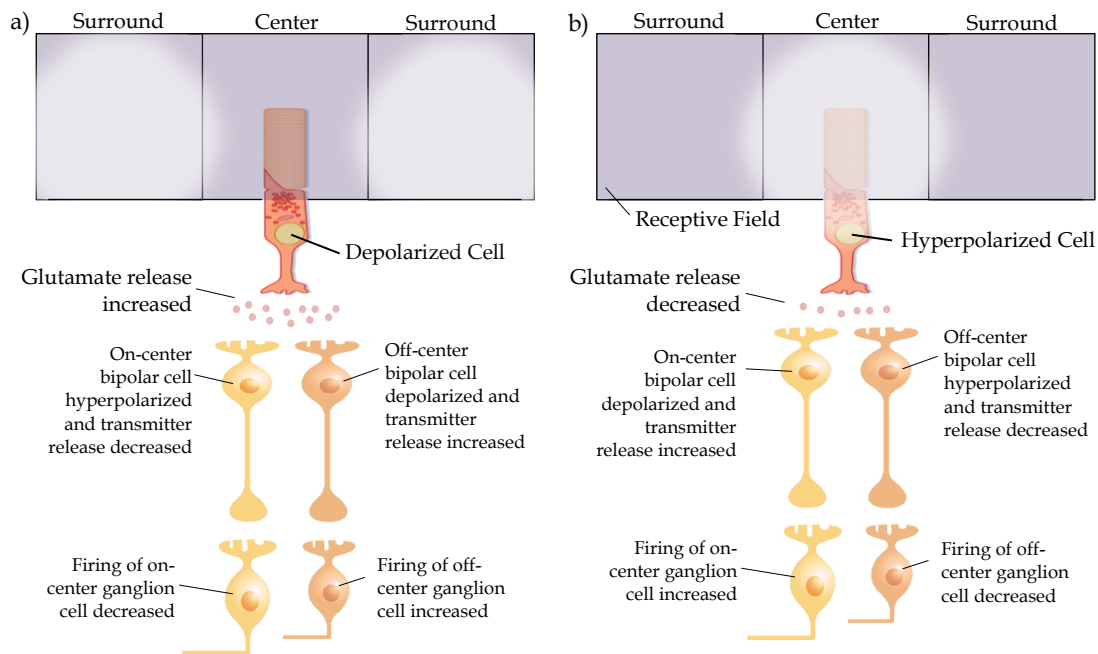


Fig. 1.10 a) “Off-center” receptive field; b) “On-center” receptive field.

### 1.7.5. Light and Dark Adaptation

Visual adaptation is a complex process of adjustment of the visual system to its environment. The following two processes are the most common [Ebrey, 2001; Rattay, 2012]:

Dark adaptation reduces light intensity. Its process consists of an increase of cone sensitivity so that light-sensitive pigments increase their concentration. Human retina has three different kinds of cones and each contains different light-sensitive pigments that respond best to certain wavelengths. Such kinds are L-cones, M-cones and S-cones that respond optimally to long



wavelengths (reddish color), medium wavelengths (greenish color), and short wavelengths (bluish color), respectively. Cones are fully dark-adapted within five or ten minutes.

Dark adaptation also increases sensitivity of rods so that light-sensitive pigments increase their concentration. Rods are fully dark-adapted within twenty or thirty minutes. Once an increase of sensitivity is produced, the threshold for detecting light is reduced, allowing the eye to build a representation of its surroundings.

Light adaptation operates such that as levels of illumination increases both the sensitivity of rods and cones decreases, preventing the receptors from saturating and thereby greatly extending the range of light intensities over which they operate.

### 1.7.6. Receptive Fields

As light rest on different parts on the retina after striking the cornea and then the lens, each retina contains a two-dimensional representation of visual space.

The region of space where a stimulus influences the response of receptor cell (cone, rod, bipolar or ganglion) is called receptive field. Such field is always determined relative to the receptor under consideration. The direction of light on the receptive field of ganglion cells is used to distinguish their responses: 1) an “on-center” bipolar or ganglion cell increases its response when light is directed towards the center of its receptive field, see fig. 1.10b; 2) an “off-center” bipolar or ganglion cell increases its response when darkness is directed towards the center of its receptive field, see fig. 1.10a. When light does not fill either the center or the surround, or it overlaps both, the outcome would be an algebraic summation of “on” and “off” responses (for more information about this topic, see [Gabbiani, 2010]).

## 1.8.Functional Electrical Stimulation

### 1.8.1. Basics of Electrical Stimulation

In functional electrical stimulation (FES), computer technology sends low-level electrical impulses to activate specific muscles in your legs, arms, hands or other areas. The electrical impulses are sent to the muscles either through surface electrodes on the skin or through electrodes implanted just under the skin. Electrical stimuli can cause your muscles to contract, which may promote increased muscle bulk or muscle control.

FES may improve your range of motion, your strength, and the functional use of your hands, arms or legs. It may help you perform activities such as grasping or holding an item with your hand or moving your arms or legs in a cycle or stepping motion. FES is useful in the treatment of some neurological disorders such as deep brain stimulation in the cases of epilepsy, depression, Parkinson’s or dystonia.

FES is also useful for restoring physiological functions through the use of electronic implants such as pacemaker, bladder prosthesis and the phrenic pacer. It has also been used for restoring the movement of extremities by using Functional Neuromuscular Stimulation (FNS) in the case of neuromuscular deficits caused by spinal cord injury, multiple sclerosis or stroke.

Moreover, an improvement of blood circulation, aerobic conditioning, heart health, movement patterns of muscles, prevention of bone mineral density loss, reduction of muscle

spasms and overall fitness can be exercised by FES. As the computer sends signals to the tissues, the biological electric current, by definition, is carried by ions and flows in the direction of positive ions. Subsequently, it distributes itself radially throughout the tissues.

When the intensity of electric current is sufficiently increased, though, some current enters the fiber membrane. As soon as sufficiently positive ions are accumulated inside, the membrane potential begins to change and the action potential is generated.

The action potential follows the all-or-nothing law: if the electrical stimulus exceeds the threshold potential, the nerve or muscle fiber will provide full response that is independent of the strength of the stimulus; otherwise, there is not such response.

### 1.8.2. Pulse Shapes and Timing

Common stimulation protocols used in clinical FES involves trains of electric pulses. Pulse duration, pulse amplitude and pulse frequency are the key parameters that are regulated by the FES devices. The FES devices can be current or voltage regulated. Current regulated FES systems always deliver the same charge to the tissue regardless of the skin/tissue resistance. Because of that, the current regulated FES systems do not require frequent adjustments of the stimulation intensity.

Pulse shapes can be any waveform of any kind, but the idea of FES is to transmit low charge and energy to ultimately trigger an action potential. As for the waveform, it can be either biphasic-balanced, biphasic-imbalanced and monophasic. As for each pulse shape reversible and irreversible faradaic reactions behave differently, therefore each may damage the tissue in their own manner.

#### 1.8.2.1. Monophasic Pulse Shape

Such pulse shape injects electrical current to the body with either cathodic or anodic pulse sign, see fig. 1.11a. Stimulation begins with an open-circuit potential and applying, for instance, a single cathodic pulse, the injected charge is being stored reversible on the double layer capacitance.

After the first pulse is finished, the charge of the double layer starts to discharge through Faradaic reactions. Assuming that another single pulse is delivered with a train whose period is small with respect to the time constant for discharge, almost all charge injected will be delivered to the irreversible Faradaic reactions.

If the pulse duration rises until attaining at least five time constants, though, gradually more current flows across the parallel charge transfer resistance and the patient is more at risk due to irreversible Faradaic reactions. Here, almost all current flows through the charge transfer resistance and thus is fully injected into the tissues via faradaic process. As a result, the electrochemical reactions involved in charge transfer process will diffuse causing chemical injury.

Although monophasic is the most efficient pulse for stimulation because of the action potential initiation and the potential becomes insufficiently positive (using cathodic pulses) where electrode corrosion may occur, though, it is not used in continuous pulses where tissue damage is to be avoided [Merrill, 2005]. In previous published works [Halliwell, 1992; Imlayl, 2003; Bergamini, 2004; Stohs, 1995] there has been sufficient evidence that monophasic pulse

allows the formation of Faradaic reduction reactions. If oxygen is present, these reactions may include reduction of oxygen and formation of reactive oxygen species associated in tissue damage.

#### 1.8.2.2. Biphasic Pulse Shape

A commonly used approach is applying a pulse of equivalent charge of the opposite polarity. Charge-balanced pulse shape, for instance, fig. 1.11b, is a biphasic pulse method for stimulation that consists of cathodic then anodic pulse, or vice versa. Such kind of pulse shape strategy attempts to prevent progressive accumulation of charge at the electrode interface that would lead to irreversible Faradaic reactions. Note that while balancing the charge has generally been well-accepted to minimize irreversible oxidation and reduction reactions, it cannot prevent damage if the electrode potential within anodic pulse exceeds the voltage window, leading to corrosion [De Vittorio, 2014].

Charge-balanced pulse is employed as it improves safety of electrical stimulation and minimizes some of the adverse effects. Rubinstein and colleagues [Rubinstein, 2001] stated that single-unit recordings demonstrated that spikes resulting from monophasic and biphasic stimuli have different thresholds and latencies.

[Avram et al., 1990] results indicated that imbalanced biphasic stimulation can be tolerated safely by tissue at or below a current density of  $35 \mu\text{A}/\text{mm}^2$ . The damaging electrochemical process that takes place during a cathodic stimulation pulse can be reversed by an anodic pulse having substantially less charge than its companion cathodic pulse.

#### 1.8.2.3. Charge-imbalanced Pulse Shape

Charge-imbalanced pulse shape, fig. 1.11c, is a biphasic pulse method for stimulation that involves a cathodic then anodic pulse; however, the latter pulse injects less charge than the former. Such kind of pulse shape has been shown to significantly increase charge injection without electrode corrosion [Zhou, 2010]. As regarding to retinal cell activation, cathodic-first biphasic current pulses are more effective than anodic-first pulses for evoking spiking responses in rat *A2-type* retinal ganglion cells. Hadjinicolaou and colleagues [Hadjinicolaou, 2015] suggested that charge-imbalanced pulse of  $60 \mu\text{s}$  -  $480 \mu\text{s}$  cathodic-anodic pulses was preferred among *a2-type* ganglion cells tested. That finding is consistent with predictions from computational modelling [Rattay, 2012] and with previous studies involving epiretinal electrical stimulation of retinal ganglion cells in other species e.g., rat, guinea pig and monkey retina [Sekirnjak, 2006] and rabbit retina [Eickenscheidt, 2012].

### 1.8.3. Tissue Damage

Such process refers to the oxidation-reduction reaction of water that generates hydrogen at the cathode and oxygen at the anode when a voltage is applied to water. At the cathode, when a voltage is applied to electrodes in this solution, electrons are given to hydrogen ions at the cathode, producing hydrogen by a reduction reaction. At the anode, when a voltage is applied to the electrodes in this solution, electrons are removed from hydroxide ions, producing oxygen and water by an oxidation reaction.

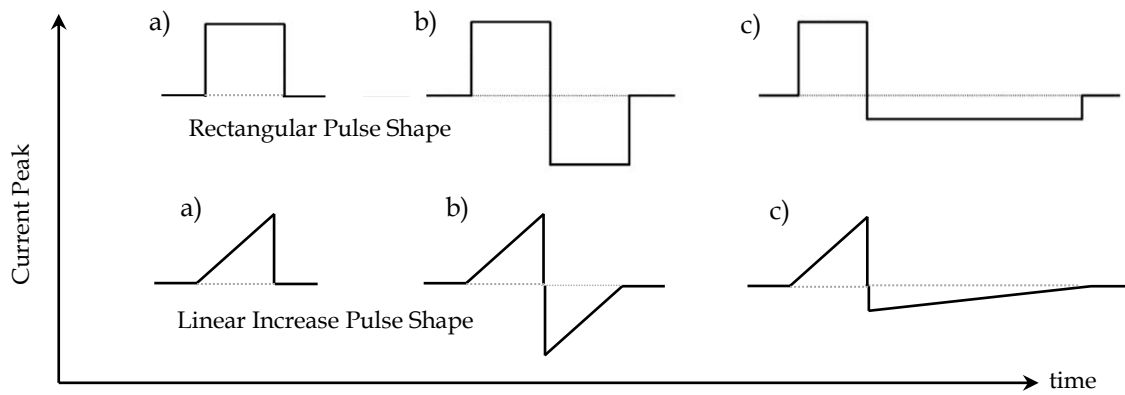


Fig. 1.11 a) Monophasic, b) Biphasic and c) Biphasic-imbalanced pulse shapes

### 1.8.3.1. Reversible and Irreversible Faradaic reactions

Irreversible electrochemical Faradaic reactions occurring at the electrode/tissue interface are a well-known problem that may lead to electrode degradation. The electrochemical reactions at the electrode-tissue interface, i.e. capacitive double-layer charging, reversible Faradaic and irreversible Faradaic reactions, carry out charge injection into the neural tissue [Merrill, 2005; Brummer, 1997; Cogan, 2008]. The latter reaction can produce electrolysis of water that leads to localized pH changes [Huang, 2001], gas bubble formation that thought to be harmful and physically disturbs the tissue [Brummer, 1997; Cogan, 2008] and chemical species formation that damage the tissue or the electrode [Merrill, 2005].

For a small enough injected charge, all charge injection is by charging and discharging of the double layer. Above some injected charge density, a second mechanism occurs consisting of Faradaic reactions where electrons are transferred between the electrode and electrolyte, thus changing the chemical composition in the electrolyte by reduction or oxidation reactions [Merrill, 2005].

A key element that should not be avoided is to monitor the charge injected into the body such that the charge injection capacity,  $Q_{INJ}$ , is not surpassed.  $Q_{INJ}$  is defined as the amount of charge per unit area that can be delivered through an electrode without causing water electrolysis.

It is a general principle when designing electrical stimulation systems that one should avoid onset of irreversible Faradaic processes which may potentially create damaging chemical species, and keep the injected charge at a low enough level where it may be accommodated strictly by reversible charge injection processes. An inappropriately designed electrical stimulation device may cause damage to the tissue or damage to the electrode itself [Merrill, 2005].

Electrolysis of water may occur as well as a result when maximum cathodic and anodic potential across the electrodes surpass the “water window” boundary [Merrill, 2005]. The water window is a potential range that is defined by the reduction of water, forming hydrogen gas, in the negative direction, and the oxidation of water, forming oxygen, in the positive direction which may cause corrosion. Once the electrode potential attains either of these two voltage window boundaries, all further injected charge goes into the irreversible Faradaic processes of water oxidation or water reduction [Merrill, 2005]. Having as a rule of thumb that one should avoid the onset of irreversible Faradaic processes when designing electrical stimulation systems,

this would impose to keep the injected charge density at a low level within reversible charge injection processes.

#### 1.8.3.2. Prevention Methods of Tissue Damage

Merrill and colleagues proposed a novel strategy [Merrill, 2005] that generally suggest keeping the pulse width narrower because it confines the amount of current that can be delivered by a stimulator, especially if it is battery operated, and provides the minimum charge that occurs when pulse width is of tens of  $\mu\text{s}$ . Doing so, any electrochemical reactions occurring at the electrode/electrolyte layer will be minimized.

Another similar strategy has been proposed by McAdams, assuring that few undesirable effects are seen using short pulses with duration less than one time constant [McAdams, 2010].

As the voltage response reaches a steady-state behavior, this indicates a pure charge transfer control. Thus, this undesirable state must be avoided by either evading long duration pulses. Accordingly, charge will be largely applied to the body via relatively safe capacitive processes.

PEDOT coat for invasive electrodes has been generated considerable attention as a supercapacitor material due to its large electroactive voltage window, high chemical stability among conductive polymers [Duay, 2012], low impedance and high charge density capacity,  $Q_{INJ}$  [Starbird, 2012]. So as to minimize electrochemical damage to the electrode and tissue, safe stimulation pulses have been used to activate nearby neurons and elicit physiologically relevant responses such as biphasic-imbalanced pulse shapes [Hadjinicolaou, 2015].

# Chapter 2

## Biophysically-based Circuit Models

### 2.1. Introduction

Circuit analysis is an important tool in circuit design. Among other advantages, such models provide the designer a tool for predicting circuit behavior without essentially processing the circuit. An equivalent model can be used to analyze, to name a few, biological systems [Hodgkin, 1952], radio-frequency integrated-circuit [Nguyen, 2015], optoelectronic integrated circuits [Gao, 2011], semiconductor device modelling [Richard, 2006].

So as to analyze the equivalent relationships in active devices, equivalent models are built in a sense of giving the same output characteristics as the active device itself. Equivalent models can refer to a theoretical circuit that describes biological systems where current does not flow in traditionally defined cables, but radially through tissues in the form of ions. In its most common form, such circuit is assembled using passive elements, e.g. resistors and capacitors, and fed by a voltage or current source. Since those models are mainly based on some fundamental equations that describe the electrical behavior of passive elements, however, a prediction of the characteristics of biological systems can be analyzed. Some crucial factors need to bear in mind, such as computation speed and outcome accuracy. On occasions, computational speed can be considerably improved by simplifying the equivalent model without significant loss in computational accuracy [Dorf, 1997]. However, the benefits and shortcomings of equivalent models should bear in mind so as to consider beforehand their use, i) representation of physical behavior is by mathematical means; ii) simplified model yields physical insight, allowing engineer to design a system to operate in specified manner; iii) approximations neglect small but complicating phenomena; iv) model possible refinement is essential once basic insight has been gained when some phenomena is neglected.

The modern biophysically-based neural modelling is frequently based on the mathematical framework developed by Hodgkin and Huxley in 1952. They thoroughly validated how ionic currents can be understood as regards of changes in  $\text{Na}^+$  and  $\text{K}^+$  conductances in the axon membrane. Using this knowledge, a detailed mathematical model of the voltage-dependence and time-dependence was developed. The existent analytical power of the model became evident when numerical integration accurately reproduced all the key biophysical properties of the action potential. Thus, a neural-based model similar to ours that involves the activation of axons or body cells in the form of extracellular stimulation must include the mathematical framework of Hodgkin and Huxley.

Here, the mathematical framework developed by [Hodgkin and Huxley, 1952] and the repetitive firing of action potentials in ganglion cells by [Fohlmeister, 1989] will be explained.

## 2.2.Developed Circuit Models

### 2.2.1. Hodgkin and Huxley Modelling of Giant Axon

An example of such circuits is the conductance-based model developed in early 1950's by Sir Alan Hodgkin and Sir Andrew Huxley [Hodgkin, 1952]. In this biophysically-based neural modeling, Hodgkin and Huxley modeled a segment of a squid giant axon using an electrical equivalent circuit, see fig 2.1.

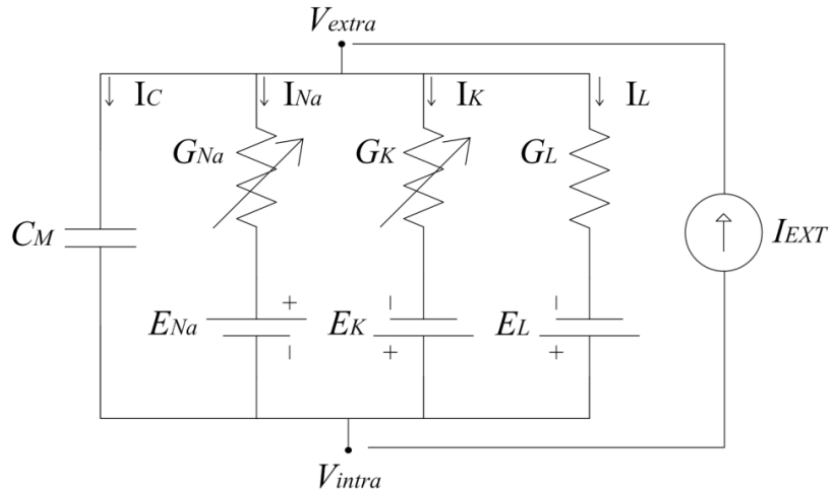


Fig. 2.1 Equivalent circuit model of the cell membrane [Hodgkin, 1952].

Batteries represent the electrochemical potentials determined by differing intra- and extracellular-ion concentrations. Capacitors model the charge storage capacity of the cell membrane and resistors model the different kinds of ion channels surrounded in the membrane.

In the circuit,  $C_M$  is the membrane capacitance.  $G_{Na}$  and  $G_K$  are sodium and potassium voltage-dependent conductances, respectively.  $G_L$  corresponds to chloride conductance which is taken to be constant.  $V_{intra}$  and  $V_{extra}$  are the intra- and extracellular potential at the membrane, respectively.  $I_{EXT}$  is the extracellular current input.  $E_{Na}$ ,  $E_K$  and  $E_L$  are the equilibrium potentials of sodium, potassium and chloride, respectively.

$I_C$  is the capacitive current defined as the rate of change of charge  $q$  at the membrane:  $I_C = dq/dt$ . The charge  $q(t)$  is related to the instantaneous membrane voltage  $V_M(t)$  and the membrane capacitance by the traditional relationship  $q = C_M \cdot V_M$ . Hence, the membrane capacitance can be written as  $I_C = C_M dV_M/dt$ . The ionic current  $I_{ION}$  is subdivided into three distinct components, sodium current  $I_{Na}$ , potassium current  $I_K$  and chloride current  $I_L$ .

The behavior of any electrical circuit model of the style indicated in fig. 2.1 can be described by a differential equation of the general form

$$C_M \frac{dV_M}{dt} + I_{ION} = I_{EXT}, \quad (2.1)$$

$I_{ION}$  is the algebraic sum of the individual contributions from all participants ' $x$ ' of channel types in the membrane

$$I_{ION} = \sum_X I_X = \sum_X G_X (V_M - E_X), \quad (2.2)$$

which expands to the following expression

$$I_{ION} = G_{Na}(V_M - E_{Na}) + G_K(V_M - E_K) + G_L(V_M - E_L). \quad (2.3)$$

Each individual ion channel can be thought of as containing one or more physical gates that regulate the flow of ions through the channel. An individual gate can be either open or closed. The voltage-dependence of ionic conductances is incorporated into the model by assuming that the probability for an individual gate to be open or close state depends on the value of the membrane voltage. So as to model  $G_{Na}$ ,  $G_K$  and  $G_L$ , gates labeled " $m$ ", " $\eta$ " and " $h$ " are used:

$$G_{Na} = g_{Na} m^3 h, \quad (2.4)$$

$$G_K = g_K \eta^4, \quad (2.5)$$

$g_{Na}$  and  $g_K$  are the maximum conductances of sodium and potassium. The gates are calculated as follows:

$$\frac{dx}{dt} = \alpha_x(1-x) - \beta_x x, \quad (2.6)$$

$\alpha_x$  and  $\beta_x$  are the rate constants.  $x$  correspond to each corresponding gate " $m$ ", " $\eta$ " or " $h$ ".

This mathematical framework for novel biophysically-based neural modeling describes how action potentials are initiated and propagated.

Hodgkin and Huxley systematically demonstrated how the macroscopic ionic currents in the squid giant axon could be understood in terms of changes in  $Na^+$  and  $K^+$  conductances in the axon membrane. Further, it approximates the electrical characteristics of excitable cells such as neurons.



### 2.2.2. Repetitive Firing of Action Potential in Ganglion Cells

As regards to the second example, an equivalent model of ganglion cell action potential initiation and propagation was proposed by J.F. Fohlmeister and colleagues [Fohlmeister, 1989]. Such model follows the approach of Hodgkin and Huxley like modelling.

Ganglion cells of the vertebrate retina constitute a pathway by which the retina communicates with the brain. Fohlmeister and colleagues analyzed the contributions of each channel using voltage clamp experiments of ganglion cells in tiger salamander.

The voltage clamp is an experimental method to measure ion currents through membranes of excitable cells while holding the membrane voltage at a set level. Since membranes contain diverse ion channels, some of are voltage-gated, this study allows the membrane voltage to be manipulated independently of the ionic currents, allowing the current-voltage relationships of membrane channels to be studied. Such experiments suggested that at least five different ionic currents may be present among these neurons. A kinetic model was constructed based on formerly reported ganglion cell voltage clamp data and the contribution of those five non-linear channels.

Four conductances associated to voltage-gated channels were considered and the last modeled as  $Ca^{2+}$ -gated:  $Ca^{2+}$  calcium channel;  $Na^{+}$  sodium channel;  $K^{+}$  non-activating channel (delayed rectifier);  $AK^{+}$  inactivating channel (*A type*);  $Ca^{2+}K^{+}$  calcium-activated channel was gated by  $Ca^{2+}$  and modelled on that basis, fig. 2.2.

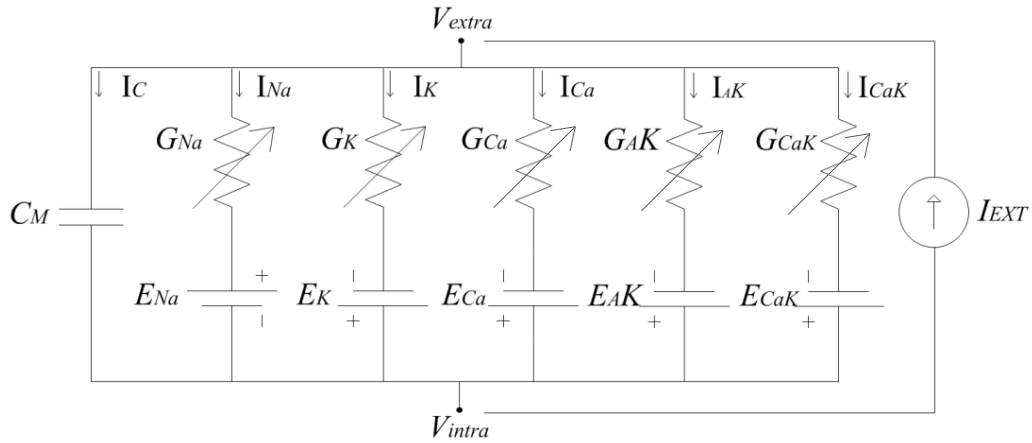


Fig. 2.2 Equivalent circuit model of the cell membrane [Fohlmeister, 1989].

The retina ganglion cell model has a basic mathematical structure for voltage-gating based on Hodgkin and Huxley like equations. Several variations of the original model are present due to new conductances are introduced. However, the gates are modeled as in the Hodgkin and Huxley model with their own different rate constants.

$$G_{Ca} = \overline{g_{Na}} c^3, \quad (2.7)$$

$$G_{AK} = \overline{g_{AK}} a^3 h_A. \quad (2.8)$$

The conductance  $G_{CaK}$  was modeled as

$$G_{CaK} = g_{CaK} \frac{(C_a^{2+} / C_{a\text{diss}}^{2+})^2}{1 + (C_a^{2+} / C_{a\text{diss}}^{2+})^2}, \quad (2.9)$$

$g_{CaK}$  is the maximum conductance;  $C_{a\text{diss}}^{2+}$  is  $10^{-6}$  M.  $C_a^{2+}$  can be calculated as a function of  $I_{Ca}$

$$\frac{dC_a^{2+}}{dt} = -15 \cdot 10^{-6} I_{Ca} - 0.02(C_a^{2+} - 1 \cdot 10^{-4}), \quad (2.10)$$

$I_{Ca}$  is the ionic current of the calcium channel with units of  $\mu\text{A}/\text{cm}^2$  and  $C_a^{2+}$  of units of mM. This mathematical framework for novel biophysically-based neural modeling describes how action potentials are initiated as regards to ganglion cells.

### 2.2.3. Summary

This chapter explained briefly the mathematical framework of [Hodgkin and Huxley, 1952] which inspired [Fohlmeister, 1989] to develop a modern biophysically-based neural model of the ganglion cells at the retina. The latter neural model will allow us throughout this report a condition of stimulation by observing the response of membrane potential at various levels of extracellular stimulation.

# Chapter 3

## Feasibility of a 32 x 32 Electrode Array

### 3.1. Lessons learnt: Basis for this Chapter

Fundamental research stipulated around 1000+ electrodes per single array are needed to upgrade basic issues such as mobility, independent living and navigating on interior and exterior environments.

Currently, a small number of companies such as Second Sight Medical Products, Retina Implant GmbH and Intelligent Medical Implants GmbH have developed a complete visual prosthesis device. Clinical trials *in-vivo* reported that patients have perceived sensations of spots of light, object localization, distinguish objects, motion and differentiate simple patterns of lines and letters. In spite of the overall success of current visual devices, significant vision restoration has become a major challenge. Current implant patients cannot yet recognize the details of faces or objects [Weiland et al., 2014]. In order to reach this significant goal, the resolution of implants must be increased, by increasing both the number and the density of electrodes.

Intelligent Medical Implants, Retina Implant GmbH and Second Sight Medical Products have implanted their corresponding devices in patients with an array of 16, 49 and 60 electrodes with large electrode sizes. Although offering some vision, the major requirement lies in activating at least 1000+ or more electrodes for attaining functional vision. Nowadays, an artificial vision device that exceeds 100 electrodes per single array has not been implanted. This insight has generated considerable interest amongst groups of engineers to upgrade such devices.

Those sight improvements, despite being advantageous for a sight deteriorated patient, need a significant enhancement to be aligned with the success of today's cochlear implant technology.

## 3.2. Selection Of A Suitable Visual Prosthetic Design for Simulation

### 3.2.1. Circuit Modelling Design

Equivalent models describes biological systems where current flows in defined circuits through cables. In its most common form, circuit modelling brings together the associated resistors, capacitors and voltage or current source. Despite that those models are mainly based on some fundamental equations that describe the electrical behavior of passive elements, however, a prediction of the characteristics of biological systems can be analyzed.

Recently, Lujan et al. developed an accurate circuit model to simulate functional electrical stimulation [Lujan, 2012; 2013], see fig. 3.1. This model is based on electrodes placed on the skin and electrical current pulse is applied across the active and ground electrode. This circuit shows a clearly granular discretization of an inherently three-dimensional flow problem as a series of 'tissue subsystems'. For any biophysically-based circuit model must be settled with components that behave comparable to the human tissue. As such, Lujan et al. treated each subsystem independently using values of electrical properties from the literature.

TABLE 3.1

Domain	Circuit/Passive Elements	Frequency (Hz)				Thickness	Source
		976	1953	3906	7812		
Electrode-Electrolyte Interface <sup>1</sup>	20 mA	16	13	9	10	1 mm	Experimentally
	$R_{ct} (\Omega)$						
	30 mA	18	12	13	11		
	40 mA	18	16	14	14		
	20 mA	376	318	243	216		
	$C_{dl} (nF)$						
	30 mA	319	354	247	262		
	40 mA	319	356	243	288		
Gel	$R_{gel} (\Omega)$			106		-	Experimentally
Gel-Skin Interface <sup>2</sup>	$R_{gs} (k\Omega)$	6.01	5.64	2.12	0.518	-	Experimentally
	$C_{gs} (nF)$	459	368	354	328		
Lower Layers (longitudinal parameters ll; transversal lt)	$\sigma (S/m)$			0.2		4.8 mm	Literature [Miklavcic, 2006]
	$\epsilon (\times 10^5)$	2.2	1.8	1.4	1.1		
Muscle <sup>3</sup> (longitudinal parameters ml; transversal mt)	$\sigma_l (S/m)$	0.24	0.25	0.3	0.34	0.5 mm	Literature [Miklavcic, 2006]
	$\sigma_t (S/m)$	0.12	0.12	0.16	0.16		
Stratum Corneum (longitudinal parameters sl; transversal st)	$\sigma (\mu S/m)$	27	60	80	140	22 $\mu m$	Literature [Miklavcic, 2006]
	$\epsilon (\times 10^3)$	2	2	1.9	1.7		

<sup>1</sup>Electrode-electrolyte properties have frequency and current dependency. Results of normal peak current values of transcutaneous stimulation are given. <sup>2</sup>Results of gel-skin interface are average values of experimental comparison. <sup>3</sup> $\sigma_l$  and  $\sigma_t$  correspond to longitudinal and transverse anisotropic characteristics of muscle. Electrode dimensions are 45 x 80 mm<sup>2</sup>. Electrode distance is 10.5 cm center-to-center.  $V_{hp}$  corresponds to the half-cell potential.

Electrode-electrolyte dependence on frequency and current, anisotropic characteristics of the muscle and the non-linear behavior of the human skin is taken into consideration. The sub-

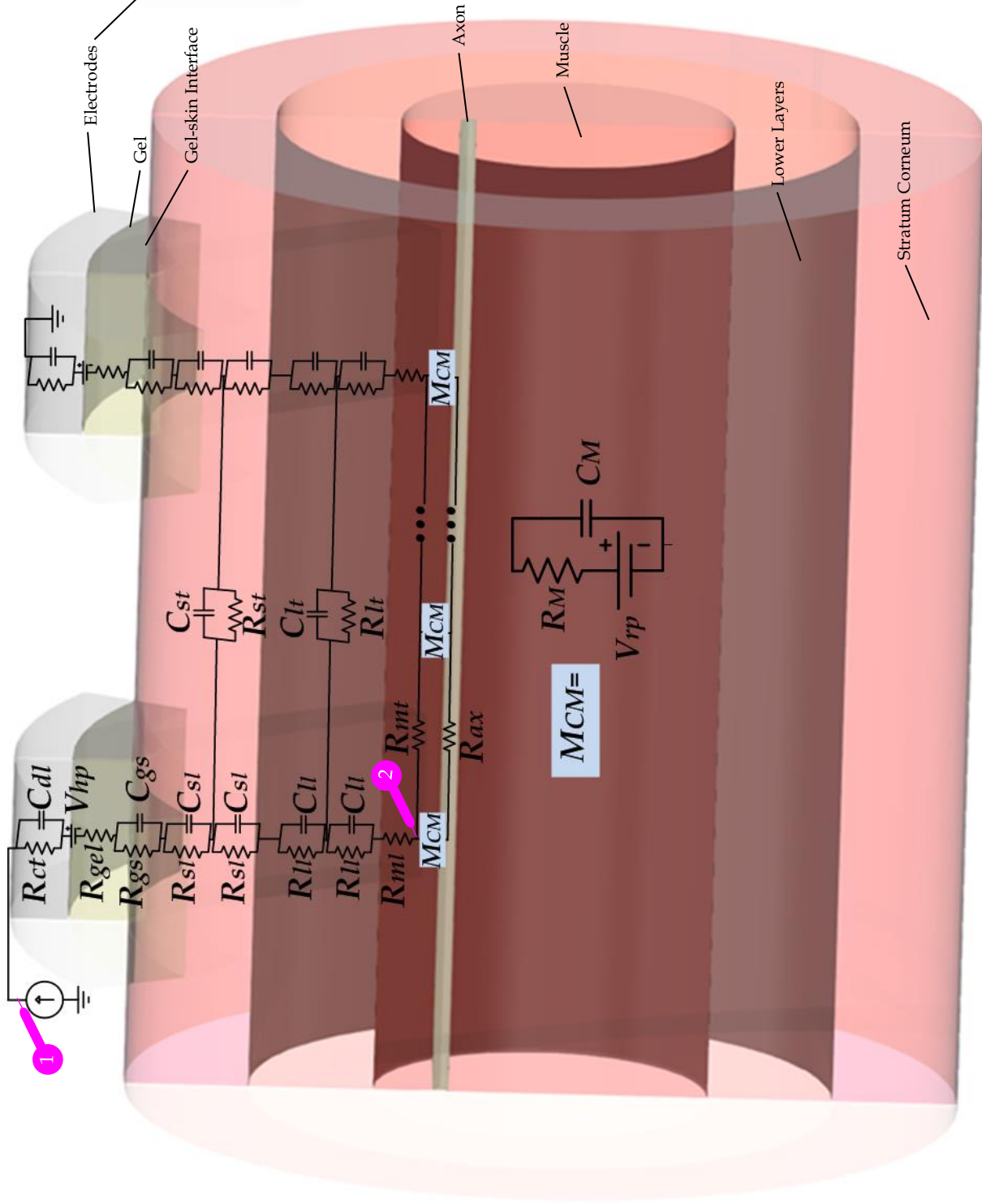


Fig. 3.1 Complete equivalent model for electrical stimulation [Lujan, 2012; 2013]. The circuit model indicates a three-dimensional flow problem solved as a series of 'tissue subsystems' labelled electrode, gel, gel-skin interface, stratum corneum, lower layers (epidermis, dermis and subcutaneous fat), muscle and axon. Thickness of each domain is not drawn to scale. AutoCAD software was used for the creation of this figure.

threshold model of the neuron cell membrane was incorporated to observe a single axon response. Cell membrane potential was monitored until it reaches threshold. Table 3.1 lists the values of the passive elements included in the circuit model with their proper conductivity and permittivity taken experimentally or from the literature.

The differences between some traditional circuit models and the one discussed so far are to separate extensively the tissues from the electrodes to the neuron cell membrane and characterize the tissues based on frequency and current density dependencies. Almost all models present so far present only a simplified view on tissue layers and do not include a model of a nerve. The aims of the circuit model developed by Lujan et al. are

1. Discretization of human tissue with circuit elements.
2. Circuit model includes all regions from the electrodes to the neuron cell membrane.
3. Analyze the biological behavior of tissue as current is applied.
4. Longitudinal circuit elements included so as to mimic radial flow of current density.
5. Experimental and simulation comparison of voltage response across the electrodes using the strength-duration curve.

The circuit model developed by Lujan and colleagues yielded interesting results i) computationally efficient implementation by modelling such circuit model with a discretization of passive elements; ii) voltage drop in the human tissue is less than 20% of that across the electrodes. The remaining drop can be attributed to the gel-skin interfaces; iii) accurate results of voltage response as several current amplitudes are applied across the electrodes. Precision persisted as the frequency and input current from the stimulator device are varied; iv) analyze variation of input current as it is distributed into the membrane. Figure 3.2, right  $y$ -axis, displays input membrane current of rectangular and linear increase. Despite that linear increase requires higher input current for twitch response, see fig. 3.2 left  $y$ -axis, less charge is delivered to the electrodes, safeguarding the tissue by electrochemical hazards; v) expresses the possibility to simulate the voltage response of nerve and muscle stimulation using passive elements and the measured electrical parameters of the electrode-electrolyte gel interface.

### 3.2.2. Is Circuit Modelling Suitable for Retinal Prosthetic Simulation?

Despite its relatively coarse lumped-element approximation of an inherently three-dimensional flow problem, circuit models can be useful as a simplification of realistic load models. Such approximations can be beneficial to develop e.g. stimulation circuits.

Circuit modelling of biological systems can help for obtaining basic understanding concerning the magnitudes of the stimulation in the different layers of human tissue and to clarify basic relationships and parameters for the development of an advanced 3D FEM-based model. Nevertheless, as it provides a basic insight of the given problem, circuit models additionally deliver several questions for further improvement

1. How the distribution of current and potential behaves around the cell?
2. Assuming to have a population of cells in some medium and the current density injected from the active electrode, how much current density receives each cell and how much is wasted in the medium?
3. How is the extent of circuit discretization to reach optimal accuracy?

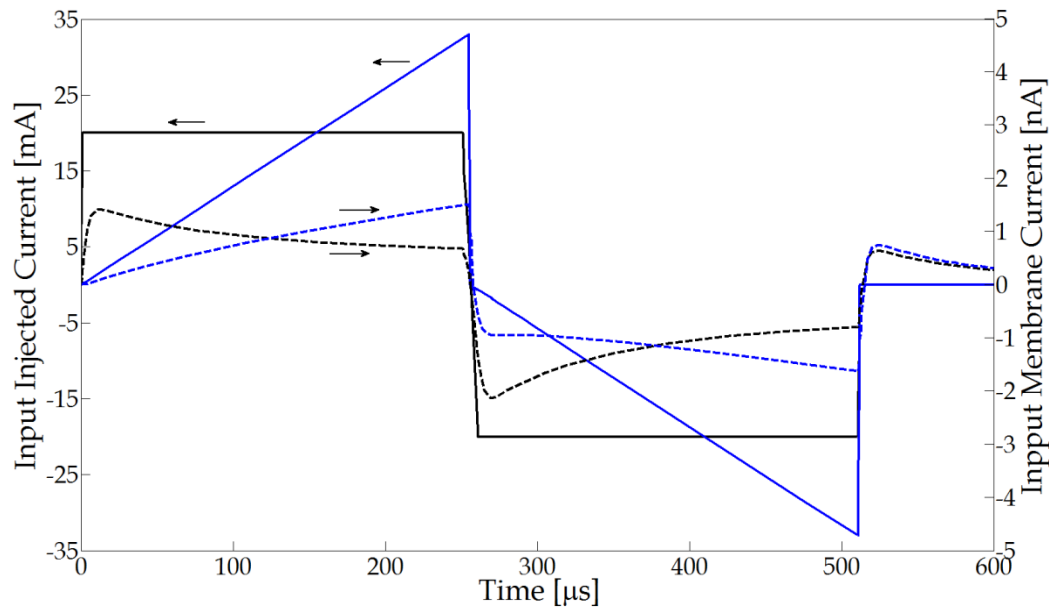


Fig. 3.2 Input injected current measured with probe 1, left  $y$ -axis, and input membrane current measured with probe 2, right  $y$ -axis, of rectangular and linear increase waveform. Note that input injected current for each case reaches membrane threshold at some time. The area of probe 1 and 2 are related to the cross-section area of the electrode and the axon, respectively.

#### 4. How does the current and voltage distribute along the cell boundary?

The possibility for constructing an equivalent circuit model that delivers the right answers for any given problem is present. However, the complexity of building such model rises because the amount of passive elements in the model is proportional to its accuracy. Next, the shortcomings of the simplified equivalent circuit model are listed:

1. Two-dimension representation of the medium.
2. High complexity to realize three-dimensional models.
3. Restriction to use cables that represent the biological environment of tissues.
4. The entire amount of current enters to the soma once it passes the ganglionic layer.
5. 1024 electrode array, meaning many of passive elements.
6. Model results would be confined to the low resolution
7. Model ignores significant phenomena such as boundary problems.
8. Averaging approximation of the system cannot be considerable accurate.

#### 3.2.3. Finite Element Method (FEM) Modelling Design

Finite element method is a numerical technique for solving problems of engineering and mathematical physics, yielding accurate solutions of complex models. Over the years, FEM has been considered to be one of the best methods for solving a wide variety of practical problems efficiently. The solution region in FEM is considered as build-up of many small, interconnected subregions called finite elements. In each element, a convenient approximate solution is assumed and the conditions of overall equilibrium of the model are derived. This idea of cutting a complex structure in small elements is considered as one of the key contributions in the development of FEM [Rao, 2011].

The advantages of FEM are i) FEM delivered by a digital computer provides a rapid means of performing many calculations involved in finite element analysis; ii) the application of FEM has been progressed at a very impressive rate, providing advanced software; iii) FEM can be used for solving a wide variety of practical problems with high efficiency, such as heat conduction, fluid dynamics, seepage flow, and electric and magnetic fields; iv) boundary value and other complex problems can be solved with FEM [Rao, 2011]. One of the main disadvantages of FEM is the economic and time-consuming costs involved in the solution of the problem [Mukhopadhyay, 2005].

Despite the shortcomings of FEM, the advantages to solve boundary value problems of current density or electric field on some cell placed in space becomes extremely attractive for our situation. Therefore, to attain a comprehensive understanding of any given biologically-based model, the distribution of current and potential must to be addressed in a three-dimensional model of distributed elements, e.g. FEM-based modelling scheme.

### 3.3.FEM-based Modelling for Visual Prosthesis

#### 3.3.1. Introduction

##### 3.3.1.1. Lessons learnt: Basis for this Chapter

Modern biophysical based models can yield accurate responses of membrane potential for various levels of extracellular stimulation. The modern biophysically-based neural modelling is frequently based on the mathematical framework developed by [Hodgkin and Huxley, 1952]. The existent analytical power of using Hodgkin and Huxley-like equations can produce accurate responses of axons and body cells and reproduce all the key biophysical properties of the action potential. Thus, the neural-based model presented here includes this mathematical framework in ganglion cells developed by [Fohlmeister, 1989], see unit 2.2.2. This application serves as a condition of body cells to identify their activation in the form of extracellular stimulation.

##### 3.3.1.2. Aims

There is plenty of evidence that a high number of electrodes ranging from 625 [Margalit et al., 2002] to 1000+ [Chader et al., 2009] can enhance visual resolution originated by electrical stimulation. This insight is well-correlated to acquire functional vision, i.e. upgrade mobility, independent living and walking in crowded environments [Cha et al., 1992], face recognition [Thompson et al., 2003], reading large-sized letters [Bagnoud et al., 2001; Dagnelie et al., 2006; Chai et al., 2007]. Nowadays, an artificial vision device that exceeds 100 electrodes per single array has not been implanted. Thus, the main inquiry in advanced visual devices remains: Is it feasible to drive 1000+ electrodes inside the retina?

Thus, a simplified 3D FEM neural-based model that addresses a  $32 \times 32$  electrode array is developed here. In this arrangement, the activation of a cell with the minimum threshold current as seen in earlier experimental works will be followed [Keserü et al., 2012; Jepson et al., 2012]. Basic relationships of threshold injected current and distance of the cells to electrodes are analyzed. Experimental results of the perceptual thresholds by [Jensen, 2005] and voltage across



the electrodes by [Meza et al., 2014] are compared with our retinal-model. Electrochemical safety is examined in terms of charge density, electrode voltage, heat dissipation and current injection. The magnitudes of input stimulating and geometric parameters of the high-level scheme are given such as domain definitions, electrode data (32 x 32, size) and domain dimensions. At the end, the parameters that must be carefully observed and minimized for safe delivery of stimulus are provided.

### 3.3.2. FEM-based Modelling for Retinal Considerations

#### 3.3.2.1. Simplified FEM Simulation Model

Simulation-based findings can provide safe avenues to ensure long-term stable performance of visual prosthesis. As simulations operate in a computer, a vast number of electrodes can be applied so as to observe the behavior of the tissue environment and to define harmless strategies for future planned devices. As such, an array that includes 1000 or more electrode sites can be simulated.

The simplified 3D neural-model of the retina is presented in fig. 3.3 [Lujan (a), 2016; (b); (c)]. The model consists of seven domains: polyimide carrier of electrodes; photoreceptor layer; vitreous medium; retina ganglion cell layer; retinal pigment epithelium; ganglion cell soma,  $S_G$ ,

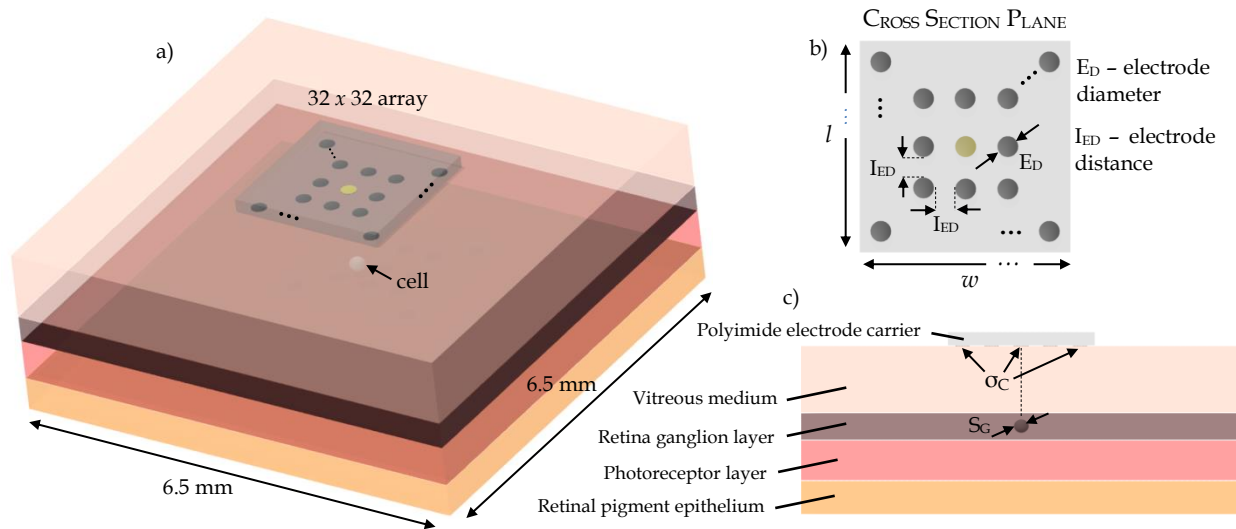


Fig. 3.3 a) Three-dimensional retinal scheme. b) Array consists of a square grid arrangement of an active electrode (in yellow) surrounded by eight guards (in black) in order to stress the isolation of the active electrode, to confine the stimulus current to a small volume around the ganglion cell and to minimize electrode cross-talk during stimulation. The thickness of each domain is not drawn to scale. c) Two dimensional representation of model with domains.

and the electrode array. The ganglion cell soma was placed inside the retina ganglion cell layer exactly below the center of active electrode and was enclosed with the cell membrane. The extracellular and intracellular compartments of the membrane were modelled with their respectively electrical properties. The model presented above can be implemented in Comsol Multiphysics.

### 3.3.2.2. Numerical Fitting on Gold Electrodes Coated with PEDOT-NaPSS

PEDOT coat for invasive electrodes has been generated considerable attention in terms of electrical properties and biocompatibility. As neural prosthesis demand large number of electrodes with low dimensions which allow selective stimulation of a population of neurons, PEDOT provides low impedance and high charge injection capabilities. Therefore, the electrical properties of PEDOT-NaPSS electrode deposition found in [Starbird, 2012] were included in the retinal-model.

Starbird and colleagues built a macro- and microelectrode set of gold electrodes with PEDOT-NaPSS electrodeposition with several charge densities. The areas of gold electrodes are of 0.5, 1 and 2 mm<sup>2</sup> for macro- and 177, 413 and 1000 μm<sup>2</sup> for microelectrodes. PEDOT was applied by immersing the electrodes in a solution of the monomer with a specific concentration and a known current for a determined time. The charge density can be adjusted because the thickness of polymeric coating is dependent in each contact.

To characterize the electrical properties, the polymer-coated electrodes were immersed in an aqueous solution with ionic conductivity, representing the tissues at the implanted site. An alternating square voltage of 50 mV was applied at frequencies between 20 Hz to 1 MHz to obtain the Bode plot impedance curve. For more data, see [Starbird, 2012] and [Montero, 2015].

Experimental data of a set of 24 electrodes was selected and such set was divided in three groups of eight fabricated with diameters of 0.5, 1 and 2 mm<sup>2</sup>. A charge density of 40mC/cm<sup>2</sup> was used to apply PEDOT-NaPSS in gold electrodes. The information was fitted into a double-layer model using LEVMV, numerical fitting software program built by [Macdonald, 2013] based on the Levenberg-Marquardt algorithm. A similar approach of double-layer equivalent circuit model was used to characterize the contact interfaces of both materials by performing precise numerical fitting [Starbird, 2012].

The physical representation of the double layer model, fig. 3.4, consists on a solution resistance,  $R_s$ ; a contact capacitance,  $C_c$ , describing the accumulation of charge between the metal and the polymer; a second capacitance of the double layer,  $C_{dl}$ , describing the accumulation of charge between the polymer and the solution; a contact resistance,  $R_c$ , between the metal and the polymer and a charge transfer resistance,  $R_{CT}$ , between the metal and solution.

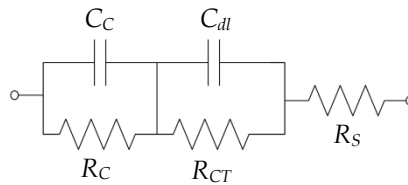


Fig. 3.4 Double-layer equivalent circuit model for electrode/electrolyte representation.

Numerical fitting results showed that the charge transfer resistance between the metal and solution is 8.6 kΩ and 30 times greater than the contact resistance between metal and polymer. Thus, to reduce computational effort and time consumed, the electrode domain of gold was omitted at Comsol simulations and the inclusion of PEDOT-NaPSS deposition at the polyimide carrier was assumed. This assumption reduced the time consumed to 2.5 minutes. These results also suggest that for further simulation schemes, the parallel arrangement of  $C_c$  and  $R_c$  can be neglected and the major emphasis should be placed on the electrode/electrolyte interface.

The dimensions of the model were similar to previously published models [Kasil, 2011; Abramian, 2012; Werginz, 2004]. The model geometry consisted of  $6.5 \times 6.5 \text{ mm}^2$  at its bottom area. Table 3.2 lists the thickness and the electrical properties of each domain included in the model. PEDOT polymer is good conductor with  $40\text{e}3 \text{ S/m}$  of conductivity. The contact conductivity,  $\sigma_C$ , between PEDOT-NaPSS and tissue was calculated as  $1/(R_{CT} \cdot A_C)$ , where  $A_C$  is the cross section area of the electrode where the slope of  $R_{CT}$  versus  $A_C$  in log-log scale resembles a  $1/A_C$  shape. Hence,  $\sigma_C$  is  $321 \text{ S/m}^2$ .

TABLE 3.2

Layer	$\epsilon$	$\sigma \text{ (S/m)}$	Thickness ( $\mu\text{m}$ )
Vitreous Humor	98	1.5	$I_{CED}$
Polyimide Electrode Carrier	1	$1\text{e-}17$	75
PEDOT-NaPSS Electrode	1	40000	0.2
Ganglionic Layer	80	0.01	35
Retinal Pigment Epithelium	1	0.002	20
Photoreceptor Layer	1	0.0285	200
Cell Membrane ( $b$ )	$8.8\text{e-}11$	$1\text{e-}8$	0.005
Axoplasm	$3.98\text{e-}11$	0.01	$G_D - b$

$b$  refers to the cell membrane thickness;  $G_D$  to ganglion cell diameter. Note that vitreous humor thickness is related to the cell-electrode distance  $I_{CED}$ .

### 3.3.2.3. Electrode Distribution

We propose an evenly distributed  $32 \times 32$  electrode array, see fig. 3.3b. Each electrode is separated with an electrode distance. The length,  $l$ , and width,  $w$ , of the electrode carrier are assumed to be equal and calculated as

$$w = l = (I_{ED} + E_D) * (\sqrt{e_T} + 1) \quad (3.1)$$

$e_T$  is the total number of electrodes inside the carrier,  $E_D$  is the electrode diameter and  $I_{ED}$  is the electrode distance. The electrode carrier area is given by

$$A = l^2. \quad (3.2)$$

Assembling the electrodes evenly gives the advantage to program each to function as an active or ground electrode and to determine the optimal configuration of ganglion cell stimulation per each case. When an edge electrode is selected as active, its surrounding can be used as ground. Nevertheless, an unwanted effect of stimulating more ganglion cells may occur because of an uneven current density distribution.

The electrode array configuration is shown at the cross section plane in figure 3.3b. This arrangement is analogous to [Lovell, 2005; Dommel, 2009], however it consists of an active electrode (in yellow) surrounded by eight guards (in black). This arrangement highlights the isolation of the active electrode, the stimulus current is confined to a small volume around the ganglion cell and the electrode cross-talk during stimulation is minimized. The geometry

selected consists of circular electrodes that reduce elevated charge densities arising from irregular shapes [Fried, 2006].

#### 3.3.2.4. Ganglion Cell Model

Visual transmission beginning at the photoreceptors consists in the segregation of opposite light and dark signals into *ON* and *OFF* responses, depending on the bipolar cell types [Nakanishi, 2013].

*ON*-pathway responds once a light image is pictured upon a darker background, e.g. night vision. *OFF*-pathway detects the opposite [Kristensson, 2014]. Retinitis pigmentosa (RP), a leading cause of visual injury, affects primarily the rod photoreceptors light sensitive cell [Maureen, 2015] which are activated at low light levels.

Rods selectively contact only with depolarizing *ON* bipolar cells and create *ON* visual pathways [Stephen, 2012]. There may be some involvement on retinal cone cells, which detect bright light and provide color vision [Maureen, 2015]. Recent findings support the evidence of preferential loss of *ON*-pathway during degenerative process of RP [Fransen, 2013].

Age-related macular degeneration (AMD), a second cause of visual impairment, also experience poor night vision symptoms [Kathryn, 2013]. [Gui-shuang et al., 2008] suggested that assessing night vision symptoms may be useful to identify patients with early or intermediate AMD who are at relatively high risk of progression.

Since *ON*-pathway is preferentially impaired while being affected by RP or AMD, electrical stimulus via electrode array is required for restoring light sensitive cells performance and for improving visual transmission. Therefore, *ON*-ganglion cell model is selected because *ON*-pathway is more affected by the diseases previously mentioned.

Ganglion cell model has a basic mathematical structure based on the formerly addressed model of Hodgkin and Huxley that use partial differential equations to describe voltage-gating ion channels [Hodgkin, 1952] and is modelled with an equivalent circuit previously discussed in section 2.2.2, for repetitive firing of retinal ganglion cells [Fohlmeister, 1989].

The parameters and equations that describe the dynamics of the ionic channels were kept as in the original model. As a reminded, four conductances associated to voltage-gated channels were considered: calcium  $g_{Ca}$  channel; sodium  $g_{Na}$  channel; non-activating  $K^+$  (delayed rectifier)  $g_K$ ; inactivating  $K^+$  (A type)  $g_{aK}$ ; calcium-activated  $K^+$   $g_{kCa}$  channel was gated by calcium  $Ca^{2+}$  and modelled on that basis.

*OFF*- and *ON*-ganglion cells receive the signal separately, satisfying parallel pathways of *OFF*- and *ON*-bipolar cells and amacrine cells [Guyton, '1986]. For our circumstance, we used *ON*-ganglion cell model.

Ganglion cell model comprises the calculation of extracellular peak-threshold current density of the ganglion cell,  $J_E$ , using the cell model explained at section 2.2.2.

The peak current amplitude was applied at 500 pps, taking into account absolute and refractory period of an action potential.

Peak current was swept with a resolution of  $1 \mu A/cm^2$  until it was found the threshold current density that fires a train of action potential, see fig. 3.5. A monophasic rectangular pulse waveform was used with some pulse duration.

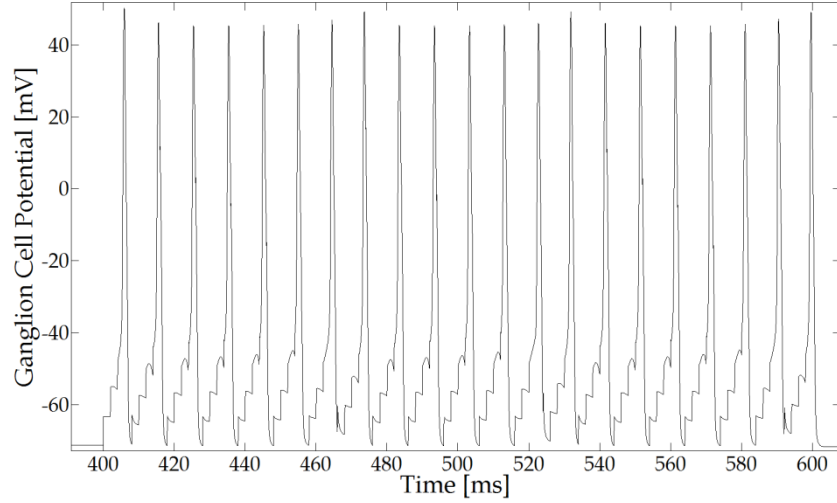


Fig. 3.5 Ganglion cell response of  $120\mu\text{A}/\text{cm}^2$  current injection using monophasic rectangular pulse shape,  $100\ \mu\text{s}$  pulse duration

### 3.3.2.5. FEM-based Model Simulation (Comsol)

The retinal model is shown in figure 3.3. Once obtaining a value of the extracellular peak-threshold current density that fire a train of action potential at the cell, that result was used to match the peak boundary current density of the cell membrane,  $J_B$ , in the ganglion cell soma at Comsol simulations. The threshold current from the electrodes was obtained using the following condition by applying current from the active electrode

$$\frac{|J_B - J_E|}{J_D} \leq 0.05. \quad (3.3)$$

$J_D$  has a value of  $1\ \mu\text{A}/\text{cm}^2$ .

The flowchart of our simulation procedure is shown in figure 3.6. The variables listed are the following:  $\Delta t$  is the pulse duration;  $J_{\text{ext}}$  is the extracellular current density injected to the ganglion cell;  $J_E$  is the extracellular peak-threshold current density used to match with the peak boundary current density of ganglion cell at Comsol simulations. Pulse durations and pulse shapes are identical as in Matlab.

$I_{CED}$  is the cell-electrode distance;  $I_{\text{ele}}$  is the current applied at the electrodes in Comsol;  $E_D$  is the electrode diameter;  $P_{\text{DEVAVE}}$  is the average power density at the device;  $T_D$  is the change of

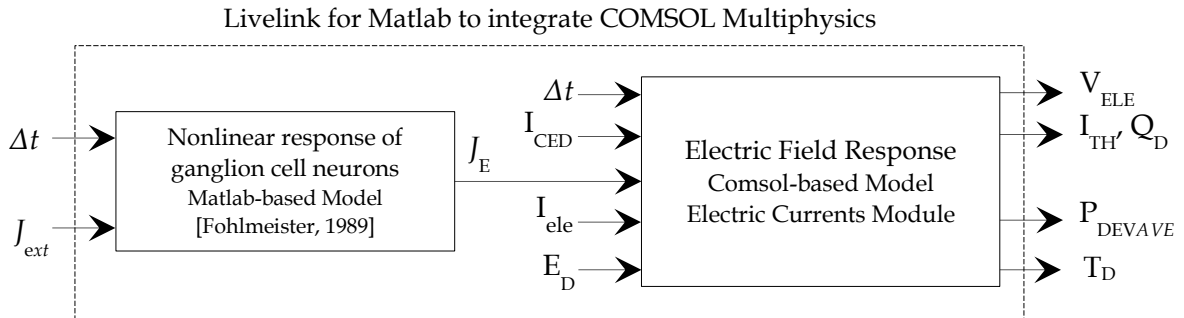


Fig. 3.6 Flowchart of simulation

temperature;  $V_{ELE}$  is the electrode voltage;  $I_{TH}$  and  $Q_D$  are the threshold current and the charge density from the electrodes.

The assumptions are i) single ON ganglion cell where activation can be described by a single membrane potential (ON-model choice is clarified in section 3.3.2.4); ii) exclusion of retinal network model, i.e. bipolar cell, horizontal and amacrine cells, either ON- or OFF-network, because of severe rod and cone photoreceptor impairment that cannot drive synaptic connection started with a photocurrent input; iii) extracellular current density across the cell membrane at Comsol simulations is equal as in the equivalent circuit of ganglion cell [Fohlmeister, 1989] which is modelled as voltage-gated channels.

Hodgkin and Huxley-like equations can describe the eliciting of action potential at the cell membrane, see Chapter 2; iv) the sum of the power of the transistors that drive the electrodes and the power consumed per LSUs is sufficient to describe the total average power density of the device.

### 3.3.2.6. Charge Density Calculation

Charge density was obtained by integrating the current delivered by the active electrode over time and dividing it by the electrode area

$$Q_D = \frac{4}{\pi E_D^2} \cdot \int_0^{\Delta t} I_{ele} dt \cdot \quad (3.4)$$

It is worth to mention that all eight surrounding electrodes including the active changed their dimensions accordingly. The limit for gas-free and erosion-free operation is 0.35 mC/cm<sup>2</sup> and for neural damage is 1 mC/cm<sup>2</sup>. The assumption of reaching irreversible Faradaic reactions, if present, will occur such that the charge density surpasses the  $Q_{INJ}$  limit.

### 3.3.2.7. Voltage Across Electrodes

Voltage across the electrode was computed within Comsol framework using a measuring probe. PEDOT voltage window extends beyond conductive materials, such as  $MnO_2$ , from 1.5 V [Boretius, 2010] up to 1.7 V [Duay, 2012]. As there is no evidence about voltage window on PEDOT-NaPSS low electrode area, we used the limit of 1.7 V. The assumption of reaching irreversible Faradaic reactions, if present, will occur such that the anodic peak potential at the electrode surpass the voltage window boundary.

### 3.3.2.8. Power Consumption and Heat Dissipation

The major aim in ganglion cell activation, using either epi- or subretinal technique, is to deliver functional vision that comes from 1024 image pixels with at least 20 images per second. To achieve this request, the feasibility of using 1024 electrode array is studied by attaching 16 scalable chips of 64 electrodes each with a daisy chain configuration as seen in [Meza, 2014] with low power consumption of 56  $\mu$ W per Local Stimulation Unit (LSU).

The stimulation waveform has a monophasic rectangular shape with a total image frequency,  $f$ , of 20 Hz, fig. 3.7. The main target is, within time duration of  $1/f$ , to *individually* trigger 1024

pixels with pulse duration and have a full image. Using the features of [Meza, 2014], each electrode can have a different timeslot.

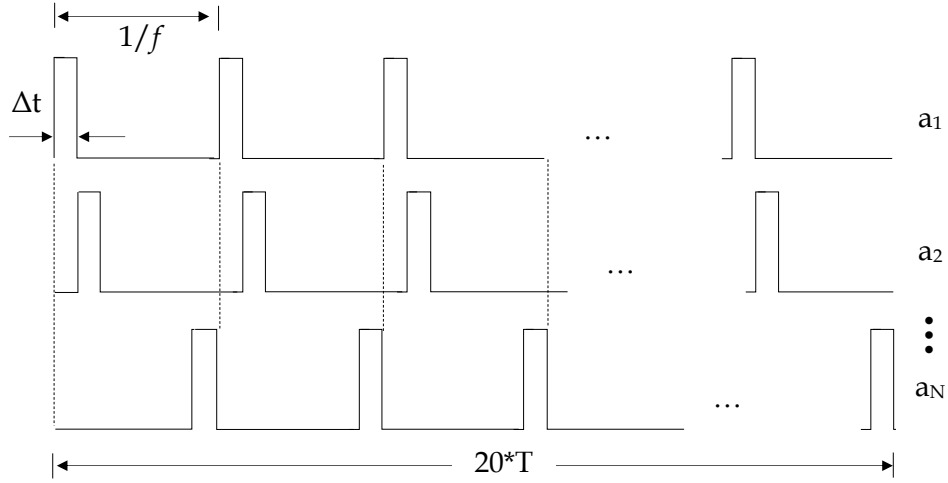


Fig. 3.7 Device activation per pulse duration

To achieve the main target, however, a limitation to complete a full image of 1024 pixels may occur within  $1/f$  with known pulse duration. The minimum number of electrodes activated per pulse duration can be calculated as

$$e_{ON} = 2(e_T \cdot f \cdot \Delta t), \quad (3.5)$$

$e_T$  is the total number of pixels considered, i.e. 1024 for our specific case. The total number of active electrodes activated per pulse duration can be computed as

$$e_{AN} = e_{ON} / 2. \quad (3.6)$$

The device activation shown in figure 3.7 as 'a', corresponds to the triggering of active electrodes. The total number of device activations is calculated as

$$a_N = e_T / e_{AN}. \quad (3.7)$$

The average power density of the device,  $P_{DEVAVE}$ , is calculated considering the power of the transistors that drive one of the electrodes,  $P_T$ , during the pulse of stimulation and the power per Local Stimulation Unit (LSU),  $P_{LSU}$ .  $P_T$  is calculated using a simplified electrical circuit of a retinal implantable device powered by a voltage source  $V_{DD}$ , see fig. 3.8.

Each branch labeled, 'b', has two transistors which drive the active and ground electrodes and the load which is associated to the tissue, fig. 3.8. For sake of simplicity, we assumed that the voltage drop in the tissues is equal to the voltage drop across the electrodes. Since each active or ground electrode is equivalent to one transistor [Meza, 2014], the total number of transistors is equal to  $e_{ON}$ . Since each branch contains two such transistors, the total number of

branches is  $e_{ON}/2$ . A single branch is activated per single pulse duration.  $V_T$  is the voltage drop in the transistors that drive the electrodes.

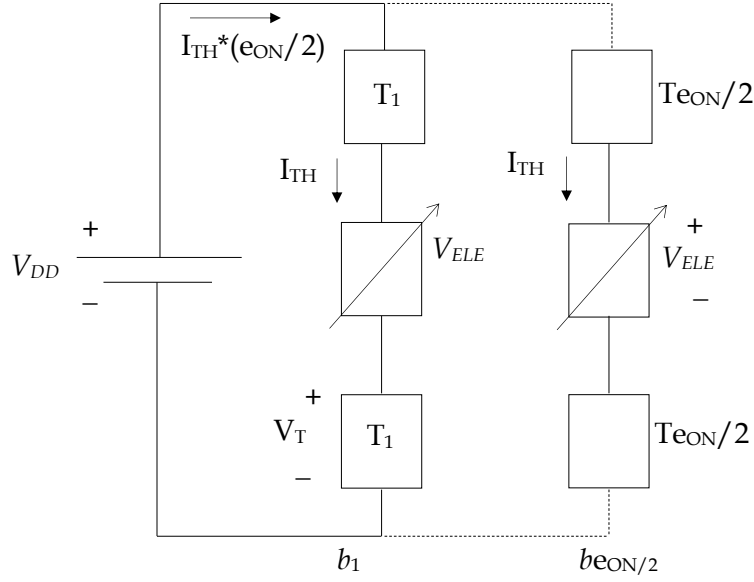


Fig. 3.8 Simplified electrical circuit of a retinal implantable device

$I_{TH}$  is the threshold current.  $P_T$  is given by

$$P_T = I_{TH} (V_{DD} - V_{ELE}). \quad (3.8)$$

The voltage drop across the branches is assumed approximately the same and there is an equal distribution of current across the branches. The average power density at the device with units of [mW/cm<sup>2</sup>] then is computed as follows

$$P_{DEVave} = \frac{e_T \Delta t}{A_D T} (P_T + 2P_{LSU}), \quad (3.9)$$

$\Delta t/T$  defines the duty cycle of stimulation.  $\Delta t$  is the pulse duration and  $T$  is the inverse of the total image frequency of 20 Hz.  $A_D$  is the total chip surface area of 0.68 cm<sup>2</sup> and  $P_{LSU}$  is the power consumption per electrode or LSU of 56  $\mu$ W [Meza, 2014].

The neural tissue heating from the retina implant is calculated using the average power density at the device,  $P_{DEVAVE}$ , in the linear approach of  $\Delta T = 1$  °C per 12.2 mW/cm<sup>2</sup> [Sohee, 2006] assuming only heat conduction. Body temperature of 37° degrees was the initial temperature.

### 3.3.2.9. Boundaries Addressed

Charge density plays an important role in retinal prosthesis due to the electrochemical reactions that can be caused by charge injection into the neural tissue. During stimulation of an implanted neural device at the retina, not only the charge should be monitored and minimized, but also the temperature dissipated by the device and voltage across the electrodes. Water



electrolysis may occur as a result once the maximum cathodic and anodic potential across the electrodes surpasses the “water window” boundary.

The temperature is also a key element that should be monitored because the tissue surrounding the implant in the eye and overall the human body is usually highly sensitive to temperature rise. As such, that power consumption must be small to prevent tissue damage [Garrison, 2010]. Major limitations in epiretinal, subretinal and suprachoroidal device implantations are listed next, i) charge density required for eliciting activity in neurons [Lujan (b), 2016]; ii) proximity of cells to the electrodes for exciting cells because the electric current injected from the device is proportional to the square of that distance [Lujan (a), 2016]; iii) fluctuation of injected current for cell activation that can occur due to an unstable positioning of the electrode array and due to an unwanted lifting off of the array from the retinal surface [Mahadevappa, 2005]; iv) electrochemical alterations in the electrode [Kasil, 2011]; v) mistakenly used materials in the electrode array leading to inflammatory response in tissues due to biodegradation; vi) electrical biocompatibility in invasive prosthesis [Starbird, 2012]; vii) high charge density leading to gas bubble formation [Brummer, 1977]; viii) high voltage leading to metal oxidation and corrosion [Merrill, 2005]; ix) temperature dissipated on the surrounding volume of the electrode array.

Energy considerations have also a role in the design of implanted biomedical systems, particularly when these are battery-powered. In implantable neural prosthetic devices, the energy needed for the generation of stimulation pulses is high. As the energy dissipated during stimulation decreases, thus the battery lifetime of the device is extended and the costs related to battery replacements is reduced.

Some other examples of implanted neural prosthetic devices include heart pacemakers, paralyzed subjects, and deep brain stimulation system for Parkinsonian tremor suppression. One possibility for energy minimization is to monitor twitch response so as to excite the nervous tissue with the least possible energy sufficient to generate action potentials propagation. Another possibility is to analyze other pulse shapes rather than the nowadays most-widely used rectangular pulse shape.

### 3.4. Feasibility of a 32 x 32 Electrode Array in Epiretinal Implants

#### 3.4.1. Motivations

The feasibility of a 32 x 32 array of electrodes is investigated. The simplified 3D neural-model of the retina defined in section 3.3 is applied. It is based on a single ganglion cell *ON*-model simulated with PEDOT-NaPSS arranged electrode array. Livelink for Matlab is used to integrate Comsol Multiphysics to the Matlab environment. The parameters defined in section 3.3 will be a guidance to calculate the charge density and heat dissipated by the device.

The model is based on an existing scalable 64 channel stimulator that can be realized for a fully implantable device of 1000+ electrodes for epiretinal stimulation [Meza, 2014]. Using this design, it is possible to attach 16 chips in daisy chain configuration with low area requirement, low power consumption and low residual charge using a 130 nm CMOS process and PEDOT-NaPSS electrode deposition. Low power consumption can support large scale of Local Stimulation Units (LSUs) with less heat delivered by the device. Other enquiries investigated are

minimum electrode size, electrode voltage and proximity of cell to the electrodes that ensure electrochemical safety.

### 3.4.2. Electrode Amount per Single Array

In neural stimulation for restoring vision, i.e. retinal, visual nerve, lateral geniculate, or cortical implants, between 600 to 1000 electrodes are required for upgrade basic issues such as mobility, independent living, navigating on interior and exterior environments and reading large-sized text. Further, from theoretical modelling, it is projected that a 1000+ electrode device could achieve the previous tasks [Chader, 2009].

### 3.4.3. Neurostimulator Scheme

The visualization of this work is based on an integrated neurostimulator formed by 64 local stimulator units (LSU) or channels constructed with 130nm CMOS transistor process [Meza, 2014]. Using the advantage of daisy chain configuration, the chip can be fully scalable so as to increase the number of stimulation channels, as is it required in retinal prosthesis stimulation. The features of such chip are

1. On-chip module capable to control the electropolymerization process of the electrodes.
2. Each LSU can have a different timeslot so as to prevent cross electrode stimulation.
3. PEDOT deposition on each electrode.
4. Low power consumption of each electrode.
5. Low residual charge.
6. Several pulse shapes available.
7. Small chip area.

The ASIC consists on a matrix of 64 LSUs: 32 P type and 32 N type. Adjacent LSUs from each other are of different types. The advantage of such arrangement is any LSU can interact with another being either on top, bottom, left or right. Each ASIC can control 64 electrodes with 32 stimulation sites. The total area of chip is 4.25 mm<sup>2</sup>, i.e. 1.924 x 2.209 mm<sup>2</sup>. For more information, see figure 4 in original manuscript [Meza, 2014].

A single LSU is of size 188 x 209  $\mu\text{m}^2$  (single pixel size of 0.039mm<sup>2</sup>) and is composed of an 8 bit DAC, digital stage and output multiplexer. The DAC offers the ability to deliver several waveforms in order to save energy. Table 3.3 lists some visual prosthesis devices currently developed without implantation and clinical trials.

### 3.4.4. Small Electrode Size

Although the ability to create visual sensations is now well established [Cai, 2011], the quality of vision elicited by retinal implants is facing further challenges for safely electrode implantation. The acuity of normal vision commonly referred as the clarity of vision, is quite high because the ganglion cells are tightly-packed especially at the fovea. The total amount of ganglion cells is of around 1.5 million in the human eye. Each cell extracts different information only from a narrow fragment of the visual space. As an array of electrodes is implanted in the eye with some diameter higher than the cell size and their inter distance, as a result, each electrode can stimulate more than a single ganglion cell, thereby greatly reduce resolution.

TABLE 3.3

Reference	No. of Electrodes	Cathodic-Anodic Mismatch	Power Consumption per electrode [mW]	Channel Stimulator Size [mm]	CMOS Technology [nm]	Voltage Supply [V]	Stimulus Current [ $\mu$ A]	Pixel Size <sup>1</sup> [mm <sup>2</sup> ]
[Meza, 2014]	64	4.7nA	$\approx 0.056$	1.924 x 2.209	130	3.3	0 - 50	0.039
[Tran, 2014]	256	0.5%	0.129	2.76 x 2.91	65	2	0 - 465	0.0225
[Monge, 2013]	512	5%	N/A	4.5 x 3.1	65	2	0 - 50	0.017
[Chen, 2013]	1024	N/A	N/A	5.7 x 6.6	180	12	3 - 500	0.102
[Chen, 2010]	256	2.9%	N/A	4.2 x 5	180	12	3 - 500	0.0806
[Ortmanns, 2007]	232	5%	N/A	4.9 x 4.5	35	3.3	0 - 2000	0.0718
[Rothermel, 2008]	1600	N/A	N/A	3 x 3.5	350	5	0 - 100	0.0049
[Noorsal, 2012]	1000	15%	0.120 @ 5V 0.720 @ 20V	0.2mm <sup>2</sup> each	35	20	0 - 1000	0.2

<sup>1</sup> Pixel size is equal to the electrode driver size or channel stimulator area. <sup>2</sup> Power consumption without load.

Due to their close juxtaposition of diverse cells to one another, the stimulation from a large electrode is likely to elicit analogous spiking patterns in multiple cells, thus sending a non-physiological signal to the brain. Therefore a low electrode diameter should be used. Note that when electrode size is minimized, high charge density is required to activate nearby cells.

### 3.4.5. Short-Current Pulse Duration

[Fried et al., 2006] suggested to apply stimulus pulses lower than 0.15 ms because of the fact that each pulse consistently elicited a single spike to activate neighboring cells. Experimental findings by [Jepson, 2012] support this observation, stating that the characteristic of direct ganglion cell activation is originated using short pulse durations of 100  $\mu$ s and small electrodes of 15  $\mu$ s of diameter. Electrical stimulation with white rabbits suggest that spiking response is the result of a direct spike in ganglion cell along with a complex interaction between presynaptic neurons that results in a variable number of late phase spiking [Fried, 2006]. The term late phase spiking is defined as the existence of a spike within 50 ms of the leading edge of the first pulse.

Fried and colleagues observed that excitatory input elicited by stimulation is proportional to the pulse duration, i.e. longer pulse widths generated late phase spiking. Thus, decreasing pulse duration might reduce or eliminate excitatory inputs to ganglion cells. As to eliminate further late phase response and elicit just a single spike, Fried suggest that precise temporal patterns of spiking, together with those of elicited by light, can be produced using programmed arrays of short pulses. Matching common light spike patterns deliver a better physiological signal to the brain that may lead to the generation of more meaningful percepts.

As previously discussed, [Merrill et al., 2005] proposed a novel strategy that generally suggest keeping the pulse width narrower because it confines the amount of current that can be

delivered by a stimulator and provides the minimum charge that occurs when pulse width is of tens of  $\mu\text{s}$ . Doing so, any electrochemical reactions occurring at the electrode/electrolyte layer will be minimized. Another similar strategy has been proposed by McAdams, assuring that few undesirable effects are seen using short pulses with duration less than one time constant [McAdams, 2010].

[Suzuki, 2004] observed that in normal and *rd* mice, short pulses were more efficient with respect to total charge used, but required a higher current. In normal mice, sine wave stimulation was significantly more efficient than a biphasic pulse of the same duration.

#### 3.4.6. PEDOT\_NaPSS Electrode Array

PEDOT has a high charge injection capacity in combination of Faraday (charge transfer) and non-Faraday (double layer capacitance) processes. The larger porous area reported for PEDOT also increases biocompatibility and improves the interaction with biological environments.

Further, using an arrangement consisting of an active electrode surrounded by eight guards is beneficial because the isolation of the active electrode is stressed-out, the stimulus current is confined to a small volume around the ganglion cell and electrode cross-talk during stimulation is minimized [Lujan (b), 2016].

#### 3.4.7. Methods

##### 3.4.7.1. Ganglion Cell Simulation – Matlab (Refer to Section 3.3.2.4)

The extracellular peak-threshold current density ( $J_E$ ) was found by injecting current density to the ganglion cell model [Fohlmeister, 1989] with pulse duration of 50, 100  $\mu\text{s}$ . The results of strength duration curve are 330 and 120  $\mu\text{A}/\text{cm}^2$  for 50 and 100  $\mu\text{s}$ , respectively. Pulse durations lower than 150  $\mu\text{s}$  are analogous in [Fried, 2006] to directly stimulate the ganglion cell and to elicit solely a single spike with precise temporal pattern.

##### 3.4.7.2. FEM-based Model Simulation – Comsol (Refer to Section 3.3.2.5)

Pulse duration, electrode diameter and proximity of cell to the electrode were varied to analyze charge density limitations, high stimulus frequency limitations, safely injecting current impulses without exceeding temperature increase limit of  $1^\circ\text{C}$  and maximum output voltage of operation.

The electrode distance is constant with a value of 100  $\mu\text{m}$ . Proximity distance was varied with values of 2, 10 and 100  $\mu\text{m}$ . This variation is in order to simulate the changeability of threshold current and charge density due to the lifting off of the electrode array from the retinal ganglion cell layer surface.

The values simulated are analogous to the experimental findings in [Kasi, 2011]. Pulse duration was varied with values of 50 and 100  $\mu\text{s}$ . The electrode diameters tested are 2, 10, 50 and 100  $\mu\text{m}$  and are analogous to [Cai, 2011; Fried, 2006; Rizzo III et al., 2003; Werginz, 2004].

Once the threshold current was found, charge density, electrode voltage, power consumption and the increase of heat at the device were calculated as explained in section 3.3.2.6, 3.3.2.7 and 3.3.2.8, respectively. As such, the results were compared with their own harmful limits of 1 mC/cm<sup>2</sup>, 1°C [Singh, 2008] and 1.7 V [Duay, 2012].

### 3.4.8. Results

#### 3.4.8.1. Proposed ASIC Attachment

The proposed ASIC attachment is shown in fig. 3.9. The area of one ASIC consists of the dimensions of 1.92 mm x 2.2 mm for a single chip [Meza, 2014] and the gap distance on each edge of 1 mm for wire bonding. The total width,  $w_s$ , and the length,  $l_s$ , of a single ASIC is 3.94 and 4.2 mm, all respectively.

We selected a two layer arrangement of 2 x 4 each to minimize the total area of their attachment. In total we have 16 chips of 64 electrodes each. The total width, ' $w_T$ ', the length, ' $l_T$ ' and of one layer arrangement is 15.7 and 8.4 mm, respectively. The total area of a single layer is 1.32 cm<sup>2</sup>. The height,  $h_T$ , between the layers is 1 mm.

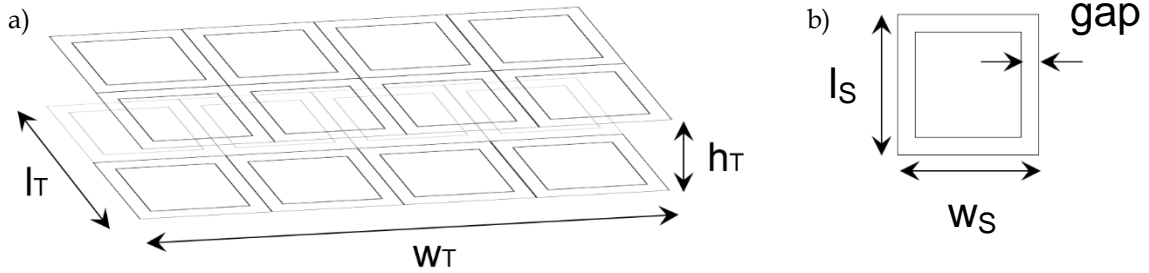


Fig. 3.9 a) ASIC attachment consisting of 16 chips on daisy chain configuration; b) single chip

#### 3.4.8.2. Electrochemical Safety

Figures 3.10 and 3.11 show the threshold charge density, threshold current and electrode voltage at bottom  $x$ -axis. The temperature dissipation is displayed at top  $x$ -axis. Each plot shows the results for a specific proximity distance. Monophasic rectangular pulse shape was used throughout our study. Harmless and harmful zones are separated at the electrode diameter where the limit boundary of charge density, electrode voltage or heat increased is exceeded.

#### 3.4.8.3. Electrode Distribution

For electrode diameter from 2 to 100  $\mu$ m and knowing the electrode distance of 100  $\mu$ m to be constant, the electrode carrier area of 1024 evenly distributed electrodes is in the range from 11.3 to 43.56 mm<sup>2</sup>. Using the total area of the attachment of 1.32 cm<sup>2</sup>, the carrier area would occupy from 8 to 33% of the total area of the chip arrangement.

A large electrode carrier area, however, has its own advantages. The visual field is directly related to the size of stimulated area of the retina and hence the diameter of the electrode array. The projected visual field for every 1 mm of the retina is about  $3.35^\circ$  [Tychsen, 1992]. For our case, it will provide a central vision with a field of view of about  $11^\circ \times 11^\circ$  for  $11.3 \text{ mm}^2$  to  $22^\circ \times 22^\circ$  for  $43.56 \text{ mm}^2$ . Currently, electrode arrays implanted in animals or humans range from  $9 \text{ mm}^2$  to  $33 \text{ mm}^2$  in area [Yanai, 2007; Majji, 1999; Walter, 2005].

### 3.4.9. Discussion

#### 3.4.9.1. Charge Density

The foremost concern on advanced visual prosthesis and current status on clinical trials lies on that atypical patterns of retinal activity are induced by stimulation [Stingl et al., 2013; Humayun et al., 2012]. Current prosthetic devices developed by [Mahadevappa et al., 2005], [Reinhard et al., 2006], [Rizzo et al., 2003], [Humayun et al., 2012] and [Klauke et al., 2011] use big-sized electrode diameter of 500, 200 and  $100 \mu\text{m}$ . Large diameter of stimulating electrodes in such implanted devices [Rizzo III et al., 2003; Stingl et al., 2013; Reinhard et al., 2006] likely activates hundreds or thousands of cells over their area of stimulation. Not only this coarse stimulation of cells restricts the detail perception, but also the activity generated by stimulation remains dissimilar from a healthy retina [Horsager et al., 2011]. Electric current fields from relatively large electrodes indiscriminately drive local retinal circuits in an unnatural way, leading to complex retinal responses [Horsager et al., 2011]. As such, safe charge density boundary which limits the miniaturization of implanted electrodes is currently a major concern [Lujan (a), 2016; Lujan (b), 2016; Kasi, 2011; Horsager et al., 2011].

The simplified 3D retinal-model suggested that below  $10 \mu\text{m}$  cell-electrode distance, electrode sizes between 2 to  $100 \mu\text{m}$  and pulse durations of 50 and  $100 \mu\text{s}$  deliver safe stimulus. This is valid for PEDOT voltage window limit of 1.7 V and safe charge density of  $0.35 \text{ mC/cm}^2$  for gas-free and erosion-free operation and  $1 \text{ mC/cm}^2$  for neural damage. For more information on the results of such proximity of cell to the electrodes, see [Lujan (a), 2016]. Small electrode dimension can produce greater resolution patterns of artificial-elicited activity that are closer to light-elicited patterns [Cai, 2011], however, additional experimental testing of small electrodes is still required to verify our results.

The result of our simulation suggest that electrode diameters of  $9.7$  and  $9.6 \mu\text{m}$  are sufficient for delivering safe stimulus to the retina at proximity lower than  $100 \mu\text{m}$ , see figs. 3.10 and 3.11. This suggestion applies to 50 and  $100 \mu\text{s}$  pulse duration, respectively. In such figures, harmless and harmful zones of retinal stimulation are separated at the electrode diameter where the boundary of charge density is exceeded. Table 3.4 lists the minimum electrode diameter that can be used with their corresponding limit. Green boxes indicate the suitability to use electrodes of  $2 \mu\text{m}$  of diameter.

A key challenge that artificial visual devices are facing is the avoidance of stimulating retinal ganglion cell axons [Jensen, 2005; Weiland, 2014]. This issue has been addressed by Jensen and Rizzo III [Jensen, 2005]. In their study, short-current pulses of  $100 \mu\text{s}$  or less are preferable because passing retinal ganglion cell axons can be avoided while stimulation. Choosing that pulse duration, the amount of current needed to generate a cell response is much lower than that required to generate an axonal response. Throughout our simulation, minimum pulse

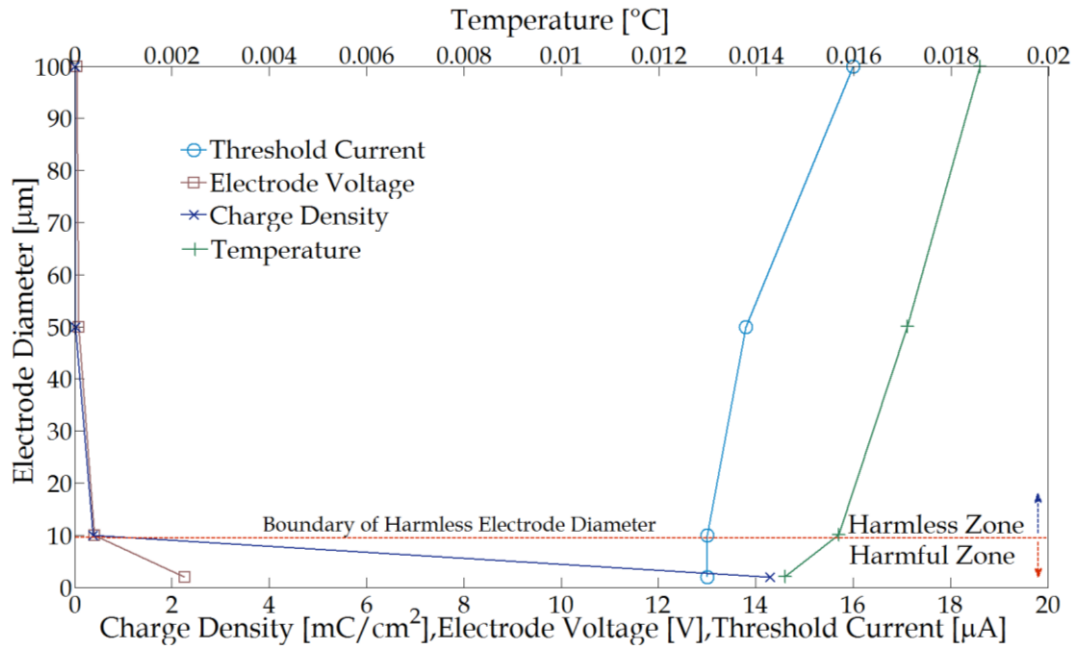


Figure 3.10 Electrode diameter relationship with charge density, electrode voltage, threshold current and temperature increase at the device. Here, pulse duration of 100  $\mu\text{s}$  and proximity 100  $\mu\text{m}$  of cell to the electrodes were used. Safe charge density of 1  $\text{mC}/\text{cm}^2$  was applied. Harmless and harmful zones are separated at the electrode diameter of 9.6  $\mu\text{m}$  where the boundary of charge density is exceeded. Rectangular pulse was simulated. Data points from [Lujan (a), 2016].

duration of 50 and 100  $\mu\text{s}$  was used. As such, lowest pulse width less than 0.15 ms provides a method to send a more natural signal to the brain and to generate meaningful percepts [Fried, 2006].

TABLE 3.4  
Charge Density Limits for Rectangular Pulse Shape

Proximity of Cell to Electrode	0.35 $\text{mC}/\text{cm}^2$ limit		1 $\text{mC}/\text{cm}^2$ limit	
	50 $\mu\text{s}$	100 $\mu\text{s}$	50 $\mu\text{s}$	100 $\mu\text{s}$
2 $\mu\text{m}$	Yes	Yes	Yes	Yes
10 $\mu\text{m}$	Yes	Yes	Yes	Yes
100 $\mu\text{m}$	18 $\mu\text{m}$	14 $\mu\text{m}$	9.7 $\mu\text{m}$	9.6 $\mu\text{m}$

#### 3.4.9.2. Threshold Current

The results in our simulation indicate that a higher threshold current was delivered when the proximity of cells to the electrodes became higher (Results not shown. For more information, see original manuscript in [Lujan (a), 2016]). As such, threshold currents in experiments were found to increase with time after surgery, most likely due to the lifting off of the electrode array from the retinal surface [Chader, 2009]. Experimental findings [Mahadevappa et al., 2005] confirm that this anomaly was particularly noticeable in the first postoperative weeks. To verify the response of threshold current to generate percepts, thresholds for activation in rabbit retinal

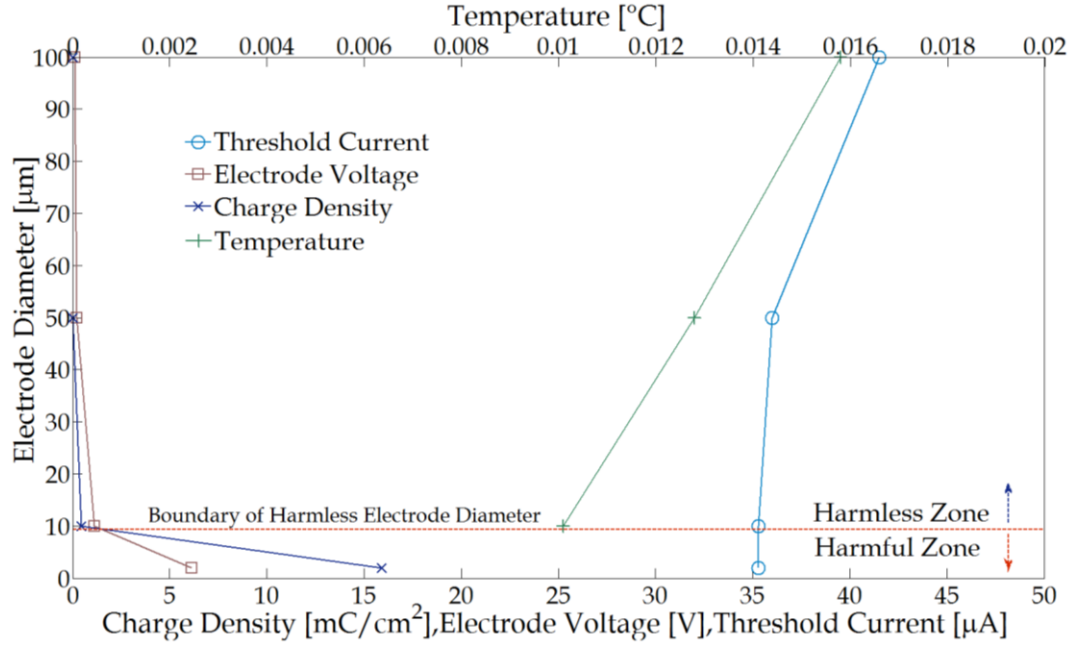


Figure 3.11 Electrode diameter relationship with charge density, electrode voltage, threshold current and temperature increase at the device. Here, pulse duration of 50  $\mu\text{s}$  and proximity 100  $\mu\text{m}$  of cell to the electrodes were used. Safe charge density of 1  $\text{mC}/\text{cm}^2$  was applied. Harmless and harmful zones are separated at the electrode diameter of 9.7  $\mu\text{m}$  where the boundary of charge density is exceeded. Rectangular pulse was simulated. Data points from [Lujan (a), 2016].

ganglion cell [Jensen, 2005] were compared with the same configuration of electrode size and cell-electrode distance using our model. The experimental responses of rabbit were performed with 125 and 500  $\mu\text{m}$  electrode diameter comparable in size to those used in human studies [Rizzo III et al., 2003; Mahadevappa et al., 2005]. In that study, stimulation thresholds were determined by increasing subthreshold current until action potentials were elicited  $> 50\%$  of the time for five or more consecutive stimulations. The comparison was carried out only with 100  $\mu\text{m}$  electrode diameter and with pulse duration of 100  $\mu\text{s}$  because of producing a fair comparison with parameters. The tendency of current along the proximities in simulations is consistent with experimental outcomes, see fig. 3.12.

#### 3.4.9.3. Heat Limitations

Power consumption in retinal stimulator devices is restricted firstly because inductive coupling is used to power the device and secondly because the increase of temperature at the device is well associated to power consumption.

Top  $x$ -axis in figs. 3.10 and 3.11 display the increase of temperature at the device. For each case, the change of temperature slightly rises as the electrode diameter increases. This tendency can be attributed to the influence of electrode impedance and therefore the rise of its voltage which sequentially decreases the voltage at the device and its power consumption. As aforementioned, that influence states an advantage to work with short pulse durations unless the electrode voltage does not exceed  $V_{DD}$ . The temperature results in our study did not exceed the temperature limit of  $1^\circ\text{C}$ . This behavior can be attributed to the use of the duty cycle and few LSU per pulse duration. Assuming a linear approach of heat increase of  $1^\circ\text{C}$  per  $12.2 \text{ mW}/\text{cm}^2$ ,



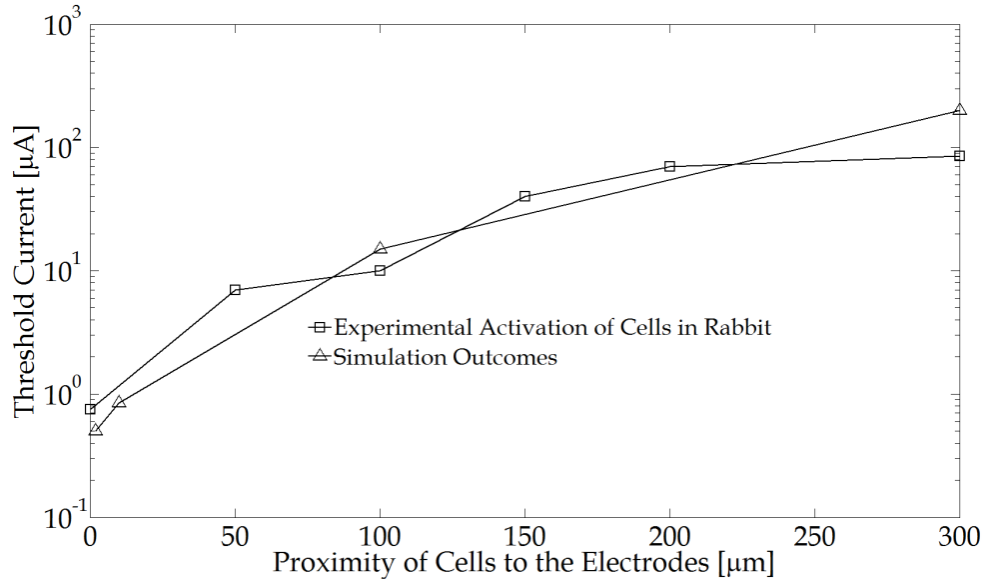


Fig. 3.12 Comparison with experimental activation of cells in rabbit. Experimental data points from [Jensen, 2005].

our simulations suggest is safe within the limits of delivering stimulus using electrode diameter between 2 until 100  $\mu\text{m}$  and pulse duration of 50 and 100  $\mu\text{s}$ .

#### 3.4.9.4. Maximum Voltage of Operation

The voltage across the electrodes was used as the maximum output voltage of operation while stimulating the retina. Figures 3.10 and 3.11, bottom  $x$ -axis, display the electrode voltage. Each result of potential was compared with voltage supply of  $3.3 V_{DD}$  and  $1 V_{DD}$  as a condition boundary of voltage of operation. Table 3.5 lists the results for both limits and is indicated the minimum electrode diameter for the corresponding condition boundary. Green boxes indicate the suitability to use electrodes of 2  $\mu\text{m}$  of diameter.

TABLE 3.5  
Condition Boundary for Voltage of Operation

Proximity of Cell to Electrode	$1 V_{DD}$		$3.3 V_{DD}$	
	50 $\mu\text{s}$	100 $\mu\text{s}$	50 $\mu\text{s}$	100 $\mu\text{s}$
2 $\mu\text{m}$	Yes	Yes	Yes	Yes
10 $\mu\text{m}$	Yes	Yes	Yes	Yes
100 $\mu\text{m}$	15.5 $\mu\text{m}$	7.5 $\mu\text{m}$	6.5 $\mu\text{m}$	Yes

#### 3.4.9.5. Perceptual Threshold Comparison

In recent years, epi- and subretinal electrode array implants have been developed. Humayun in several publications [Humayun et al., 1996; 1999; 2003] and [Rizzo III et al., 1997], amongst recent clinical trials [Stingl et al., 2013; Humayun et al., 2012] have reported that blind patients perceived sensations of spots of light while the retina was electrically stimulated. These

TABLE 3.6  
Threshold Current Comparison

Reference	Setup	Electrode Size [ $\mu\text{m}$ ]	Pulse Duration [ms]	Threshold Current [ $\mu\text{A}$ ]	Proximity <sup>2</sup> [ $\mu\text{m}$ ]
[Rizzo III, 2003]	Epiretinal, Human	400	4	25-475 <sup>3</sup>	-
[Mahadevappa, 2005]	Epiretinal, Human	500	1.95	25-702	-
[Mahadevappa, 2005]	Epiretinal, Human	250	1.95	24-143	-
[Lujan (a), 2016]	Epiretinal, Simulation	100/50/10/2	0.1	0.8/0.5/0.3/0.24	2
[Lujan (a), 2016]	Epiretinal, Simulation	100/50/10/2	0.05	2.2/1.2/0.8/0.65	2
[Lujan (a), 2016]	Epiretinal, Simulation	100/50/10/2	0.1	0.5/0.2/0.07/0.06	10
[Lujan (a), 2016]	Epiretinal, Simulation	100/50/10/2	0.05	1.3/0.5/0.2/0.16	10
[Lujan (a), 2016]	Epiretinal, Simulation	100/50/10/2	0.1	16/14/13/12	100
[Lujan (a), 2016]	Epiretinal, Simulation	100/50/10/2	0.05	42/36/35/34	100
[Jensen, 2005]	Epiretinal, Rabbit	125	0.1/2/50	0.75/0.4/0.35	-
[Jensen, 2005]	Epiretinal, Rabbit	500	0.1/2/50	6.9/2/1.9	-
[Humayun et al., 1999]	Epiretinal, Human	400	2	200-300 <sup>3</sup>	-
[Hesse et al., 2000]	Epiretinal, Cat	100	0.4	35-50	-
[Schwahn et al., 2001]	Subretinal, Rabbit	100	0.4	17.5-125 <sup>3</sup>	-
[Greenberg et al., 1997]	Epiretinal, Amphibian	50	0.1	71	-
[Keserü et al., 2012]	Epiretinal, Human	200 <sup>1</sup>	3	11.3-198 <sup>3</sup>	-
[Keserü et al., 2012]	Epiretinal, Human	360 <sup>1</sup>	3	6.7-256 <sup>3</sup>	-
[Eckmiller et al., 1997]	Epiretinal, Human	500	0.1	12-95	-

<sup>1</sup>Keserü et al used a ring-approach of 6 and 12 round electrodes of 50  $\mu\text{m}$  to form the electrode array of 200 and 360  $\mu\text{m}$  respectively. <sup>2</sup>The proximity is defined as the distance of the cells to the electrode array. <sup>3</sup>They provided threshold charges. Threshold current was calculated assuming biphasic rectangular pulse shape delivery.

experiments clearly validated the viability of producing perception of light patterns in blind patients by electrically activate nearby ganglion cells.

As each experimental setup was carried out with different input variables, however, table 3.6 shows the threshold current comparison of our simulation-based findings and the current trials found in the literature.

#### 3.4.10. Electrode Voltage Comparison

A comparison of the voltage across gold electrodes coated with PEDOT-NaPSS is presented between the measurements by [Meza et al., 2014] and our simulation-based findings.

[Meza et al., 2014] developed an array that consists of eight electrodes. The size of each is 95 nm thick made of gold deposited over a 75  $\mu\text{m}$  flexible polyimide thick substrate. Each electrode has a diameter of 35.7  $\mu\text{m}$  with electrode distance of 5 mm. The array was immersed in EDOT-NaPSS micellar dispersion. PEDOT was electrodeposited by delivering 5nA for the time frame of 360 sec. Gold electrode fabrication and PEDOT polymerization were implemented according to [Starbird et al., 2012]. Subsequently, the stimulator developed by [Meza et al., 2014] performed several tests. The stimulator was programed to activate three pairs of channels and deliver stimulus within a biphasic current pulse of 288  $\mu\text{s}$  of duration with anodic phase first.

The amplitudes of each channel were 50, 30 and 20  $\mu\text{A}$ , respectively. Each pair had its own time slot to deliver the stimulus. The electrode array was immersed in a glass recipient containing saline solution and the peak electrode voltage per pair of electrodes was measured.

The measured results by [Meza et al., 2014] were compared with the 3D retinal-model shown in fig. 3.3 that uses a 32 x 32 array of electrodes coated with PEDOT-NaPSS. The input parameters stated in table 3.2 are kept except where expressly varied. The electrode size was set to 35.7  $\mu\text{m}$  of diameter. The size of polyimide carrier was set to accommodate eight electrodes forming an array with electrode distance of 5 mm. Pulse duration is 288  $\mu\text{s}$ . The pulse shape is biphasic rectangular, anodic first. One simulation was executed by activating three pairs of electrodes and delivering 50, 30 and 20  $\mu\text{A}$  of amplitude, respectively. Each pair of electrodes had its own time slot. The electrode voltage was calculated according to section 3.3.2.7.

The results are listed in table 3.7. The simulations of the simplified FEM 3D retinal-model delivered a good agreement with the measurements. This suggests that experimental data of electrodes coated with some material can be fitted in a circuit modelling using passive elements, see section 3.3.2.2. As such, the domain definitions listed in table 3.2 can deliver accurate results of the electric field distribution throughout the retinal tissue.

TABLE 3.7  
Electrode Voltage Comparison

	50 $\mu\text{A}$	30 $\mu\text{A}$	20 $\mu\text{A}$
[Meza et al., 2014]	1.2 V	0.7 V	0.6 V
FEM Simulation	1 V	0.6 V	0.5 V

### 3.4.11. Voltage Limitations

Although that the charge density has been the major limitation observed in this study, small electrodes have high voltage drop because 1) high current requirement to activate neighboring cells and 2) the high impedance at the electrodes. Further, as the proximity of cells to the electrode increases, the limitation of the compliance voltage to drive the electrodes has a high impact. Stimulators for epiretinal prostheses require an output compliance voltage of  $\pm 10$  V to elicit light perception of various brightness levels. This, however, requires area-consuming high-voltage (HV) transistors [Sooksood, 2011]. The compliance voltage is the maximum voltage that the current source can supply to a load.

Figure 3.13 illustrate the relationship between electrode voltage, electrode diameter and the proximity of cells to the electrodes. The latter variable plays a major role in visual prosthetic to activate nearby cells. A distant proximity of the retina to the electrode array contributes to the varying current spread from the active electrode causing changes in the area of stimulation and thus affects the resolution of the visual prosthetic [Kasi, 2011].

A closer proximity of the cells to the electrodes reduces threshold current and thus the electrode voltage drop, see fig. 3.13. Moreover, power consumption and thus heat generated by the device [Sohee, 2006] is minimized allowing small electrodes to generate phosphenes within safe heat limits [Horsager et al., 2011]. Despite that a safe stimulus is delivered by approaching the electrode carrier to the surface of the retina, however, surgical challenges are thus delivered to maintain the proximity as close as possible. Advance technology limits this challenge, therefore proper understanding of this matter must be considered for device implantation.

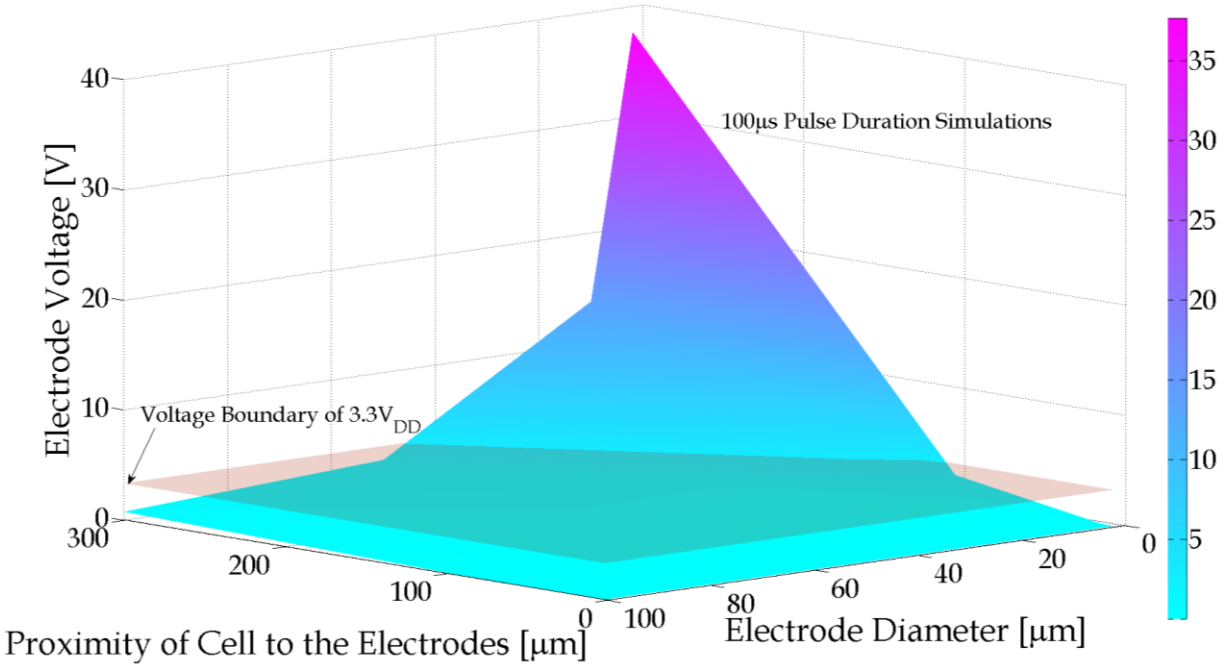


Fig. 3.13 Relationship between electrode voltage, electrode diameter and the proximity of cells to the electrodes. A voltage of  $3.3 V_{DD}$  indicates the boundary of operation. The results are related to simulations using  $100 \mu s$  pulse duration.

#### 3.4.12. Trade-off in Visual Prosthesis

The main goal of artificial vision is to provide the patient a useful visual perception. This challenge can be attained by associating precise stimulation of cells as an array of independent phosphenes created under accurate control of the electrode carrier. However, this challenge demands 1) small electrode usage to independently activate each ganglion cell and replicate natural patterns of activity in the retina and 2) proximate the electrode carrier to the surface of the retina. This is advantageous because the flow of a small current can be contained in a small volume that surrounds the cell and thus more likely to elicit a single cell [Lujan (c), 2016].

As formerly observed in fig. 3.10, harmless and harmful zones are separated at the electrode diameter of  $9.6 \mu m$  where the boundary of charge density is exceeded. This case is of pulse duration of  $100 \mu s$  and proximity of cells to the electrodes of  $100 \mu m$ .

As an exemplary case, our FEM-based model was simulated with proximity of  $300 \mu m$  and monophasic rectangular pulse applied within pulse duration of  $100 \mu s$ , see fig. 3.14. As the distance of cells to the electrodes increases, the injected current and thus charge density and electrode voltage rise for cell activation. Therefore, electrochemical safety suggests increasing electrode diameter in order to reduce 1) electrode impedance and 2) charge density injection.

Thus, a concern of this magnitude implies a trade-off with respect to precise stimulation of cells (array of independent phosphenes) and electrochemical safety. Current artificial vision devices approved by federal agencies safeguard their long-term performance of electronics by implanting large-sized electrodes of  $200 \mu m$  [Humayun et al., 2012],  $100 \mu m$  and  $360 \mu m$  [Hornig, 2007] and  $100 \mu m$  [Roessler, 2009]. Thus, for achieving precise stimulation, the distance of the electrodes towards the cells is crucial for guaranteeing safe delivery of stimulus.

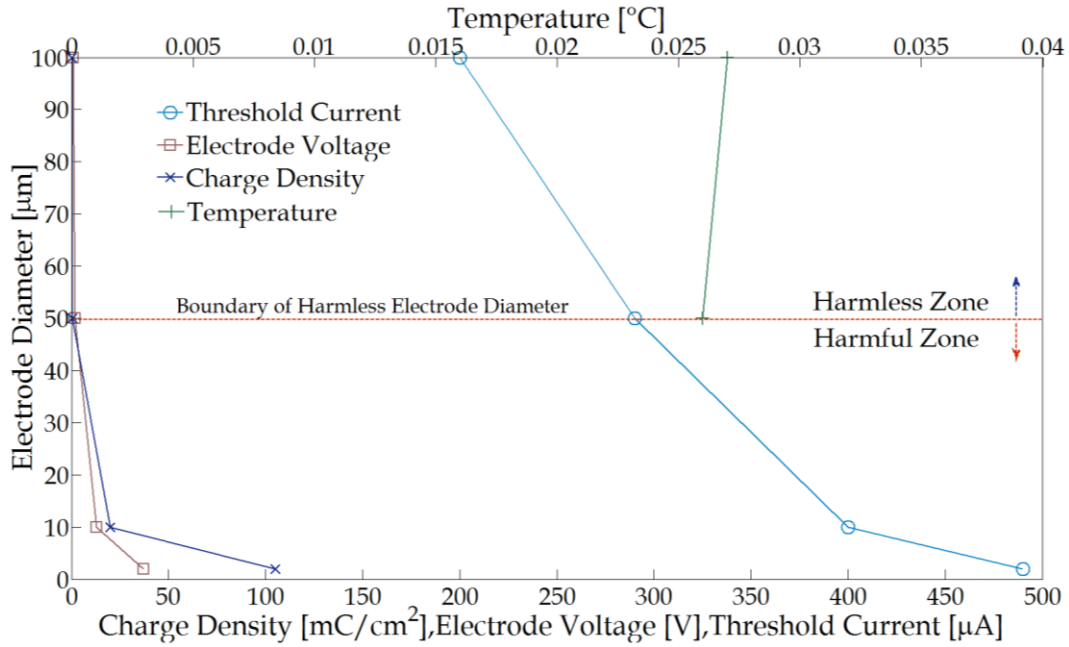


Figure 3.14 Electrode diameter relationship with charge density, electrode voltage, threshold current and temperature increase at the device. Here, pulse duration of 100  $\mu\text{s}$  and proximity 300  $\mu\text{m}$  of cell to the electrodes were used. Safe charge density of 1  $\text{mC}/\text{cm}^2$  was applied. Harmless and harmful zones are separated at the electrode diameter of 50  $\mu\text{m}$  where the boundary of charge density is exceeded. Rectangular pulse was simulated.

### 3.5. Outline for the High-level Theoretical Scheme

#### 3.5.1. Domain Dimensions and Domain Definitions

The threshold currents delivered by a simple square grid electrode distribution have a strong correlation to experimental outcomes. First, their tendency along the proximities in simulations is consistent with experimental outcomes [Jensen, 2005], see fig. 3.12. Second, despite that the experimental setup was carried out with different input variables and the proximity of the cells to electrodes was not given, the experiments conducted by [Jensen, 2005] and [Schwahn et al., 2001] generated results comparable to ours. Third, the comparison of the peak voltage across the electrodes with [Meza et al., 2014] delivered accurate agreement, see table 3.7. This suggests that experimental data of electrodes coated with some material can be fitted in a circuit modelling using passive elements, see section 3.3.2.2. Accordingly, the sequence of the domains, their sizes and parameters earlier defined (i.e. conductivity and permittivity), also the definitions of the biocompatible coating material used (PEDOT-NaPSS) can deliver accurate results of the electric field distribution throughout the retinal tissue, see table 3.2.

#### 3.5.2. Electrode Data

A square grid distribution of 32 x 32 electrodes confirmed safety by delivering stimulus. The arrangement of enclosing the active electrode by eight guards can highlight its isolation as the stimulus is confined to a small volume around the ganglion cell. As such, the electrode cross-talk during stimulation can be minimized [Wong, 2007].

The simplified 3D retinal-model suggests the feasibility to apply an array of  $32 \times 32$  electrodes with the following requirements, i) proximity up to  $10 \mu\text{m}$ : reduce electrode diameter to  $2 \mu\text{m}$ . Maximum output voltage of operation of 1V. Work with either 50 or  $100 \mu\text{s}$  low pulse duration.  $11.3 \text{ mm}^2$  electrode carrier area; ii) proximity up to  $100 \mu\text{m}$ : reduce electrode diameter to  $14 \mu\text{m}$  only with  $100 \mu\text{s}$  pulse duration. For  $50 \mu\text{s}$ , electrode diameter should be  $18 \mu\text{m}$ . Maximum output voltage of operation of 1 V for both cases. This means a better freedom of choosing a CMOS process. Carrier area consists of  $14 \text{ mm}^2$  for electrode diameter of  $14 \mu\text{m}$  and  $15 \text{ mm}^2$  for  $18 \mu\text{m}$ . Each configuration works with PEDOT-NaPSS electrode deposition and circular electrodes. These results are valid for a constant electrode distance of  $100 \mu\text{m}$ , safe temperature increase of  $1^\circ\text{C}$  and charge density limits of  $0.35 \text{ mC}/\text{cm}^2$ .

### 3.5.3. Proximity of the Cell to Electrodes

To avoid further issues caused by implantation of an epi-, sub-retinal or suprachoroidal implant, the proximity of cell to the electrodes plays a major role for a successful retina implant. One of the major limitations, however, is attributed to the charge density required elicit a train of spikes at the ganglion cell and to elicit activity in neurons at the retina. Heat dissipated by the device has lower values which can be attributed to use duty cycle during stimulation and hybrid architecture at the stimulator device which lowers the power consumption [Meza, 2014].

The results indicated that electrode size mainly depends on the proximity of cells to the electrodes. Large-sized electrodes are a characteristic when proximity increases because high current and thus high current density is needed to activate nearby cells. This increase is a well-known problem that is particularly visible in the first postoperative weeks [Mahadevappa et al., 2005]. Large electrode usage is a requirement to ensure electrochemical safety. This technique is frequently used in current visual devices [Eger et al., 2006; Mahadevappa et al., 2005; Rizzo III et al., 2003; Humayun et al., 2012; Klauke et al., 2011]. However, packages of cells are activated by a single electrode leading to a low visual resolution. Reducing electrode diameter will lead to an activation of small groups of cells. This will result in high resolution patterns. Depending on the reduction of electrode diameter, this may also involve a trade-off of exceeding electrochemical boundaries at some proximity.

### 3.5.4. General Outline

The simplified 3D computational model suggested basic relationships and parameters for the development of an advanced technique that addresses pixel-wise vision. In general, an array of  $32 \times 32$  electrodes with square-grid distribution,  $100 \mu\text{m}$  of proximity or below and electrode size of  $14$  and  $18 \mu\text{m}$  can deliver safe stimulus for pulse duration of 100 and  $50 \mu\text{s}$ , respectively. This is valid for a limit of  $0.35 \text{ mC}/\text{cm}^2$ . For a limit of  $1 \text{ mC}/\text{cm}^2$ , however, electrode size of  $10 \mu\text{m}$  is adequate for both pulse durations.

Experimental outcomes of [Jensen, 2005] regarding thresholds for the activation of cells and [Meza et al., 2014] regarding peak electrode voltage yielded comparable results with our simulations. Thus, the high-level scheme can replicate the domain geometries and definitions used in previous simulations. Charge density must be subjected to a thorough minimization for ensuring safe delivery of stimulus. A system can be realized with an attachment of 16 existing scalable chip of 64 electrodes [Meza, 2014]. Coating electrodes with PEDOT-NaPSS can boost biocompatibility and decrease electrode impedance [Starbird, 2012].

# Chapter 4

## Parameter Minimization

### 4.1.Introduction

#### 4.1.1. Lessons learnt: Basis for this Chapter

The third chapter yielded valuable understandings regarding artificial vision. One of the most significant is the viability to apply an array of  $32 \times 32$  electrodes in a single carrier. The conditions to achieve such aim are promising. An electrode diameter of 10 or 14  $\mu\text{m}$  is adequate for pulse duration of 100  $\mu\text{s}$  using limits of 1 and 0.35  $\text{mC}/\text{cm}^2$ . As such, high resolution patterns elicited by stimulation can be enhanced by reducing electrode diameter [Cai, 2011]. This configuration can yield safe stimulus up to 100  $\mu\text{m}$  of proximity of cells to the electrodes. Maximum output voltage of operation of 1 V for both cases, meaning a better freedom of choosing a CMOS process [Lujan (a), 2016].

Having argued in the previous chapter, the 3D computational model implemented in Comsol gave accurate results of threshold currents and voltage, see fig. 3.12 and table 3.7, respectively. The definitions of the domains formerly stated can deliver accurate results of the electric field distribution throughout the retinal tissue. A system realization can be achieved by using an existing 16 scalable chip attachment of 64 electrodes each with daisy chain configuration [Meza, 2014]. PEDOT-NaPSS coat deposition can be used to enhance biocompatibility and reduce electrode impedance [Starbird, 2012]. Despite that threshold currents were found to increase with the rise of proximity of cells to the electrodes, the requirements of applying a  $32 \times 32$  array of electrodes within 100  $\mu\text{m}$  of proximity are still promising.

Chapter three provided several limitations. One of those in retinal prosthetics is the charge density required to activate a single cell. Safeguarding the operation of stimulators and of the sensitive tissue is by far most a crucial issue in neural activation. Thus, parameter minimization of this value must be present in the design of retinal implants. As a result of the neural tissue heating by the implant, which I established in the last chapter, turns out not to be a constraint [Lujan (a), 2016]. This can be attributed to use duty cycle through stimulation and hybrid architecture at the stimulator device which lowers the power consumption [Meza, 2014].

#### 4.1.2. Aims

The use of small-sized electrodes has become a cornerstone in retinal implants to activate small areas of the retina and achieve pixel-wise vision [Weiland et al., 2008]. The activation of small groups of cells can be produced by using small electrode size. This would lead to high resolution patterns of prosthetic-elicited activity and improve visual reception [Fried, 2006]. This challenge, however, requires higher charge density that can cause breakdown of the electrode as well as adverse tissue reactions [Fried, 2006]. Moreover, electrode voltage is constrained by the water-voltage limits and the power consumption which can originate excessive tissue heating.

The minimization of such parameters has been previously investigated while the pulse shape and its duration are varied [Lujan (b), 2016; Meza, 2012]. This technique has generated interesting outcomes as regards prolonging battery lifetime and increasing patient safety. Here, rectangular and linear increase pulse shapes and two pulse durations are investigated in terms of charge density injection, electrode voltage and threshold current. The simplified 3D computational model of the retina is used, see fig. 3.3. The magnitudes of input stimulating parameters of the high-level scheme are given such as pulse duration and shape for the sake of delivering safe stimulus to the retinal tissue and electrode/electrolyte interfaces.

### 4.2. Pulse Shape Selection for Simulation

[Meza, 2012] analyzed the response of different pulse shapes for functional electrical stimulation. The experiments were performed by injecting a single biphasic current pulse of rectangular, sinusoidal, linear increase or linear decrease in human volunteers. Two fully gelled electrodes of sizes 45x80 mm<sup>2</sup> (PG473, FIAB) were used to contact with human skin. The muscle reaction was measured with an accelerometer. Despite that pulse train is a requirement to perform stimulation for real-like applications; however, the scope of this report was to compare the properties of different pulse shapes based on charge delivered to the body. The reasons for using a single pulse is to trigger only a single action potential and to leave out other parameters as interphase distance between pulses or width of the train. The use of an accelerometer gives a quantitative metric to compare the muscle reaction against stimuli with the different waveforms. The results of charge, left  $y$ -axis, and voltage, right  $y$ -axis, are shown in fig. 4.1. The pulse duration shown in the  $x$ -axis corresponds to a full width of biphasic pulse. As such, the results indicated that single linear increase pulse shape of pulse duration lower than 0.15 ms (i.e. one-half of the full pulse width) delivers lower charge than rectangular, sinusoidal and linear decrease. Irreversible Faradaic reactions, i.e. gas-bubble formation and electrolysis of water may be avoided by changing the pulse shape to linear increase.

[Jezernik et al., 2005] derived an energy-optimal pulse shape based on an analytical nerve membrane model and optimal control theory of dynamical systems. As their assumptions were



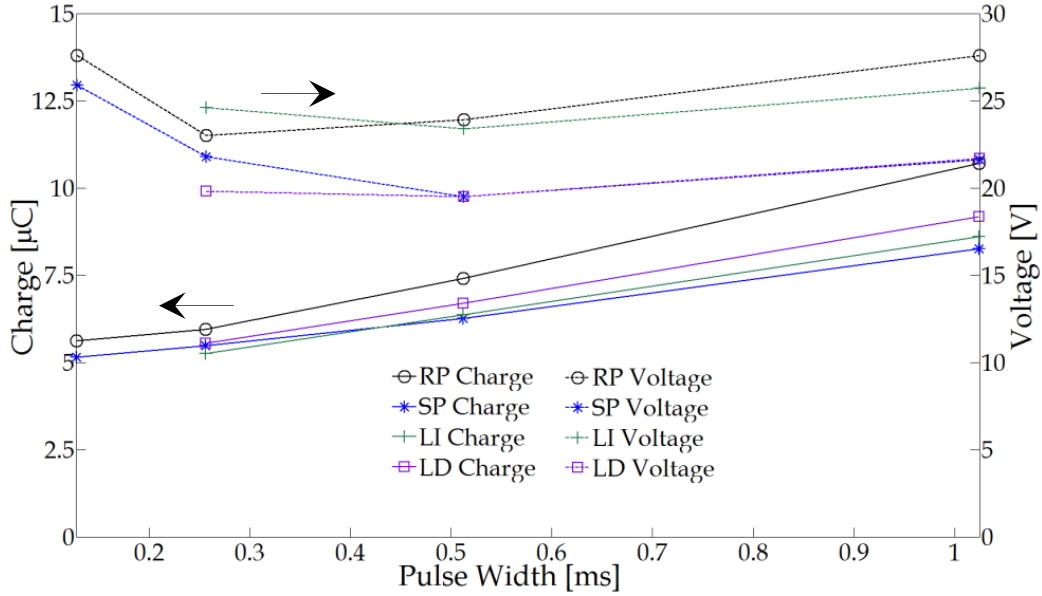


Fig. 4.1 Charge and voltage responses of experimental stimulation in human volunteers. RP: rectangular pulse, SP: sinusoidal pulse, LI: linear increase pulse, LD: linear decrease pulse shapes. Data points from [Meza, 2012].

a single nerve fiber somewhere placed in space and electrically stimulated by a *point* electrode, the boundary problem of the cross-section area of electrode and cell was neglected. As such, an exponentially increasing pulse shape was derived with

$$\chi = \frac{g_m}{C_m}, \quad (4.1)$$

$g_m$  is the membrane conductance of 30.4 mS/cm<sup>2</sup>, and  $C_m$  is the membrane capacitance with a normal value of 2 μF/cm<sup>2</sup>. The 'optimal' pulse shape is given by

$$i^* = \frac{g_m V_{th}}{\sinh(\chi \cdot t_f)} e^{\chi \cdot t}, \quad (4.2)$$

$t_f$  is the final time of stimulation, i.e. pulse width,  $V_{th}$  is the threshold voltage and  $t$  is the time.

[Lujan et al., 2015] performed an experimental study of transcutaneous stimulation to compare the 'optimal' pulse shape indicated in eq. (4.2) with the widely-used rectangular pulse. Experimental setup consisted on measuring energy dissipation, charge delivering and current injected for each pulse shape with one human volunteer. So far nobody has, to our knowledge, tried to apply exponentially increasing waveforms at experimental transcutaneous stimulation on a human subject.

Fully gelled electrodes of size 30 x 30 mm<sup>2</sup> were placed on top of the extensor muscles in the forearm of the volunteer. A stimulator device built at the Institute of Nano and Medical Electronics at the TUHH provided first anodic then cathodic biphasic rectangular and exponentially increasing pulse shape derived in that study. Visual observation of two experts was used to monitor muscle contraction. In this experiment, exponentially increasing pulse shape was drawn using Matlab and transmitted to the stimulator device via serial port. The time constant used is 26.7 s<sup>-1</sup> with a membrane capacitance of 1.5 μF/cm<sup>2</sup>.

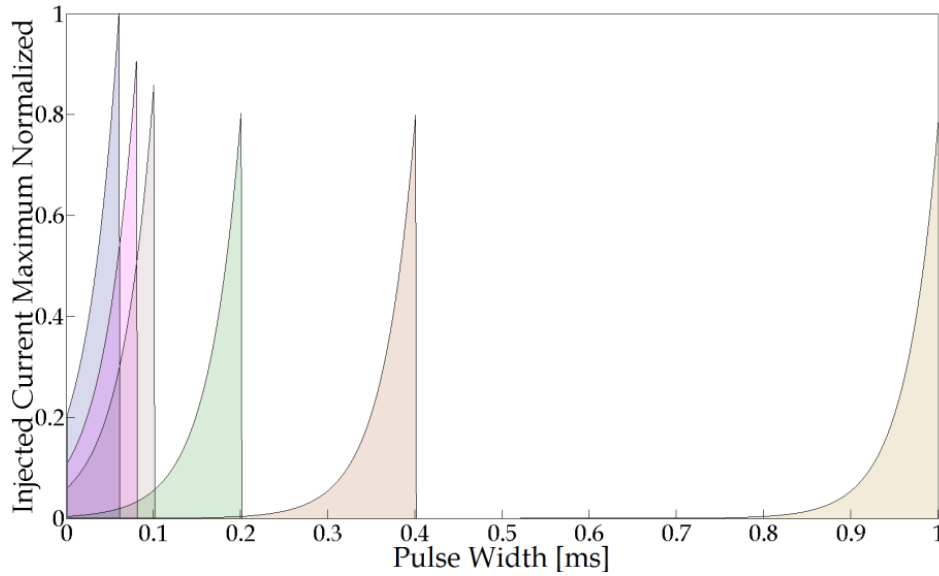


Fig. 4.2 Current injected by exponentially increase pulse shape. Results are normalized based on the maximum value of current injected. Data points from [Lujan et al., 2015].

Figure 4.2 displays the exponentially increasing pulse shape injected (maximum normalized). The experimental results of energy, left  $y$ -axis, and charge, right  $y$ -axis, for rectangular and exponentially increasing pulse shape are indicated in figure 4.3. Strength duration curve for both pulse shapes are illustrated in figure 4.4. Shown in that figure, the rectangular pulse was superior with minimum energy of  $17.1 \mu\text{J}$  at  $60 \mu\text{s}$  pulse width, while at  $1 \text{ ms}$  pulse width, the exponentially shape reached  $19.5 \mu\text{J}$ .

Despite of the exponentially shape saving a prominent amount of energy at high pulse widths, 90 % at  $1 \text{ ms}$ , the rectangular pulse was superior at low pulse durations, i.e.  $60 \mu\text{s}$ , saving 32 %. Rectangular pulse shape saves a prominent amount of current at low pulse durations, i.e.  $60 \mu\text{s}$  reaching 58%. At high pulse width, rectangular is superior to exponentially shape saving 78% of current. Exponentially increasing shape has better charge-saving results at all pulse durations, saving 41% at  $60 \mu\text{s}$  and 92% at  $1 \text{ ms}$ .

Even though the exponentially increasing pulse shape shows low energy and less charge for high pulse widths, it is not recommended for use in practice because, 1) energy saved with respect to the minimum-energy rectangular pulse is small and does not justify the increased hardware effort to generate the exponential pulse shape; 2) peak currents of the exponential pulse shape require rather high voltages to be generated in the stimulator which may have negative effects on the hardware and/or the patient; 3) time constant at exponentially increasing pulse shape varies with subjects and can have a high impact on charge and energy delivered; 4) peak current ratio of exponentially increasing to rectangular shape is 3.3 on average, meaning that the former pulse shape may cause gas-bubbling formation using invasive electrodes.

### 4.3. Summary

Since charge density and electrode voltage have a major role to ensure safe implementation in retinal considerations, a pulse shape different than rectangular waveform is needed to decrease charge density to a feasible extent. Such pulse shape should not increase hardware effort to

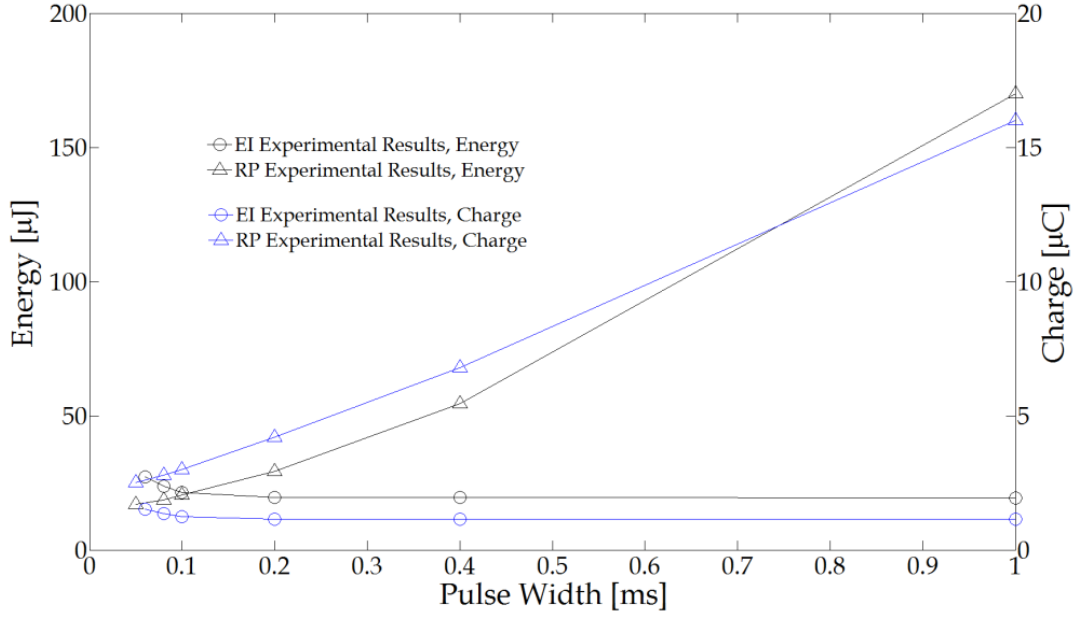


Fig. 4.3 Energy and charge comparison between exponentially increase and rectangular pulse shapes. Data points from [Lujan et al., 2015]

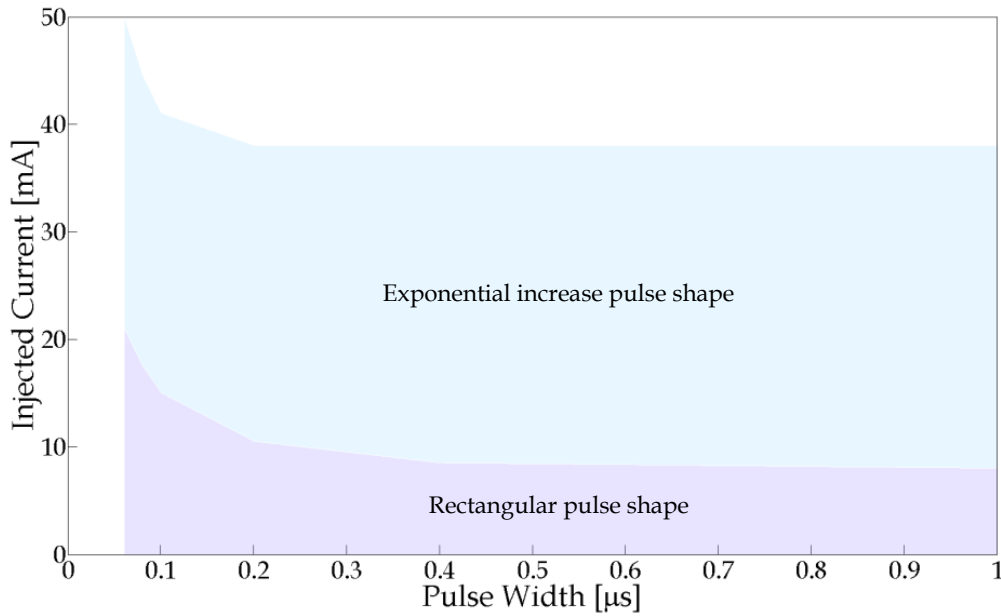


Fig. 4.4 Injected current comparison between exponentially increase and rectangular pulse shapes. Data points from [Lujan et al., 2015].

reproduce and the generated voltages of the stimulator should not have negative effects on the hardware and/or the patient. Experimental findings [Meza, 2012] demonstrated that linear increase delivers lower charge than rectangular, sinusoidal and linear decrease, see fig. 4.1. Simulation-based findings support this evidence, fig. 4.3.

Thus, a study was performed to compare rectangular and linear increase pulse shapes. The main objective is to compare charge injection capacity between pulse shapes. Voltage window, threshold current and the increase of heat at the device was included in the study.

## 4.4. Methods

### 4.4.1. Ganglion Cell Simulation – Matlab (Refer to Section 3.3.2.4)

The extracellular peak-threshold current density ( $J_E$ ) was found by injecting current density to the ganglion cell model [Fohlmeister, 1989]. Here, rectangular and linear increase pulse shapes were tested with pulse duration of 50, 100  $\mu$ s. The results of strength duration curve of rectangular shape are 330 and 120  $\mu$ A/cm<sup>2</sup> for 50 and 100  $\mu$ s, respectively. At linear increase pulse shape, the outcomes are 340 and 160  $\mu$ A/cm<sup>2</sup> for the respective pulse durations. Pulse durations lower than 150  $\mu$ s are analogous in [Fried, 2006] to directly stimulate the ganglion cell and to elicit solely a single spike with precise temporal pattern.

### 4.4.2. FEM-based Model Simulation – Comsol (Refer to Section 3.3.2.5)

Electrode distance is constant with a value of 100  $\mu$ m. Proximity of cell to electrodes was varied with values of 2, 10 and 100  $\mu$ m. Pulse duration was varied with values of 50 and 100  $\mu$ s. Electrode diameter tested are 2, 10, 50 and 100  $\mu$ m and are analogous to [Fried, 2006; Rizzo III, 2003; Werginz, 2004; Cai, 2011]. Each variable was varied to analyze i) possibility of gas-bubbling formation due to charge density, ii) possibility of corrosion caused due to voltage across the electrodes, iii) injected current to the retinal tissue.

In previous published works there has been sufficient evidence that monophasic pulse allows the formation of Faradaic reduction reactions. If oxygen is present, these reactions may include reduction of oxygen and formation of reactive oxygen species associated in tissue damage. Although monophasic is the most efficient pulse for stimulation because of the action potential initiation and the potential becomes insufficiently positive (using cathodic pulses) where electrode corrosion may occur, however, it is not used in continuous pulses where tissue damage is to be avoided [Merrill, 2005]. In our study, however, monophasic rectangular and linear increase shapes were used with a single anodic pulse for the sole intention to reduce the computational time consumed. Once the threshold current was found, charge density, electrode voltage, power consumption and the increase of heat at the device were calculated as explained in section 3.3.2.6, 3.3.2.7 and 3.3.2.8, respectively. As such, the results were compared with their own harmful limits of 1 mC/cm<sup>2</sup>, 1°C [Singh, 2008] and 1.7 V [Duay, 2012].

## 4.5. Results

Figures 4.5 and 4.6 display the threshold charge density, threshold current and electrode voltage at bottom  $x$ -axis. Heat increase at the device is shown at top  $x$ -axis. Each plot shows the results for a specific cell to electrode distance. The results of monophasic linear increase pulse shape for pulse duration of 50 and 100  $\mu$ s are shown with proximity of 100  $\mu$ m. For more information of proximities 2 and 10  $\mu$ m, see original manuscript in [Lujan (b), 2016]).

Figure 4.7a and 4.7b show the comparison of threshold current and threshold charge density of monophasic rectangular and linear increase pulse shapes. Here only the outcomes of the cell to electrode distance of 100  $\mu$ m are illustrated. Figure 4.8 displays the comparison of electrode voltage between rectangular and linear increase waveforms.

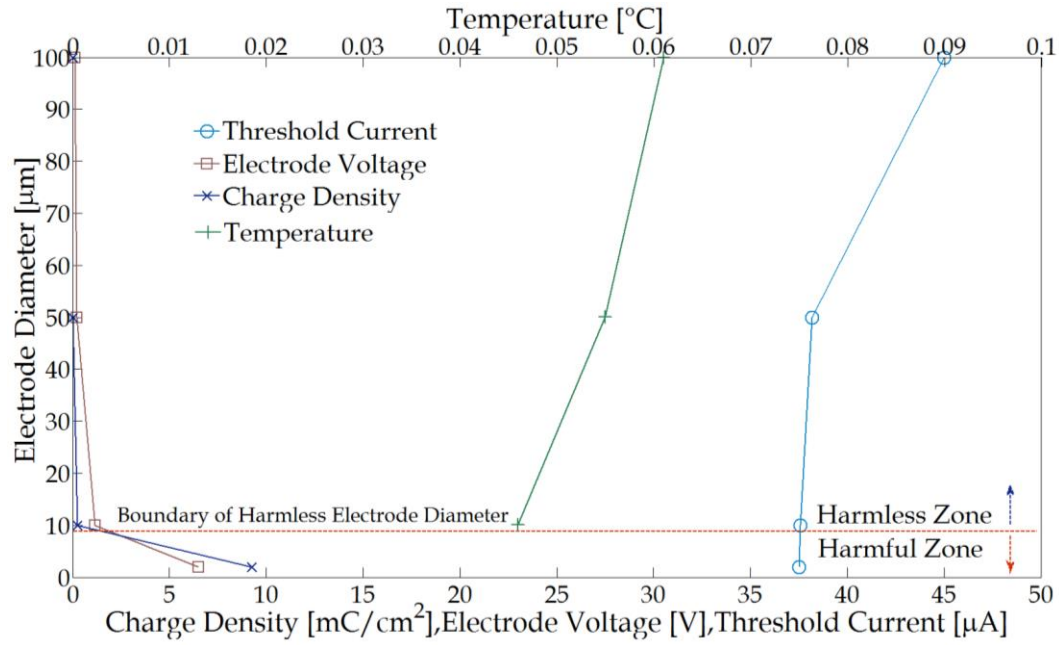


Fig. 4.5 Electrode diameter relationship with charge density, electrode voltage, threshold current and temperature increase at the device. Here, pulse duration of 50  $\mu\text{s}$  and proximity 100  $\mu\text{m}$  of cell to the electrodes were used. Safe charge density of 1  $\text{mC}/\text{cm}^2$  was applied. Harmless and harmful zones are separated at the electrode diameter of 9.3  $\mu\text{m}$  where the boundary of charge density is exceeded. Linear increase pulse was simulated. Data points from [Lujan (b), 2016].

## 4.6. Discussion

### 4.6.1. Electrochemical Safety

#### 4.6.1.1. Charge Density Limitations

The outcomes of our simulation suggest that is safe to inject current density using linear increase pulse shape with electrode sizes from 2 to 100  $\mu\text{m}$  and pulse durations of 50 and 100  $\mu\text{s}$  within proximity of cell to the electrode below 10  $\mu\text{m}$ . For more information on the results of such proximity of the cell to the electrodes, see [Lujan (b), 2016]. This simulation-based finding assumes PEDOT voltage window limit of 1.7 V, a theoretical safe charge density of 0.35  $\text{mC}/\text{cm}^2$  for gas-free and erosion-free operation and 1  $\text{mC}/\text{cm}^2$  for neural damage.

Our simulation-based observations also suggest that electrode diameter of 9.3  $\mu\text{m}$  is sufficient for delivering safe stimulus to the retina using linear increase pulse shape. This result is related to proximity lower than 100  $\mu\text{m}$ , see fig. 4.5 and 4.6. This suggestion applies to both 50 and 100  $\mu\text{s}$  pulse duration. In such figures, harmless and harmful zones of retinal stimulation are separated at the electrode diameter where the boundary of charge density is exceeded.

Linear increase pulse shape delivers a better response than rectangular related to threshold charge density, see fig. 4.7b. Charge density reduces up to  $40 \pm 2.4\%$  in average by applying 50  $\mu\text{s}$  pulse duration in practice. As for 100  $\mu\text{s}$ , threshold charge density decreases  $30 \pm 1.3\%$  (for more information, see [Lujan (b), 2016]). For real-case applications related to retinal implants, linear increase usage means a promising technique to avoid irreversible Faradaic reactions. Although that linear increase distributes the stimulus with low charge density, though, rectangular pulse

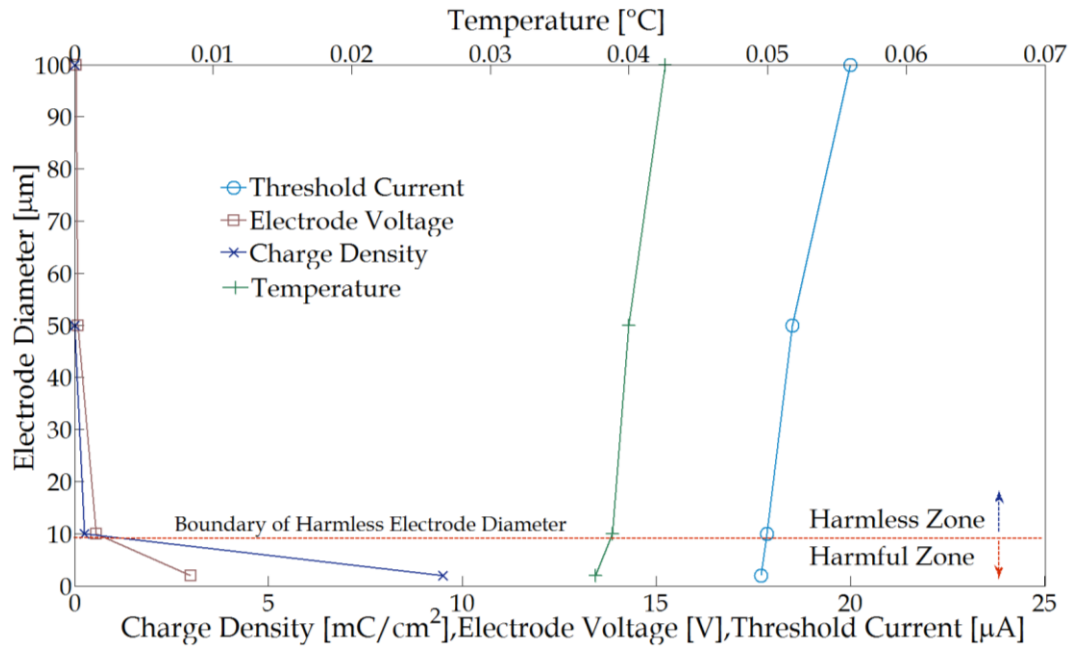


Fig. 4.6 Electrode diameter relationship with charge density, electrode voltage, threshold current and temperature increase at the device. Here, pulse duration of 100  $\mu$ s and proximity 100  $\mu$ m of cell to the electrodes were used. Safe charge density of 1  $\text{mC}/\text{cm}^2$  was applied. Harmless and harmful zones are separated at the electrode diameter of 9.3  $\mu$ m where the boundary of charge density is exceeded. Linear increase pulse was simulated. Data points from [Lujan (b), 2016].

shape shows a safe delivery with electrode diameter of 2  $\mu$ m, 50  $\mu$ s or 100  $\mu$ s pulse duration and cell-electrode distance lower than 10  $\mu$ m (data not shown; see [Lujan (b), 2016]).

As formerly stated, the proximity of cells to the electrodes plays a major role in visual prosthetic to activate nearby cells. A closer proximity of the cells to the electrodes reduces threshold current and the charge density. Despite that a safe stimulus is delivered from the electrodes by approaching the electrode carrier to the surface of the retina, however, a surgical challenge is thus delivered to maintain the proximity as close as possible. The constraint of the distance of cells to the electrode is shown in fig. 4.7b where charge density is attributed as the main limitation for activation nearby cells. Here, the proximity tested is 100  $\mu$ m. For more information of proximities 2 and 10  $\mu$ m, see original manuscript in [Lujan (b), 2016]. Table 4.1 lists the minimum electrode diameter that can be used with their corresponding limit. Green boxes indicate the suitability to use the minimum electrode diameter tested of 2  $\mu$ m. For achieving a better response in continuous pulses, charge-imbalanced biphasic waveform provides a method to reduce the irreversible charge density as reactions occurring in one phase (cathodic or anodic) are reverse in the following [Merrill, 2005].

TABLE 4.1  
Charge Density Limits for Rectangular/Linear Increase Pulse Shapes. Data from [Lujan (b), 2016].

Proximity of Cell to Electrodes	0.35 $\text{mC}/\text{cm}^2$ limit		1 $\text{mC}/\text{cm}^2$ limit	
	50 $\mu$ s	100 $\mu$ s	50 $\mu$ s	100 $\mu$ s
2 $\mu$ m	Yes/Yes	Yes/Yes	Yes/Yes	Yes/Yes
10 $\mu$ m	Yes/Yes	Yes/Yes	Yes/Yes	Yes/Yes
100 $\mu$ m	18/9.9 $\mu$ m	14/9.9 $\mu$ m	9.7/9.3 $\mu$ m	9.6/9.3 $\mu$ m

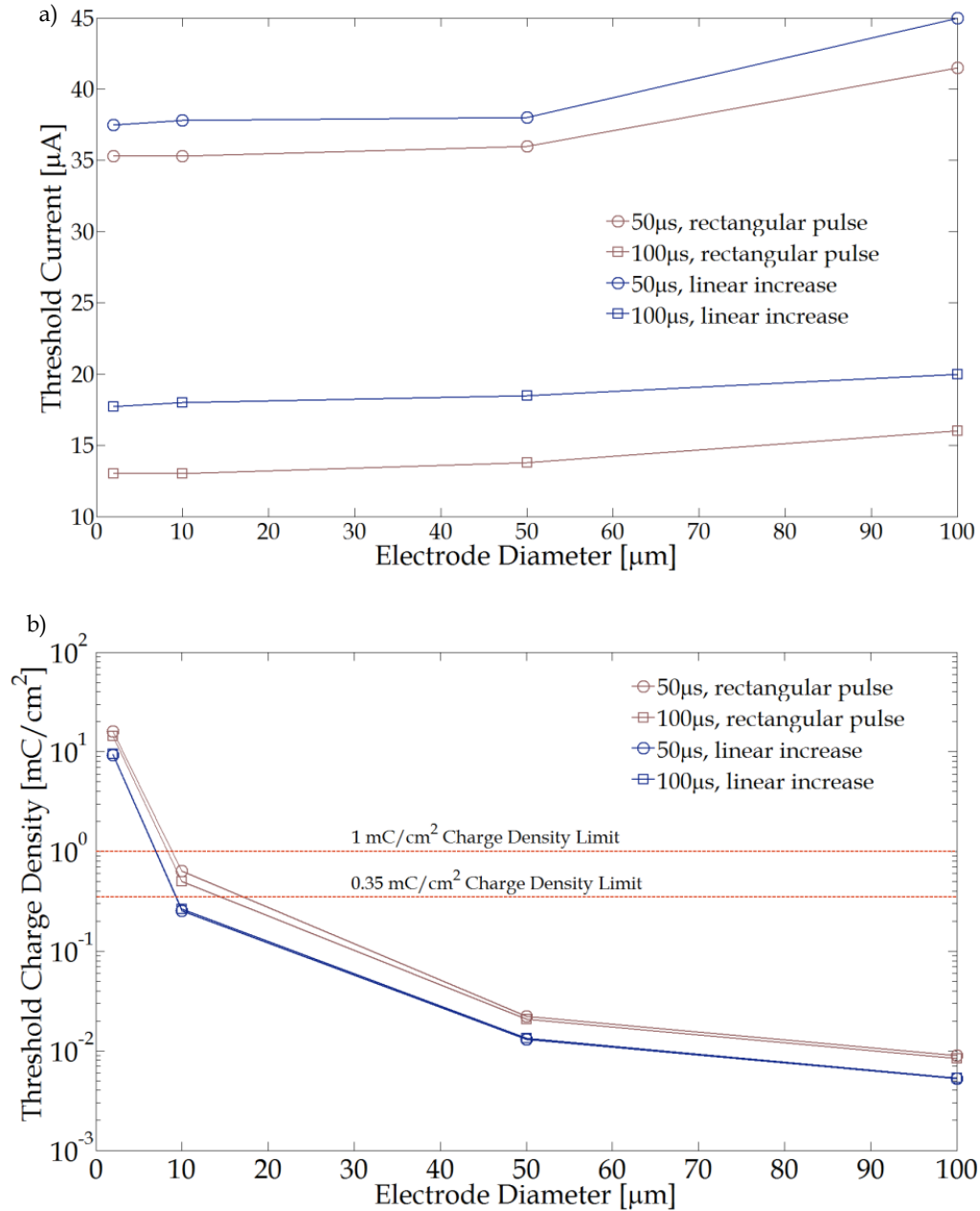


Fig. 4.7 a) Threshold current and b) threshold charge density for 100  $\mu\text{m}$  cell-electrode distance. Data points from [Lujan (b), 2016].

#### 4.6.1.2. Electrode Voltage

Our simulation-based findings show that 100  $\mu\text{s}$  pulse duration was inferior than 50  $\mu\text{s}$  with minimum electrode voltage, saving 63% and 54% for both rectangular and linear increase pulse shapes, respectively; see fig. 4.8. In spite of this technique may avoid corrosion, the constraint of voltage window limit originates mainly when cell-electrode distance is greater than 10  $\mu\text{m}$  (for more information, see [Lujan (b), 2016]). For attaining a better response in successive pulses, the charge-imbalanced waveform has advantages in avoiding corrosion by decreasing the maximum positive potential since the anodic phase is no longer constrained to be equal to the

cathodic phase as charge-balanced pulse, thus the electrode potential reaches less positive values [Merrill, 2005; Scheiner, 1990].

Table 4.2 lists the minimum electrode diameter that can be used for the corresponding limit. Green boxes indicate the suitability to use the minimum electrode diameter tested of 2  $\mu\text{m}$ .

TABLE 4.2  
Voltage Limits for each Pulse Shape. Data from [Lujan (b), 2016].

Proximity of Cell to Electrodes	Rectangular		Linear Increase	
	50 $\mu\text{s}$	100 $\mu\text{s}$	50 $\mu\text{s}$	100 $\mu\text{s}$
2 $\mu\text{m}$	Yes	Yes	Yes	Yes
10 $\mu\text{m}$	Yes	Yes	Yes	Yes
100 $\mu\text{m}$	9 $\mu\text{m}$	4.42 $\mu\text{m}$	9.2 $\mu\text{m}$	6.3 $\mu\text{m}$

It should be noted the fact that irreversible processes might occur at potentials within the voltage window, such as irreversible oxygen reduction, as opposed to the opinion in many studies that states reversible charge storage capacity, or  $Q_{\text{INJ}}$ , can be applied without the electrode potential exceeds the voltage window during pulsing [Merrill, 2005]. Therefore,  $Q_{\text{INJ}}$  and voltage window limits need to be analyzed separately.

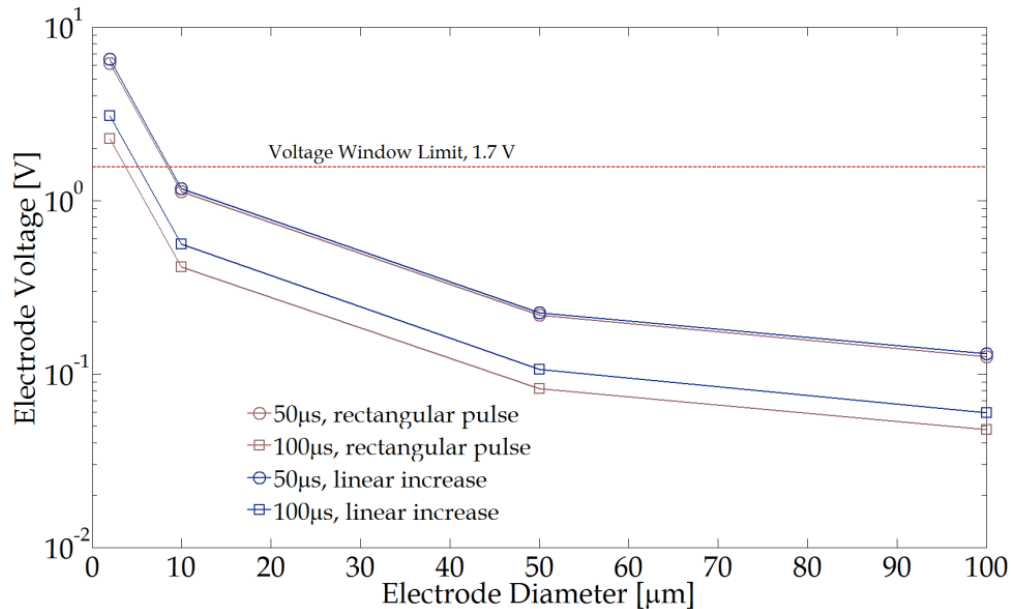


Fig. 4.8 Electrode voltage for 100  $\mu\text{m}$  cell-electrode distance. Data points from [Lujan (b), 2016].

## 4.7. Outline for the High-level Theoretical Scheme

### 4.7.1. Pulse Shape and Duration

Exponential increase pulse shape generates high voltages in the stimulator (due an increase current peak to elicit a response) which may have negative effects on the hardware and/or the



patient [Lujan, 2015], see fig. 4.3 and 4.4. Moreover, high voltages may cause corrosion because “water window” positive (anodic) limit can be exceeded.

Experimental verification confirmed that charge delivered by linear increase pulse shape has better response than rectangular shape [Meza, 2012], see fig. 4.1. Simulation-based findings support this evidence stating that charge density is reduced up to 40% in average using linear increase at 100  $\mu\text{s}$  pulse duration. This means a promising technique to avoid irreversible Faradaic reactions [Lujan (b), 2016], see fig. 4.7b. Despite that charge density is reduced, the difference in minimum electrode diameter with rectangular pulse shape is 4 and 0.3  $\mu\text{m}$  for 0.35 and 1  $\text{mC}/\text{cm}^2$  charge density boundaries, respectively (see table 4.1, 100  $\mu\text{m}$  proximity). This does not justify the increasing hardware effort to generate linear increase pulse shape.

There is not much difference when applying 50 or 100  $\mu\text{s}$  pulse length in rectangular shape concerning charge density delivery, see figs. 3.10 and 3.11 or 4.7b. Chapter four generated similar results regarding linear increase pulse shape. On the other hand, rectangular pulse shape reduces electrode voltage up to 63% when 100  $\mu\text{s}$  pulse duration is used instead of 50  $\mu\text{s}$ , fig. 4.8. For linear increase, it is reduced up to 54%. Comparing both pulse shapes, rectangular pulse has a better response than linear increase by reducing electrode voltage up to 22% in average. Despite that, both may reduce electrode corrosion by choosing this pulse duration [Lujan (b), 2016], see fig. 4.8.

If pulse trains are needed, the charge-imbalanced waveform has added advantages in avoiding corrosion and reducing irreversible charge densities that leads to either electrode or tissue damage [Merrill, 2005]. Maximum output voltage of 1 V can be used on either rectangular or linear increase pulse shape placing the electrode array within a distance of 10  $\mu\text{m}$  of the cell to the electrodes. This means a better freedom to choose a CMOS process [Lujan (b), 2016], see fig. 4.8.

#### 4.7.2. General Outline

An array of 32 x 32 electrodes with square-grid distribution, 100  $\mu\text{m}$  of proximity or below, and electrode size of 10  $\mu\text{m}$  can deliver safe stimulus using rectangular pulse shape at duration of 100  $\mu\text{s}$ . This is valid for a limit of 1  $\text{mC}/\text{cm}^2$ . At proximities below 10  $\mu\text{m}$ , electrode size of 5  $\mu\text{m}$  is sufficient for safe stimulus for limits of 0.35 and 1  $\text{mC}/\text{cm}^2$  [Lujan (b), 2016].

Overall, the high-level scheme can replicate the stimulating parameters of rectangular pulse shape and pulse duration of 100  $\mu\text{s}$ . These stimulating parameters are suitable for reducing electrode potential and ensuring safe charge density values. Another advantage is given that nowadays the most widely used waveform for electrical neurostimulation is rectangular pulse. Electrode sizes of 5 or 10  $\mu\text{m}$  (depending on the proximity used) are suggested.

# Chapter 5

## High-level Theoretical Scheme

### 5.1.Introduction

#### 5.1.1. Lessons learnt: Basis for this Chapter

Chapter three presented a simplified 3D computational model implemented in Comsol Multiphysics. Such model provided the excitation of a single cell with the minimum threshold current needed to generate visual perceptions as seen in several experimental studies [Keserü et al., 2012; Jepson et al., 2012]. The threshold currents delivered by a simple square grid electrode distribution have a strong correlation to experimental outcomes, see table 3.6 and fig. 3.12. Experimental outcomes of peak electrode voltage by [Meza et al., 2014] yielded comparable results with our simulations, table 3.7. Thus, the sequence of the domains, their sizes and parameters earlier defined in chapter three (i.e. conductivity and permittivity), also the definitions of the biocompatible coating material used (PEDOT-NaPSS) can deliver accurate results of the electric field distribution throughout the retinal tissue, see table 3.2.

Likewise, the arrangement of enclosing the active electrode by eight guards can highlight its isolation as the stimulus is confined to a small volume around the ganglion cell. As such, the electrode cross-talk during stimulation can be minimized. [Wong et al., 2007] compared the cortical stimulation of one-and six-ground settings of current steering techniques. Experimental findings in animals suggested that six-ground setting was efficient because of the smaller area of cortical activation and of a reduction of unwanted interactions between multiple stimulation sites.

The simplified 3D neural model unveiled that mainly the charge density required to activate a cell must be carefully observed and minimized for safe delivery of stimulus. Heat dissipated by the device has lower values which can be attributed to use duty cycle through stimulation and hybrid architecture at the stimulator device which lowers the power consumption.

Likewise, it could clarify that the electrode size mainly depends on the proximity of cells to the electrodes. As the proximity increases, high current is needed to activate nearby cells leading to high current density. This increase is a well-known problem that is particularly noticeable in the first postoperative weeks [Mahadevappa et al., 2005]. As a result, large-sized electrodes are a requirement to ensure electrochemical safety. Large electrode diameter can safeguard sensitive retinal tissue against irreversible reactions at the electrode interface. This technique is frequently used in current visual devices [Mahadevappa et al., 2005; Eger et al., 2006; Rizzo III et al., 2003; Humayun et al., 2012; Klauke et al., 2011]. However, bundles of cells are activated by a single electrode leading to a low visual resolution. As such, a trade-off is exhibited between reaching a better quality of visual resolution and safety. By reducing electrode diameter, small groups of cells can be activated resulting in high resolution patterns. Depending on the reduction of electrode diameter, this involves a trade-off of exceeding charge density boundaries at some proximity. The simplified 3D model suggested basic relationships and parameters for the development of an advanced retinal-model. In general, 100  $\mu\text{m}$  of proximity or below, electrode size of around 10  $\mu\text{m}$  can deliver safe stimulus for pulse duration of 100 and 50  $\mu\text{s}$  at electrode density of around 82  $\text{mm}^{-2}$ , assuming a charge density limit of 1  $\text{mC}/\text{cm}^2$ .

Chapter four considered the results of chapter three in order to provide significant insights about a better pulse length and shape for delivering stimulus to the cells. There is evidence that short pulse length is of general interest to minimize any electrochemical reactions occurring on the electrode surface. At long pulse durations, the charge required for activation increases due to i) few redistributed charge along the length of an axon participate for shifting the membrane potential [Warman, 1992] and ii) increased sodium inactivation occurs over a period of several milliseconds [Merrill, 2005]. [Fried, 2006] suggest applying stimulus pulses lower than 150  $\mu\text{s}$  because of the fact that each pulse consistently elicited a single spike to activate neighboring cells.

Earlier chapters yielded several key-points that differentiate 50 and 100  $\mu\text{s}$  pulse duration. First, there is not much difference when applying 50 or 100  $\mu\text{s}$  pulse length in rectangular shape concerning charge density delivery, see figs. 3.10 and 3.11 or 4.7b. Chapter four generated similar results regarding linear increase pulse shape. Second, a significant improvement on electrode voltage is exhibited when comparing both pulse durations, fig. 4.8. Electrode voltage is reduced up to 63% in average by applying rectangular pulse at 100  $\mu\text{s}$  pulse duration instead of 50  $\mu\text{s}$ . For linear increase, it is reduced up to 54%. This means a promising technique to avoid electrode corrosion [Lujan (b), 2016]. Thus *pulse duration of 100  $\mu\text{s}$*  is more suitable to use because i) electrode potential is highly reduced by comparing with 50  $\mu\text{s}$ ; ii) each electrode can have different timeslot to prevent cross electrode stimulation. As such, each can be activated independently with a total image frequency of 20 fps. Duty cycle can be applied during stimulation which can reduce power consumption; iii) short pulses deliver one spike per pulse with a predicted spike latency that replicated the normal light patterns [Fried, 2006]; iv) experimental observations indicated short-current pulses of 100  $\mu\text{s}$  are preferable because passing retinal ganglion cell axons can be avoided while stimulation [Jensen, 2005]; v) experimental findings exhibited single spike responses with sub-millisecond latency which are a characteristic of direct ganglion cell activation using short pulse durations of 100  $\mu\text{s}$  and small electrodes of 15  $\mu\text{m}$  of diameter [Jepson, 2012].

Likewise, chapter four provided significant aspects that differentiate rectangular and linear increase pulse shapes. Despite that charge density is reduced up to 40% using linear increase, the difference in minimum electrode diameter with rectangular pulse shape is 4 and 0.3  $\mu\text{m}$  for 0.35 and 1  $\text{mC}/\text{cm}^2$  charge density boundary (see table 4.1, 100  $\mu\text{m}$  proximity). This does not justify the increasing hardware effort to generate linear increase pulse shape. Comparing both pulse shapes at 100  $\mu\text{s}$  pulse duration, electrode potential is reduced up to 22% in average by applying rectangular pulse, fig. 4.8. This means a suitable method to avoid electrode corrosion. As such, *rectangular pulse shape* is more suitable to use and also because is nowadays the most widely used waveform for electrical neurostimulation.

As a whole, the conclusions obtained in earlier chapters facilitated the implementation of the high-level scheme. Input geometric and stimulating parameters listed in figure 5.1 were selected based on the guidelines listed in chapters three (section 3.5) and four (section 4.7). More specifically, chapter three contributed in the domain dimensions and definitions (conductivity and permittivity), electrode data (32  $\times$  32, size, distribution), basic relationships of threshold injected current and proximity of cells to the electrodes. Chapter four contributed in pulse shape and pulse duration. These relationships were the foundation of the high-level scheme. As a result of what was learnt, this will ensure accurate results of threshold currents, high resolution patterns and safety of an array of 32  $\times$  32 electrodes while pixel-wise stimulation is reached.

### 5.1.2. Motivation

Currently, a small number of companies such as Second Sight Medical Products (SS), Retina Implant (RI) GmbH and Intelligent Medical Implants (IMI) GmbH have developed a complete visual prosthesis device. Clinical trials experiments in-vivo state that patients have perceive light, object localization, distinguish objects, motion and simple patterns of lines and letters [Keserü et al., 2012; Stingl et al., 2013; Humayun et al., 2012].

However, these trials do demonstrate that patients do not obtain such flawless pixelized sight as shown in many publications [Humayun et al., 2012; Stingl et al., 2013]. Recent clinical trials associated with Argus II developed by SS Medical Products exhibited a best measured visual acuity of 20/1260 in 7 out of 30 test volunteers [Humayun et al., 2012]. Similar conclusions have lately been reached by Alpha IMS developed by RI GmbH that reported a best visual acuity of 20/546 in 2 out of 9 test volunteers [Stingl et al., 2013].

Retinal implant devices previously stated likely activate hundreds of ganglion cells simultaneously over a particular region due to the size of the electrode used. Beyond just this coarse stimulation of cells restricts the spatial resolution, the activity generated by stimulation remains dissimilar from a healthy retina too. Those sight improvements, despite being advantageous for a sight deteriorated patient, need a significant enhancement to restore functional vision to the patients.

Spatial resolution generated by stimulation must be sufficient to distinguish faces and objects so as to be potentially useful for visual perception. Static and dynamic scenes of everyday life require a more complex scheme to reproduce natural spatial patterns of activity among cells. Decreasing electrode dimensions may provide activation of small groups of cells that lead to high resolution patterns of prosthetic-elicited activity [Fried et al., 2006]. This challenge, though, requires higher charge density that can cause breakdown of the electrode as well as adverse tissue reactions [Fried et al., 2006].

Despite some efforts, state-of-the-art electronics have cross the boundary to produce a 1000+ electrode array [Chen et al., 2013; Rothermel et al., 2008; Noorsal et al., 2012]. Although achieving high electrode density, however, questions remain about how to arrange such system to attain high-resolution vision on a consistent basis. Clinical trials are required to overcome major challenges for bioelectronics implants including long-term safety performance of implanted electronics and safe surgical implantation procedure.

## 5.2.High-level Theoretical Scheme

The high-level model is presented in fig. 5.1. It is based on a complex 3D retinal-model and on different but related algorithms that represent a stepwise refinement of electrode stimulation over single cells. As a whole, it can generate a well-defined localization of electrode stimulus and reinforce single-cell selectivity, as it is required for an array of independent phosphenes under accurate control of the electrodes. This scheme can treat randomly distributed cells inside the complex 3D model built to a greater degree of anatomical likeness.

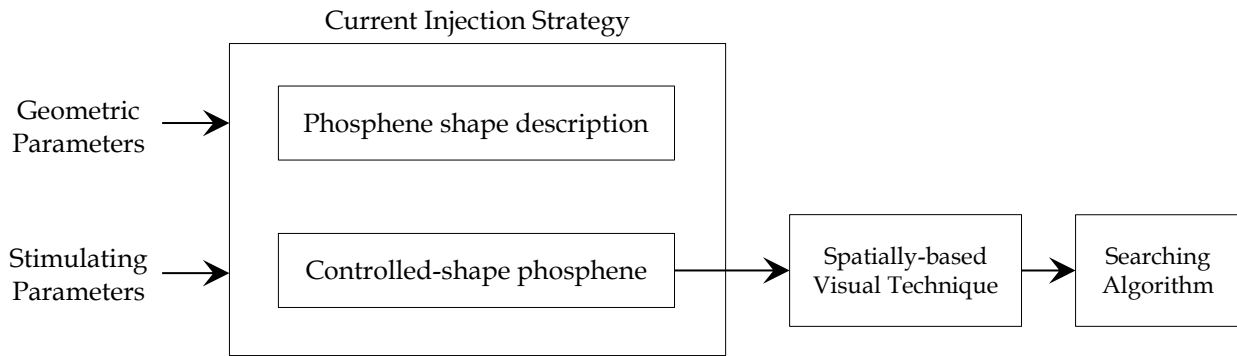


Fig. 5.1 Algorithm that represents the high-level theoretical scheme. The inputs of the scheme are geometric parameters, i.e. domain dimensions, proximity of cell to electrode, electrode data and cell location. The stimulating parameters are the injected current, pulse duration, pulse shape, and domain electrical properties. Current injection strategy is based on two approaches, phosphene shape description and controlled-shape phosphene. The visual technique investigates the best mixture of the shape of phosphenes and electrode density. The searching algorithm provides flexibility to the retinal implants to select single- or multi-site electrode stimulation.

A first overview of the scheme is as follows. The current injection strategy is designed as to meet two paths, 1) phosphene shape description based on a predefined current injection and 2) controlled-shape phosphene based on a specific current injection. Essentially, the current injection strategy is associated with the area generated by the stimulus where the injected current in effect triggers a response of some cell. This concept is called the activation area.

The high-level scheme uses the spatially-based technique and the searching algorithm each created as a thoughtful method for boosting the control of the electrodes over single cells and providing the flexibility of selecting stimulating electrode arrays for the need of specific patients, respectively. These techniques have the objective to create an array of independent phosphenes under accurate control of the electrode carrier as the electrodes stimulate single ganglion cells. Although researchers associate the stimulation of nearby cells as the definition of pixel-wise [Weiland, et al. 2014], our definition is that a single cell must be activated by a single electrode.

A thoughtful explanation of the high-level scheme is presented in four steps. *The first step* uses the phosphene shape description method to prove conclusively the activation area. This will be done by comparing clinical trials outcomes of [Keserü et al., 2012] related to perceptual thresholds and shape of visual perception. This step is essentially based on reaching a clean comprehension of the physical aspects of phosphenes generated by electrical stimulation.

*The second step* uses the controlled-shape phosphene method to narrow the shape of the activation area and to lead the required space for cell activation. The aims are providing key advantages to design optimal electrode arrays and stimulus parameters for artificial vision. A comparison based on the broadness of the area of stimulation and the number of cell activation is made between the electrode arrangement developed by Keserü and our proposal of  $32 \times 32$  electrodes with square grid distribution.

*The third step* introduces the spatially-based visual technique. The aim of such technique can be understood as enhancing the control of the electrodes to selectively activate single cells. This can be treated by constraining the space of cell stimulation using a mixture of appropriate current injection and electrode density.

*The fourth step* introduces the searching algorithm designed for the flexibility of visual devices to integrate single-site or multi-site electrode stimulation in their systems. This is required to overcome limitations generated by the proximity of cells to the electrodes, lifespan of cells and the unpredictability of their position. These realistic situations of preserved cells in patients might require adaptability to indicate a special configuration of stimulating electrode array for the need of specific patients.

## 5.3. Phosphene Shape Description – Understanding the Physical Aspects of Phosphenes

### 5.3.1. Introduction and Aims

In this section, the phosphene shape description method and the activation area are properly introduced. Clinical trial results of visual perception previously reported by [Keserü et al., 2012] will be directly compared with outcomes based on our simulation framework. Simulation-based findings related to this method are used as a valuable activation strategy to understand the causal mechanisms of phosphenes.

Prosthetic vision is built upon phosphenes [Chen et al., 2009]. A phosphene is defined as any visual sensation represented as a spot of light in the visual field caused by methods other than stimulation of the visual system by light. Phosphenes can be elicited by mechanical forces [Križaj et al., 2014], magnetic stimulation [Bonmassar et al., 2012; Walsh, 1946; Walsh, 1998] or by electrical stimulation [Humayun et al., 1996, 1999, 2003, 2004; Rizzo III et al., 1997, 2003; Mahadevappa et al., 2005; Eger et al., 2006; Klauke et al., 2011; Keserü et al., 2012].

In recent years, epi- and subretinal electrode array implants have been developed. Humayun in several publications [Humayun et al., 1996, 1999, 2003, 2004; Mahadevappa et al., 2005], [Rizzo III et al., 1997, 2003], [Klauke et al., 2011], [Eger et al., 2006] and [Keserü et al., 2012] amongst recent clinical trials [Humayun et al., 2012; Stingl et al., 2013] have reported that blind patients perceived sensations of spots of light while the retina was electrically stimulated. These experiments clearly validated the viability of producing perception of light patterns in blind patients by electrically activate nearby ganglion cells.

In recent years, Humayun et al. [Humayun et al., 1999, 2004; Mahadevappa et al., 2005], [Dobelle et al., 1974, 2000], [Zrenner et al., 2006, 2007], [Brindley et al., 1986], [Rushton et al., 1978], [Keserü et al., 2012], and [Hornig et al., 2005] have reported a viable possibility to form recognizable symbols and simple shapes from simultaneously elicited phosphenes.

Phosphenes have been observed in the form of elongated shapes [Brindley et al., 1986; Rizzo III et al., 2003], lines/bars [Rizzo III et al., 2003; Veraart et al., 1998], triangles [Veraart et al., 1998], doughnut-shaped [Humayun et al., 2003], punctuate spots of light when are close to the center of the visual field [Dobelle et al., 1974, 2000] and more complicated patterns [Veraart et al., 1998]. Phosphenes are commonly described as “round” spots of light [Humayun et al., 2003, 2004; Mahadevappa et al., 2005; Keserü et al., 2012; Rizzo III et al., 2003; Weiland et al., 2003] and carrying some color, such as red [Veraart et al., 1998], blue [Humayun et al., 2003; Rushton et al., 1978; Veraart et al., 1998], yellow [Humayun et al., 2003; Rushton et al., 1978; Veraart et al., 1998], orange [Humayun et al., 2003; Dobelle et al., 1974; Veraart et al., 1998] and multicolor [Veraart et al., 1998].

Visual prostheses would ideally reproduce accurately natural spatiotemporal patterns of activity in ganglion cells which requires the capacity of each electrode to reach nearby cell selectively [Jepson et al., 2014]. This can be understood as a transmission to the brain of different characteristics from a narrow portion of the visual space because ganglion cells are tightly-packed at the ganglionic layer, mainly at the fovea.

Forasmuch as phosphenes are the single elementary building block in visual prostheses, investigators have sought to create richer and more complex patterns to represent visual scenes while the retina is electrically stimulated. As such, the foremost concern in advanced visual prosthetics and current status on clinical trials lies in that atypical patterns of retinal activity are induced by stimulation [Humayun et al., 2012; Stingl et al., 2013].

Large diameter of stimulating electrodes in such implanted devices [Mahadevappa et al., 2005; Eger et al., 2006; Rizzo III et al., 2003; Humayun et al., 2012; Stingl et al., 2013] likely activates hundreds or thousands of cells over their area of stimulation. Not only does this coarse stimulation of cells restrict detailed perception, but also the activity generated by stimulation remains dissimilar to the healthy retina [Horsager et al., 2011].

Moreover, current strategies in existing implanted devices for reaching single-cell selectivity are proven inadequate [Humayun et al., 2012; Stingl et al., 2013]. To evoke a narrow visual spot of light that resembles a natural signal to the brain, each electrode should activate a single cell. This can provide a building block for the pattern of visual phosphene [Andrew et al., 2015].

As artificial vision is currently in an early-stage of maturity, the physical basis of phosphenes in prosthetic vision demands a better understanding. Visual perception is often considered as sufficient and as potentially useful once faces and objects are distinguishable. Together with a grasp of attaining single-cell stimulation would be then a requirement to align retinal prosthesis with a high-stage of maturity.

### 5.3.2. Proof of Concept

#### 5.3.2.1. Definition of Activation Area

The activation area main goal is to argue for its applicability as a tool for defining a space where the stimulus initiated at the active electrode in effect triggers a cell response. Amongst of

all purposes, the activation area can estimate the broadness of the region of stimulation, the amount of cells activated and the shape of visual perception.

The criterion for the applicability of the activation area states that a cell located inside the activation area is activated by the respective electrode. Otherwise, the cell is not activated by this electrode. Thus the activation area is defined as a triggering boundary where the spreading current across the electrodes is high enough to stimulate a response of some ganglion cell.

For instance, the activation area associated to the flexible film electrode carrier developed by Keserü and colleagues is used for a specific charge density injected by the electrodes, see figs. 5.2 and 5.3.

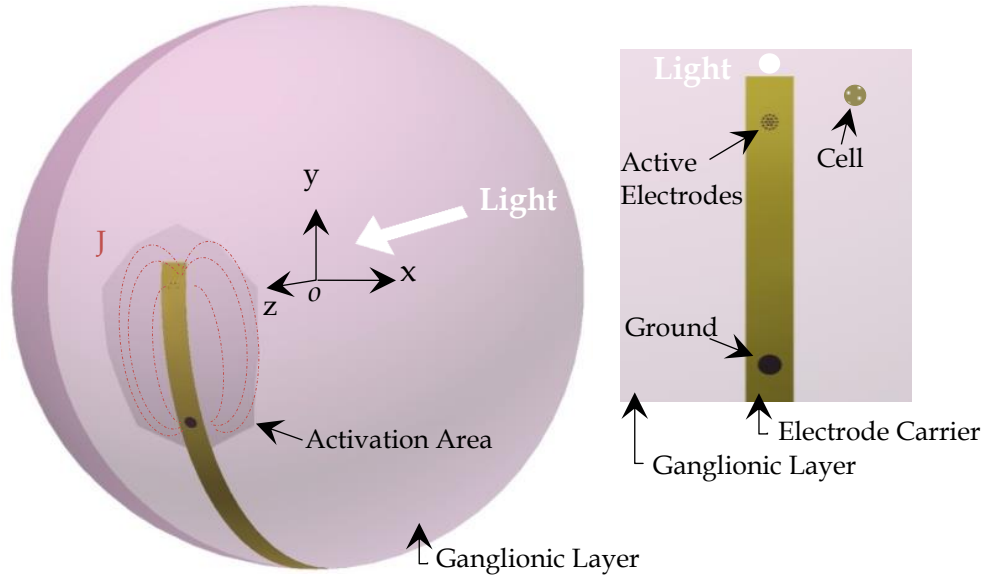


Fig. 5.2 Activation area related to the flexible film electrode carrier by applying some charge density. The shape of the activation area is associated to the spread of current throughout the medium to the electrode ground. The broadness is related to the amount of peak charge injected. AutoCAD software was used for the creation of this figure. Data from [Lujan et al., 2017].

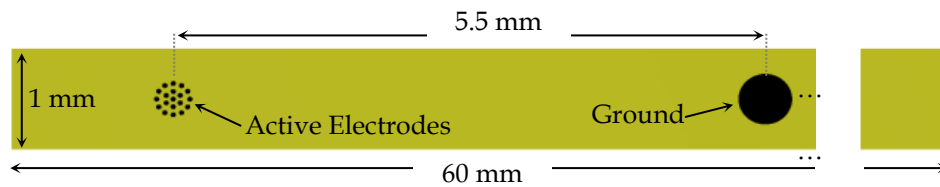


Fig. 5.3 Electrode carrier with an effective electrode diameter of 50, 200 and 360  $\mu\text{m}$ . Data from [Keserü et al., 2012].

In this figure, multiple electrode stimulation injects current density so as to trigger a response of some ganglion cell. The shape of the activation area is related to the spreading direction of current density from the active electrodes to the ground. The broadness of the activation area has a close relationship with the amount of peak current injected to the electrode for a given set of stimulating parameters.

The current density spreads throughout the medium that consists of layers of tissue. At the location of the electrodes, the intensity of the current density has its highest degree. As the



distance from some point to the electrodes increases, the current density becomes insufficient to trigger a response of the cell and the activation area is brought to an end. Therefore the visual sensations or phosphenes generated by artificial stimulation can be associated to the activation area.

Prior to device implantation in the retina, simulation-based findings of the activation area can be beneficial to understand lifelike situations of phosphenes. Accordingly the physical aspects related to the generation of phosphenes in prosthetic vision can be better understood by applying in practice the activation area.

### 5.3.2.2. Benefits of Activation Area

The activation area can yield key advantages to design optimal electrode arrays and stimulus parameters for artificial vision.

Within all the purposes of the activation area, its application can lie anywhere on the wide range of concerns related to visual prosthetics. In essence, the leading struggle to date of the visual prosthesis is to induce natural patterns of retinal activity generated by stimulation [Humayun et al., 2012; Stingl et al., 2013]. This challenging concern is related to the detail perception of artificial vision that requires electrode enhancement strategies to attain nearby cell activation [Jepson et al., 2014; Weiland et al., 2014].

The difficulties associated with pixelized visual perception and detail perception are associated with the formerly stated challenge. Essentially, the appropriateness of the activation area can address these particular issues.

For a particular set of stimulating electrodes, i.e. their sizes, the amount, and the configuration for activation, e.g. single or multiple electrode stimulation, a specific strategy for activation can be reached using the activation area. As such, the activation area can yield a discrimination of the area in which a stimulus would spread through the medium to the ground electrode.

For each stimulating electrode, the size of its activation area should be such that stimulation of a single cell is attained for a given cell density

$$G = \rho_C \cdot A_A, \quad (5.1)$$

$G$  is the cell stimulated,  $\rho_C$  is the cell density and  $A_A$  is the value of the area of activation.

Following this strategy, detail perception generated by stimulation would be related to the size of the activation area and would be correlated to an array of narrow spots of light. The technique underlying the activation area can yield a significant relationship between the estimation of cell activation and pixel wise stimulation, and amongst the extent of stimulation and the shape of visual perception.

### 5.3.2.3. Drawbacks of Activation Area

The flexibility to trigger near or far localized cells should not be misinterpreted. An inappropriately designed electrical stimulation device may cause damage to the tissue or damage to the electrode itself [Merrill et al., 2005].

Despite that a larger activation area influences a distant cell to be activated, however, not only the stimulus could reach undesirable localities where additional cells could be stimulated, thereby reducing focal activation and greatly decrease resolution, but also the high stimulus could cause irreversible reactions. Reducing electrode dimension, however, the latter situation could cause a breakdown of the electrode and adverse tissue reactions due to a high charge density demand [Fried et al., 2006; Brummer et al., 1997].

Safeguarding the operation of stimulators is by far most a crucial issue in neural activation. Safety, in terms of electrical performance, is mainly related to three factors: charge density injection level, heat generated at tissue due to power dissipation, and the water-voltage window [Lujan (a), 2016, (b), (c)].

It is a general principle when designing electrical stimulation systems that the onset of irreversible Faradaic processes should be avoided because damaging chemical species may potentially be created.

Therefore, as a rule-of-thumb, the injected charge should be kept at a low level where it may be accommodated strictly by reversible charge injection processes. Electronics of any kind dissipates a certain amount of power. Temperature increase at tissue exhibits a linear relationship with power dissipation of  $\Delta T = 1^\circ\text{C}$  per  $12.2\text{mW}/\text{cm}^2$  [Sohee, 2006] assuming only heat conduction. Thus, as a rule-of-thumb, the implanted device should not exceed  $12.2\text{mW}/\text{cm}^2$  of power.

### 5.3.3. Phosphene Shape Description Method

The algorithm of the phosphene shape description method shown in fig. 5.4 uses geometric and stimulating parameters that serve as inputs. Its aim is to generate the activation area in order to evaluate the extent of stimulation and to estimate the shape of visual perception. Each processing step is further explained in sequential order based on its appearance. This phosphene description method is executed until enough boundary points are recorded to enclose the area of activation, see section 5.3.3.6. Looking closely, though, the algorithm shown in fig. 5.4 is similar to the flowchart of simulation depicted in fig. 3.6. However, the main difference lies that the phosphene shape description can estimate the shape and extent of visual sensations.

#### 5.3.3.1. Electric field response

A complex 3D neural-model of the retina was implemented in Comsol Multiphysics software, see fig. 5.5. This model is similar to the simplified retinal-model, fig. 3.3 in section 3.3, and consisted on simulating only the retina layer of one half of a sphere representing a segment of the human eye. The inner surface of the retina has a diameter of 22 mm.

Fixed inputs during the implementation are all the geometric parameters, i.e. domain dimensions, proximity of cell to electrode, electrode data. For the stimulating parameters, the fixed values are injected current, pulse duration, pulse shape, and domain electrical properties. The geometric parameter of cell location is a varied parameter and is explained in the corresponding, see section 5.3.3.5.

As previously stated in fig. 3.3, the layers included in the simulation model are polyimide carrier of electrodes, vitreous medium, photoreceptor layer, ganglionic layer, ganglion cell soma and retinal pigment epithelium. This schematic representation of the retina is built to a greater degree of anatomical likeness than previously published works [Kasi et al., 2011].

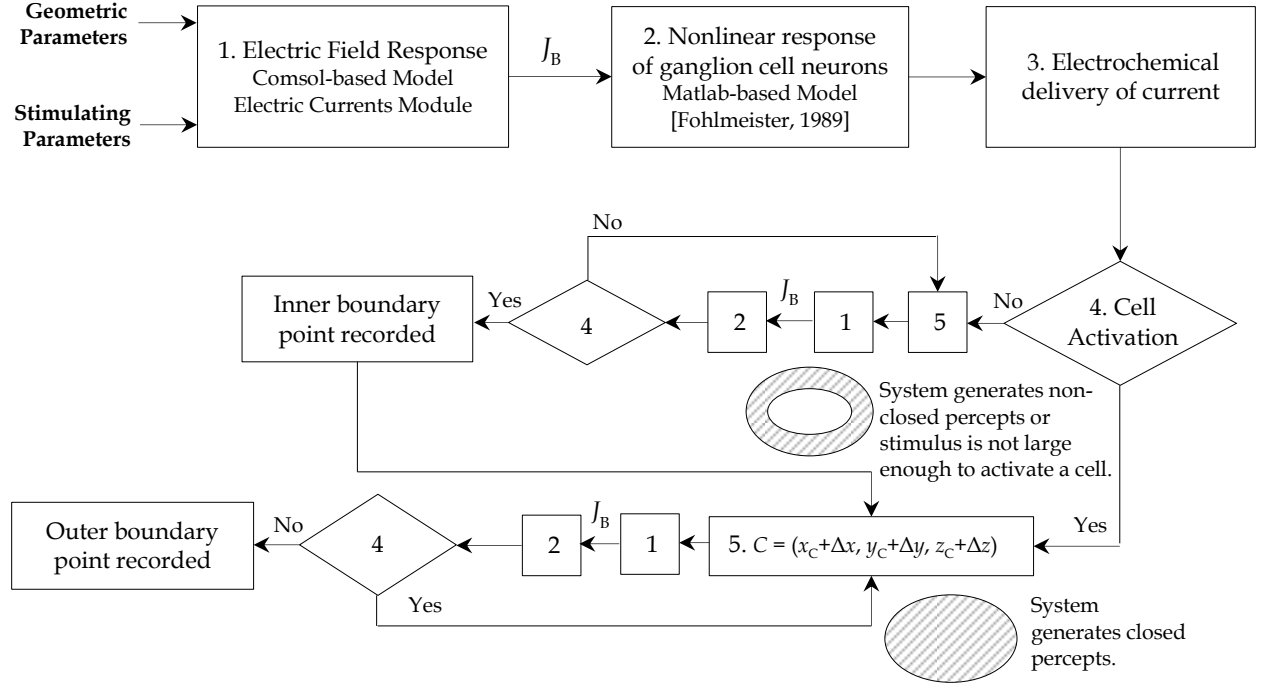


Fig. 5.4 Algorithm that represents the phosphene shape description method. Geometric and stimulating parameters serve as inputs during the operation. Nonlinear response of ganglion cell uses the peak boundary current density in the membrane,  $J_B$ , from COMSOL simulation as an input in the circuit modelling developed by [Fohlmeister et al., 1989]. The algorithm addresses electrochemical delivery of stimulus and can ensure cell activation. Cell location is labeled as  $C$ .  $(x_C, y_C, z_C)$  defines the initial position of the cell. The ganglion cell is initially placed inside the ganglionic layer, exactly below the center of active electrode and enclosed with the cell membrane. The algorithm is implemented until the area of activation becomes an enclosed-based percept. Data from [Lujan et al., 2017(a); 2017(b)].

The retinal network model, i.e. bipolar, horizontal and amacrine cells, ON- and OFF network, are excluded because of severe rod and cone photoreceptor impairment that cannot drive synaptic connection started with a photocurrent input. The proper conductivity, permittivity and thickness of the layers formerly mentioned in table 3.2 can be found in table 5.1 [Werginz et al., 2004; Abramian et al., 2012; Kasi et al., 2011; Starbird, 2013; Yin et al., 2010; Kameneva et al., 2011]. The 3D model operates with an array of electrodes. Monophasic pulses of uniform current

TABLE 5.1

Layer	Conductivity [S/m]	Permittivity [-]	Thickness [ $\mu\text{m}$ ]
Polyimide Carrier	1e-17	1	75
Vitreous Humor	1.5	98	22e3 <sup>2</sup>
Epithelium Layer	2e-3	1	65 <sup>1</sup>
Photoreceptor Layer	28.5e-3	1	200
Intracellular space	0.01	3.98e-11	$G_D - b$
PEDOT-NaPSS coating	40e3	1	0.2
Contact conductivity <sup>3</sup>	321	-	-
Cell membrane	1e-8	8.8e-11	0.005 <sup>4</sup>
Ganglionic Layer	0.01	80	65 <sup>1</sup>

<sup>1</sup> Comsol minimum thickness of surface sphere is 65  $\mu\text{m}$ . <sup>2</sup> Diameter of vitreous humor. <sup>3</sup> Conductivity is of the contact of PEDOT-NaPSS deposition and tissue. <sup>4</sup> Thickness of cell membrane.  $G_D$  is ganglion cell diameter.  $b$  is cell membrane thickness.

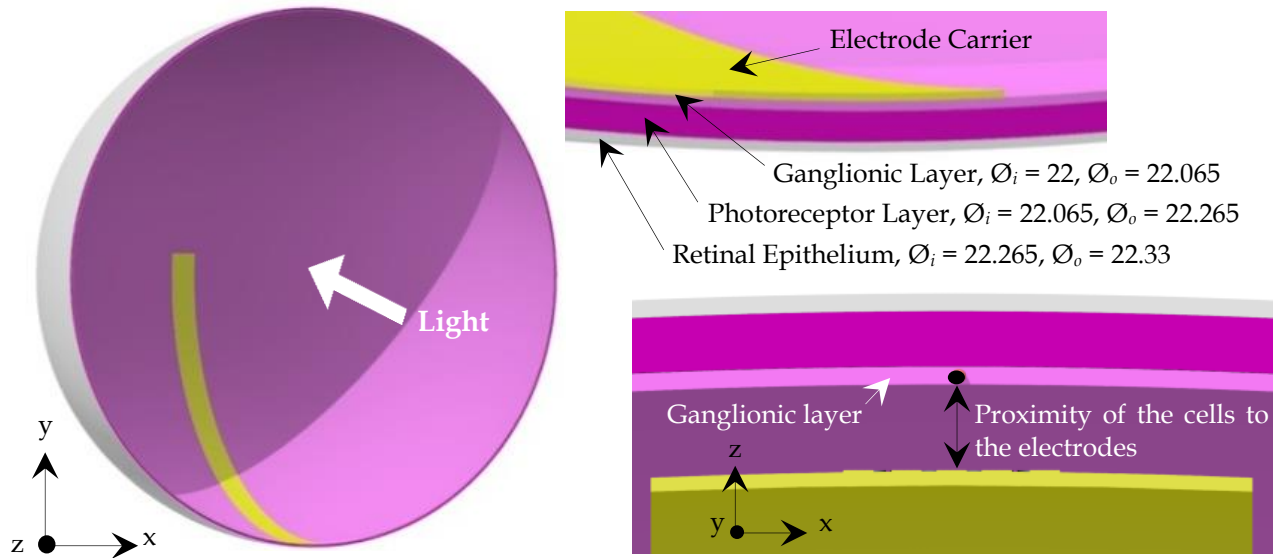


Fig. 5.5 Complex 3D neural-model of the retina built in Comsol Multiphysics.  $\varnothing_i$  and  $\varnothing_o$  are defined as inner and outer surface diameter in units of millimeters. Complete information of each domain is listed in table 5.1. AutoCAD software was used for the creation of this figure. Data from [Lujan et al., 2017(a); 2017(b)].

are injected from the active to ground electrodes to drive the stimulation of some cell. The peak boundary current density in the membrane that encloses the ganglion cell,  $J_B$ , serves as an output parameter from COMSOL simulation. Other extracted data are the voltage across the electrodes and current delivered by the electrode.

#### 5.3.3.2. Nonlinear response of ganglion cell

A Matlab script based on the ganglion cell circuit modelling developed by [Fohlmeister et al., 1989] can be sufficient to compute the threshold current density in the membrane, see section 2.2.2.

The peak boundary current density in the cell membrane from COMSOL simulation serves as an input parameter in the circuit modelling of the ganglion cell. This externally applied current density is distributed to the participating channel types found in this particular cell membrane. LiveLink™ for Matlab was used to integrate the 3D computational model built in COMSOL Multiphysics to the Matlab scripting environment.

This peak current was applied at 500 pps, taking into account absolute and refractory period of an action potential. Peak current was swept with a resolution of  $1 \mu\text{A}/\text{cm}^2$  until it was found the threshold current density that fires a train of action potential. Monophasic rectangular pulse waveform was used with some pulse duration.

The threshold injected current required for activation of a cell by means of extracellular stimulation must generate a voltage shift of around +20 mV for full depolarization in the cell membrane.

Extracellular current density across the cell membrane computed in COMSOL simulation is assumed to be equal as in the circuit modelling of ganglion cell. Hodgkin and Huxley-like equations can describe the eliciting of action potential in the cell membrane.

#### 5.3.3.3. Electrochemical safety

Safe stimulus delivery must guarantee that voltage across the electrodes, local charge density in the electrode and heat generated by the device must be below the electrochemical limits. As such, the formation of corrosion [Fried et al., 2006], electrolysis of water [Merrill et al., 2005; Brummer et al., 1997] and significant damage to various cellular functions due to an excessive tissue heating [Sohee, 2006] must be avoided.

The Matlab script organized the extracted data of voltage across the electrodes and current delivered by the electrode and performed several tasks to obtain the heat dissipated at the device and charge density in the electrode.

Charge density, electrode voltage, power consumption and the increase of heat at the device were calculated as explained in sections 3.3.2.6, 3.3.2.7 and 3.3.2.8, respectively. As such, the results were compared with their own harmful limits of 1 mC/cm<sup>2</sup>, 1.7 V [Duay et al., 2012] and 1°C [Singh et al., 2008].

#### 5.3.3.4. Cell activation

The threshold current necessary for cell activation in the form of extracellular stimulation must produce depolarization in the cell membrane. The circuit modelling of the ganglion cell in the tiger salamander retina developed by [Fohlmeister et al., 1989] is sufficient to describe the cell depolarization in response to various levels of extracellular stimulation. Hence, the amplitude of the injected current from the active electrode must be large enough to attain the formerly stated task.

#### 5.3.3.5. Cell location

As previously stated, the cell is initially placed inside the retina ganglion cell layer and exactly below the center of active electrode.

If the peak boundary current density is large enough to trigger a response (*Yes-decision*) a percept where the surface forms a closed geometry is generated. Then, the cell is shifted inside the ganglionic layer (see fig. 5.5) until the boundary of inactivation (outer boundary) is found. Next, the boundary point can be recorded.

Once the peak boundary current density is not enough for stimulation (*No-decision*), two possibilities occur; i) a phosphene where the surface forms a non-closed geometry is created, e.g. ring-shaped percept, or ii) there is no such thing as electrical stimulation.

For the former case, the cell is shifted inside the ganglionic layer until the boundary of activation (inner boundary) is found. Then, the boundary point surrounding the active electrode can be recorded. For the latter case, if the cell has been shifted without having stimulation, an increase of the injected current must be performed.

#### 5.3.3.6. Enclosed area generation

The algorithm is implemented until the area of activation becomes an enclosed-based percept. If the area of activation is not an enclosed geometry, the cell location returns to its initial value of being exactly below the center of active electrode and the cell is shifted but in another

direction. Since the number of points to enclose a region can be as finite as the desire of the user, a recommendation would be to enclose the percept using an octagonal-based framing.

Once the activation area is generated, the criterion for its applicability asserts that a cell located inside the activation area is activated by the respective electrode. Otherwise, the cell is not stimulated by this electrode.

#### 5.3.4. Principle-based Experimental Observations

[Keserü et al., 2012] developed a stimulator device that ensures high-standard of safety for applications related to visual prosthesis. The stimulator device consists of a camera chip, digital signal processor, image processor algorithms, wireless transmitter and receiver for energy and data and an electrode array with microelectrodes. The electrode carrier consists of a flexible film of around 10  $\mu\text{m}$  thick, 1 mm wide and 60 mm long. The electrode carrier followed a ring-electrode approach with effective electrode diameter of 50, 200 and 360  $\mu\text{m}$ . The ground electrode has a diameter of 560  $\mu\text{m}$  and is placed 5.5 mm away from the stimulation electrodes, see fig. 5.3 or 5.6a.

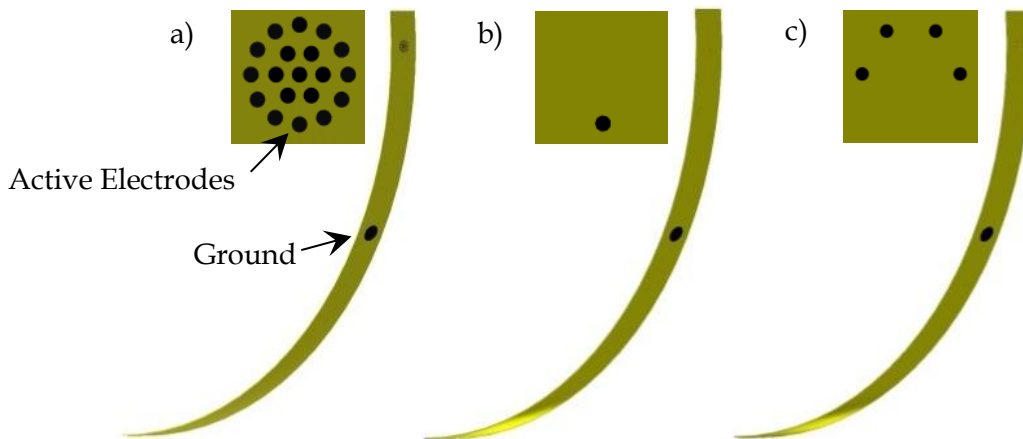


Fig. 5.6 Three different electrode arrays. a) Electrode array of 50, 200 and 360 effective diameters [248]. b) Single electrode stimulation. c) Multiple electrode stimulation. The electrodes are in contact with the retinal surface layer. AutoCAD software was used for the creation of this figure. Data from [Keserü et al., 2012].

The electrodes were coated with iridium oxide (IrOx) and have a charge injection capacity of 1  $\text{mC}/\text{cm}^2$ . Charge injection capacity is defined as the amount of charge per unit area that can be delivered through an electrode without causing water electrolysis. Charge-imbalanced rectangular pulse shape is delivered with anodic first with pulse duration of 2 ms followed by cathodic with pulse duration of 1 ms. In-between anodic and cathodic pulse the system is open-circuited with a delay of 100  $\mu\text{s}$ . A clinical trial was carried out to test the electrode carrier that was implanted in 20 volunteers with different stages of retinal degeneration. The study was conducted in accordance with the provisions of the Declaration of Helsinki, the guidelines for good clinical practice and approved by the ethics committees of the participating centers.

The visual acuities from the patients ranged from 4/200 to no light perception, indicating that their diagnosis was in effect retinitis pigmentosa, rod-cone dystrophy or usher syndrome. The objectives of the study were to measure the perception threshold and to identify the shape of the visual perception. For more information about threshold response verification see [Keserü et al.,

2012]. The perceptual threshold was measured in 15 patients using an effective electrode diameter of 360  $\mu\text{m}$ , see fig. 5.6a, and selecting either a single, see fig. 5.6b, or multiple electrode stimulation, see fig. 5.6c.

The results revealed a wide range of perceptual thresholds ranging from 20 to 768 nC (i.e. from 0.02 to 0.75  $\text{mC}/\text{cm}^2$ ) for both single and multiple electrode stimulation. The patients were asked to describe the perceived objects in their own words. Although a single electrode was active, a wide range of shape responses were revealed, such as a circle, ring, rectangle, hash mark, half paperclip, '@' sign, fan-like arrangement, etc. Due to the timeslot between stimulation and postoperative interviews, the patients were not able to assign the perceptual shapes to individual stimulation sequences.

### 5.3.5. Verification of FEM-based Modelling of Retina

Keserü and colleagues coated the electrodes with IrOx. IrOx allows considerably greater levels of charge injection without electrode dissolution or electrolysis of water. Within all its purposes, IrOx has been used to coat a variety of electrodes including deep brain, nerve cuff, pacing, and defibrillation electrodes [Meyer et al., 2001; Weiland et al., 2000; Niebauer et al., 1997]. Despite that the specifics of IrOx deposition and contact conductivity with tissue were not published in [Keserü et al., 2012] there is evidence that carbon nanotube-polyelectrolyte electrodes coated with IrOx at 160  $\text{mC}/\text{cm}^2$  charge density deposition [Jan et al., 2009] have similar impedance characteristics to PEDOT-NaPSS nanotubes [Starbird, 2013] up to 10 kHz.

However, for coating materials such as IrOx [Jan et al., 2009] and PEDOT-NaPSS deposition [Starbird, 2013], thickness and impedance differ by altering the deposition charge density. Likewise, the technique of deposition, layer thickness, chemical composition and micro/nanoscale morphology and topography have a considerable influence on the electrical, mechanical and biological interfacing properties of the electrodes [Jan et al., 2009].

Keserü et al. stated that for single electrode stimulation and a charge of 380 nC, a mean voltage amplitude of 1.82 V was measured. Hence, a prior verification of the model shown in figure 5.5 was performed using Comsol Multiphysics. The definition of the domains is listed in table 5.1. PEDOT-NaPSS contact conductivity with tissue calculated in [Lujan (a), 2016] was used. The contact conductivity listed in that table is related to the interaction of charge transfer to the tissues. Since the specifics of the single electrode were not indicated, the electrode selected in this prior verification is shown in figure 5.6b. The stimulating parameters of pulse shape and duration were kept as in the original experiment, i.e. rectangular biphasic, anodic first of 2 ms of pulse duration followed by cathodic of 1 ms of pulse duration.

The outcome of our simulation model revealed a good agreement to the experimental findings by reaching a value of 1.784 V with 2 % of error. Accordingly, PEDOT-NaPSS conductivity with tissue and the definitions of the domains formerly stated can deliver accurate results of the electric field distribution throughout the retinal tissue.

### 5.3.6. Proof of the Activation Area

#### 5.3.6.1. Methods

The experimental observations of perceptual thresholds and the wide range of shape responses found by Keserü and colleagues were used to prove conclusively the applicability of

the activation area. To achieve such challenge, the procedure to obtain the activation area consists in following the phosphene shape description method shown in fig. 5.4.

Keserü et al. developed a stimulator device that ensures high-standard of safety for applications related to visual prosthesis. Thus, the evaluation to ensure electrochemical safety was disregarded.

Since details of the exact active electrodes were not published in [Keserü et al., 2012] the arrangements chosen in single and multiple electrode stimulation are shown in figure 5.6b and 5.6c, respectively. The stimulating parameters of pulse shape and duration were kept as in the original experiment.

Charge densities of 0.02, 0.1, 0.35 and 0.75 mC/cm<sup>2</sup> were applied across single or multiple (four electrodes) electrode stimulation. Charge injection capacity of 1 mC/cm<sup>2</sup> was the limit of comparison in [Keserü et al., 2012] using IrOx coated electrodes. The charge capacity of an electrode material is calculated as the maximum amount of charge per unit area that can be passed in a biphasic pulse without causing eventual electrode damage [Keserü et al., 2012].

Thus, the peak current applied across the electrodes was calculated as

$$i = \frac{\sigma_q \cdot A_E}{t}, \quad (5.2)$$

$\sigma_q$  is the charge density applied,  $A_E$  is the electrode cross section area and  $t$  is the total pulse duration of a biphasic pulse shape.

As previously stated, the range of perceptual threshold measured at 15 patients was 20 to 768 nC [Keserü et al., 2012]. The standard deviation was 229.55 nC. This high variability of standard deviation may be related to the distance between the retina surface and the electrode array in different patients along the study [Keserü et al., 2012]. Thus the distance between the surface of the retina and the electrode array tested was 10 and 1300  $\mu$ m. Following the procedure formerly explained the activation area is mapped along the space where the electrodes activated ganglion cells. We assumed a cell density of 270 mm<sup>-2</sup>.

### 5.3.7. Results

The activation areas are shown in figures 5.7 and 5.8 for several charge densities applied across a single and multiple electrode stimulation. The x-axis shows the charge densities of 0.02, 0.1, 0.35 and 0.75 mC/cm<sup>2</sup> whereas the y-axis shows the proximity of cells to the electrode array tested, namely 10 and 1300  $\mu$ m.

Figure 5.9a provides a graphic representation of the outer surface dimensions of the activation area labeled as  $a''$  to  $d''$ . Figure 5.9b shows the inner surface dimensions labeled as  $e''$  to  $g''$ . The dimensions shown in figure 5.9b were related when the activation area is a non-closed form.

Figure 5.9c shows the vertical visual angle labeled as  $\theta_v$  and figure 5.9d shows the horizontal visual angle  $\theta_h$ . In both figures  $n$  stands for the distance from the eye's nodal points to the retina,  $a''$  and  $d''$  are some of the dimensions of the activation area, see fig. 5.9a. The horizontal and vertical visual angles are calculated as

$$\theta_h, \theta_v = 180 \frac{x}{n\pi}, \quad (5.3)$$



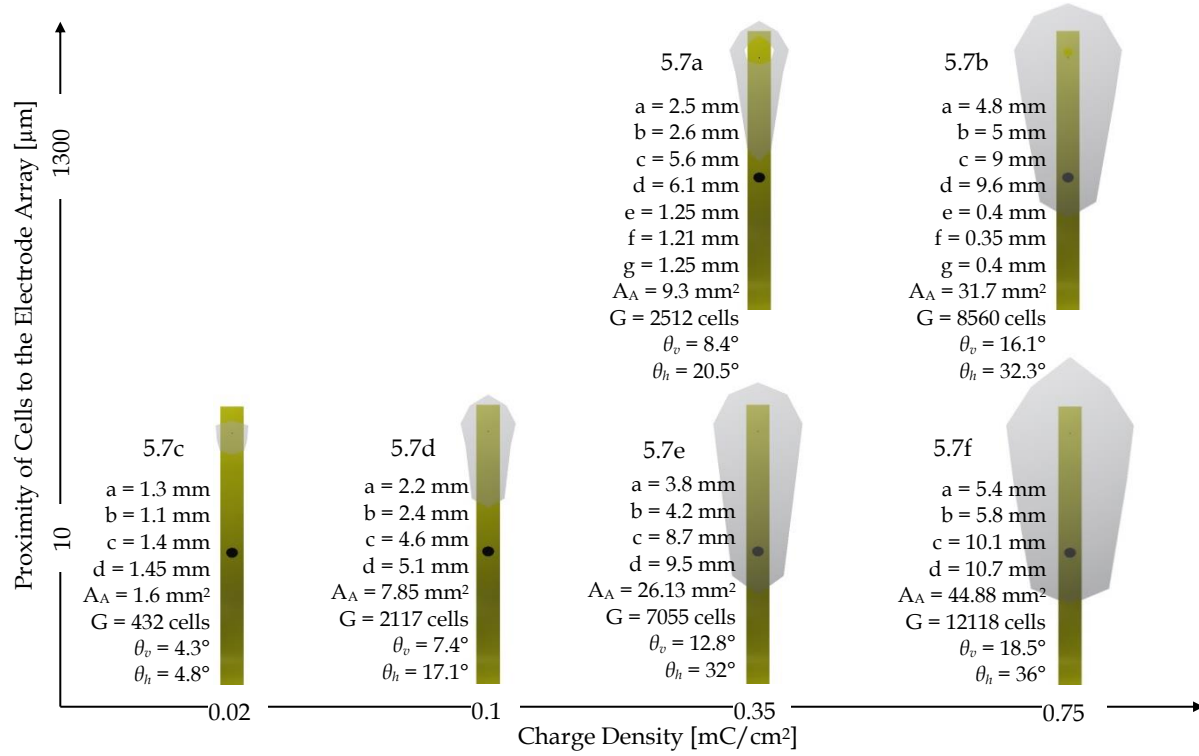


Fig. 5.7 Activation areas for single electrode stimulation. X-axis is related to the charge densities applied by the electrodes. Y-axis is associated to the proximity of the cells to the electrodes. In the lower left corner of each activation area is depicted the sizes from  $a''$  to  $d''$  for the outer surface dimensions and from  $e''$  to  $g''$  for the inner surface dimensions. An empty space inside the plot represents a case where the electrodes could not activate a cell. Data from [Lujan et al., 2017(a); 2017(b)].

$x$  is the size of  $d''$  of the activation area for horizontal visual angle and  $a''$  for vertical visual angle. The space from the nodal points to the retina  $n$  is 17 mm.

### 5.3.8. Ganglion Cell Activation

As formerly discussed, eq. (5.1) can be applied in practice to estimate the amount of cells being triggered for a given cell density. Apart of being closely correlated with the activation area, the activation of ganglion cells is associated with the following insights:

#### 1. Current / charge injected and Pulse timing

There is a close association between the broadness of the activation area and the amount of peak current injected to the electrode, see percept breadth among charge densities in fig. 5.7 and 5.8. Namely, once the injected current or charge increases, far-localized cells can be activated by a single stimulus.

Experimental findings on human volunteers of [Rizzo III et al., 2003] demonstrated conclusively that once the stimulus charge is increased the size of the percept is raised as well. Until recently, [Fried et al., 2006] demonstrated that pulses shorter than 150  $\mu$ s of duration can replicate light-elicited spiking patterns, trigger solely a single spike with precise temporal pattern, and send a more physiological signal to the brain.

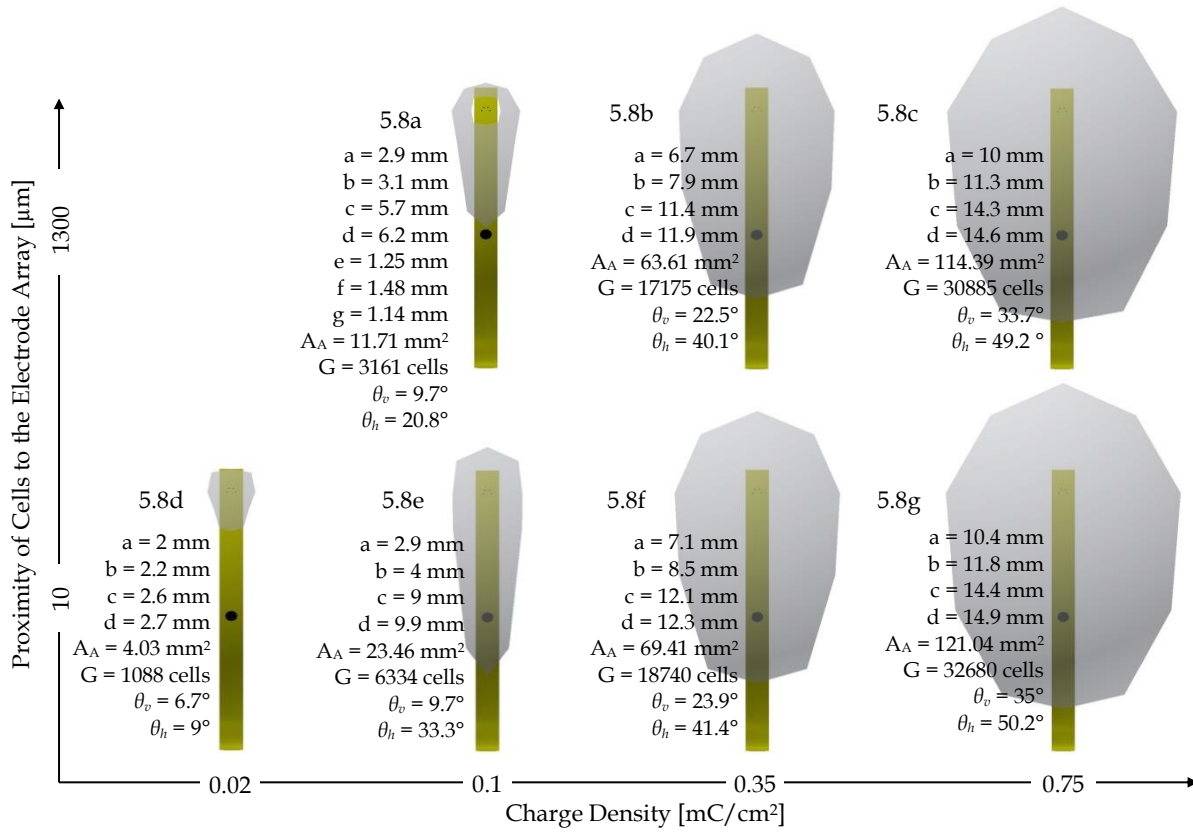


Fig. 5.8 Activation areas for multiple electrode stimulation. X-axis is related to the charge densities applied by the electrodes. Y-axis is associated to the proximity of the cells to the electrodes. In the lower left corner of each activation area is depicted the sizes from  $a''$  to  $d''$  for the outer surface dimensions and from  $e''$  to  $g''$  for the inner surface dimensions. An empty space inside the plot represents a case where the electrodes could not activate a cell. Data from [Lujan et al., 2017(a); 2017(b)].

## 2. Topology of electrode array

Electrode topology likewise plays a major role of defining the broadness of the activation area. A far placement of the ground to the active electrode causes a deep flow of the current into the tissue environment leading to the activation of cells in the interim to the ground.

As this proximity increases, though, the shape of the activation area becomes more to an elongated form; see figs. 5.7d, 5.7e and 5.8e.

## 3. Electrode size

Decreasing electrode dimension generates higher resolution patterns of prosthetic-elicited activity that are closer to light-elicited patterns and improve visual reception [Fried et al., 2006]. Currently prosthetic devices by [Mahadevappa et al., 2005], [Eger et al., 2006], [Rizzo III et al., 2003], [Humayun et al., 2012] and Klauke and colleagues [Klauke et al., 2011] used big-sized electrode diameters of 500, 200 and 100  $\mu\text{m}$ .

The electric current fields from relatively large electrodes indiscriminately drive local retinal circuits in an unnatural way, leading to complex retinal responses [Horsager et al., 2011]. As such, safe charge density boundary which limits the miniaturization of implanted electrodes is currently a major concern [Horsager et al., 2011; Lujan (a), 2016, (b); Kasi et al., 2011].

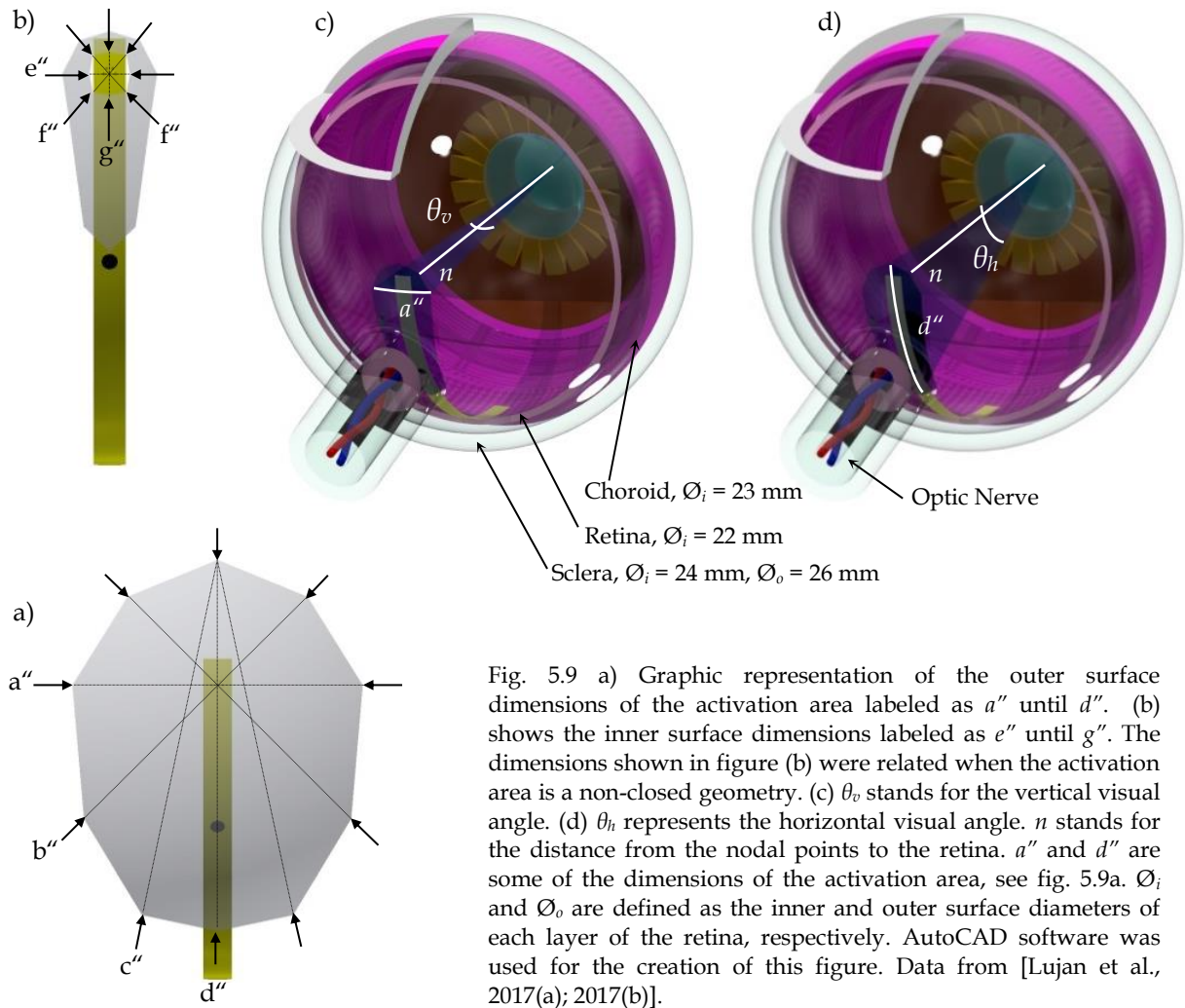


Fig. 5.9 a) Graphic representation of the outer surface dimensions of the activation area labeled as  $a''$  until  $d''$ . (b) shows the inner surface dimensions labeled as  $e''$  until  $g''$ . The dimensions shown in figure (b) were related when the activation area is a non-closed geometry. (c)  $\theta_v$  stands for the vertical visual angle. (d)  $\theta_h$  represents the horizontal visual angle.  $n$  stands for the distance from the nodal points to the retina.  $a''$  and  $d''$  are some of the dimensions of the activation area, see fig. 5.9a.  $\text{Ø}_i$  and  $\text{Ø}_o$  are defined as the inner and outer surface diameters of each layer of the retina, respectively. AutoCAD software was used for the creation of this figure. Data from [Lujan et al., 2017(a); 2017(b)].

### 5.3.9. Perceptual Thresholds

Perceptual thresholds were validated by our simulation model, which estimated the activation of cells for the charge densities and the proximities tested for single and multiple electrode stimulation, see figs. 5.7 and 5.8. These outcomes were related to the spectrum of perceptual thresholds between 0.02 to 0.75 mC/cm<sup>2</sup> found by Keserü and colleagues.

The proximity of the retina to the electrodes contributes to the increase in the area of activation and thus the amount of cells being stimulated. This consequence can be attributed to the current that spreads across the electrodes causing changes in the activation area and thus affects the visual perception generated by stimulation.

### 5.3.10. Shape of Visual Perception

As formerly described, the suitability of the activation area can estimate the shape of visual perception. The result of the clinical trial conducted by Keserü and colleagues stated that the volunteers described a wide range visual perception with different characteristics, such as a circle, ring, rectangle, hash mark, half paperclip, '@' sign, fan-like arrangement, etc.

The results of our simulation framework indicated a spectrum of elliptical-shapes, either being closed-surface geometries or non-closed, see fig. 5.7 and 5.8.

The shape of an ellipse is represented by its eccentricity, which is a measure of how much the conic section deviates from being circular. For an ellipse the eccentricity is between 0 and 1 ( $0 < \varepsilon < 1$ ). When the eccentricity tends toward 1, the ellipse gets a more elongated shape and is related to a hash mark or a rectangle. Phosphenes in the form of elongated shapes [Brindley et al., 1986; Rizzo III et al., 2003] and lines or bars [Rizzo III et al., 2003; Veraart et al., 1998] have also been observed.

Bringing the other extreme into play, an elliptical-shaped figure is closely related to a circle when its eccentricity moves away from 1. Phosphenes were frequently described as “round” spot of lights in [Humayun et al., 2003, 2004; Mahadevappa et al., 2005; Keserü et al., 2012; Rizzo III et al., 2003; Weiland et al., 2003]. Once the minor axis of the ellipse is approximated to the value of  $a''$  of the activation area, the eccentricity can be calculated as

$$\varepsilon = \frac{\sqrt{d''^2 - a''^2}}{d''}, \quad (5.4)$$

$d''$  is the size of the activation area related to the major axis of an ellipse.

Thus, the wide range of visual perceptions recorded by Keserü and co-workers can be categorized as an elliptical-shaped hash mark (or rectangle) or an elliptical-shaped circle based on their eccentricities.

Despite the fact that most phosphenes were described or otherwise implied as “round”, it is doubtful that the patients had always defined the visual perception as “perfectly circular-shaped phosphene”. Such description can thus include any shape with a smooth, curved circumference, including balls, ovals, and pebbles [Chen et al., 2009].

Having stated the above, the criterion to categorize the visual perceptions is as follows. Ring-shaped visual perceptions are related to non-closed forms.

Hash mark- or rectangular-shaped percepts are associated with eccentricities is higher than 9/10. Circular-shaped percepts are related when the eccentricity is lower than 9/10.

### 1. Ring-Shaped Visual Perceptions

Ring-shaped phosphenes belong to an activation area where the surface forms a non-closed geometry.

As such, figures 5.7a, 5.7b and 5.8a are suitable for this criterion. Looking carefully, ring-shaped responses arise once the proximity of the retina remains distant to the electrode array. Non-closed geometries such as doughnut-shapes have been reported by the patients in [Humayun et al., 2003]. Thus, close proximity of the cells to the electrode array is a critical issue for safe visual stimulation [Lujan (a), 2016, (b); Kasi et al., 2011]. This indication has four benefits on visual implants:

1. The major limitation can be attributed to the charge density required to elicit activity in neurons [Lujan (a), 2016]. As threshold current reduces with closer proximity of the cells to the electrodes, the charge density follows the same association and a safe stimulus is therefore delivered from the electrodes.
2. A distant proximity of the retina to the electrode array contributes to the varying current spread from the active electrode causing changes in the area of stimulation and thus affects the resolution of the visual prosthesis [Kasi et al., 2011].

3. A suitable current can be estimated to achieve pixel wise stimulation because the current can be contained in a small volume that surrounds the cell and thus ensures the activation of a single cell [Lujan (c), 2016].
4. Power consumption and thus heat generated by the device [Sohee, 2006] is minimized allowing small electrodes to generate phosphenes within safe heat limits [Horsager et al., 2011].

## 2. Hash mark- or Rectangular-Shaped Perceptions

These particular shaped perceptions belong to an activation area where its eccentricity is higher than 9/10. As such, figures 5.7d, 5.7e and 5.8e are appropriate to this criterion. Hash mark- or stripe-shaped phosphenes can be attributed once the ground is placed far away from the active electrode. As such, the current spreads deep into the tissues leading to an activation of cells in its path to the ground electrode.

These specific-shaped phosphenes can also be generated by unintentional activation of ganglion cell axons [Andrew et al., 2015]. Retinal ganglion cell axons pass within short distances from each other along their path to the optic nerve to the brain. In practice, though, while subjects receive single electrode stimulus, they often report a stripe-shaped phosphene, rather than a focal spot of light due to unintended stimulation of passing axons [Nanduri et al., 2012], thus making it problematic to distinguish faces and objects [Andrew et al., 2015].

## 3. Circular-Shaped Perceptions

This specific shaped perception belongs to an activation area where its eccentricity is lower than 9/10. In essence, figures 5.7c, 5.7f, 5.8b-d, 5.8f and 5.8g are suitable to this criterion.

[Chen et al., 2009] stressed that phosphenes should be preferably round because electrodes are ideally required to produce a visual perception of an  $m \times n$  array of narrow spots of light that can be precisely controlled by the system.

Highly interesting, narrow circular-shaped phosphenes occur once the proximity of cells to the electrodes is low and the injected current remains small, see 5.7c and 5.8d. The proximity of electrodes to the surface of the retina has been highly stressed among devices to lower the injected current, generate small percepts and remain far from electrochemical hazards [Lujan (a), 2016, (b); Kasi et al., 2011].

## 5.3.11. Summary

The activation area is conclusively proven by directly comparing clinical trial results of Kaserü and co-workers with outcomes based on our simulation framework. Our simulation framework showed a spectrum of elliptical-shape forms.

The viable justification of such forms is the far placement of the ground from the active electrode causing the current to flow deep down into the tissues and activating cells in its path to ground. Thus, image sharpness and detail perception is reduced because stimulation causes oblong-like shapes of light that lessen the quality of vision.

Artificial vision is currently in an early-stage of maturity. In effect, the foremost obstacle of visual prosthetics is to induce natural patterns of retinal activity generated by stimulation. This can be recognized as a misinterpretation in understanding the physical foundation of phosphenes. Likewise the formerly stated challenge is related to the detail perception that demands strategies to attain nearby cell activation [Jepson et al., 2014; Weiland et al., 2014].

Our simulation framework having as a basis the activation area proposes the following insights to explain how the shapes of the phosphenes are generated by stimulation:

1. Topology of electrode arrangement and characteristics of stimulating electrodes, i.e. dimension, amount and electrode distance.

The activation area of single and multiple topologies of stimulating electrodes revealed different shapes of phosphenes e.g. hash mark-shaped percepts and circular-shaped forms, respectively. Furthermore, experimental findings which were performed with different experimental setups of electrode topology revealed dissimilar shapes of phosphenes e.g. elongated shapes [Brindley et al., 1986; Rizzo III et al., 2003], lines/bars [Rizzo III et al., 2003; Veraart et al., 1998; Wilke et al., 2011], triangles [Veraart et al., 1998], doughnut-shaped [Humayun et al., 2003], complicated patterns [Veraart et al., 1998] and round spots of light [Humayun et al., 2003, 2004; Mahadevappa et al., 2005; Kaserü et al., 2012; Rizzo III et al., 2003; Weiland et al., 2003].

2. Current / charge flowing across the electrodes.

See section 5.3.8, at 1. Current/charge injected and pulse timing.

3. Cell density in the degenerate retina

The variability of thresholds in the experimental findings of [Kaserü et al., 2012] was attributed to a combination of a varying degree of retinal degeneration. This degree of retinal degeneration can influence the shape of the visual perception because gaps of dark vicinities would be exhibited at locations of cell depletion.

4. Electrode configuration, i.e. single or multiple electrode stimulation

Our simulation framework revealed that single and multiple electrode stimulation generated different shapes of phosphenes either circular or hash mark shaped. Experimental observations on the human volunteers of [Rizzo III et al., 2003] and Wilke et al. [Wilke et al., 2011] yielded validating evidence on different shapes of phosphenes such as spots of light or lines by driving one or a line of four electrodes, respectively.

5. Proximity of cells to the electrodes

The closeness of the cells to the electrodes influences the broadness of the activation area. An increment of the distance from some point to the electrodes causes that the current density to become insufficient to trigger a response of the cell and the activation area comes to an end. A distant proximity of the retina to the electrode array contributes to the varying current spread from the active electrode causing changes in the area of stimulation and thus affects the resolution of the visual prosthetic [Kasi et al., 2011].

## 5.4. Controlled-shape Phosphenes

### 5.4.1. Lessons learnt: Basis for this Chapter

As a result of the activation area, which I established in the last chapter, it was conclusively proven by directly comparing clinical trial results from [Kaserü et al., 2012] with findings based on our simulation framework. Having argued in the previous section, the electrode arrangement developed by [Kaserü et al., 2012] stimulates a range from 432 to 12118 for single electrode

stimulation, see fig. 5.7. For multiple-electrode stimulation, cell activation ranges from 1088 to 32680, see fig. 5.8, assuming a cell density of 270 mm<sup>-2</sup>. This coarse activation of cells not only constrains the detail perception, the activity generated by stimulation remains different from a healthy retina too.

Similarly, state-of-the-art retinal devices and current status on clinical trials of sub- and epiretinal approaches are some that demonstrate that patients do not experience such flawless pixelized sight as shown in many publications [Humayun et al., 2012; Stingl et al., 2013; Weiland et al., 2014]. Argus II [Humayun et al., 2012] and Alpha IMS [Stingl et al., 2013] stimulation strategies fall short to exhibit an outdoor image perception of  $m \times n$  array of narrow spots of light that can be precisely controlled by the system. In simple terms, they clearly activate hundreds of cells simultaneously over a particular region due to the size of the electrode used.

#### 5.4.2. Aims

In this section, I will examine the controlled-shape phosphene method. Its aim is to narrow the extent of the spreading stimulus and to generate a space required for stimulation of ganglion cells. An analogous 32 x 32 electrode array with square grid distribution used in chapter 3 will be used. Afterwards, a comparison based on the broadness of the area of stimulation and the number of cell activation is made between the electrode arrangement developed by Keserü and our proposal.

#### 5.4.3. Controlled-shape Phosphene Method

The algorithm of the controlled-shape phosphene method is as shown in fig. 5.10. Its aim is to argue for its usefulness to discriminate the region of the spreading stimulus to the space required for activation. The implementation is similar to the phosphene shape method but with some modifications. Fixed inputs during the implementation are all the geometric parameters, i.e. domain dimensions, proximity of cell to the electrodes, electrode data and cell location. For the stimulating parameters, all are fixed values, i.e. pulse duration, pulse shape and domain electrical properties, except the injected current. Its variability is explained as follows.

The cell can be moved inside the ganglionic layer and at some desired distance away from the active electrode, fig. 5.5 and 5.11. This algorithm is executed to obtain the threshold injected current across the electrodes to activate this cell. Afterwards, input stimulating parameters take this threshold as the injected current and the activation area is generated based on the phosphene shape description method. Thus, this threshold current will then discriminate the region of the stimulus. The area of perception will be controlled by this specific current injection.

As a reminder, cell location becomes a variable parameter in the phosphene shape description method. The processing steps of electric field response, nonlinear response of the cell, electrochemical delivery of current and cell activation are implemented as explained in section 5.3.3.1, 5.3.3.2, 5.3.3.3, and 5.3.3.4, respectively.

#### 5.4.4. Electrode Arrangement

As formerly explained in chapter three, we proposed an evenly distributed 32 x 32 electrode array; see fig. 5.11. As a reminder, the length,  $l$ , and width,  $w$ , of the electrode carrier are assumed to be equal and are calculated as

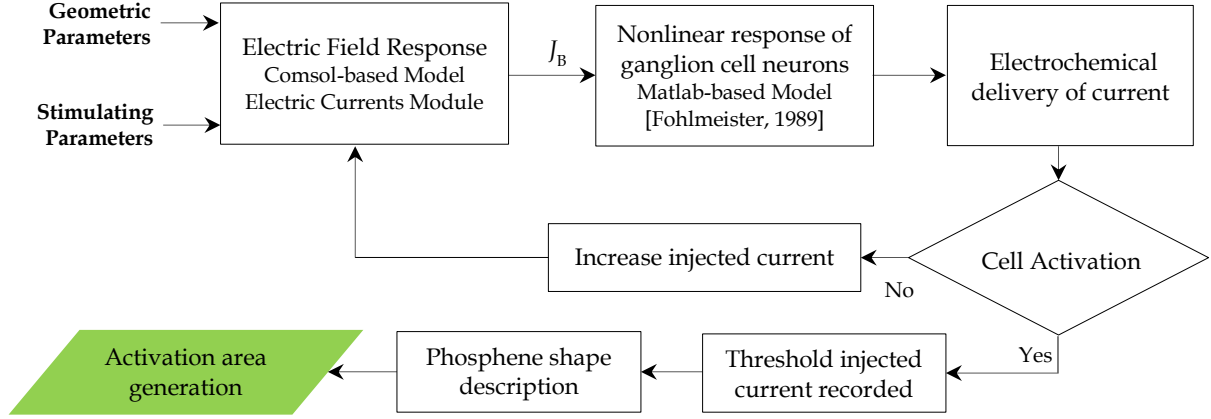


Fig. 5.10 Algorithm that represents the controlled-shape phosphene. Geometric and stimulating parameters serve as inputs during the operation. Nonlinear response of ganglion cell uses the peak boundary current density in the membrane,  $J_B$ , from COMSOL simulation as an input in the circuit modelling. The algorithm addresses safe electrochemical delivery of stimulus and can ensure cell activation. The ganglion cell is initially located inside the ganglionic layer and at some desired distance away from the active electrode. This algorithm is executed to obtain the threshold injected current across the electrodes. After finding it out, input stimulating parameters take the threshold as the injected current and the activation area is generated based on the phosphene shape description method. Data from [Lujan et al., 2017(a); 2017(b)].

$$w = l = d \cdot (\sqrt{e_T} + 1), \quad (5.5)$$

$e_T$  is the total number of electrodes inside the carrier. Let us call a square area-element inside the electrode carrier with sizes labeled as  $d$ , see fig. 5.11, where  $d$  is the electrode pitch

$$d = \frac{1}{\sqrt{\rho_E}}, \quad (5.6)$$

$\rho_E$  is the electrode density. For given electrode diameter, the electrode distance can be computed as

$$I_{ED} = d - E_D, \quad (5.7)$$

$E_D$  is the electrode diameter and  $I_{ED}$  represents the electrode distance. The electrode carrier area is given by

$$A = l^2. \quad (5.8)$$

#### 5.4.5. Input Data of the Controlled-shape Phosphene Method

A comparison is made between the electrode arrangement developed by Keserü and our proposal based on the broadness of the area of stimulation and the number of activation of cells. So as to make a fair comparison, the charge density applied across the electrodes is assured to be equal and a replica of the simulation model formerly explained in fig. 5.5 was used.

Geometric and stimulating parameters earlier defined are used. Overall, an array of  $32 \times 32$  electrodes, electrode diameter of  $5 \mu\text{m}$  and proximity of the cells to electrodes of  $10 \mu\text{m}$  are applied. Rectangular pulse shape and pulse duration of  $100 \mu\text{s}$  are used. Domain geometry and definitions similar to table 3.2 and can be found in table 5.1.



The density tested is  $270 \text{ mm}^{-2}$ . Following the formulation previously explained, the electrode distance has a value of  $55 \text{ }\mu\text{m}$  between the edges of neighboring electrodes. Throughout this study, single electrode stimulation is implemented. The stimulation arrangement consists of an active electrode (blue) surrounded by eight grounds (black) as seen in fig. 3.3.

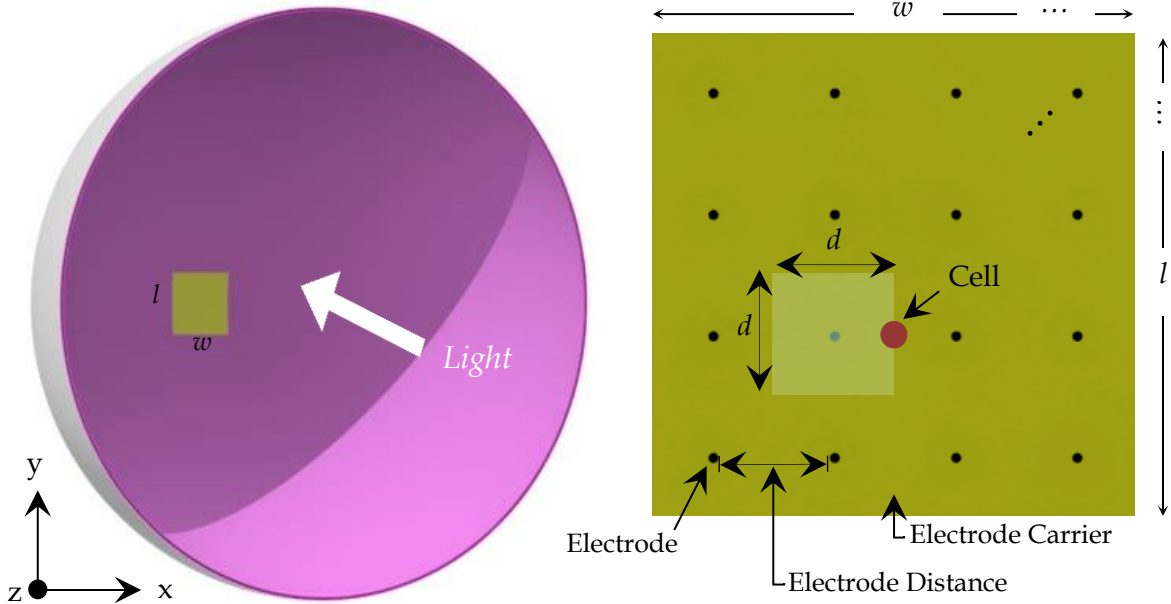


Fig. 5.11 Proposed electrode arrangement simulated in Comsol Multiphysics. The total number of electrodes is 1024. Electrodes have a diameter of  $5 \text{ }\mu\text{m}$  and are separated with an electrode distance of  $55 \text{ }\mu\text{m}$ . Width,  $w$ , and length,  $l$ , of the electrode carrier is assumed to be equal with a value of  $2 \text{ mm}$ . The electrodes are in contact with the retinal surface layer. The stimulation arrangement consists of an active electrode (blue) surrounded by eight grounds (black). AutoCAD software was used for the creation of this figure. Data from [Lujan et al., 2017(a)].

#### 5.4.6. Activation area generation

Single-cell selectivity is treated as enhancing the control of the electrodes over single cells to produce an array of independent phosphene [Weiland et al., 2014]. Thus, the stimulus that spreads through the medium must be constrained to the space required for activation. To be precise, the discrimination of the area of stimulation must be generated such that the detail perception of the visual field of view is improved.

To achieve such challenge, the procedure to generate the activation area consists in following the controlled-shape phosphene method shown in fig. 5.10. The cell is shifted inside the ganglionic layer and located at a distance of  $d/2$  away from the active electrode, see fig. 5.11. As such, the size of the area of activation must be such that the boundaries of adjacent activation areas meet but do not overlap. This area is called the non-overlapping space. The algorithm is executed to obtain the threshold injected current across the electrodes to activate this cell. Subsequently, input stimulating parameters take the threshold as the injected current and the activation area is generated based on the phosphene shape description method.

The result of the area of activation is shown in fig. 5.12(a) as a red dash-line boundary that follows a 'sinking at the diagonals' shape with an average distance of 80% of  $r$ . For simplicity, the activation area for each electrode is represented as a circular shape with some distance  $r$

from the center. The distance  $r$  is labeled the activation size and can be related to the amount of peak current injected by the electrode. The activation area can be calculated as  $\pi r^2$ .

#### 5.4.7. Results

The result of the proposed electrode array presented in this report is shown in figure 5.12(a) and (b). The area of proposed electrode array is 4 mm<sup>2</sup>. The width,  $w$ , and length,  $l$ , are assumed to have equal sizes of 2 mm.

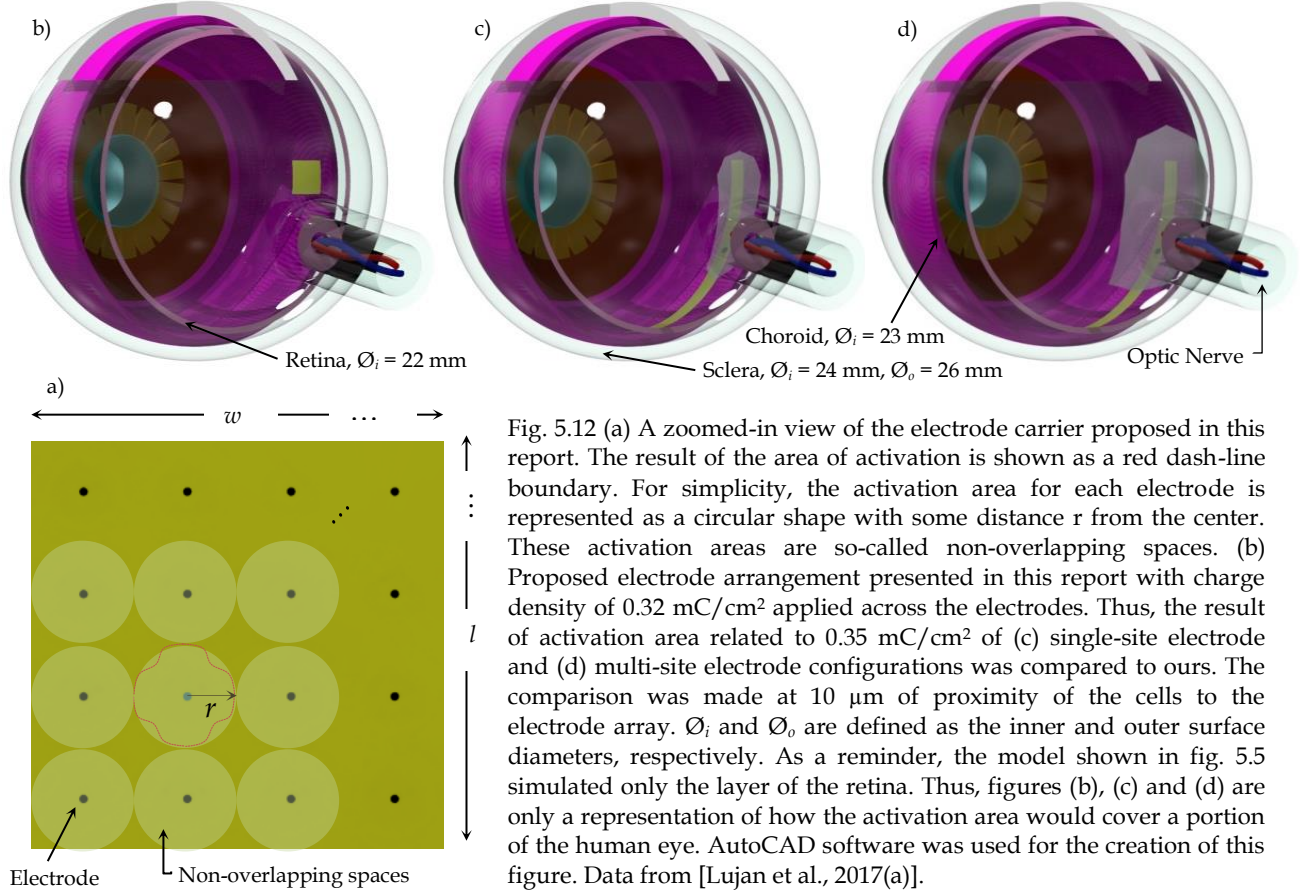


Fig. 5.12 (a) A zoomed-in view of the electrode carrier proposed in this report. The result of the area of activation is shown as a red dash-line boundary. For simplicity, the activation area for each electrode is represented as a circular shape with some distance  $r$  from the center. These activation areas are so-called non-overlapping spaces. (b) Proposed electrode arrangement presented in this report with charge density of 0.32 mC/cm<sup>2</sup> applied across the electrodes. Thus, the result of activation area related to 0.35 mC/cm<sup>2</sup> of (c) single-site electrode and (d) multi-site electrode configurations was compared to ours. The comparison was made at 10  $\mu\text{m}$  of proximity of the cells to the electrode array.  $\text{Ø}_i$  and  $\text{Ø}_o$  are defined as the inner and outer surface diameters, respectively. As a reminder, the model shown in fig. 5.5 simulated only the layer of the retina. Thus, figures (b), (c) and (d) are only a representation of how the activation area would cover a portion of the human eye. AutoCAD software was used for the creation of this figure. Data from [Lujan et al., 2017(a)].

The electrode voltage resulted in 0.07 V. The heat dissipated by the device reached 0.03°C. The threshold current of the non-activation space is 0.45  $\mu\text{A}$ . This means 0.32mC/cm<sup>2</sup> at proximity of 10  $\mu\text{m}$  of the cells to the electrode array. Thus, the result of activation area related to 0.35 mC/cm<sup>2</sup> of single and multiple electrode arrays from [Keserü et al., 2012] were compared to ours, see fig. 5.12(c) and 5.12(d), respectively. As a reminder, the complex model shown in figure 5.5 simulated only the layer of the retina. Thus, fig. 5.12(b), 5.12(c) and 5.12(d) are only a representation of how the activation area would cover a portion of the human eye.

#### 5.4.8. Discussion

It is evident that the stimulation strategy proposed in this report produces a narrower activation area than either single or multiple electrode configurations used in [Keserü et al.,

2012]. As such, the activation area that follows a non-overlapping space may enhance the detail perception of the visual field of view. This is due because the stimulus that spreads throughout the medium can be confined to the space required for activation. As such, the discrimination of the area of stimulation can be generated.

As previously stated the area of stimulation of single and multiple electrode stimulation is 26.13 and 69.41 mm<sup>2</sup>, see fig. 5.7 and 5.8. These electrode configurations activate a total of 7055 and 18740 cells per stimulation, respectively. The horizontal and vertical visual angles are 12.8° and 32° for single electrode stimulation. For multiple electrode stimulation the visual angles are 23.9° and 41.4°, respectively.

The activation area that follows the non-overlapping space has an activation size,  $r$ , of 0.03 mm and an activation area of approximately 0.003 mm<sup>2</sup>. The horizontal and vertical visual angles reach 0.2°. Thus, nearby cell selectivity would be attained by activating roughly a single cell per stimulation, assuming a cell density of 270 mm<sup>-2</sup>.

Comparable results of the simplified and the complex model were obtained using a 32 x 32 electrode array. Both models ensured safe stimulus within proximities of  $\leq 10$   $\mu$ m, electrode diameter of 5  $\mu$ m, rectangular pulse at 100  $\mu$ s of duration. Biocompatible electrode materials, image frequency of 20 fps, low power electronics and electrochemical safety were contemplated in the study. In the complex model, however, the cell was placed at the periphery of the space where the stimulus of the electrodes does not overlap, see fig. 5.11.

#### 5.4.9. Axonal Response

A key challenge that artificial visual devices are facing is the avoidance of stimulating retinal ganglion cell axons [Weiland et al., 2014; Jensen et al., 2005].

Retinal ganglion cell axons pass within short distances from each other along their path to the optic nerve to the brain. Since images are reversed horizontally and vertically on the retina by the optics of the cornea and lens, stimulation on the left side of the retina should create perceptions in the right side and vice versa. If the retinal axons coming from cells in the periphery are as well stimulated, then the perception would reflect activation of those peripheral cells and appear as an ellipse or streak [Weiland et al., 2014]. In practice, though, while subjects receive single electrode stimulus, they often report a stripe-shaped phosphene, rather than a focal spot of light due to unintended stimulation of passing axons [Nanduri et al., 2012].

This issue has been addressed by [Jensen and Rizzo III, 2005]. In their study, short-current pulses of 100  $\mu$ s or less are preferable because passing retinal ganglion cell axons can be avoided while stimulation. Choosing that pulse duration, the amount of current needed to generate a cell response is much lower than that required to generate an axonal response.

[Greenberg et al., 1999] reported that axonal threshold was 20% higher than the retinal cell threshold in simulation-based findings. [Jepson, 2012] informed experimental findings that exhibited precisely timing, sub-millisecond latency single spike responses which are a characteristic of direct ganglion cell activation using short pulse durations of 100  $\mu$ s and small electrodes of 15  $\mu$ s of diameter.

The ratio of axonal to cell threshold current response recorded by Jensen and Rizzo III was 4.5 for electrode diameter of 125  $\mu$ m. These results are related to use the threshold or minimum current to activate retinal ganglion axons and cells. Short-current pulse has the additional

benefit of reduced charge required for excitation. With reduced charge, the probability of electrode corrosion and tissue damage is lessened.

Regarding our simulation-based findings, the minimum threshold to activate a cell was increased to reach an activation size such that the activation areas do not overlap. This approach may increase the concern of generating an axonal response. That ratio of the minimum to the maximum-increased injected current in our study is 2.5, which is less than the ratio found by Jensen and Rizzo III. However, further experimental tests are required to validate our results. Throughout our study, short-current pulse of 100  $\mu$ s was used.

#### 5.4.10. Benefits of the Proposed Electrode Arrangement

To reach functional vision using visual prosthetic devices, a large number of stimulating electrodes [Weiland et al., 2014; Lujan (a), 2016, (c); Cha et al., 1992], high frequency stimulation [Humayun et al., 1999; Fried et al., 2006] and thus large peak current amplitudes are required. These peak current amplitudes should be distributed close to the active electrode in a sufficient small volume to trigger its respective cell.

[Wong et al., 2007] compared the cortical stimulation of one-and six-ground settings of current steering techniques. Experimental findings in animals suggested that six-ground setting was efficient because of the smaller area of cortical activation and of a reduction of unwanted interactions between multiple stimulation sites. Thus each electrode within a matrix requires the activation of preferably a single cell without current diversion between stimulating electrodes or electrode cross-talk.

As such, our proposal lies on the stimulation arrangement that consists of an active electrode (blue) surrounded by eight grounds (black). In effect the main reason of applying this configuration in practice is to confine the stimulus current to a small volume around the ganglion cell and to minimize electrode cross-talk during stimulation, see fig. 5.13.

Assembling the electrodes evenly yields an advantage to program each to function as an active or ground electrode with each having its own timeslot for stimulation [Meza, 2014].

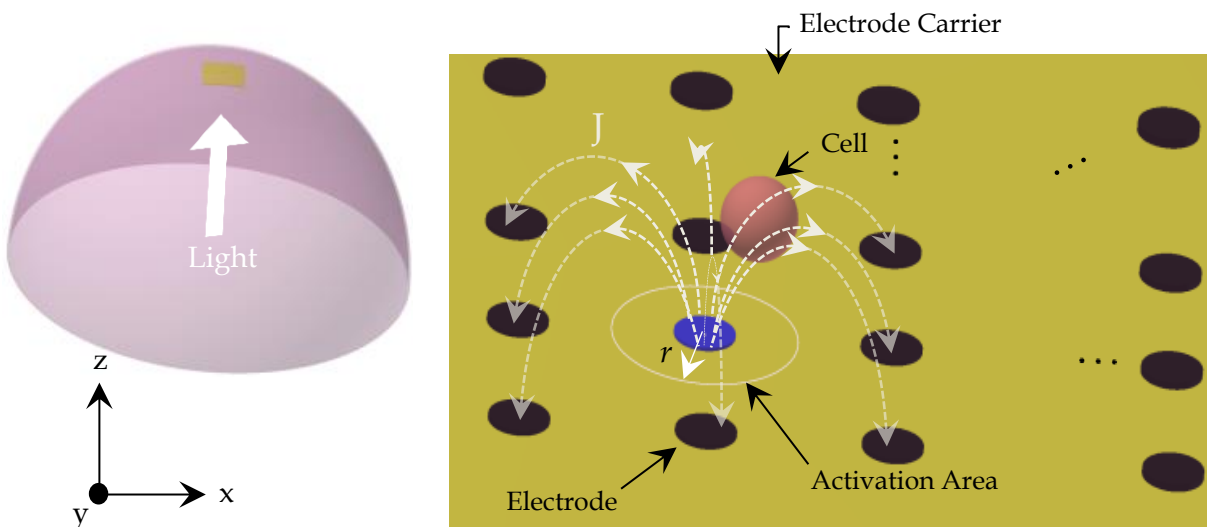


Fig. 5.13 Proposed stimulation arrangement that confines the current density stimulus  $J$  to a small volume along the surroundings of the ganglion cell. Inside the circular shape with radius  $r$  is located the activation area. AutoCAD software was used for the creation of this figure.

Applying this feature in practice allows the visual prosthetic device to be free of concerns related to neural tissue heating [Lujan (a), 2016].

#### 5.4.11. Summary

An accurate explanation of the activation area and its benefits to achieve cell stimulation are presented in this report. Furthermore the physical aspects related to the generation of phosphenes are explained and can be better understood by applying in practice the activation area.

Indeed the activation area can enhance detail perception of prosthetic vision because of a simple discrimination of area leading to a space required for cell activation. The activation area can be associated to any visual sensation represented as a phosphene while the retina is electrically stimulated. Thus, prior to device implantation in the retina, simulation-based findings of the activation area can be beneficial to understand lifelike situations of phosphenes.

The robustness of our technique is such that any cell density can be evaluated so as to direct visual prosthetic devices towards single localized stimulation which results in pixelized visual percepts. Likewise electrode topology plays a major role to achieve nearby cell selectively.

### 5.5.Spatially-based Visual Technique - Boosting Electrode Control over Single Cells

#### 5.5.1. Lessons learnt: Basis for this Chapter

As a result of the controlled-shape phosphene method, which I determined in the earlier section, it proved its usefulness to narrow the extent of the spreading stimulus and to generate a space required for stimulation of ganglion cells.

For this specific case, non-overlapping spaces of each electrode in a  $32 \times 32$  array confirmed the selectivity of a small number of cells. As formerly stated, the spatially-based visual technique uses a combination of proper current injection and electrode density to strengthen the control of electrodes over single cells. The injected current for the specific case of producing non-overlapping spaces will be used in this section.

#### 5.5.2. Aims

In this section, I will examine the spatially-based visual technique. Its aim can be understood as enhancing the control of the electrodes to selectively activate single cells. This can be treated by constraining the space of cell stimulation using a mixture of appropriate current injection and electrode density. Although researchers associate the stimulation of nearby cells as the definition of pixel-wise [Weiland, et al. 2014], our definition is that a single cell must be activated by a single electrode. The electrode density will be tested in this study as an exemplary case using the spatially-based visual technique.

Moreover, the feasibility of a  $32 \times 32$  electrode array will be investigated using biocompatible electrode materials, image frequency of 20 fps, low power electronics, small-size electrode and electrochemical safety.

### 5.5.3. Introduction

As we have learned throughout this report, retinal prosthetic devices have struggled for several decades to replace the functionality of photoreceptors lost because of degenerative diseases such as retinitis pigmentosa or age-related macular degeneration.

In recent years, epi- and subretinal electrode array implants have been developed. Humayun in several publications [Humayun et al., 1996, 1999, 2003, 2004; Mahadevappa et al., 2005], [Rizzo III et al., 1997, 2003], [Klauke et al., 2011], [Eger et al., 2006] and [Keserü et al., 2012] amongst recent clinical trials [Humayun et al., 2012; Stingl et al., 2013] have reported that blind patients perceived sensations of spots of light while the retina was electrically stimulated. These experiments clearly validated the viability of producing perception of light patterns in blind patients by electrically activate nearby ganglion cells.

Nevertheless, current status on clinical trials exhibit that patients do not encounter such flawless pixelized sight as shown in many publications [Weiland et al., 2014; Stingl et al., 2013; Humayun et al., 2012]. Recent clinical trials related to Argus II developed by Second Sight Medical Products in the United States did not exhibit an outdoor image perception of  $m \times n$  array of narrow spots of light that can be precisely controlled by the system.

Argus II best measured visual acuity was 20/1260 [Humayun et al., 2012]. This result was obtained in 7 of 30 test subjects. Alpha IMS developed by Retina Implant AG in Germany, reported the visual acuity in 2 of 9 test volunteers with a best measured of 20/546 [Stingl et al., 2013].

Forasmuch as some boundaries in the performance of implanted devices have been crossed, though, artificial vision is currently in an early-stage of maturity. Improvements related to detail perception coming from previous devices fall short of providing a suitable visual acuity which will be naturally reached by approaching single-cell selectivity. Visual and spatial perception of retinal prosthesis demands new techniques that allow devices to independently activate each ganglion cell and replicate natural patterns of activity in the retina.

### 5.5.4. Literature Review

[Jepson, 2014] investigated spatial patterns of current injection by considering two- and three-electrode settings so as to enhance spatial resolution while cells were electrically evoked. Although their findings could be helpful to understand the influences on current amplitude flowing through neighboring cells, however, a theoretical argument that clarifies on the preference of cell triggering for a specific two-electrode setting remains unclear considering that cells clearly follow a random distribution. Further, the correlation on cell-electrode distance for activation as a function of the current amplitude strength was disregarded as well as the number of cells probably activated as a function of cell-electrode distance for activation.

[Matteucci et al., 2013] proposed current steering or current focusing as a suitable method to enhance spatial localization. In that report, the effects of using a distant monopolar and hexapolar return setting were investigated. Nevertheless, it remains unclear to localize the area of cell response and the amount of current amplitude at scales that approach single-cell resolution.

[Wong et al., 2007] compared the cortical stimulation of two-, three- and six-ground settings of current steering techniques. Later, he concluded that six-ground setting was efficient because

of the smaller area of cortical activation. Nevertheless, settings with more than six-grounds have not been investigated.

[Bonham et al., 2008] investigated the spatial response only within the expected depth of current flowing into the body in cochlear implant. For all stated above, thus, pixelized visual perception is a major issue which needs to be addressed.

#### 5.5.5. Challenges at Hand - Cell and Electrode Density

A key challenge that visual prosthetic devices are currently facing is that the number of electrodes and their position remain fixed whereas the cell density degenerates with time because of the sight disease evolution.

The cell density as it is reduced single electrode site is more concentrated to stimulate a single cell, however, groups of electrodes are purely useless and are carelessly used [Lujan (c), 2016]. This might cause discrepancies as to how many cells are activated by a single electrode.

Conversely, once the electrode density is further reduced compared to the cell density, the ganglion cells are more tightly-packed than electrodes. As a result, single electrode activates a bundle of cells, thereby reducing focal activation and greatly decreasing resolution.

Cell density in patients blinded by photoreceptor progressive diseases, such as retinitis pigmentosa (RP) or age-related macular degeneration (AMD), is purely a constraint for visual prosthesis because single cells should be activated by single electrodes to a feasible extent. As such, this can be treated by controlling the space of each electrode to independently activate adjacent cells and to form an array of independent phosphenes.

Critical AMD and RP patients have cell densities of around 585, 536, 329 and 824 mm<sup>-2</sup> at the temporal, superior, inferior and nasal segment of the eye, all respectively, assuming that 30% of cells are preserved [Santos et al., 1997] and that safe navigation in dynamic out-door environments requires the placement of the carrier around 15° of eccentricity [Cha et al., 1992].

Nowadays, microelectrode arrays are developed with large electrode diameter and small electrode density far from what is preserved in the inner retinal region of AMD and RP patients [Humayun et al., 2012; Cha et al., 1992; Mahadevappa et al., 2005; Rizzo III et al., 2003; Klauke et al., 2011] see table 5.2, for mention a few. Thus, one aim in this study is of principal interest in comparing the effect of the electrode density to investigate the amount of nearby cells activated by each electrode in order to optimize pixel-wise stimulation.

TABLE 5.2

Visual Prosthesis	Number of Electrodes	Electrode diameter [μm]	Electrode spacing <sup>1</sup> [μm]	Electrode density [mm <sup>-2</sup> ]
[Humayun, 2001]	16	520, 260	800	1.5
[Mahadevappa, 2005]	16	500	800	1.5
[Eger et al., 2006]	24	100	750	1.78
[Rizzo III et al., 2003]	20	100	620	2.6
[Humayun et al., 2012]	60	200	575	3
[Klauke et al., 2011]	25	100	500	4
[Rizzo III et al., 2003]	100	50	220	20

<sup>1</sup>Spacing is center-to-center.

### 5.5.6. Spatially-based Visual Technique Method

The algorithm of the visual technique is as displayed in figure 5.14. Each processing step is further explained in sequential order based on its appearance.

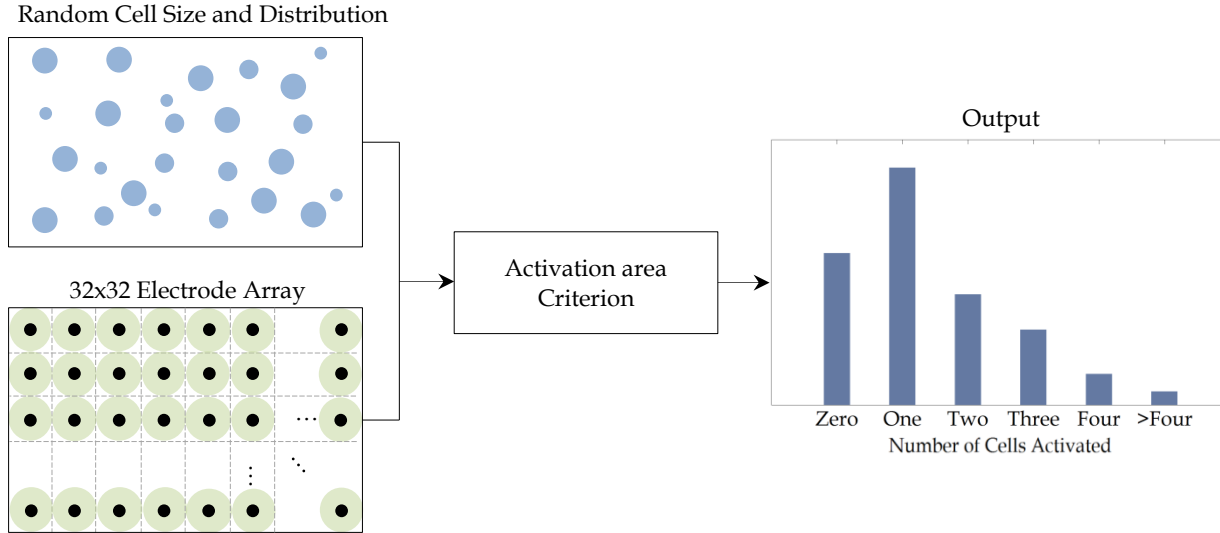


Fig. 5.14 Algorithm of the visual technique. The decision-making step of cell activation uses a 32 x 32 electrode array with square grid distribution, a random distribution of cells with some cell density and the activation area originated from the controlled-shape phosphene. Then, the activation area criterion is implemented. That is, if stimulation of some electrode is achieved inside its own activation area, a counter increases its value by 1 in this electrode. Otherwise the counter remains unchanged. The output corresponds to a bar table that indicates the percentage of electrodes ( $y$ -axis) that activate a specific number of cells ( $x$ -axis).

#### 5.5.6.1. Electrode Array Coding

The allocation of a 32 x 32 electrode array was coded in Matlab as a simple *square grid* that followed the directions explained in section 5.4.4.

#### 5.5.6.2. Cell Density Coding

The distribution of cells was coded in Matlab and on the electrode carrier such that the distances to the neighboring cell (or the edges) in each axis are *randomly* distributed. This can be understood as an attempt of reaching a real *randomness* scenario of cell position and have meaningful conclusions in cell activation and electrode usage. The cell radius was as well *randomly* distributed between 5, 10 and 15  $\mu\text{m}$  to characterize small, medium and large ganglion cells found in experiments [Wenzhi, 2002]. The cell density,  $\rho_c$ , was obtained by interpolating the actual number of cells calculated as the total number of cells randomly dispersed inside the electrode carrier minus the overlapping cells inside an area of 1mm<sup>2</sup>.

#### 5.5.6.3. Activation of Cell

The activation of nearby cells was coded in Matlab and obeyed the condition of the activation area. This states that a ganglion cell located inside the activation area of an electrode is activated. Otherwise, the cell is not stimulated.



As a reminder, the activation area is defined as a two-dimensional space along the retinal surface where the current spread across the electrodes is sufficient to trigger a response of the cell. Its area main goal is to argue for its applicability as a tool for defining a space where the stimulus initiated at the active electrode in effect triggers a cell response. As formerly stated, the current flowing across the electrodes can be constrained as the activation area discriminates the space required for cell activation.

Hence, the current applied to the electrodes should be such that each electrode will cover a sufficient space of stimulation without overlapping with neighboring electrodes. Applying this approach in practice, the stimulation of bundles of cells by a single electrode would be reduced and detailed perception can be achieved. For more information, see section 5.4.

#### 5.5.6.4. Output

The condition to compute the quantity of cells stimulated by each electrode is as follows. If stimulation of some electrode is achieved inside its own activation area, a counter increases its value by 1 in this electrode. Otherwise the counter remains unchanged. The output corresponds to a bar table that indicates the percentage of electrodes that activate a specific number of cells.

For each implementation, the script used a total of 1 cycle as each electrode investigated if cells were inside its activation area. This was followed so as to attempt reaching a real case randomness scenario of cell distribution and have meaningful conclusions of the electrode stimulation profile. Overall, the visual technique algorithm was repeated 100 times to obtain probabilistic values of the results.

#### 5.5.6.5. Assumptions

The assumptions in the visual technique are i) assemble the array of electrodes homogeneously so as to give the advantage to program each to function as an active or ground electrode; ii) each electrode can have a different timeslot and each can be activated independently with a total image frequency of 20 Hz [Lujan (a), 2016; Meza, 2014]; iii) irreversible Faradaic reactions, i.e. electrolysis of water and corrosion, if present, will occur such that charge density or electrode voltage surpasses their own limit; iv) the cell can move only along the ganglionic layer.

### 5.5.7. Visual Field of View Relationship

The main goal of artificial vision is to provide the patient a useful visual perception. Thus, an additional aim that should bear in mind is to provide an adequate large-sized visual field of view with such quality for, e.g. face recognition.

Since our principal interest is the effect of electrode density in order to optimize pixel-wise stimulation, the following relationship highlights the knowledge of the size of visual field of view as a function on the electrode density. The size of visual field of view, see fig. 5.15, can be computed as

$$L = 2D \tan\left(\frac{V}{2}\right), \quad (5.9)$$

$V$  is the visual angle subtended by the visual field of view with sizes  $W$  and  $L$  located in some distance  $D$  from the point  $O$ .

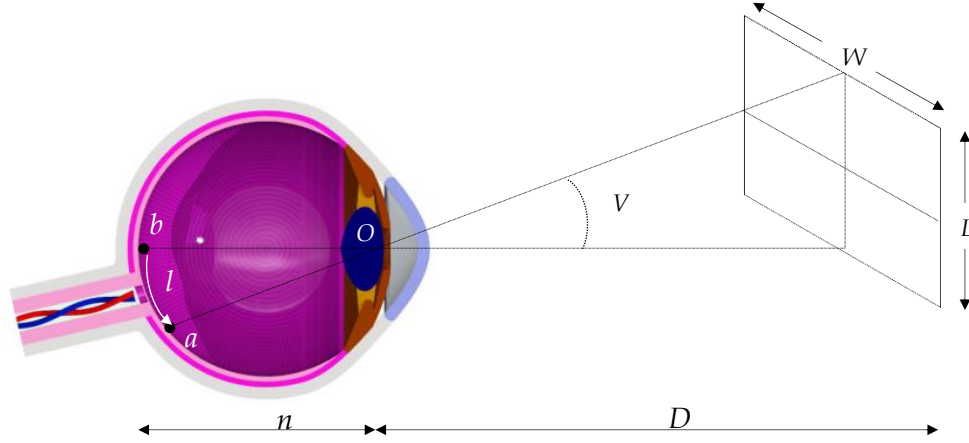


Fig. 5.15 Typical diagram of the visual angle subtended by some visual field of view. The diagram shows the visual angle  $V$ , visual field of view with sizes  $W$  and  $L$ , and the location of the electrode carrier placed on the surface of the retina between points  $a$  and  $b$  with carrier length  $l$ .

The visual prosthetic is placed epiretinal between points ' $a$ ' and ' $b$ ', see fig. 5.15. The angle between both points can be calculated as

$$V = \arctan\left(\frac{l}{n}\right), \quad (5.10)$$

$n$  is the distance from the nodal points to the retina and  $l$  is the length of the electrode carrier.

As formerly explained in section 3.3.2.1 and 5.4.3, the electrodes are evenly distributed in a  $32 \times 32$  in a single array, see fig. 5.11. Each electrode is separated with an electrode distance. Its length,  $l$ , and width,  $w$ , are assumed to be equivalent. Thus,  $W$  and  $L$  of the visual field of view follow the same association.

The substitution of (5.6) through (5.5) into (5.10) leads to (5.11)

$$V = \arctan\left(\frac{1}{n\sqrt{\rho_E}}(\sqrt{e_T} + 1)\right). \quad (5.11)$$

Finally, the substitution of (5.11) into (5.9) leads a relationship of the electrode density as a function of the size of the visual field of view

$$L = 2D \tan\left[\frac{1}{2} \arctan\left(\frac{1}{n\sqrt{\rho_E}}(\sqrt{e_T} + 1)\right)\right]. \quad (5.12)$$

However the following relationship provides very close approximations

$$L = \frac{D}{n\sqrt{\rho_E}}(\sqrt{e_T} + 1), \quad (5.13)$$

if

$$\rho_E \gg \frac{1}{n^2} (e_T + 2\sqrt{e_T} + 1). \quad (5.14)$$

### 5.5.8. Input Data of the Visual Technique

The controlled-shape phosphene method, see section 5.4, displayed its utility to confine the scope of the spreading stimulus and to produce an area necessary for cell stimulation. For this specific case, non-overlapping spaces bounded in a 32 x 32 electrode array strengthened the activation of a small number of cells. Thus, the activation area similar to those will be used in this section. As formerly stated, electrode densities in current devices are far from what it is preserved in RP or AMD patients. In this study, electrode density behaves as a variable to investigate single cell selectivity among the densities tested.

The distribution of the ganglion cells can be estimated using the results of [Curcio, 1990] who provided densities of all coordinates of young retinas at eccentricity of 15° and assuming that safe navigation in dynamic out-door environments requires stimulation around that eccentricity [Cha et al., 1992]. The density of cells for RP or AMD can be calculated as 25% of the total ganglion cells which are preserved in the inner retinal region [Santos et al., 1997], see table 5.3. Electrode carrier is assumed to be located on the temporal segment of the eye having a fixed cell density,  $\rho_C$ , of approximately 585 mm<sup>-2</sup>. The electrode density,  $\rho_E$ , was varied with values of 4  $\rho_C$ , 2  $\rho_C$ ,  $\rho_C$ , 1/2  $\rho_C$ , and 1/4  $\rho_C$ .

As formerly stated, geometric and stimulating parameters defined in earlier chapters were used. Overall, an array of 32 x 32 electrodes with diameter of 5  $\mu$ m was used. Proximity of cells to the electrodes is 10  $\mu$ m. Rectangular pulse shape was applied with pulse duration of 100  $\mu$ s. Domain geometry and definitions similar to table 3.2 and can be found in table 5.1.

TABLE 5.3

	Temporal	Superior	Nasal	Inferior
Heathy Retina[cells/mm <sup>2</sup> ]	2339	2144	3294	1316
Degenerated Retina [cells/mm <sup>2</sup> ]	585	536	824	329

### 5.5.9. Results and Discussion

The results of the study are displayed in figure 5.16. The  $y$ -axis indicates the percentage of electrode sites that activate a specific number of cells denoted in the  $x$ -axis. The arrangement is based on showing the results of each electrode density as a bar graph fashion and the standard deviation of each case.

### 5.5.10. Analysis of Electrode Density and Cells Activated

Electrode density as it comes closer to the cells several benefits can be achieved while cells are stimulated, i) one-to-one cross section area of cell and electrode is more likely to be attained and ii) the control of each electrode stimulus is confined to each cell. The result as the densities are matched indicated that indeed the constraint of electrodes over single cells is achieved reaching 53% of the total amount of electrodes, see fig. 5.16. However, the percentage of electrode sites

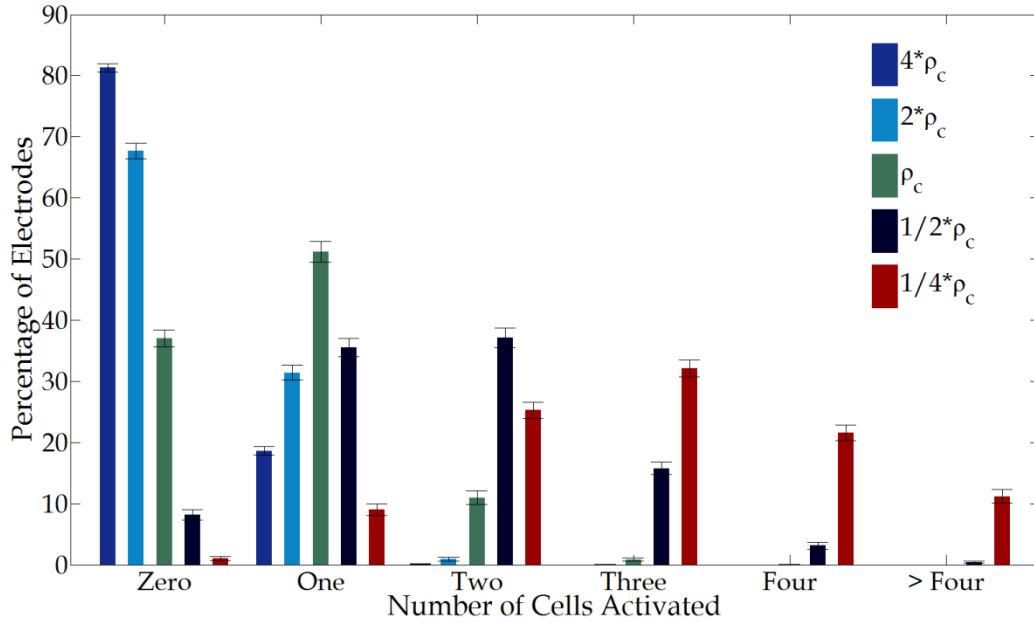


Fig. 5.16 Percentage of electrodes that activate a specific number of cells. The arrangement is based on showing the results of each electrode density as a bar graph fashion and the standard deviation of each case. The electrode density,  $\rho_E$ , was varied with values of  $4\rho_c$ ,  $2\rho_c$ ,  $\rho_c$ ,  $1/2\rho_c$ , and  $1/4\rho_c$ .

that did not accomplished stimulation reaches to 37%. A small percentage of 10% stimulated more than one cell.

This idea of matching the densities of electrodes and cells may be suitable because it would lead that more than a half of the electrodes inside the array are contributing for pixel-wise stimulation. Nevertheless, real situations of preserved cells in patients may impose constraints for achieving pixel-wise activation. The variability of ganglion cell position and lifetime might require some flexibility to choose different array configurations to improve the performance of visual prosthetics, e.g. multiple-site electrode stimulation. Choosing parallel stimulation would require low power consumption of each local stimulator unit to minimize neural tissue heating. Accordingly, advance biocompatible materials must be put forward to overcome major challenges of bioelectronics implants including long-term steady performance of implanted electronics.

The electrode density as it is increased compared to the cells, single electrode sites are more concentrated to stimulate single cells. Though, groups of electrodes cannot achieve stimulation and are carelessly used [Lujan (c), 2016]. Having stated the above, the results of electrode density by doubling and quadrupling the cells reached 31 and 18% of activating a single cell, respectively. Nevertheless, a high number of electrodes of around 67 and 81%, all correspondingly, are misused. Conversely, the electrode density as it is further reduced compared to the cells, the ganglion cells are more tightly-packed than electrodes. As a result, single electrodes activate a bundle of cells, thereby reducing focal activation and greatly decreasing resolution. This might cause discrepancies as to how many cells are activated by a single electrode.

The electrode density as it halves the density of the cells would decrease the situations of electrodes being misused reaching values less than 10%. The situation of activating one and two electrodes is nearly at the same level achieving 35%. This situation formerly stated is more

visible once the electrode density takes values less than a half of the cell density. In the specific case of electrode density quartering the cells, the results of activating a single cell reached less than 10%.

Despite these results are promising for pixel-wise stimulation, a different interpretation may arise amongst one another. Current devices apply electrode density far from than that is preserved in the inner retina. Argus II is currently implanting a retinal device with an electrode density of around 3 mm<sup>-2</sup>. The electrode carrier has dimensions of around 3 x 5 mm<sup>2</sup> with an electrode diameter of 200 µm and electrode distance of approximately 375 µm. The outcomes presented in figure 5.16 can direct the understanding of the performance of electrodes while they are activating nearby cells. As an electrode carrier with an electrode density lower than the cells is implanted inside the eye, the ganglion cells are more densely-compacted than electrodes. Accordingly, a bundle of cells may be activated by a single electrode.

#### 5.5.11. Is Cell Density Data a Requirement?

As formerly stated, the cell density of a sight-deteriorated patient should be known parameter in order to determine the electrode density and the distribution of the electrodes in a single array for a given electrode diameter. Nowadays a realistic count of cell density can be reached by morphometric analysis [Santos et al., 1997].

Once the cell density is not known, however, PR or AMD consequences related to cell degeneration due to sight disease evolution are well known. Santos et al. estimated that 25% to 30% of ganglion cell are preserved in the inner retinal region in patients with AMD and RP [Santos et al., 1997]. The distribution of the electrodes in a single array can be estimated using the results of [Curcio, 1990] who provided densities of all coordinates of young retinas at eccentricity of 15°, and assuming that safe navigation in dynamic out-door environments requires stimulation around that eccentricity [Cha et al., 1992]. Table 5.4 lists an example of the dimensions of the electrode carrier and visual field of view size based on the average of cells densities of each coordinate.

Equations (5.5), (5.7), (5.8), (5.11) and (5.12) were used to compute the electrode carrier length, electrode distance, electrode carrier area, visual angle and the size of the visual field of view, all respectively. Electrode diameter of 5 µm was used in equation (5.7). The inputs to calculate the electrode carrier length and the size of the field of view are the total number of electrodes of 1024. The distance of some object away from the eye is 6 meters. The distance from the nodal points to the retina is 17 mm. The electrode density is equal to the cells.

Table 5.4 can be used for developing an efficient electrode array by choosing the position of the electrode carrier inside the human eye.

#### 5.5.12. Electrode Size

Electrode size is perhaps the variable much investigated when an electrode carrier array is developed [Chen et al., 2013; Rothermel et al., 2008; Lujan (c), 2016; Tran et al., 2014; Monge et al., 2013; Chen et al., 2010; Ortmanns et al., 2007]. It is well known that decreasing electrode dimension will generate higher resolution patterns of prosthetic-elicited activity that are closer to light-elicited patterns and improve visual reception [Fried et al., 2006].

[Mahadevappa et al., 2005] developed two electrode arrays. Each corresponds to an arrangement of 4 x 4 platinum electrodes. The first set corresponds to an electrode diameter of

TABLE 5.4

	Temporal	Superior	Nasal	Inferior
Cell density [mm <sup>-2</sup> ]	585	536	824	329
Electrode density [mm <sup>-2</sup> ]	585	536	824	329
Electrode Carrier Length [mm]	1.36	1.42	1.14	1.82
Size of the field of view [m]	0.48	0.5	0.4	0.67
Electrode Distance [ $\mu$ m]	36.3	43.19	34.8	55.21
Electrode Carrier Area [mm <sup>2</sup> ]	1.86	2.03	1.32	3.32
Visual Angle [°]	4.59	4.79	3.86	6.11

500  $\mu$ m and an electrode distance of 300  $\mu$ m. The second use a 250  $\mu$ m electrode diameter with an electrode distance of 550  $\mu$ m. Assuming that a patient has some number  $x$  of cells per mm<sup>2</sup>, the first set of electrodes developed by Mahadevappa using electrode diameter of 500  $\mu$ m would cover  $x/4$  of 1 mm<sup>2</sup> and may afocally stimulate roughly  $x/4$  cells per mm<sup>2</sup> if the density of cells is larger than 4 mm<sup>-2</sup>.

The cell density calculated in this study for severe RP or AMD patient is roughly 585 mm<sup>-2</sup>, assuming to place the array at the temporal segment of the eye. Thus, electrode diameter of 500  $\mu$ m would afocally evoke approximately 145 cells.

Argus II [Humayun et al., 2012] was developed using a rectangular electrode carrier with an electrode diameter of 200  $\mu$ m and electrode distance of approximately 375  $\mu$ m. Using the formerly approach to calculate the number of cells activated by a single electrode, i.e. afocally stimulation, an electrode of 200  $\mu$ m size would cover and stimulate roughly  $x/25$  cells per mm<sup>2</sup>. Thus, approximately 23 cells per electrode.

A useful technique to define the electrode diameter would be to determine it such that the electrode is contained by the area element of  $d^2$ , see fig. 5.11. The electrode pitch,  $d$ , can be defined assuming that the electrode density in an epiretinal system would be equal to the cells, see eq. 5.6. The activation area, see section 5.4, can be beneficial to cover the remaining space where a ganglion cell would be located. Following this strategy, the hazard of the retinal tissue is reduced as high charge density is required by using very small electrode size.

### 5.5.13. Activation Size: Benefits and Shortcomings

Once the activation size increases, far localized cells can be evoked. Nevertheless, the flexibility of increasing the injected current so as to reach more neighborhoods should not be misinterpreted.

Safeguarding the operation of stimulators is by far most a crucial issue in neural activation. Safety, in terms of electrical performances, is mainly related to four factors: charge density injection level, heat generated at tissue due to power dissipation, DC current flow into tissue, and surpassing water-voltage window.

The electrochemical reactions at the electrode-tissue interface, i.e. capacitive double-layer charging, reversible Faradaic and irreversible Faradaic reactions, carry out charge injection into the neural tissue [Brummer et al., 1977; Merrill et al., 2005; Cogan et al., 2008].

The latter reaction can produce electrolysis of water that leads to localized pH changes [Huang et al., 2001], gas bubble formation that thought to be harmful and physically disturbs the tissue [Merrill et al., 2005; Cogan et al., 2008] and chemical species formation that damage the tissue or the electrode [Brummer et al., 1977].

Electrolysis of water may occur as well as a result when maximum cathodic and anodic potential across the electrodes surpass the “water window” boundary [Merrill et al., 2005]. The water window is a potential range that is defined by the reduction of water, forming hydrogen gas, in the negative direction, and the oxidation of water, forming oxygen, in the positive direction which may cause corrosion.

#### 5.5.14. Visual Acuity

Visual acuity is defined as the ability of the eye to perceive fine details and is measured as the fineness of some object that can be detected. Visual acuity in Snellen notation is given by the relation

$$VA = \frac{d'}{D'}, \quad (5.15)$$

$d'$  refers the space in meters between the subject and some object. A reference value of  $d'$  is 6 meters. Distance  $D'$  denotes to the space at which a person with 6/6 acuity would discern the same object. A reference value above which visual acuity is considered normal is called 6/6 vision.

The reciprocal of the Snellen Notation equals the angle measured in arc minutes. A healthy subject with 6/6 visual acuity can resolve two points of light separated by a visual angle of 1 minute of arc. Visual acuity can be additionally measured as the smallest visual angle a person can detect subtended from some visual element of an object, regardless of whether such element represent a line, spot or alphabetic character identity [Lehto et al., 2012]

$$VA = \frac{1}{V}, \quad (5.16)$$

$V$  represents the visual angle. A normal person with 6/6 visual acuity can resolve two points of light separated by a visual angle of 1 minute of arc. As such, 1/60 of an angle of 1° corresponds to 1 arc minute. Substitution (5.16) into (5.17) leads a relationship to compute distance  $D'$  and thus the fraction of the visual acuity can be attained

$$D' = d' \frac{V}{a'}, \quad (5.17)$$

$a'$  corresponds to 1 minute of arc.

Electrode diameter of 500  $\mu\text{m}$  used in the device developed by Mahadevappa can produce a visual angle of 1.68° using equation (5.11). The result of such device would be equivalent to 101 arc minute. The visual acuity would be then 6/606.

Argus II can produce a visual angle of 0.67° using an electrode diameter of 200  $\mu\text{m}$ , which is equivalent to a 40 arc minute response. Thus, the visual acuity would be 6/240.

The best result observed in this study is related to use the activation size of 20  $\mu\text{m}$  at electrode density of 585  $\text{mm}^{-2}$ . Assuming that the detail perception would be associated to the space of the

activation size, a visual angle of  $0.13^\circ$  can be produced using our technique, which is equal to 8.3 arc minute and a better visual acuity of 6/50.

#### 5.5.15. Dark Gap Response

The controlled-shape phosphene method, see section 5.4, provided a useful technique to constraint the spreading stimulus from the active electrode and to produce a required region of stimulation for the purpose of reaching pixel-wise stimulation. For this particular case, non-overlapping spaces were created.

Once the activation size is small, the electrode strength to activate single cells is constrained by a small area and the injected current might not be enough to trigger a response. Thereby it influences the visual and spatial recognition and perception on the visual field of view. As the activation size increases, however, the electrode strength can reach a far localized cell and the restriction to trigger a response is minimized. This size increase, though, should not be overestimated because tissue and electrode damage may occur once the charge density and voltage surpass their own harmless limits [Scheiner et al., 1990].

A dark gap response might occur between the electrodes if the activation size is not enough to cover the space associated to the non-overlapping area. Previously published reports stated that electrodes with 5  $\mu\text{m}$  of diameter can attain 6/6 visual acuity [Palanker et al., 2005]. Using equation (5.10), the visual angle of 5  $\mu\text{m}$  of length is 0.016, which is equal to roughly 1 arc minute and correlated with that visual acuity. Assuming that the detail perception would be related to the space of the activation size, a dark gap response may happen if the activation size is equal to the electrode radius. More precisely, the stimulus would activate cells in an area covered by the electrode. As a result, the visual perception will be composed of small bright dots surrounded by dark vicinities correlated to the space where no electrode can stimulate. Accordingly, an unclear visual field image will be created if the stimulation scheme neglects the insight of incrementing the injected current such that cells located in far vicinities can be activated.

Once the electrode distance lengthens its size, a comparable response may occur. Each phosphene generated by stimulation may be surrounded by a dark space and might produce an undistinguishable field of view. It might be argued that, by increasing the electrode distance so as to make the electrode carrier larger and the visual field of view bigger, a better visual perception will be reached. Argus II electrode array activates cells with an electrode spacing of 575  $\mu\text{m}$ . Mahadevappa et al. developed an electrode arrangement that used 800  $\mu\text{m}$  of electrode distance, for mention a few, see table 5.2 for more examples.

The cell density of degenerated retina ranges from 329 to 824 cells/ $\text{mm}^2$ , see table 5.4, assuming that 25% of ganglion cell are preserved in cases of RP or AMD. Thus, following our approach, the optimal electrode spacing varies from 78 to 49  $\mu\text{m}$  center-to-center, all respectively. We believe it is useful to resolve first the issues related to far localized cell stimulation. Then, a better outdoor image will come naturally.

#### 5.5.16. Probability Derivation of Cells inside an Arbitrary-Sized Activation Area

To improve pixelized visual perception, high spatial resolution must be addressed. In other words, electrodes require the capacity to follow single-cell selectivity and to activate cells to a feasible extent.



This in principle requires the space of the activation size to be sufficient to reach a cell and produce a bright pixel related to its size generated by stimulation. For a given size of the activation area, then each point in the electrode carrier area belongs to one of two different regions: 1) inside the activation area or 2) outside of activation area. In each case, the summation of the areas of these two regions divided by the area of the electrode carrier gives two numbers  $n_1$  and  $1 - n_1$ .

If we now randomly place a cell into the electrode carrier area,  $n_1$  is the probability of a cell to be inside the activation area and  $1 - n_1$  is the probability of a cell to be outside of the activation area.

$$n_1 = \pi A^{-1} \sum_{k=1}^{e_r} r_k^2. \quad (5.18)$$

If the activation size is related to the non-overlapping space,  $n_1$  is independent of the electrode density and results with a probability of around 3/4.

#### 5.5.17. Feasibility of 32 x 32 Array with High Electrode Densities and High Proximities

This section investigated the feasibility of a 32 x 32 electrode array with electrode densities equal to the cells between 100 and 2000 mm<sup>-2</sup>. As such, the investigation included cell densities commonly seen in RP or AMD patients, assuming to place the electrode carrier around 10° to 15° of eccentricity [Cha et al., 1992]. Biocompatible electrode materials, image frequency of 20 fps, low power electronics, small-size electrode and electrochemical safety are contemplated in this study. This inquiry included proximities of cells to the electrodes of 100 μm.

In this specific investigation, the controlled-shaped algorithm was implemented as explained in section 5.4 such that the non-overlapping spaces were generated. The input parameters stated in section 5.4 are kept except where expressly varied. Electrode diameters tested were 5, 10 and 20 μm. Electrochemical considerations, see fig. 5.10, ensure that electrode voltage, charge density and heat generated by the device must be below their limits to avoid the formation of corrosion [Brummer et al., 1977], electrolysis of water [Merrill et al., 2005] and significant damage to various cellular functions due to an excessive tissue heating [Sohee et al., 2007].

The results of 5 μm electrode diameter are illustrated in figure 5.17. The main limitation as it is formerly found in chapter 3 can be attributed to the charge density delivered into the tissue. As such, innovative coat materials with high charge density capability are a requirement for protect the sensible retinal tissue against the hazards of electrolysis of water. Heat dissipated into the tissue remains with low values. The performance of the device can be attributed to the hybrid architecture of the DACs (digital-to-analog converter) as it has benefits regarding low power consumption. Further, this behavior can be attributed to the use of the duty cycle and few LSU per pulse duration. Generally, high proximities of cells to the electrodes require a large size of the electrodes such that the charge density delivered remains below the limit of electrolysis of water.

The results of 10 μm electrode diameter are illustrated in figure 5.18. Using this small-sized electrode, the limitation of charge density is exceeded at around 100 mm<sup>-2</sup>. The boundary of electrode voltage is later exceeded at around 900 mm<sup>-2</sup>. Comparable results of the simplified and the complex model were obtained using a 32 x 32 electrode array at high proximities of 100 μm. Both models guaranteed safe stimulus with electrode diameter of around 10 μm at electrode densities of 82 and up to 150 mm<sup>-2</sup>, see figs. 3.10 and 5.18, all respectively.

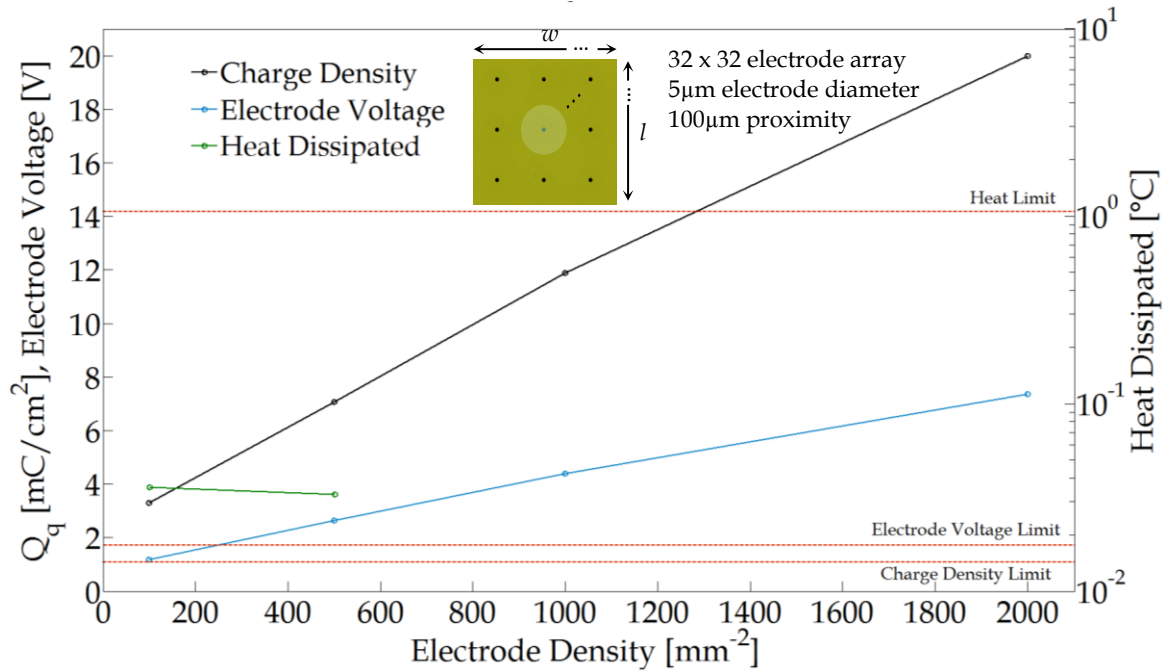


Fig. 5.17 Feasibility of a 32 x 32 electrode array reaching non-overlapping space at proximity of cells to the electrodes of 100  $\mu\text{m}$ . Electrode diameter of 5  $\mu\text{m}$  is tested.  $Q_q$  represents the charge density delivered to the tissue. The limits of each parameter are 1  $\text{mC}/\text{cm}^2$  for charge density, 1.7 V for water voltage limit and 1°C for heat limit.

The results of 20  $\mu\text{m}$  electrode diameter are illustrated in figure 5.19. The boundary where the charge density is exceeded is around 1000  $\text{mm}^2$  of electrode density. The water voltage limit is exceeded later at electrode density of 1700  $\text{mm}^2$ . Back again, the charge density can be attributed as the main limitation at high proximity of cells to the electrodes.

Close proximity of the cells to the electrode array is a critical issue for safe visual stimulation [Nanduri et al., 2012; Lujan (b), 2016]. Nowadays state-of-the-art visual implants secure the electrode array with small tacks to the retina [Humayun et al., 2012].

Once the electrode array is fastened to the surface of the retina, a safe stimulus can be delivered from the electrodes. As threshold current reduces with closer proximity of the cells to the electrodes, the charge density follows the same association and a harmless stimulus is thus delivered.

Further, a distant proximity of the retina to the electrode array contributes to the varying current spread from the active electrode causing changes in the area of stimulation and thus affects the resolution of the visual prosthesis [Kasil et al., 2011].

Electrode diameter of 20  $\mu\text{m}$  can generate the non-overlapping space in electrode densities up to 1000  $\text{mm}^2$ . Assuming that electrode density would match the cells, this approach can be useful to place the microelectrode array close to the fovea and increase spatial resolution.

This electrode dimension of 20  $\mu\text{m}$  is still a small-sized electrode. Existing artificial devices developed by [Mahadevappa et al., 2005], [Reinhard et al., 2006], [Rizzo et al., 2003], [Humayun et al., 2012] and [Klauke et al., 2011] use big-sized electrode diameter of 500, 200 and 100  $\mu\text{m}$ . Large-sized electrodes in such implanted devices [Rizzo III et al., 2003; Stingl et al., 2013; Reinhard et al., 2006] likely activates hundreds or thousands of cells over their area of stimulation.

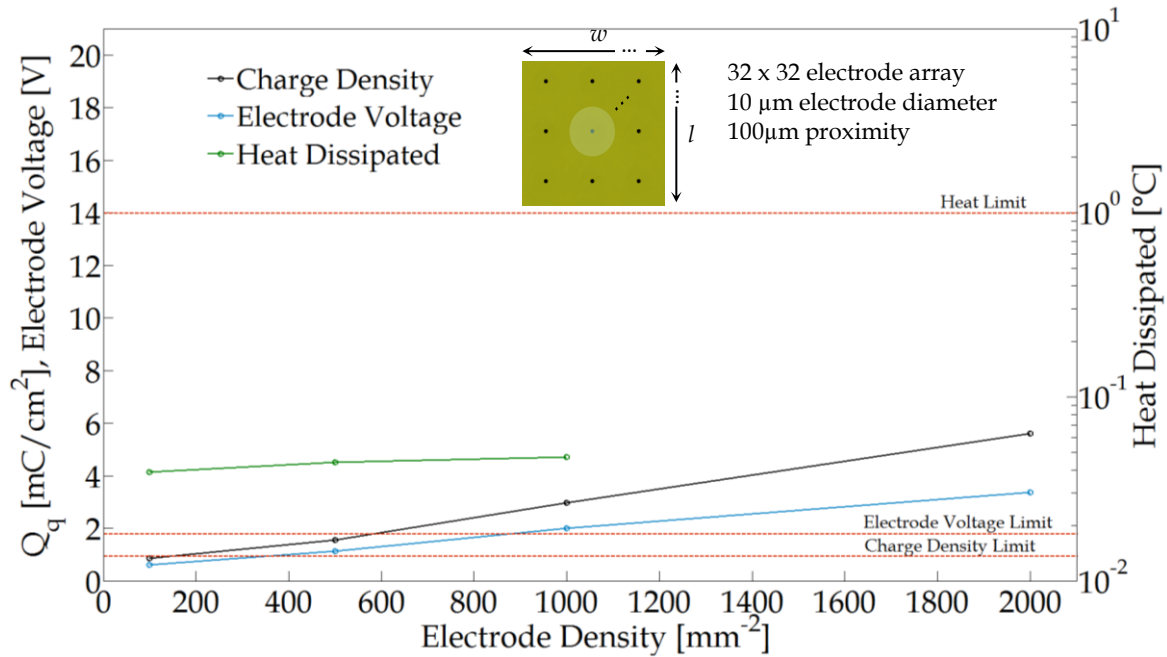


Fig. 5.18 Feasibility of a 32 x 32 electrode array reaching non-overlapping space at proximity of cells to the electrodes of 100  $\mu\text{m}$ . Electrode diameter of 10  $\mu\text{m}$  is tested.  $Q_q$  represents the charge density delivered to the tissue. The limits of each parameter are 1  $\text{mC}/\text{cm}^2$  for charge density, 1.7 V for water voltage limit and 1°C for heat limit.

#### 5.5.18. Safe Electrode Carrier Size

Electrode carrier size is limited up to 5 mm due to the small incisions that must be made in the eyewall [Weiland, 2014]. The relationship between the visual field of view, left y-axis, and electrode density, x-axis, is depicted in figure 5.20. Electrode distance and electrode carrier size (length,  $l$ , or width,  $w$ ) are additionally shown at right y-axis for electrode diameter of 5  $\mu\text{m}$ .

Equations 5.5, 5.7 and 5.12 were used to calculate the electrode carrier size, electrode distance and size of the visual field of view, respectively. The inputs are the total number of electrodes of 1024. The distance of some object away from the human eye is 6 meters. The distance from the nodal points to the retina is 17 mm. On top of the plot of the electrode carrier size are indicated the results of electrode densities that can be used for placing the microelectrode carrier at eccentricity of 15°. Four electrode densities are displayed, corresponding to each segment of the eye, assuming that the electrode density in an epiretinal system would be equal to the cells, see table 5.4.

The results indicate that microelectrode arrays being suitable for pixel-wise stimulation are within the safe region of size for implantation, regardless of using 5 or 20  $\mu\text{m}$  electrode diameter.

#### 5.5.19. Summary

The following rules-of-thumb are given as opening guidelines when considering the starting point of developing a retinal implant of 1024 electrodes to enhance pixelized visual perception and to guarantee electrochemical safety,

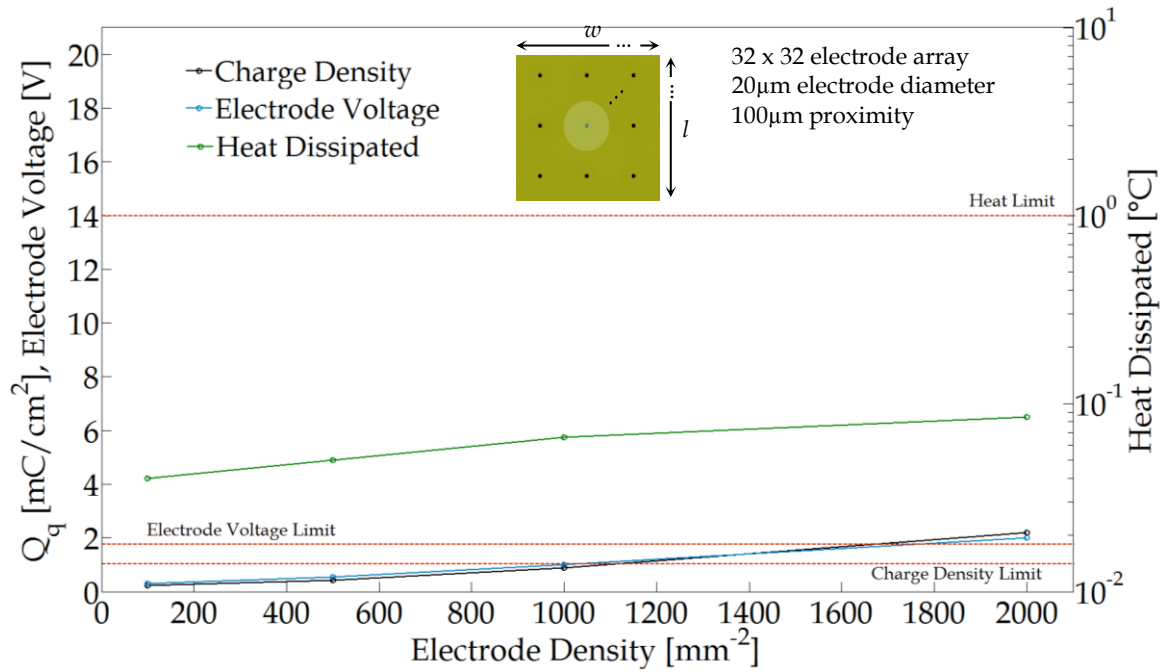


Fig. 5.19 Feasibility of a 32 x 32 electrode array reaching non-overlapping space at proximity of cells to the electrodes of 100 µm. Electrode diameter of 20 µm is tested.  $Q_q$  represents the charge density delivered to the tissue. The limits of each parameter are 1 mC/cm<sup>2</sup> for charge density, 1.7 V for water voltage limit and 1°C for heat limit.

1. Electrode density is preferable to be equal to the cell density, for more information, see section 5.5.10.
2. The current applied to the electrodes should be such that each electrode will cover a sufficient space of stimulation without overlapping with neighboring electrodes, see section 5.4 for more information.
3. Pulse duration is preferable to be small around 100 µs to minimize charge density [Lujan (b), 2016] and thus irreversible Faradaic reactions [Merrill et al., 2005] and to avoid axonal stimulation [Jensen et al., 2005].
4. Electrode size can be determined such that the electrode is contained by the area element of  $d^2$ , see fig. 5.11. The electrode pitch (eq. 5.6),  $d$ , can be defined assuming that the electrode density in an epiretinal system would be equal to the cell density. The activation area, see section 5.4, can be beneficial to cover the remaining space where a ganglion cell would be located. Following this strategy, the hazard of the retinal tissue is reduced as high charge density is required by using very small electrode size.

## 5.6. Searching Algorithm

### 5.6.1. Lessons learnt: Basis for this Chapter

We have learnt from section 5.5 that nearly 50% of the electrodes inside the carrier can reach single-cell selectivity assuming that electrode and cell densities are matched and that single-site electrode stimulation and non-overlapping spaces are used. Indeed, matching both densities

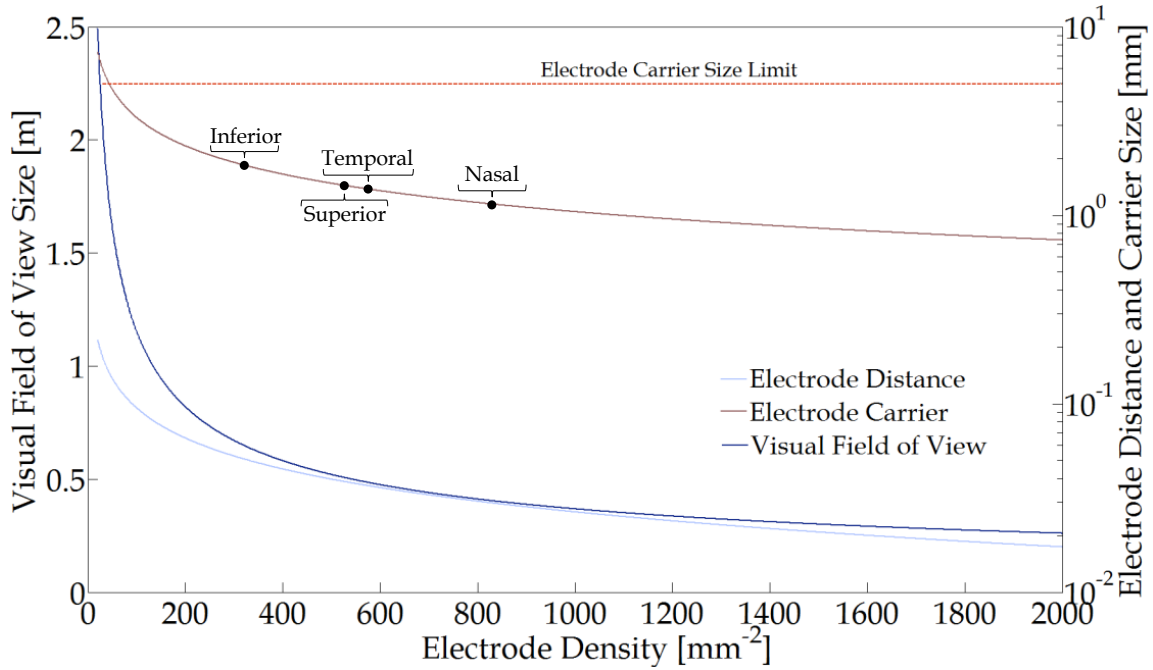


Fig. 5.20 Visual field of view, electrode distance and electrode carrier size relationship with the of electrode density. Electrode carrier size is limited up to 5 mm due to the small incisions that must be made in the eyewall [Weiland, 2014].

provides quite a few advantages i) single electrode stimulus can be narrowed to each cell and ii) one-to-one cross section area of cell and electrode is more expected to be achieved.

However, there are still several challenges that must be addressed. One of those is that more than a half of electrodes that are certainly contributing to pixel-wise are misused, see fig. 5.16. A small percentage of 10% stimulated more than one cell.

### 5.6.2. Aims

In this section, I will examine the searching algorithm. Its aim is allow artificial vision devices to integrate single- or multi-site electrode stimulation in their systems. This is required because existent conditions of conserved cells in patients may implement several limitations for attaining pixel-wise activation. The unpredictability of the location and lifetime of ganglion cells might require some flexibility to select different arrangements of stimulating electrodes to improve the functionality of retinal implants, e.g. multiple-site electrode stimulation.

However, selecting multi-site electrode stimulation obliges low power consumption of each local stimulator unit to minimize neural tissue heating. As a result, up-to-date biocompatible materials must be present for ensuring long-term steady performance of visual electronics.

### 5.6.3. System Realization

A system that supports single-site and multi-site electrode stimulation is presented in fig. 5.21. The electrode arrangement consists of a 32x32 electrode array mounted on a flexible substrate. Assembling the electrodes evenly gives the advantage to program each to function as an active or ground electrode. For practical applications, a flexible polyimide substrate can be

applied as seen in [Meza, 2014]. The proximity of cells to the electrodes is one of the main limitations for visual prosthetics. Mainly it can determine the size of the electrodes for ensure the activation of nearby cells, see chapter three. While the proximity increases, electrode size must be adapted to ensure electrochemical safety. This leads to large-sized electrodes and low resolution. One solution currently used is multi-site electrode stimulation, see fig. 5.21. Likewise, the irregularity of cell position and their lifespan may cause to increase the amount of stimulating electrode for the need of specific patients.

The main contribution of the electrode array presented here to the performance of visual prosthesis is the flexibility to apply single-site or multiple-site electrode stimulation. In fig. 5.21, 'i' and 'j' addresses a defined size of stimulation array based on the depth of stimulation. The effective electrode diameter is usually defined as the summation of the diameters of the electrodes used as seen in [Keserü et al., 2012]. Green lines indicate the current distribution throughout the medium of retinal tissue.

Applying this technique in practice, small-sized electrodes can be practical to address the problems previously stated and still have a suitable dimension to achieve high resolution patterns. This system can be applied with both epi- and subretinal approaches. For the latter approach, however, adjustments of the models presented here must be performed to reach a realistic similarity to the retinal anatomy.

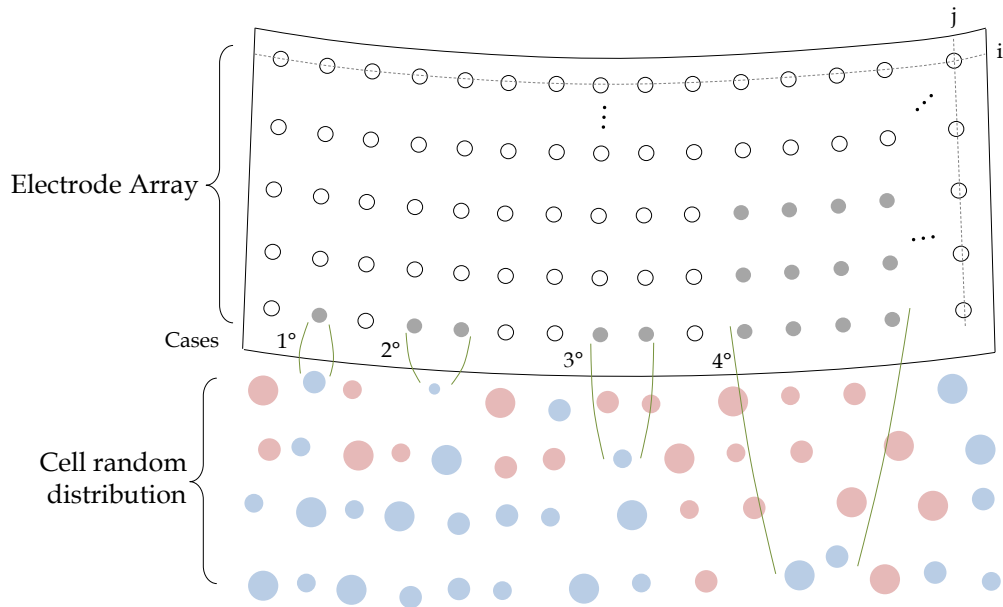


Fig. 5.21 Multi electrode array for specific stimulation. On top, a 32 x 32 electrode array is presented with an electrode distribution and electrode distance. , 'i' and 'j' addresses a defined size of stimulation array based on the depth of stimulation. On bottom of the figure, a random distribution of cells is shown separated with layers of proximities between cells and electrode array. Dead and alive cells are highlighted in red and blue, respectively. Green lines indicate the current distribution throughout the medium of retinal tissue. Gray and white electrodes correspond to active and ground.

#### 5.6.3.1. Single-site electrode Array

Single-site stimulation consists on a single electrode that delivers stimulus through the medium for triggering nearby cells; see case 1° in fig. 5.21. Visual prosthesis is mostly limited by

the charge density injected to the electrodes. Conventional electrode materials can reach a charge density capacity of  $1\text{mC}/\text{cm}^2$ . As the proximity of cells to the electrodes increases, the injected current must rise for triggering a specific cell and may exceed safe boundaries. Thus, single-site electrode stimulation is valid for low proximities. Several key advantages are associated with this kind of electrode topology, 1) single-localized stimulation of cells is more likely to occur because the current can be contained in a small volume that surrounds the cell. As a result, a narrow spot of light can be generated; 2) visual acuity is improved because the brain collects different characteristics from a narrow portion of the visual space because ganglion cells are tightly-packed at the ganglionic layer, mainly at the fovea.

Despite constructive effects can be delivered, single-site stimulation has drawbacks, 1) as the proximity of cells to the electrodes increases, charge density delivered to the electrodes may exceed its limit leading to irreversible reactions, 2) electrode potential may increase its voltage-window limit because of a large impedance in small-sized electrodes, 3) electrode size must increase, leading to a reduced detail perception.

#### 5.6.4. Multi-site electrode Array

Multi-site stimulation consists on an active electrode array that delivers stimulus through the medium for triggering nearby cell; see cases 2°, 3° and 4° in fig. 5.21. This stimulation profile is commonly used in current devices [Keserü et al., 2012; Humayun et al., 2012; Stingl et al., 2013]. The effect of electric crosstalk that may occur in multi electrode array must be taken into consideration [Moghadam et al., 2013]. Electric crosstalk has a constructive effect on visual prosthesis as the effect on field summation can be improved with synchronized monopolar electrodes, leading to a decrease of activation threshold for each electrode [McCreery et al., 2002]. This effect of lowering the overall stimulus current reduces the power consumption and the charge density for cell activation. As such, the time until recharging the battery that powers the implant increases.

One key limitation of visual prosthesis can be attributed to the charge density required for stimulation and the charge density capacity of the electrode material. Argus II and Alpha IMS used platinum gray and titanium nitride respectively. Typical electrode material in neurostimulation is bulk platinum. The charge injection capacity for such material is  $0.1\text{-}0.35\text{mC}/\text{cm}^2$ . Platinum gray can inject up to  $1\text{mC}/\text{cm}^2$  and titanium nitride until  $0.9\text{mC}/\text{cm}^2$ , which represents an important step for implantable bioelectronics. As the threshold activation for each electrode decreases for synchronized electrode stimulation [McCreery et al., 2002], the charge density delivered to the electrodes is safeguarded because the current-summation effect can lead to effective stimulation. Moreover, coordinated stimulation can prevent electrodes exceeding the charge density limitation that can cause gas bubbling formation [Moghadam et al., 2013].

A common limitation in artificial vision devices is the large voltage at the stimulator output driver that takes place by using large number of small electrodes. Thus, high-output voltage compliance is needed due to small physical electrode size and corresponding large impedance. Conventional visual prosthesis can achieve  $\pm 20\text{ V}$  for 232 channels [Ortmanns et al., 2007],  $\pm 10\text{ V}$  for 1024 channels [Chen et al., 2013] and  $\pm 2\text{ V}$  for 1600 channels [Rothermel et al., 2008]. As the threshold current for each electrodes is reduced for synchronized electrode stimulation, the voltage needed to drive the electrodes is then decreased even with small-sized electrodes.

Although constructive effects of crosstalk exist in cell activation, cell stimulation exhibits a disadvantage as undesirable activation of remote ganglion cells occur due to the overlap of the



fields [Moghadam et al., 2013]. Conventional visual prosthetic devices drive the stimulus between single- or multi electrode arrangements to a distant common electrode [Keserü et al., 2012]. The far placement of the ground electrode from the active causes the current to flow deep down into the tissues and activate cells in the course to the ground. Thus, image sharpness and detail perception is reduced because stimulation causes oblong-like shapes of light that lessen the quality of vision, see section 5.3.

### 5.6.5. Searching Algorithm

The searching algorithm is shown in fig. 5.22. Its aim is to provide flexibility to visual devices to integrate single- or multi-site electrode stimulation in their systems. This is required to overcome realistic limitations such as proximity of cells to the electrodes, lifespan of cells and the unpredictability of their position. These lifelike situations of preserved cells in patients might involve adaptability to indicate a special configuration of stimulating electrode array for the need of specific patients.

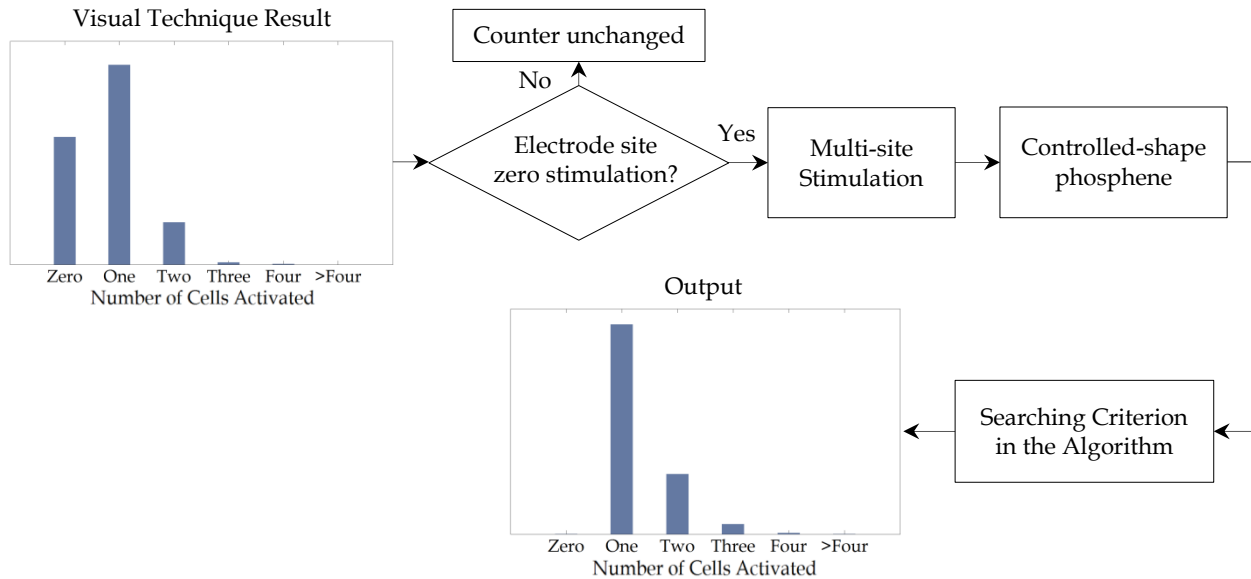


Fig. 5.22 Searching algorithm is shown in this figure. The input of the algorithm is the result from the visual technique that uses some electrode and cell density. If some electrode site could not stimulate a cell, multi-site stimulation is generated using this electrode site and its surrounding companions forming an array of stimulating electrodes. The controlled-shape phosphene is used as a cell is placed inside the ganglionic layer with some distance away from the array of stimulating electrodes. Once the threshold current is found, the activation area can be generated using the phosphene shape method. The searching criterion is explained in its corresponding section. The output corresponds to a bar table that indicates the percentage of electrodes ( $y$ -axis) that activate a specific number of cells ( $x$ -axis).

The aim of the searching algorithm is to increase the percentage of stimulating electrodes by searching for single cells located inside the vicinities where the activation areas cannot reach. Figure 5.23(a) displays this problem using non-overlapping spaces. It was calculated that a probability of around  $1/4$  occurs for cells inside those neighborhoods, see eq. 5.18. Thus, multi-site electrode stimulation is used in the searching algorithm just in the needed cases that an electrode site could not reach stimulation and is searching preferably for single cells, figs. 5.23(b) and (c). These electrodes are called searching active electrodes.



### 5.6.5.1. Generation of the Area of Activation

The input of the searching algorithm is the result from the visual technique that uses some electrode and cell density. In this specific case, non-overlapping spaces are used. In these needed cases of an electrode cannot reach activation, multi-site is created using the searching electrode site and its companions, forming an array of stimulating electrodes. The aim is to increase single-cell cases by reducing situations of zero stimulation.

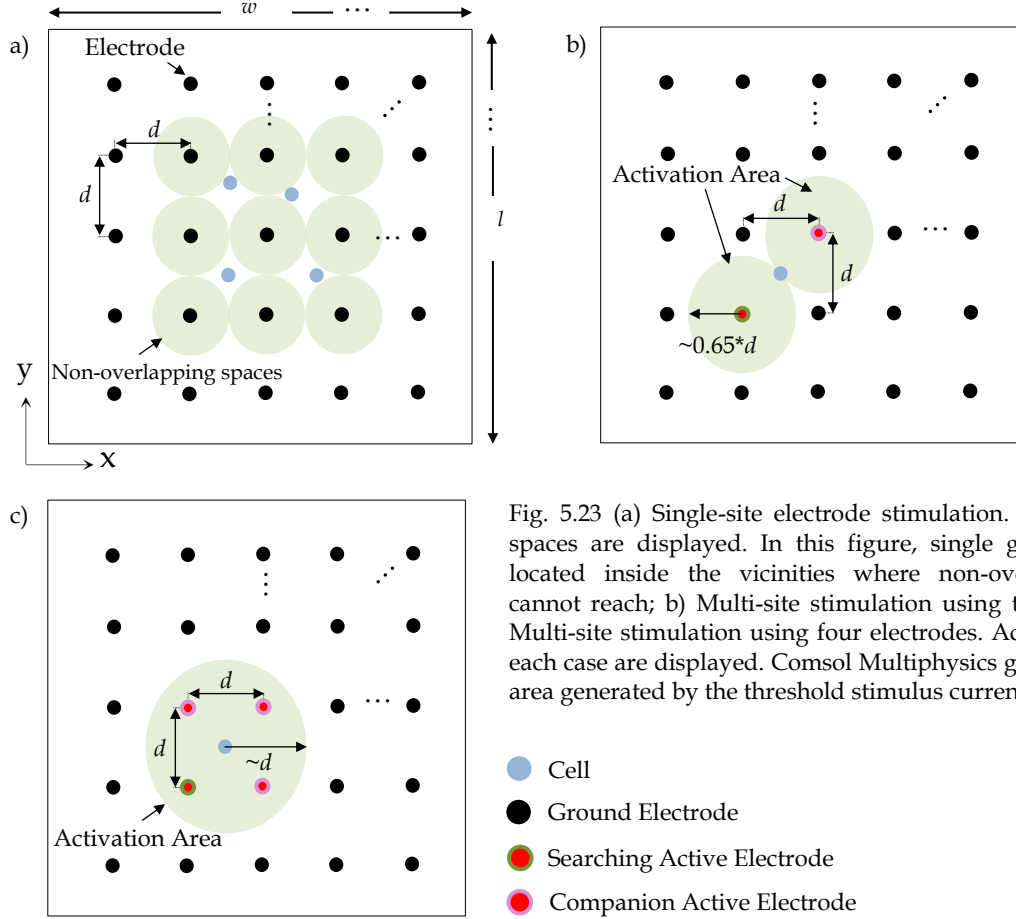


Fig. 5.23 (a) Single-site electrode stimulation. Non-overlapping spaces are displayed. In this figure, single ganglion cells are located inside the vicinities where non-overlapping spaces cannot reach; b) Multi-site stimulation using two electrodes; c) Multi-site stimulation using four electrodes. Activation areas for each case are displayed. Comsol Multiphysics gave the activation area generated by the threshold stimulus current for each case.

The controlled-shape method is used in the searching algorithm. For more information of this method, see section 5.4. The cell is shifted inside the ganglionic layer and at the distance  $(d/2, d/2)$  away from the searching electrode.  $d$  is the electrode pitch calculated as  $1/\rho_E^{0.5}$ .  $\rho_E$  is the electrode density. Multi-site stimulation using two electrodes, fig. 5.23b, and four electrodes, fig. 5.23c, are shown.

This algorithm is executed to obtain the threshold injected current across the electrodes for each case. This threshold current will then discriminate the spreading current from the active electrodes to ground and therefore the area of perception will be controlled by this specific current injection. Afterwards, input stimulating parameters take the threshold as the injected current and the activation area is generated based on the phosphene shape description method. As a reminder, cell location becomes a variable parameter in this case. Comsol generated the areas of activation of the cases with two- and four-electrode stimulation, see figs. 5.23(b) and (c), respectively. Table 5.5 shows the results for each case.

#### 5.6.5.2. Searching Criterion in the Algorithm

The main objective of visual implants lies on reaching pixel-wise stimulation. Based on our definition, this requires that a single cell must be reached by a single electrode site. As such, the visual perception of the incident image must have resolutions similar to an array of independent percepts. Thus, the criterion of the searching algorithm must accentuate an arrangement of active electrodes that satisfies pixel-wise stimulation. Although researchers associate the stimulation of nearby cells as the definition of pixel-wise [Weiland, et al. 2014], our definition is that a single cell must be activated by a single electrode.

As a reminder, the searching active electrode represents the electrode site that is misused (zero cells activated) and is searching preferably for single cells. Four cases of multi-site stimulation involving the searching and a companion active electrode are displayed in fig. 5.24. Each separately investigated the number of ganglion cells activated inside the vicinities covered by the activation areas. The searching algorithm looks for the case that activates the least amount of cells. This sequence was also implemented for multi-site array with four electrodes.

The activation of nearby cells was coded in Matlab and obeyed the condition of the activation area. This states that a ganglion cell located inside the activation area of an electrode is activated. Otherwise, the cell is not stimulated. As a reminder, the activation area is defined as a two-dimensional space along the retinal surface where the spreading current across the electrodes is enough to activate the response of the cell.

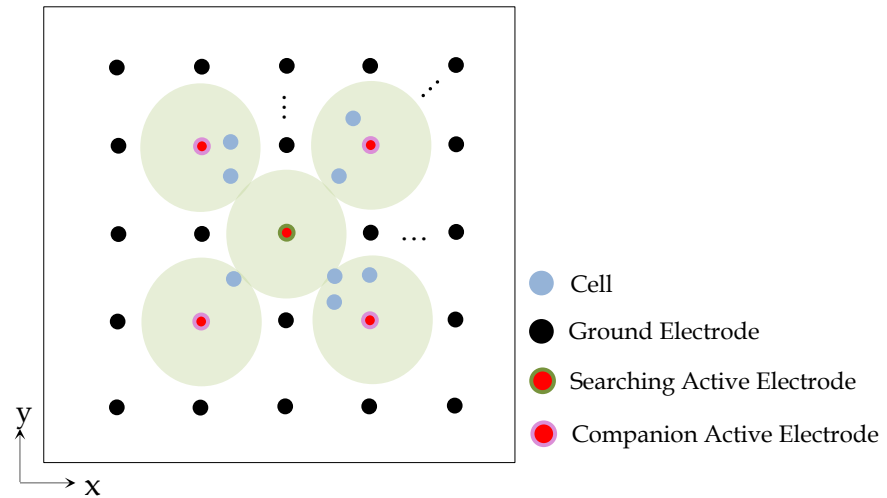


Fig. 5.24 Sequence of the searching algorithm using two electrodes in multi-site stimulation. Four cases are displayed involving the searching and a companion active electrode. Each case separately investigated the number of ganglion cells activated inside the vicinities covered by the activation areas. The searching algorithm looks for the case that activates the least amount of cells. This sequence was implemented for multi-site array with four electrodes.

Clinical trials that involve grouping electrodes together in parallel have been formerly performed [Keserü et al., 2012; Humayun et al., 2012; Stingl et al., 2013]. These experimental observations are extremely helpful to investigate the performance of the microelectrode array. Since the electrode properties are unable to alter once the electronics are implanted, visual prosthetics requires some flexibility to optimize their functionality. As such, the amount of stimulating electrodes and the stimulating parameters must be adapted for the need of a defined patient.

Although challenges are present in visual prosthesis to achieve pixel-wise stimulation, several techniques are performed. One of those is a real-time visual questionnaire to the patient [Keserü et al., 2012]. While the array of stimulating electrodes is changed, the answers from each trial can be a guidance to modify the stimulating parameters. As a result, an improvement can be achieved in terms of the signal transmission to the brain and to enhance visual perception.

The aim of the searching algorithm resembles the technique previously presented. Single- and multi-site stimulation can be selected only in the needed cases that an electrode site could not reach a cell. The searching algorithm adapts the stimulating parameters to reach the least amount of cells and to improve visual perception.

#### 5.6.5.3. Output

The condition to compute the quantity of cells stimulated by the searching electrode is as follows. If stimulation is achieved inside the activation area, a counter increases its value by 1 in the searching electrode site. Otherwise the counter remains unchanged. The sequence shown in fig. 5.24 is implemented for each searching electrode. The searching algorithm selects the case that activates the least amount of cells.

The output corresponds to a bar table that indicates the percentage of electrodes that activate a specific number of cells. For each configuration, the script used a total of 1 cycle for its implementation as each searching electrode preferably investigated for single cells inside the activation area. Overall, the searching algorithm was repeated 100 times to obtain probabilistic values of the results.

#### 5.6.6. Input Data of the Searching Algorithm

The input parameters stated in section 5.5 are kept except where expressly varied. The electrode and cell density are equal with a value of  $585 \text{ mm}^{-2}$ .

#### 5.6.7. Results

The results of the study are displayed in figure 5.25. Single and multi-site stimulation with two and four electrodes are displayed. The  $y$ -axis indicates the percentage of electrode sites that activate a specific number of cells denoted in the  $x$ -axis. The arrangement is based on showing the results of each electrode density as a bar graph fashion and the standard deviation of each case. Table 5.5 lists the stimulating comparison of a cell located at a distance ( $d/2$ ,  $d/2$ ) away from the searching electrode. The results of single- and multi-site arrays are displayed.

TABLE 5.5

Electrode Arrangement	Threshold [ $\mu\text{A}$ ]	Charge Density [ $\text{mC}/\text{cm}^2$ ]	Heat Dissipated [ $^{\circ}\text{C}$ ]
Single-site <sup>1</sup>	1	0.16	0.02
Multi-site, two electrodes	0.84	0.13	0.06
Multi-site, four electrodes	0.4	0.064	0.1

<sup>1</sup> The outcomes of single-site arrangement are related to stimulate a cell located at a distance ( $d/2$ ,  $d/2$ ) away from the electrode.

### 5.6.8. Discussion and Summary

The results originated from section 5.5 of the spatially-based visual technique are displayed in figure 5.25 as green bars. What we have learnt from this section is that single-cell selectivity can be boosted by matching electrode and cell density. However, we have also learnt that indeed matching both densities is not enough for pixel-wise stimulation. Misused electrode percentage reached nearly 34%, see fig. 5.25. This means that one third of the overall amount of electrodes represents the unpredictability of the position of cells in stimulation. Hence, the flexibility to select different arrangements of stimulating electrodes to activate the remaining cells must be present in visual prosthetics.

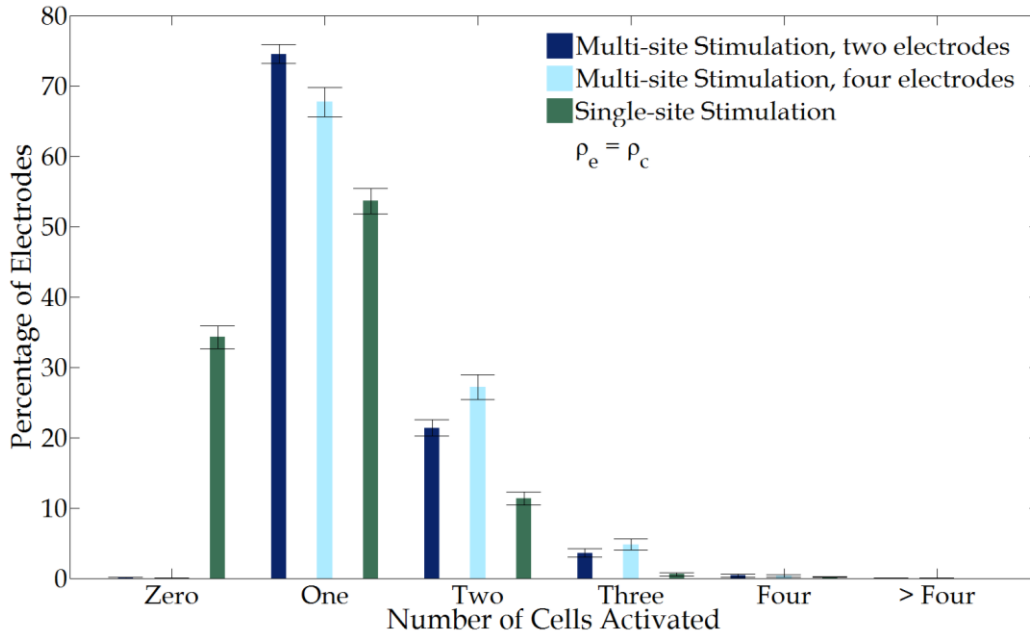


Fig. 5.25 Single- and multi-site comparison for cell activation. The outcomes of single-site are related to the responses of electrodes over cells in the visual technique, see section 5.5. Electrode density is equal to cell density. Two and four electrodes were used in parallel stimulation.

Increasing the stimulating electrode sites up to four generates several advantages. Threshold injected current to activate some cell has the lowest value comparing with single-site and multi-site (two electrodes) stimulation. This specific case saves 60% of current. The charge density has as well the lowest. This means that the electrode/electrolyte interfaces and retinal tissue might be free of electrolysis of water. The percentage of electrodes reaching a single cell increased up to 67%. A percentage of electrodes of nearly 26% stimulated two cells.

Multi-site stimulation with two electrodes saves 16% of current compared with single-site stimulation. The charge density follows this tendency by reaching 0.13mC/cm<sup>2</sup>. This specific case has the highest percentage of electrodes that reach a single cell achieving 75%, opposed to nearly 50% using a single electrode. A percentage of electrodes of nearly 21% reached two cells.

Indeed as seen in fig. 5.25, multi-site electrode stimulation can yield advantages to electrodes over cells to attain single selectivity. In effect, Argus II clinical trial revealed that 55% of single electrodes could produce a perception within the stimulation safety limits. As regards to Alpha IMS device, it was not certainly revealed that single electrodes can produce a perception. In both

devices, electrodes grouped together in parallel forming multi-site stimulation are used to elicit a response if a single electrode cannot [Weiland et al., 2014].

The question on how the patient would perceive the phosphenes created by stimulation remains to be seen. There is experimental evidence that blind patients report percepts that match the pattern of multi-electrode stimulation [Rizzo III et al., 2003]. Eighty-four trials tested this hypothesis, which for several subjects satisfied nearly 32% in average of the time of the experiment. Multi-electrode stimulation using two electrodes was also performed to test two-point discrimination. Six trials driving two electrodes, 1860  $\mu\text{m}$  spacing, produced one percept five times. Two trials generated “objects close together” once. Another experiment was conducted, delivering stimulation through a second remote electrode while driving the first, which produced a “pea”-sized image initially and then a doubly bright “dime” -sized image. Overall, no difference was reported with simultaneous stimulation of two adjacent versus two end electrodes using identical charge, yielding single percepts. However, several trials reported seeing a “line” through two adjacent electrodes stimulation.

#### 5.6.9. Challenges of the Multi electrode Array

A distant proximity of the retina to the electrode array contributes to the spreading current from the active electrode causing changes in the area of stimulation and thus affecting the resolution of the visual prosthesis [Kasi et al., 2011]. As formerly discussed, the closeness of electrodes to the cells determines the size of the electrodes. Large-sized electrodes are frequently used to ensure electrochemical safety [Humayun et al, 2012; Roessler, 2009; Mahadevappa et al., 2005; Rizzo III et al., 2003]. One solution that has been implemented to minimize electrode size and improve visual resolution is multi-site stimulation [Hornig, 2007]. Hence, the closeness can define the number of active electrodes for triggering a specific cell. In this specific case, the effective electrode diameter is usually defined as the summation of the diameters of the electrodes used as seen in [Keserü et al., 2012]. However, current amplitudes should be distributed in a sufficient small volume to trigger single cells and improve visual acuity. This is related to elicit punctuate spots of light. Thus, a decrease of electrode size [Fried, 2006; Jepson et al., 2014; Weiland et al., 2008] and an increase of the both the amount of electrodes and the density of electrodes [Weiland et al., 2014] must be implemented. This mixture of stimulating parameters may increase the threshold current and reduce the visual field of view.

##### 5.6.9.1. Procedure

Here, an exemplary case of using low electrode density at high proximities is presented. Multi-site electrode stimulation is tested using the phosphene shape description method shown in figure 5.4. By knowing that the activation area can be related to any visual sensation represented as a percept while stimulation, simulation-based findings can be beneficial to analyze phosphene patterns of lifelike situations prior to device implantation in the retina.

The input parameters stated in section 5.4 are kept except where expressly varied. The electrode arrangement is shown in fig. 5.26. Red electrodes correspond to active, whereas black electrodes indicate ground. The length and width of the electrode carrier can be computed with eq. 5.5. The inputs of the model are pulse duration of 100  $\mu\text{s}$ , proximity of cells to the array of 300  $\mu\text{m}$ , electrode diameter of 20  $\mu\text{m}$  and electrode density of 70  $\text{mm}^{-2}$  (electrode distance of 100  $\mu\text{m}$ ). Fixed peak current of 30  $\mu\text{A}$  was applied across the electrodes. The stimulus delivered was monophasic rectangular pulse. For more information of this procedure, see section 5.3.

### 5.6.9.2. Results and Summary

The result of the activation area is illustrated in fig. 5.26. The outcomes indicated that current amplitude of  $30\ \mu\text{A}$  and electrode diameter of  $20\ \mu\text{m}$  is sufficient to activate some cells, opposed to  $290\ \mu\text{A}$  and electrode size of  $50\ \mu\text{m}$  using single-site stimulation, compare to fig. 3.14. Multi electrode activation contributes to the spread of current because of the effect of current summation through the medium. As a result, threshold current for each electrode decreases and therefore small-sized electrodes can be used.

Despite that multi-site stimulation lowers electrode size, power consumption and charge density injection, complex phosphene patterns may be generated, see fig. 5.26. Ring-shaped phosphene belongs to an activation area where its surface is a non-closed geometry and arises once the proximity of the retina remains distant to the electrode array. Non-closed geometries such as doughnut-shaped have been reported by the patients in [Humayun et al., 2003].

In spite that non-closed percepts can be narrower by making the electrode distance shorter, this has several drawbacks, 1) visual field of view generated by electrically activated cells may be small because its dimensions are related with the electrode carrier; 2) electrode distance plays a major role to trigger action potential, because the depth of the current flow is influenced. When electrode distance increases, the current density penetrates deeper into the tissues and thus elicits activity in distal ganglion cells, thereby greatly reduce detail resolution. Vice versa, when electrode distance decreases, the current density passes superficially through the tissues. For the latter situation, current amplitude must increase in order to activate some cells. That can lead to irreversible reactions once some electrode exceeds their own charge density capacity.

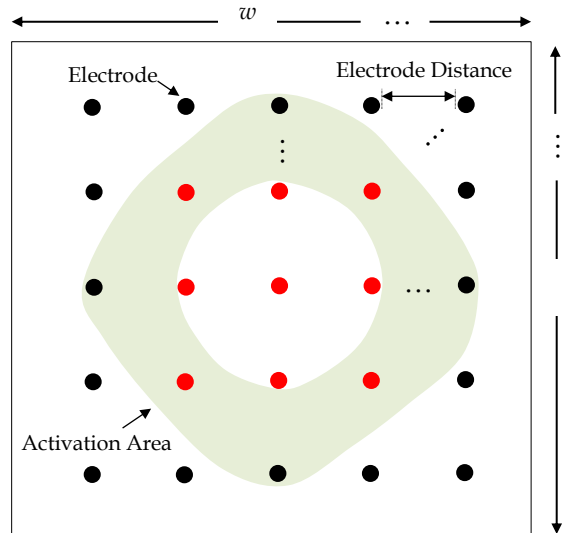


Fig. 5.26 Electrode carrier of  $32 \times 32$  electrodes. A single array is shown with sizes of length,  $l$ , and width,  $w$ . Electrodes are distributed as a square grid and separated with an electrode distance. Red electrodes correspond to active, whereas black electrodes indicate ground. The activation area or phosphene is highlighted with a gray line-pattern.

Therefore, biocompatible materials that can support high charge densities must be developed for cases of small electrode distance. Doing so, small-sized electrodes with a proper electrode density can be applied. Likewise, advanced techniques must be elaborated to fasten the electrode array close to the retinal surface.

# Chapter 6

## Summary and Outlook

Visual perception coming from electrically activated cells needs noteworthy progress for generating a full image, thus pixel-wise vision is introduced in this report. Pixel-wise visual perception is defined as the generation of very small and independent spots of light by electrode stimulation. These single small spots of light can be thought as one-to-one, electrode-to-pixel, scoreboard-like experience with punctate individual phosphenes. That is, the response per electrode must consist of a small visual perception that carries different information of the external image to the brain. By this means, as incorporating the entire response of the array of electrodes, the cluster of these useful dots of light will generate the target image. In this regard, it is assumed that a full image can be realized by single cell activation per stimulating electrode generating a visual sensation that the brain may interpret as a small spot of light.

Doing so, visual devices can provide partial sight restoration and improve vision in the everyday lives of patients. In this work, a high-level theoretical scheme of realistic neural responses in the retina is modeled to address pixel-wise vision as single cells are electrically stimulated by single electrodes. The main focus of this theoretical scheme was to function as a stepwise refinement of electrode stimulation to reach single-cell selectivity. This is a requirement of pixel-wise stimulation as electrodes must maintain accurate control over single cells, creating an array of independent phosphenes. The theoretical scheme obtained input geometric and stimulating parameters from previous top-level steps that contributed significantly to ensure accurate results of threshold currents, high resolution patterns and safety of an array of  $32 \times 32$  electrodes while pixel-wise stimulation is reached. The development of the high-level theoretical scheme was of particular importance as it is demonstrated that clinical trials of both subretinal

and epiretinal implants do demonstrate that patients do not experience idealized pixel-wise vision [Weiland et al., 2014].

This high-level theoretical study contemplates i) an analysis of phosphene patterns generated by electrical stimulation, ii) a method that controls the size of percepts as it is required to generate punctuate spots of light, iii) a visual technique that enhances the control of the electrodes to selectively activate single cells and iv) searching algorithm that provides flexibility to select single- or multi-site electrode stimulation as it is required in realistic applications in retinal implants.

## 6.1. Main Findings and Discussion

In order to gain a comprehensive understanding of the objectives of sight restoration through pixel-wise vision, it is necessary to treat firstly the activation of 1000+ electrodes per single array. This is a significant requirement for visual prosthesis to upgrade basic issues such as mobility, independent living, navigating on interior and exterior environments and reading large-sized text. Currently, an artificial vision device that exceeds 100 electrodes per single array has not been implanted. Thus, the main inquiry in advanced visual devices remains: Is it feasible to drive 1000+ electrodes inside the retina?

Chapter 3 introduced a simplified FEM neural-based scheme that consists on a 3D computational model of the retina, see fig. 3.3. This neural model is based on activating single cells with the minimum threshold current as seen in earlier experimental works [Keserü et al., 2012; Jepson et al., 2012]. Hodgkin and Huxley-like equations that accurately reproduce all the key biophysical properties of the action potential were included in the criterion of cell stimulation. The objectives of these simulations are to meet input geometric and stimulating parameters for the high-level theoretical scheme. The tendency of threshold currents, fig. 3.12, and electrode voltage, table 3.7, in simulations displayed accurate comparison results with experimental outcomes. This precision persisted as the proximity of cell to the electrodes is varied in the case of threshold currents. This expresses the possibility to simulate cell excitation using 3D FEM neural-based models by defining the domains in terms of experimental data, see table 3.2 and 5.1. One of the key insights of our model is that electrochemical safety was treated in the response of electrodes and cells.

The high-level scheme used a more complex FEM 3D neural-modelling of the retina, see chapter 5. It consisted on simulating one half of a sphere that represents a segment of the human eye. This complex model learnt from the earlier about the limits of electrode sizes, parameters affecting electrochemical safety and delicate issues such as proper pulse shape, pulse duration, domain parameters (conductivity and permittivity) and electrode data.

Comparable results of the simplified and the complex model were obtained using a  $32 \times 32$  array at low and high proximities of the cells to the electrodes. Both models guaranteed safe stimulus within proximities of  $\leq 10 \mu\text{m}$ , electrode diameter of  $5 \mu\text{m}$ , rectangular pulse at  $100 \mu\text{s}$  of duration. For proximity of  $\leq 100 \mu\text{m}$ , both estimated that  $10 \mu\text{m}$  electrode diameter deliver safe stimulus at electrode densities of 82 and up to  $150 \text{ mm}^{-2}$ , see figs. 3.10 and 5.18, respectively. For high electrode densities up to  $1000 \text{ mm}^{-2}$ , the complex model approximated that  $20 \mu\text{m}$  electrode diameter is adequate for safe stimulus, fig. 5.19. In both models, the feasibility of a  $32 \times 32$  electrode array, biocompatible electrode materials, image frequency of 20 fps, low power electronics, small-size electrode and electrochemical safety were contemplated. In the complex model, however, the cell was placed at the periphery of the space where the stimulus of the



electrodes does not overlap, see fig. 5.12a. This method of stimulation confirmed the selectivity of a small number of cells by enclosing the electrodes in non-overlapping spaces in a 32 x 32 electrode array. Simulation-based findings indicate the feasibility to apply the amount of electrodes previously mentioned. Small electrode diameter can be applied, allowing excitation of small groups of ganglion cells.

Both models were based on an existing electronic scheme that consists of a 64 scalable channel stimulator with low power consumption and small chip area [Meza, 2014]. The electronics are built with 130nm CMOS transistor process. The circuitry consists on a matrix of 64 electrodes or LSU's: 32 P type and 32 N type. A single LSU is of size 188 x 209  $\mu\text{m}^2$  (single pixel size of 0.039mm<sup>2</sup>), resulting with a total area of chip is 4.25 mm<sup>2</sup>. For more information, see figure 4 in original manuscript [Meza, 2014]. A fully implantable device of 1000+ electrodes can be realized by attaching 16 ASIC in daisy chain configuration. Two layer arrangement of 2 x 4 ASIC was selected in this report with low area requirement of 1.32 cm<sup>2</sup>, meaning 15.7 and 8.4 mm, see fig. 3.9. Low power consumption will be around 55.2 mW [Meza, 2014]. The advantage of daisy chain configuration is that the chip can be fully scalable and increase the number of stimulation channels, as is it required in retinal prosthesis stimulation. The schemes currently presented can support the following benefits: 1) 1000+ electrodes in a single array, 2) hybrid architecture so as to minimize power consumption and thus heat generated (existing in device, 3) PEDOT-NaPSS coat deposition that enhance biocompatibility and reduce electrode impedance (existing in device) and 4) flexible polyimide substrate with small thickness. The electrode carrier proposed follows a simple square grid distribution involving 1024 electrodes separated with some electrode distance, see fig. 3.3 or 5.11. In effect the main reason of applying this configuration in practice is to confine the stimulus current to a small volume around the ganglion cell and to minimize electrode cross-talk during stimulation.

Safeguarding the operation of stimulators is by far most a crucial issue in neural activation. In general, charge density and electrode voltage have a major role to ensure safe implementation in visual prosthetics. Small electrode size can allow excitation of small groups of cells. Despite that visual reception is improved; however, the exposure of sensitive retinal tissue must be safeguarded because of the charge density required by small electrode dimensions.

In chapter 4, experimental evidence indicated that exponential increase pulse shape was not adequate for safe stimulus as many believed. Exponential increase generates high voltages in the stimulator (due an increase current peak to elicit response) which may have negative effects on the hardware and/or the patient, see fig. 4.3 and 4.4. Further, such pulse shape may cause corrosion due to a high voltage that may surpass the "water window" positive (anodic) limit.

Experimental findings [Meza, 2012] demonstrated that linear increase delivers lower charge than rectangular, see fig. 4.1. Simulation-based findings shown in Chapter 4 support this evidence, see fig. 4.7b. Charge density is reduced up to 40% in average by changing to linear increase, meaning a promising technique to avoid irreversible Faradaic reactions. Despite this, the difference in minimum electrode diameter with rectangular pulse shape is 4 and 0.3  $\mu\text{m}$  for 0.35 and 1 mC/cm<sup>2</sup> charge density boundary, respectively (see table 4.1, 100  $\mu\text{m}$  proximity). This does not justify the increasing hardware effort to generate linear increase pulse shape.

There is not much difference when applying 50 or 100  $\mu\text{s}$  pulse length in rectangular shape concerning charge density delivery, see figs. 3.10 and 3.11 or 4.7b. Chapter four generated similar results regarding linear increase pulse shape. On the other hand, rectangular pulse shape reduces electrode voltage up to 63% when 100  $\mu\text{s}$  pulse duration is used instead of 50  $\mu\text{s}$ . For linear increase, it is reduced up to 54%. Comparing both pulse shapes at 100  $\mu\text{s}$  pulse duration,

electrode potential is reduced up to 22% in average by applying rectangular pulse shape; see fig. 4.8. This means that electrode corrosion can be avoided. Accordingly, rectangular pulse shape is more suitable to use and also because is nowadays the most widely used waveform for electrical neurostimulation. Chapter 4 yielded evidence that pulse duration of 100  $\mu$ s is more suitable for real applications in retinal implants because i) electrode potential is highly reduced compared with lower pulse durations, ii) each of the 1000+ electrodes can have different timeslot of activation. This can be done to prevent cross electrode stimulation. As such, each can be activated independently with a total image frequency of 20 fps. Duty cycle can be applied during stimulation which can reduce power consumption. Moreover, experimental observations support this statement, i) short pulses lower than 150  $\mu$ s deliver one spike per pulse with a predicted spike latency that replicated the normal light patterns [Fried, 2006], ii) pulse durations of 100  $\mu$ s are preferable because passing retinal ganglion cell axons can be avoided while stimulation [Jensen, 2005], iii) experimental findings exhibited precisely timing, sub-millisecond latency single spike responses which are a characteristic of direct ganglion cell activation using short pulse durations of 100  $\mu$ s and small electrodes of 15  $\mu$ s of diameter [Jepson, 2012]. These results provided fruitful guidance to the high-level theoretical scheme presented in chapter 5 for ensuring high resolution vision, accurate perceptual thresholds and safe stimulus delivering.

The high-level scheme, see section 5.2, uses the complex 3D retinal-model presented in chapter 5. This complex model contemplates i) 32  $\times$  32 electrode sites for reaching high resolution, ii) flicker-free vision at frame rate of 20 Hz, iii) small-sized electrodes contained by a proper electrode density for providing a pattern of independent phosphenes, iv) safe avenues during cell activation that guarantee electrochemical safety, v) neural modelling proof by experimental studies and vi) deep theoretical thinking for a possible physical realization of electronics. This thoughtful model applies what was learnt in earlier sections to ensure electrochemical safety by applying 1000+ electrodes inside the carrier.

The phosphene shape description, see section 5.3, is a method created to understand the causal mechanisms of percepts. Its aim is to generate the activation area to evaluate the extent of stimulation and to estimate the shape of visual perception. The activation area is defined as a two-dimensional space along the retinal surface where the current spread across the electrodes is sufficient to trigger a response of the cell. Thus, the activation area can be related to any visual sensation represented as a phosphene generated by electrical stimuli. The results of the phosphene shape method were conclusively proven as the wide range of shape responses formerly described in the clinical trials conducted by [Keserü et al., 2012] are highly correlated with our simulation-based findings. Prior to device implantation in the retina, simulation-based findings of this kind can be beneficial to understand lifelike situations of phosphenes.

The controlled-shape phosphene, see section 5.4, is a technique created to narrow the extent of the spreading stimulus and to generate the space required for stimulation of ganglion cells. This is of principal interest to enhance the control of the electrodes over single cells and to produce an array of independent phosphenes. Therefore, the stimulus that spreads through the medium must be constrained to the space required for activation. This method proved its usefulness to constraint the dimension of phosphenes as it is compulsory to produce narrow spots of light. For this particular case, non-overlapping spaces are created. These are defined as the space of areas of activation where the boundaries of adjacent meet but do not overlap, see fig. 5.12(a). This method of stimulation confirmed the selectivity of a small number of cells by enclosing the electrodes in non-overlapping spaces in a 32  $\times$  32 electrode array.

The spatially-based visual technique, see section 5.5, uses a combination of proper current injection and electrode density to strengthen the control of electrodes over single ganglion cells.

Matching electrode and cell densities results up to 50% of the electrodes inside the carrier that can reach single-cell selectivity. Indeed, matching both densities delivers quite a few advantages i) single electrode stimulus can be narrowed to each cell and ii) one-to-one cross section area of cell and electrode is more expected to be achieved.

Last, the searching algorithm was introduced as a method to integrate single- or multi-site electrode stimulation, see section 5.6. This is required because of realistic situations in patients, such as the proximity of cells to the electrodes, lifespan of cells and the unpredictability of their position. This might involve some adaptability to indicate a special configuration of stimulating electrode array for the need of specific patients. Simply as its name indicates, its aim is to increase the percentage of stimulating electrodes by searching preferably for single cells located inside the vicinities where the activation areas cannot reach. Figure 5.23(a) displays this issue using non-overlapping spaces. This algorithm is implemented just in the needed cases when an electrode site could not stimulate a cell and is misused. Hence, the expected outcome of the algorithm would be to minimize the cases of misused electrodes and increment single-cell situations. Multi-site stimulation with four and two stimulating electrodes increases single-cell selectivity up to 67 and 75%, respectively, see fig. and 5.25, opposed to nearly 50% using single-site electrode, see fig. 5.16. Nearly the rest of the remaining electrodes stimulate a couple of cells, achieving 28 and 22%, respectively.

In conclusion, pixel-wise vision requires an array of 1024 electrodes with small diameter, pulse duration lower than 150  $\mu\text{s}$ , high electrode density and the flexibility of visual devices to select different stimulating electrode arrays, and frequency of stimulation of around 250 Hz to achieve high temporal resolution. Thus, advanced techniques must be present for ensuring long-term steady performance of visual electronics, including low power consumption of local stimulator and biocompatible materials. Advanced methods are required to fasten the microelectrode carrier to the retinal surface.

## 6.2.Future Work

Currently, visual prosthetics are in an early-stage of maturity. Improvements related to detail perception coming from certified devices for implantation are still promising. Nevertheless, there is much to learn about nearby cell activation, pixel-wise perception, safe implantation, harmless stimulation avenues and technological advances in packaging in order to be aligned with the success of today's cochlear implant technology.

Axonal response was not addressed here because there are experimental verification that pulse duration of 100  $\mu\text{s}$  can i) deliver one spike per pulse with a predicted spike latency that replicated normal light patterns in the retina [Fried, 2006], ii) avoid stimulation of passing retinal ganglion cell axons [Jensen, 2005], and iii) exhibit direct ganglion cell activation using low electrode diameter [Jepson, 2012]. Nevertheless, axonal response has generated considerable interest amongst groups of engineers because perception as axons are stimulated might produce complex shapes such as an ellipse or streak [Weiland et al., 2014]. Thus, a comparison between axonal and body cell activation while pulse duration or shape are varied can yield interesting results related to visual perception.

The activation area addressed here is the core concept in this report. Its size can determine the amount of cells activated by a single electrode. A conclusion of such issue was resolved here such that the stimulation of each electrode does not overlap. This leads to an area of activation called the non-overlapping space. Nevertheless, the optimal size of activation area in single- and

multi-electrode must be analyzed. Doing so, a better response of single-cell selectivity might be reached. A simple square-grid electrode distribution of  $32 \times 32$  was presented in this report. Our proposal lies on a stimulation arrangement that consists of an active electrode surrounded by eight grounds. Doing so, the stimulus current is confined to a small volume around the ganglion cell and electrode cross-talk can be minimized. [Wong et al., 2007] used six-ground settings of current steering techniques. Experimental findings in animals suggested that this arrangement was efficient because of the smaller area of cortical activation and of a reduction of unwanted interactions between multiple stimulation sites. Thus, different electrode topologies and their comparison would yield interesting results related to single-cell selectivity and sizes of activation areas.

Finally, experiments must be conducted to verify our assumption that a single cell activated per stimulating electrode would generate at the retina a single and small spot of light.

# References

1. Abramian M., et al. Computational Model of Electrical Stimulation of a Retinal Ganglion Cell with Hexagonally Arranged Electrodes. 34th Annual International Conference of the IEEE EMBS, 2012
2. Ahmad Z. Principles of Corrosion Engineering and Corrosion Control. Butterworth-Heinemann, 18 Sep 2006
3. Andrew C. Weitz et al. Improving the spatial resolution of epiretinal implants by increasing stimulus pulse duration. *Sci Transl Med.* 2015 Dec 16;7(318):318ra203.
4. Arle J. Essential Neuromodulation. Academic Press, 14 Apr 2011
5. Bagnoud M, Sommerhalder J, Pelizzoni M, Safran AB. The amount of visual information required for the restoration of elementary reading abilities, using a retinal implant in patients with external retinal dystrophy: psychophysical study [in French]. *Klin Monatsblat Augenheilk.* 2001;218:360-362.
6. Balasubramanian, R; Gan, L (2014). "Development of Retinal Amacrine Cells and Their Dendritic Stratification". *Current Ophthalmology Reports* 2 (3): 100-106
7. Bergamini CM, Gambetti S, Dondi A, Cervellati C. Oxygen, reactive oxygen species and tissue damage. *Curr Pharm Des* 2004;10(14):1611-26
8. Berson, David M. (2007). "Phototransduction in ganglion-cell photoreceptors". *Pflügers Archiv - European Journal of Physiology* 454 (5): 849-55
9. Bestmann S. Computational Neurostimulation. Elsevier, 16 Nov 2015
10. Bonham B. Current focusing and steering: Modeling, physiology, and psychophysics. *Hearing Research* 242 (2008) 141-153
11. Bonmassar G., Seung Woo Lee, Daniel K. Freeman, Miloslav Polasek, Shelley I. Fried & John T. Gale. Microscopic magnetic stimulation of neural tissue. (2012) *Nature Communications* 3, Article number: 921.
12. Boretius, T., M. Schuettler, and T. Stieglitz. On the Stability of PEDOT as Coating Material for Active Neural Implants. 15th Annual Conference of the International Functional Electrical Stimulation Society, 2010
13. Brindley G. S., & Lewin, W. S. (1968). The sensations produced by electrical stimulation of the visual cortex. *Journal of Physiology (Lond)*, 196, 479-493.
14. Brummer S.B., M. J. Turner, "Electrochemical considerations for safe electrical stimulation of the nervous system with platinum electrodes," *IEEE Trans. Biomed. Eng.*, vol. 24, no. 1, pp. 59-63, Jan. 1977.
15. Cai, Q., et al. Response variability to high rates of electric stimulation in retinal ganglion cells. *J Neurophysiology*, 2011
16. Cha K., Horch K W, R.A. Normann. Mobility performance with a pixelized vision system. *Vision Research*, 32 (1992), pp. 1367-1372
17. Cha K., Horch K W, Normann R A, Boman D K. Reading speed with a pixelized vision system. *J Opt Soc Am A.* 1992;9:673-677.
18. Chader G., et al. Artificial vision: needs, functioning, and testing of retinal electronic prosthesis. *Progress Brain Research*, Vol. 175, 2009.
19. Chai X., et al. Recognition of Pixelized Chinese Characters Using Simulated Prosthetic Vision. *Artif Organs.* 2007 Mar;31(3):175-82.
20. Chen K., Y.-K. Lo, and W. Liu, "A 37.6 mm<sup>2</sup> 1024-channel high-compliance-voltage SoC for epiretinal prostheses," in *IEEE Int. Solid-State Circuits Conf., ISSCC 2013*, 2013, pp. 294-295
21. Chen K., Z. Yang, L. Hoang, J. Weiland, M. Humayun, and W. Liu, "An integrated 256-channel epiretinal prosthesis," *IEEE J. Solid-State Circuits*, vol. 45, no. 9, pp. 1946-1956, Sep. 2010.
22. Chen S., Gregg J. Suening, John W. Morley, Nigel H. Lovell. Simulating prosthetic vision: I. Visual models of phosphenes. *Vision Research* 49 (2009) 1493-1506.
23. Chen, C. The local cone and rod system function in early age-related macular degeneration. *Documenta Ophthalmologica.* July 2004, Volume 109, Issue 1, pp 1-8
24. Chow A. Y., V. Y. Chow, K. Packo, J. Pollack, G. Peyman, and R. Schuchard, B. The artificial silicon retina microchip for the treatment of vision loss from retinitis pigmentosa. *Arch. Ophthalmol.*, vol. 122, p. 460, 2004
25. Cogan, S. F. "Neural stimulation and recording electrodes," *Annu. Rev. Biomed. Eng.*, vol. 10, pp. 275-309, 2008
26. Curcio C. A., Allen, K. A. Topography of ganglion cells in human retina. *J Comp Neurol.* Vol. 300, Issue 1, pages 5-25, 1990.
27. Curcio C. A., Sloan, Kenneth R.; Kalina, Robert E.; Hendrickson, Anita E. (1990). "Human photoreceptor topography". *The Journal of Comparative Neurology* 292 (4): 497-523
28. Curcio, C. A. Photoreceptor topography in ageing and age-related maculopathy. *Eye* (2001) 15, 376-383
29. Da Cruz L., B. F. Coley, J. D. Dorn, F. Merlini, E. Filley, P. Christopher, F. K. Chen, F. Wuyyuru, J. A. Sahel, P. E. Stanga, M. S. Humayun, R. J. Greenberg, and G. Dagnelie, "The Argus II epiretinal prosthesis system allows letter and word reading and long-term function in patients with profound vision loss," *Brit. J. Ophthalmol.*, vol. 97, no. 5, pp. 632- 636, May 2013].
30. Dagnelie G. Visual Prosthetics: Physiology, Bioengineering, Rehabilitation. Springer Science & Business Media, 21.02.2011.
31. Dagnelie G., David Barnett; Mark S. Humayun; Robert W. Thompson, Jr. Paragraph Text Reading Using a Pixelized Prosthetic Vision Simulator: Parameter Dependence and Task Learning in Free-Viewing Conditions. *Investigative Ophthalmology & Visual Science* March 2006, Vol.47, 1241-1250.
32. De Vittorio M., et al. Nanotechnology and Neuroscience: Nano-electronic, Photonic and Mechanical Neuronal Interfacing. Springer, 8 Jul 2014
33. Dobelle W. H. (2000). Artificial vision for the blind by connecting a television camera to the visual cortex. *American Society for Artificial Internal Organs*, 46, 3-9.
34. Dobelle W. H., Mladejovsky, M. G., & Girvin, J. P. (1974). Artificial vision for the blind: Electrical stimulation of visual cortex offers hope for a functional prosthesis. *Science*, 183, 440-444.
35. Dommel N., et al. A CMOS retinal neurostimulator capable of focussed, simultaneous stimulation *J Neural Eng.* vol. 6, pp. 035006, 2009
36. Donaldson N., Vanhoestenbergh A. "Corrosion of silicon integrated circuits and lifetime predictions in implantable electronic devices," *J. Neural Eng.*, vol. 10, no. 3, pp. 1-13, Mar. 2013

37. Dorf R. The Electrical Engineering Handbook, Second Edition. CRC Press, 26 Sep 1997.
38. Dowling John E. Encyclopedia of the Human Brain, 2002
39. Duay, J., Eleanor Gillette, Ran Liu, Sang Bok Lee. Highly flexible pseudocapacitor based on freestanding heterogeneous MnO<sub>2</sub>/conductive polymer nanowire arrays. *Phys. Chem. Chem. Phys.*, 2012, 14, 3329–3337.
40. Ebrey T.; Koutalos, Yiannis (January 2001). "Vertebrate Photoreceptors". *Progress in Retinal and Eye Research* 20 (1): 49–94
41. Eckmiller R. Learning retina implants with epiretinal contacts. *Ophthalmic Res.* 1997;29:281–289.
42. Eger M., Reinhard Eckhorn, Marcus Wilms, Thomas Schanze. Visual resolution with retinal implants estimated from recordings in cat visual cortex. *Vision Research* 46 (2006) 2675–2690.
43. Eickenscheidt, M. Jenkner, R. Thewes, P. Fromherz, and G. Zeck, "Electrical stimulation of retinal neurons in epiretinal and subretinal configuration using a multicapacitor array," *J. Neurophysiol.*, vol. 107, no. 10, pp. 2742–2755, May 2012
44. Fay S. Tyner, John Russell Knott. Fundamentals of EEG Technology: Basic concepts and methods. Lippincott Williams & Wilkins, 1983.
45. Fekrat S., Jennifer S. Weizer. All about Your Eyes. Duke University Press, 2006.
46. Finn W. , et al. Handbook of Neuroprosthetic Methods. CRC Press, Dec 16, 2002
47. Fohlmeister J., et al. Modelling the repetitive firing of retinal ganglion cells. *Brain Research*, 1989
48. Fransen J. The retina-prosthesis interface in two rat models of retinitis pigmentosa and functional changes associated with photoreceptor loss. Dissertation, 2013
49. Fried S., et al. A Method for Generating Precise Temporal Patterns of Retinal Spiking Using Prosthetic Stimulation. *J Neurophysiol* 95: 970–978, 2006.
50. Fujii T., Y. Ibata, "Effects of heating on electrical activities of guinea pig olfactory cortical slices," *Eur. J. Physiol.*, vol. 392, pp. 257–260, 1982.
51. Gabbiani F., et al. Mathematics for Neuroscientists. Academic Press, 16 Sep 2010, page 302
52. Gao, J. Optoelectronic Integrated Circuit Design and Device Modeling. John Wiley & Sons, 19 Sep 2011
53. Garrison D. "Minimizing Thermal Effects of In Vivo Body Sensors". Retrieved May 5, 2010
54. Greenberg R J, Humayun M S and de Juan E 1997. Electrical stimulation pulse-width determines the target cell in the frog and human retina. *Invest. Ophthalmol. Vis. Sci.* 38 183–183
55. Greenberg R.J., T. J. Velte, M. S. Humayun, G. N. Scarlatis, and E. de Juan, Jr., "A computational model of electrical stimulation of the retinal ganglion cell," *IEEE Trans Biomed Eng.*, vol. 46, pp. 505–514, 1999.
56. Gui-shuang Y, et al. Night Vision Symptoms and Progression of Age-related Macular Degeneration in the Complications of AMD Prevention Trial. *Ophthalmology*, 2008
57. Guyton, A. (1986). Textbook of medical physiology (7th ed.). Philadelphia: Saunders
58. Hadjinicolaou A. E. Optimizing the Electrical Stimulation of Retinal Ganglion Cells. *IEEE Transactions on Neural Systems and Rehabilitation Engineering*. Vol 23, o 2, March 2015
59. Halliwell B. Reactive oxygen species and the central nervous system. *J Neurochem* 1992;59(5):1609–23
60. Heckenlively J., Geoffrey Bernard Arden. Principles and Practice of Clinical Electrophysiology of Vision. MIT Press, 2006
61. Hesse L, Schanze T, Wilms M and Eger M 2000 Implantation of retina stimulation electrodes and recording of electrical stimulation responses in the visual cortex of the cat *Graef Arch.Clin.Exp.* 238 840–5
62. Hodgkin AL, Huxley AF (1952) A quantitative description of membrane current and its application to conduction and excitation in nerve. *J. Physiol. (London)* 117, 500–544.
63. Honert, C. van den & Kelsall, D. C. Focused intracochlear electric stimulation with phased array channels a). *J. Acoust. Soc. Am.* 121, 3703–3716 (2007).
64. Horch K., Gurpreet S Dhillon. Neuroprosthetics: Theory and Practice. World Scientific, 2004.
65. Hornig R. et al. A method and technical equipment for an acute human trial to evaluate retinal implant technology. *J. Neural Eng.* 2 (2005) S129–S134.
66. Hornig R., T. Zehnder, M. Velikay-Parel, T. Laube, M. Feucht, and G. Richard, "The IMI Retinal Implant System," in *Artificial Sight: Basic Research, Biomedical Engineering, and Clinical Advances*, M. S. Humayun, J. D. Weiland, G. Chader, and E. X. Greenbaum, Eds. New York, NY, USA: Springer, 2007.
67. Horsager A., & Fine, I. (2011). The perceptual effects of chronic retinal stimulation. In *Visual Prosthetics: Physiology, Bioengineering, Rehabilitation*. (pp. 271–300). Springer US. DOI: 10.1007/978-1-4419-0754-7\_14.
68. Huang C. Q., P. M. Carter, and R. K. Shepherd, "Stimulus induced pH changes in cochlear implants: An in vitro and in vivo study," *Ann. Biomed. Eng.*, vol. 29, no. 9, pp. 791–802, Sep. 2001.
69. Humayun M. S. (2001). Intraocular retinal prosthesis. *Transactions of the American Ophthalmologic Society*, 99, 271–300
70. Humayun M. S., J. D. Dorn, L. Da Cruz, G Dagnelie, J. A. Sahel, P. E. Stanga, A. V. Cideciyan, J. L. Duncan, D. Elliott, E. Filley, A. C. Ho, A. Santos, A. B. Safran, A. Arditi, L. V. Del Priore, and R. J. Greenberg, "Interim results from the international trial of second sight's visual prosthesis," *Ophthalmology*, vol. 119, no. 4, pp. 779–788, Apr. 2012
71. Humayun M. S., Yanai, D., Greenberg, R. J., Little, J., Mech, B. V., Mahadevappa, M., et al. (2004). Clinical results with the model 11RP implant. In *Neural networks, 2004. IEEE international joint conference on*.
72. Humayun M.S., E.de. Juan, G. Dagnelie, R.J. Greenberg, R.H. Probst, D.H. Phillips. Visual perception elicited by electrical stimulation of retina in blind humans. *Archive of Ophthalmology*, 114 (1996), pp. 40–46
73. Humayun M.S., E.J. de Juan, J.D. Weiland, G. Dagnelie, S. Katona, R. Greenberg, and S. Suzuki, "Pattern electrical stimulation of the human retina," *Vision Research*, vol. 39, no. 15, pp. 2569–2576, 1999
74. Humayun M.S., J.D. Weiland, G.Y. Fujii, R. Greenberg, R. Williamson, J. Little, et al. Visual perception in a blind subject with a chronic microelectrode retinal prosthesis. *Vision Research*, 43 (2003), pp. 2573–2581
75. Imlay JA. Pathways of oxidative damage. *Annu Rev Microbiol* 2003;57:395–418
76. Jan E, Hendricks JL, Husaini V, Richardson-Burns SM, Sereno A, Martin DC, Kotov NA. Layered carbon nanotube-polyelectrolyte electrodes outperform traditional neural interface materials. *Nano Letters*, 2009, 9 (12), pp 4012–4018
77. Jensen RJ, et al. Thresholds for activation of rabbit retinal ganglion cells with relatively large, extracellular microelectrodes. *Invest Ophthalmol Vis Sci.* 2005 Apr;46(4):1486–96

78. Jepson L. Spatially Patterned Electrical Stimulation to Enhance Resolution of Retinal Prostheses. *The Journal of Neuroscience*, April 2, 2014, 34(14):4871– 4881.
79. Jepson, Lauren Hruby. Patterned electrical stimulation of primate retina for the development of retinal prostheses. Dissertation, 2012.
80. Jezernik S., Manfred Morari. "Energy-Optimal Electrical Excitation of Nerve Fibers". *IEEE Transactions on Biomedical Engineering*, Vol. 52, No. 4, April 2005
81. Jiang G, Zhou DD. *Implantable Neural Prostheses*. Vol. 2. Springer; New York: 2010. Technology advances and challenges in hermetic packaging for implantable medical devices; pp. 27–61.
82. Judd, D. B., Wyszecki, Günter (1975). *Color in Business, Science and Industry*. Wiley Series in Pure and Applied Optics (third ed.). New York: Wiley-Interscience.
83. Kamenewa T., H. Meffin, and A. N. Burkitt, "Modelling intrinsic electro physiological properties of ON and OFF retinal ganglion cells," *J. Comput. Neuroscience*, vol. 31, no. 3, 2011.
84. Karlheinz Graf, et al. *Physics and Chemistry of Interfaces*. John Wiley & Sons, 6 Mar 2006
85. Kasi H., W. Hasenkamp, G. Cosendai, A Bertsch, and P. Renaud, "Simulation of epiretinal prostheses - Evaluation of geometrical factors affecting stimulation thresholds," *Journal of Neuroengineering and Rehabilitation*, vol. 8, no. 1, 2011.
86. Kathryn L, et al. *Pathophysiology: The Biologic Basis for Disease in Adults and Children*. Elsevier Health Sciences, 2015
87. Kaserü M, Feuchel M, Bornfeld N, Laube T, Walter P, Rössler G, Velikay-Parel M, Hornig R, Richard G. Acute electrical stimulation of the human retina with an epiretinal electrode array. *Acta Ophthalmol*. 2012 Feb;90(1):e1-8.
88. Klauke S. et al. Stimulation with a Wireless Intraocular Epiretinal Implant Elicits Visual Percepts in Blind Humans. *Investigative Ophthalmology & Visual Science* January 2011, Vol.52, 449-455. doi:10.1167/iovs.09-4410.
89. Kolb H. *Morphology and Circuitry of Ganglion Cells*. Webvision, 2011.
90. Kolb H. *Roles of Amacrine Cells*. NCBI, 2005
91. Kristensson C. Evaluation of the retinal ON and OFF responses in the dog ERG. Faculty of Veterinary Medicine and Animal Science Department of Clinical Sciences. 2014
92. Krizaj D, Ryskamp DA, Tian N et al (2014) From mechanosensitivity to inflammatory responses: new players in the pathology of glaucoma. *Curr Eye Res* 39:105–119.
93. Kuhn Andreas. *Modeling Transcutaneous Electrical Stimulation*. Diss. ETH No. 17948, 2008
94. LaManna J. C., K. A. McCracken, M. Patil, and O. J. Prohaska, "Stimulus- activated changes in brain tissue temperature in the anesthetized rat," *Metabolic Brain Disease*, vol. 4, pp. 225–237, 1989
95. Lange C, Feltgen N, Junker B, et al. Resolving the clinical acuity categories "hand motion" and "counting fingers" using the Freiburg Visual Acuity Test (FrACT). *Graefes Arch Clin Exp Ophthalmol*. 2009; 247:137–42
96. Lea C., et al. *A2 Biology for AQA Specification B*. Heinemann, 2001
97. Legge G.E., S.J. Ahn, T.S. Klitz, A. Luebker. The visual span in normal and low vision. *Vision Research*, 37 (1997), pp. 1999–2010
98. Lehto M., Steven J. Landry. *Introduction to Human Factors and Ergonomics for Engineers*, Second Edition. CRC Press, 26 Oct 2012
99. Lim J. *Age-Related Macular Degeneration*. CRC Press, 14 Aug 2002
100. Lovell N., et al. Current distribution during parallel stimulation: Implications for an epiretinal neuroprosthesis. *IEEE Eng Med Biol Soc*, 2005
101. Lujan Villarreal D. (a), Dietmar Schroeder, and Wolfgang H. Krautschneider, "Feasibility Study of a 1000+ Electrode Array in Epiretinal Prosthesis," *International Journal of Pharma Medicine and Biological Sciences*, Vol. 5, No. 3, pp. 163-170, July 2016. 10.18178/ijpmb.5.3.163-170.
102. Lujan Villarreal D. (b), Dietmar Schroeder and Wolfgang H. Krautschneider. Charge Density Study using Low Electrode Diameter in Epiretinal Prosthesis. ICTOpen2016 Conference. Amersfoort. The Netherlands. March 22 – 23, 2016
103. Lujan Villarreal D. (c), Dietmar Schroeder, and Wolfgang H. Krautschneider, "Novel Method for Realizing 1000+ Electrode Array in Epi- or Subretinal Prosthesis," *International Journal of Pharma Medicine and Biological Sciences*, Vol. 5, No. 3, pp. 146-153, July 2016. 10.18178/ijpmb.5.3.146-153.
104. Lujan Villarreal D., Dietmar Schroeder and Wolfgang H. Krautschneider. Equivalent circuit model to simulate the neuromuscular electrical stimulation. ICT.Open, Rotterdam, 22-23 October 2012
105. Lujan Villarreal D., Dietmar Schroeder, and Wolfgang H. Krautschneider. Equivalent Circuit Model to Simulate Neurostimulation by using Different Waveforms. ICT Open 2013, Eindhoven, November 27-28, 2013
106. Lujan Villarreal, D., Aljoscha Reinert, Jan Claudio Loitz, Dietmar Schroeder and Wolfgang H. Krautschneider. Energy Efficiency Comparison for Neurostimulation using Exponentially Increasing and Rectangular Waveforms. Stimulation with Simulation Comparison. ICTOpen 2015 Conference Proceedings. Amersfoort, The Netherlands, March, 2015
107. Lujan Villarreal D. (a), Dietmar Schroeder, and Wolfgang H. Krautschneider. A Treatise of the Physical Aspects of Phosphenes and Single-Cell Selectivity in Retinal Stimulation. *Int Journal Comput Neural Eng*. 2017; 4(2):55-70.
108. Lujan Villarreal D. (b), Dietmar Schroeder, and Wolfgang H. Krautschneider. Biomimetic Stimulating Array for Single Localized Stimulation in Visual Prosthesis. *Int Journal Comput Neural Eng*. 2017; 4(3):76-90.
109. Macdonald, J. R. (2013). *Complex Nonlinear Least Squares Fitting Program*. Online at: <http://jrossmacdonald.com/>. Retrieved on 27.05.2015
110. Madou M. *Solid-State Physics, Fluidics, and Analytical Techniques in Micro- and Nanotechnology*. CRC Press, 13 Jun 2011
111. Mahadevappa, M., Weiland, J., Yani, D., Fine, I., Greenberg, R., & Humayun, M. (2005). Perceptual thresholds and electrical impedance in 3 retinal prosthesis subjects. *IEEE Transactions on Neural System Rehabilitation Engineering*, 13, 201–206
112. Majji A., M. Humayun; J. Weiland; S. Suzuki; S. D'Anna; E. deJuan Jr. (1999). "Long-term histological and electrophysiological results of an inactive epiretinal electrode array implantation in dogs". *Investigative Ophthalmology and Visual Science* 40 (9): 2073–81
113. Margalit E et al 2002 Retinal prosthesis for the blind *Surv. Ophthalmol*. 47 335–56
114. Matteucci PB, Chen SC, Tsai D, et al. Current steering in retinal stimulation via a quasimonopolar stimulation paradigm. *Invest Ophthalmol Vis Sci*. 2013; 54:4307–4320. DOI:10.1167/iov.13-11653
115. Maureen D. Optogenetics: Can This Innovative Gene Therapy Treat Degenerative Retinal Disease and Possibly Restore Sight? 2015

116. McAdams E. Biomedical Electrodes For Biopotential Monitoring and Electrostimulation. Integrated Circuits and Systems. Springer Science & Business Media, 2 Nov 2010.
117. McCreery DB, Agnew WF, Bullara LA (2002) The effects of prolonged intracortical microstimulation on the excitability of pyramidal tract neurons in the cat. *Annals of Biomedical Engineering* 30: 107–119.
118. McNeal D. Analysis of a model for excitation of myelinated nerve. *IEEE Transactions on Biomedical Engineering*, 1976
119. Merrill D. R., M. Bikson, and J. G. Jefferys, "Electrical stimulation of excitable tissue: Design of efficacious and safe protocols," *J. Neurosci. Methods*, vol. 141, no. 2, pp. 171–198, Feb. 15, 2005.
120. Meyer R.D., Cogan, S.E., Nguyen, T.H. & Rauh, R.D. Electrodeposited iridium oxide for neural stimulation and recording electrodes. *IEEE Trans. Neural Syst. Rehabil. Eng.* 9, 2-11 (2001).
121. Meza M. Stimulation of Neurons by Electrical Means. Logos Verlag Berlin GmbH. 2015
122. Meza M., D. Schroeder, and W. H. Krautschneider, "A scalable 64 channel neurostimulator based on a hybrid architecture of current steering DAC," in *Proc. Middle East Conference on Biomedical Engineering*, 2014.
123. Meza, M., Dietmar Schroeder and Wolfgang H. Krautschneider. Neuromuscular Electrical Stimulation Using Different Waveforms - Properties comparison by applying single pulses. Institute of Nanoelectronics. Hamburg University of Technology. Hamburg, Germany. 2012.
124. Miklavcic, D., Natasa Pavselj, Hart Francis. Electric Properties of Tissues. Wiley Encyclopedia of Biomedical Engineering, 2006.
125. Moghadam G., Robert Wilke, Gregg J. Suaning, Nigel H. Lovell, and Socrates Dokos. Quasi-Monopolar Stimulation: A Novel Electrode Design Configuration for Performance Optimization of a Retinal Neuroprosthesis. *PLoS One*. 2013; 8(8): e73130. doi: 10.1371/journal.pone.0073130.
126. Monge M., M. Raj, et al. "A fully intraocular 0.0169 mm/pixel 512-channel self-calibrating epiretinal prosthesis in 65 nm CMOS," in *IEEE Int. Solid-State Circuits Conf., ISSCC 2013*, 2013, pp. 296–297
127. Montero J., et al. Equivalent circuit models for electrochemical impedance spectroscopy of PEDOT-coated electrodes. 6th IEEE Germany Student Conference, 2015.
128. Mukhopadhyay, M. Mechanics of Composite Materials and Structures. Universities Press, 1 Jan 2005.
129. Nakanishi S. Processing and Integration Mechanisms of Visual Transmission in the Retinal Network. The Neural Basis of Early Vision. Springer Science & Business Media, 2013
130. Nanduri D., I. Fine, A. Horsager, G. M. Boynton, M. S. Humayun, R. J. Greenberg, and J. D. Weiland, "Frequency and amplitude modulation have different effects on the percepts elicited by retinal stimulation," *Invest. Ophthalmol. Vis. Sci.*, vol. 53, no. 1, pp. 205–214, Jan. 2012
131. Nguyen, C. Radio-Frequency Integrated-Circuit Engineering. John Wiley & Sons, 16 Mar 2015
132. Niebauer M.J. et al. Iridium Oxide-Coated Defibrillation Electrode : Reduced Shock Polarization and Improved Defibrillation Efficacy. *Circulation* 96, 3732-3736 (1997).
133. Noorsal E., et al. A Neural Stimulator Frontend with High-Voltage Compliance and Programmable Pulse Shape for Epiretinal Implants. *IEEE J. Solid-State Circuits*, vol. 47, no. 1, pp. 244–256, Sep. 2012
134. Nutt J.G., V.C.Anderson, J.H.Peacock, J.P.Hammerstad, and K.J.Burchiel, "DBS and diathermy interaction induces severe CNS damage" *Neurology*, vol. 56, pp. 1384–1386, 2001
135. Ortmanns M., A. Rocke, M. Gehrke, and H. J. A. T. H. J. Tiedtke, "A 232-channel epiretinal stimulator ASIC," *IEEE J. Solid-State Circuits*, vol. 42, no. 12, pp. 2946–2959, Dec. 2007
136. Palanker D., A. Vankov, P. Huie, and S. Baccus, B. Design of a high-resolution optoelectronic retinal prosthesis, [ *J. Neural Eng.*, vol. 2, pp. 105–120, 2005.
137. Pandey R. Handbook of Semiconductor Electrodeposition. CRC Press, 25 Apr 1996
138. Peyman G., A.Y. Chow, C. Liang, V.C. Chow, J.I. Perlman, N.S. Peachey Subretinal semiconductor microelectrode array *Ophthalmic Surgery and Lasers*, 29 (1998), pp. 234–241
139. Piyathaisere D., E. Margalit; S. Chen; J. Shyu; S. D'Anna; J. Weiland; et. al. (2003). "Heat effects on the retina". *Ophthalmic Surgery, Lasers, and Imaging* 34 (2): 114–20
140. Publio R, Oliveira RF, Roque AC (2009) A computational study on the role of gap junctions and rod Ih conductance in the enhancement of the dynamic range of the retina. *PLoS One* 4:e6970
141. Purves D, et al. Neuroscience. 2nd edition, 1997.
142. Rao, S. The Finite Element Method in Engineering. Butterworth-Heinemann, 15 Mar 2011.
143. Ratner B. Biomaterials Science: An Introduction to Materials in Medicine. Academic Press, 31 Dec 2012.
144. Rattay, L. P. Paredes, and R. N. Leao, "Strength-duration relationship for intra- versus extracellular stimulation with microelectrodes" *Neuroscience*, vol. 214, pp. 1–13, July 2012
145. Reynolds J., et al. Pediatric Retina. Springer Science & Business Media, 14 Sep 2010
146. Richard C. Dorf. Electronics, Power Electronics, Optoelectronics, Microwaves, Electromagnetics, and Radar. CRC Press, 13 Jan 2006
147. Rizzo III J. F., Wyatt, J., Loewenstein, J., Kelly, S., & Shire, D. (2003). Perceptual efficacy of electrical stimulation of human retina with a microelectrode array during short-term surgical trials. *Investigative Ophthalmology & Visual Science*, 44, 5362–5369.
148. Rizzo III J., et al. Methods and Perceptual Thresholds for Short-Term Electrical Stimulation of Human Retina with Microelectrode Arrays. *Ophthalmology & Visual Science*, December 2003, Vol. 44, No. 12
149. Rizzo III J.F., J.L. Wyatt. Prospects for a visual prosthesis. *The Neuroscientist*, 3 (1997), p. 251.
150. Robillard C., et al. Neural stimulation safety and energy efficiency: Waveform analysis and validation. 11th Annual Conference of the International FES Society, 2006.
151. Roessler G., T. Laube, C. Brockmann, T. Kirschkamp, B. Mazinani, M. Goertz, C. Koch, I. Krisch, B. Sellhaus, H. K. Trieu, J. Weis, N. Bornfeld, H. Röhthgen, A. Messner, W. Mokwa, and P. Walter, "Implantation and explantation of a wireless epiretinal retina implant device: Observations during the EPIRET3 prospective clinical trial," *Invest. Ophthalmol. Vis Sci.*, vol. 50, no. 6, pp. 3003–3008, Jun. 2009.
152. Rothermel A., et al., "A 1600-Pixel Subretinal Chip with DC-Free Terminals and  $\pm 2V$  Supply Optimized for Long Lifetime and High Stimulation Efficiency," *ISSCC Dig. Tech. Papers*, pp. 144–145, Feb. 2008.



153. Rushton D. N., & Brindley, G. S. (1978). Properties of cortical electrical phosphenes. In S. J. Cool & E. J. I. Smith (Eds.), *Frontiers in visual science*. New York: Springer-Verlag.
154. Santos A, et al. Preservation of the Inner Retina in Retinitis Pigmentosa. A Morphometric Analysis. *Arch Ophthalmol*. 1997
155. Scheiner A., J. Thomas Mortimer, Uros Roessmann. Imbalanced biphasic electrical stimulation: Muscle tissue damage. *Annals of Biomedical Engineering*. July 1990, Volume 8, Issue 4, pp 407-425
156. Schwahn H N, Gekeler F, Kohler K, Kobuch K, Sachs H G, Schulmeyer F, Jakob W, Gabel V P and Zrenner E 2001 Studies on the feasibility of a subretinal visual prosthesis: data from Yucatan micropig and rabbit Graef *Arch. Clin. Exp.* 239 961-7
157. Seese T. M., H. Harasaki, G. M. Saidel, and C. R. Davies, "Characterization of tissue morphology, angiogenesis, and temperature in the adaptive response of muscle tissue in chronic heating," *Lab. Investigation*, vol. 78, pp. 1553-1562, 1998.
158. Sekirnjak C., P. Hottowy, A. Sher, W. Dabrowski, A. M. Litke, and E.J. Chichilnisky, "Electrical stimulation of mammalian retinal ganglion cells with multielectrode arrays," *J. Neurophysiol.*, vol. 95, no. 6, pp.3311-3327, June 2006
159. Shintani, Kelly; Shechtman, Diana L.; Gurwood, Andrew S. (2009). "Review and update: Current treatment trends for patients with retinitis pigmentosa". *Optometry* 80 (7): 384-401
160. Shire D., W. Ellersick, S. Kelly, P. Doyle, A. Priplata, W. Drohan, O.Mendoza, M. Gingerich, B. McKee, J. Wyatt, and J. Rizzo, "ASIC design and data communications for the Boston retinal prosthesis," in *Proc. Int. Conf. IEEE Eng. Med. Biol., EMBC 2012*, Aug. 28-Sep. 1 2012, pp. 292-295
161. Siegel A., et al. *Essential Neuroscience*. Lippincott Williams & Wilkins, 2006
162. Singh V., A. Roy, R. Castro, K. McClure, R. Dai, R. Agrawal, R. Greenberg, J. Weiland, M. Humayun, and G. Lazzi, "On the thermal elevation of a 60-electrode epiretinal prosthesis for the blind," *IEEE Trans. Biomed. Circuits Syst.*, vol. 2, no. 4, pp. 289-300, 2008.
163. Sivaprakasam M., W. Liu, G. Wang, J. D. Weiland, and M. S. Humayun, "Architecture tradeoffs in high-density microstimulators for retinal prosthesis," *IEEE Trans. Circuits Syst. I, Reg. Papers*, vol. 52, no. 12, pp. 2629-2641, Dec. 2005
164. Sohee Kim, et al. Preliminary study of the thermal impact of a microelectrode array implanted in the brain. *Engineering in Medicine and Biology Society*, 2006. EMBS'06. International Conference of the IEEE
165. Sohee Kim, Member, IEEE, Prashant Tathireddy, Richard A. Normann, Member, IEEE, and Florian Solzbacher, Member, IEEE. Thermal Impact of an Active 3-D Microelectrode Array Implanted in the Brain. *IEEE Transactions on Neural Systems and Rehabilitation Engineering*, Vol. 15, No. 4, December 2007
166. Sooksood K., et al., "A Neural Stimulator Front-End with Arbitrary Pulse Shape, HV Compliance and Adaptive Supply Requiring 0.005mm<sup>2</sup> in 0.35μm HVCMOS," *ISSCC Dig. Tech. Papers*, pp. 306-308, Feb. 2011
167. Soucy, E; Wang, Y; Nirenberg, S; Nathans, J; Meister, M (1998). "A Novel Signaling Pathway from Rod Photoreceptors to Ganglion Cells in Mammalian Retina". *Neuron* 21 (3): 481-93
168. Splinter R. *Handbook of Physics in Medicine and Biology*. CRC Press, 5 Apr 2010
169. Srinivasan S. *Fuel Cells: From Fundamentals to Applications*. Springer Science & Business Media, 5 May 2006.
170. Starbird R., "Study of organic materials to improve electrical properties of neural stimulation electrodes," *Dissertation*, 2013.
171. Starbird, R. et al. Electrochemical properties of PEDOT-NaPSS galvanostatically deposited from an aqueous micellar media for invasive electrodes, *IEEE BMEICON*, 2012.
172. Stephen J. R, et al. *Retina*. Elsevier Health Sciences, 2012
173. Stingl K., K. U. Bartz Schmidt, D. Besch, A. Braun, A. Bruckmann, F. Gekeler, U. Grepmaier, S. Hipp, G. H'ortd'orfer, C. Kernstock, A. Kusnyerik, A. Schatz, K. T. Stingl, T. Peters, B. Wilhelm, and E. Zrenner, "Artificial vision with wirelessly powered subretinal electronic implant alpha-IMS," *Proc. Royal Soc. B: Biol. Sci.*, vol. 280, no. 1757, pp. 1-8, Apr. 2013
174. Stohs SJ. The role of free radicals in toxicity and disease. *J Basic Clin Physiol Pharmacol* 1995;6(3-4):205-28
175. Stratton JA (1941): *Electromagnetic Theory*, McGraw-Hill, New York.
176. Suzuki S. Comparison of Electrical Stimulation Thresholds in Normal and Retinal Degenerated Mouse Retina. *Japanese Journal of Ophthalmology*. July 2004, Volume 48, Issue 4, pp 345-349
177. Thompson R. W. Jr, G. David Barnett, Mark S. Humayun, Gislin Dagnelie. *Facial Recognition Using Simulated Prosthetic Pixelized Vision. Investigative Ophthalmology & Visual Science*, November 2003, Vol. 44, No. 11.
178. Tran N., et al. A Complete 256-Electrode Retinal Prosthesis Chip. *IEEE Journal of Solid-State Circuits*. Vol. 49. No. 3, March 2014
179. Tychsen L. In: *Binocular Vision*, in *Adler's Physiology of The Eye*. Hart WM, editor. Mosby Year Book; St. Louis: 1992. pp. 773-853
180. Veraart C., Raftopoulos, C., Mortimer, J. T., Delbeke, J., Pins, D., Michaux, G., et al. (1998). Visual sensations produced by optic nerve stimulation using an implanted self-sizing spiral cuff electrode. *Brain Research*, 813, 181-186.
181. Walsh P., Magnetic stimulation of the human retina. *Fed Proc.* 5, 109-110. 1946.
182. Walsh V., Cowey A. Magnetic stimulation studies of visual cognition. *Trends Cogn. Sci.* 2, 103-110. 1998.
183. Walter P., Mokwa W. Epiretinal visual prostheses. *Ophthalmologe*. 2005
184. Warman EN, Grill WM, Durand D. Modeling the effects of electric fields on nerve fibers: determination of excitation thresholds. *IEEE Trans Biomed Eng* 1992;39(12):1244-54.
185. Weiland J. D., and Mark S. Humayun. Retinal Prosthesis. *IEEE Transactions on Biomedical Engineering*, Vol. 61, No. 5, May 2014
186. Weiland J. D., and Mark S. Humayun. Visual Prosthesis. *Proc. IEEE*, vol. 96, no. 7, pp. 1076-1084, Jul. 2008.
187. Weiland J. D., Yanai, D., Mahadevappa, M., Williamson, R., Mech, B. V., Fujii, G. Y., et al. (2003). Electrical stimulation of retina in blind humans. In 25th international conference of the IEEE engineering in medicine and biology society.
188. Weiland J.D. & Anderson, D.J. Chronic neural stimulation with thin-film, iridium oxide electrodes. *IEEE Trans. Biomed. Eng.* 47, 911-918 (2000).
189. Wenzhi Sun, N Li, S He. Large-scale morphological survey of mouse retinal ganglion cells. *Journal of Comparative Neurology* 451 (2), 115-126, 2002.
190. Werginz P., H. Benav, E. Zrenner, and F. Rattay, "Modeling the response of ON and OFF retinal bipolar cells during electric stimulation," *Vision Research*, vol. 111, pp. 170-181, 2004.
191. Wilke R. et al. Spatial Resolution and Perception of Patterns Mediated by a Subretinal 16-Electrode Array in Patients Blinded by Hereditary Retinal Dystrophies. *Investigative Ophthalmology & Visual Science* July 2011, Vol.52, 5995-6003. doi:10.1167/iovs.10-6946.

192. Wong YT, Dommel N, Preston P, et al. Retinal neurostimulator for multifocal vision prosthesis. *IEEE Trans Neural Syst. Rehabil Eng.* 2007;15:425-434
193. Xiao X., J. Wang, C. Liu, J. A. Carlisle, B. Mech, R. Greenberg, D. Guven, R. Freda, M. S. Humayun, J. Weiland, and O. Auciello, B In vitro and in vivo evaluation of ultrananocrystalline diamond for coating of implantable retinal microchips,[ *J. Biomed. Mater. Res. B: Appl. Biomater.*, vol. 77, pp. 273-281, 2006
194. Xiao-Zi Riny Yuan. *Electrochemical Impedance Spectroscopy in PEM Fuel Cells: Fundamentals and Applications*. Springer Science & Business Media, 25 Nov 2009
195. Yanai D., J. D. Weiland, M. Mahadevappa, R. J. Greenberg, I. Fine, and M. S. Humayun, B. Visual performance using a retinal prosthesis in three subjects with retinitis pigmentosa, *Amer. J. Ophthalmol.*, 2007
196. Yin L., et al. Chromatic Properties of Horizontal and Ganglion Cell Responses Follow a Dual Gradient in Cone Opsin Expression. *The Journal of Neuroscience*, November 22, 2006. 26(47):12351-12361
197. Yin S., N. H. Lovell, G. J. Suening, and S. Dokos, "A continuum model of the retinal network and its response to electrical stimulation," in *Proc. IEEE EMBS*, 2010.
198. Zhou D., et al. *Implantable Neural Prostheses 2: Techniques and Engineering Approaches*. Springer Science & Business Media, 10 Jul 2010
199. Zrenner E. (2002). "Will retinal implants restore vision?". *Science* 295: 1022-5.
200. Zrenner E. Subretinal implants for the restitution of vision in blind patients, presented at the ARVO Annu. Meeting, Ft. Lauderdale, FL, USA, 2007
201. Zrenner E., Besch, D., Bartz-Schmidt, K. U., Gekeler, F., Gabel, V. P., Kutteneuler, C., et al. (2006). Subretinal chronic multi-electrode arrays implanted in blind patients. *Investigative Ophthalmology & Visual Science*, 47, 1538. E-Abstract.
202. Zrenner E., Wilke, R., Zabel, T., Sachs, H., Bartz-Schmidt, K., Gekeler, F., et al. (2007). Psychometric analysis of visual sensations mediated by subretinal microelectrode arrays implanted into blind retinitis pigmentosa patients. *Investigative Ophthalmology & Visual Science*, 48, 659. E-Abstract.

# Lebenslauf

Name	Luján Villarreal
Vorname	Diego
Geburtsdatum	04. März 1983
Geburtsort, -land	Monterrey, Nuevo León. Mexiko

## Schulbildung

08.1998 – 08.2001	Gymnasium in Instituto Tecnológico y de Estudios Superiores de Monterrey (ITESM). Campus Eugenio Garza Lagüera. Monterrey, Mexiko.
08.2001 – 12.2006	Studium an der ITESM in Campus Monterrey. Bachelor in Mechatronik.
10.2008 – 12.2010	M.Sc. Microelectronics and Microsystems. Technische Universität Hamburg-Harburg. Hamburg, Deutschland.

## Berufstätigkeit

06.2007 – 07.2008	Berater bei Deloitte in Monterrey, Mexiko. Abteilung: Enterprise Risk Services.
01.2011 – 02.2012	Projektleiter bei der School of Medicine ITESM. Abteilung: Research & Development.
02.2012 – 12.2017	Wissenschaftlicher Mitarbeiter im Institut für Nano- und Medizinelektronik Technische Universität Hamburg-Harburg. Hamburg, Deutschland.

## Praktikum

03.2005 – 09.2005	SICK AG in Walldkirch, Deutschland. Abteilung: Research & Development.
-------------------	--